

FINAL REPORT
Grant No. N00014-98-1-0740

July 1, 1998 – June 30, 2002

**MECHANISMS OF CRACK TIP HYDROGEN EMBRITTLEMENT IN
HIGH STRENGTH ALLOY STEELS FOR MARINE APPLICATIONS**

Submitted to:

**Office of Naval Research
1401 East Broad Street
Richmond, VA 23219**

Attention: John A. Sedriks, ONR 332

Submitted by:

**Richard P. Gangloff
Professor**

**John R. Scully
Professor**

**SEAS Report No. UVA/525522/MSE03/101
October 2002**

DEPARTMENT OF MATERIALS SCIENCE AND ENGINEERING

**SCHOOL OF
ENGINEERING 
& APPLIED SCIENCE**

**University of Virginia
Thornton Hall
Charlottesville, VA 22903**

**DISTRIBUTION STATEMENT A:
Approved for Public Release -
Distribution Unlimited**

20021105 066

UNIVERSITY OF VIRGINIA
School of Engineering and Applied Science

The University of Virginia's School of Engineering and Applied Science has an undergraduate enrollment of approximately 1,500 students with a graduate enrollment of approximately 600. There are 160 faculty members, a majority of whom conduct research in addition to teaching.

Research is a vital part of the educational program and interests parallel academic specialties. These range from the classical engineering disciplines of Chemical, Civil, Electrical, and Mechanical and Aerospace to newer, more specialized fields of Applied Mechanics, Biomedical Engineering, Systems Engineering, Materials Science, Nuclear Engineering and Engineering Physics, Applied Mathematics and Computer Science. Within these disciplines there are well equipped laboratories for conducting highly specialized research. All departments offer the doctorate; Biomedical and Materials Science grant only graduate degrees. In addition, courses in the humanities are offered within the School.

The University of Virginia (which includes approximately 2,000 faculty and a total of full-time student enrollment of about 17,000), also offers professional degrees under the schools of Architecture, Law, Medicine, Nursing, Commerce, Business Administration, and Education. In addition, the College of Arts and Sciences houses departments of Mathematics, Physics, Chemistry and others relevant to the engineering research program. The School of Engineering and Applied Science is an integral part of this University community which provides opportunities for interdisciplinary work in pursuit of the basic goals of education, research, and public service.

REPORT DOCUMENTATION PAGE

Form Approved
OMB No. 074-0188

Public reporting burden for this collection of information is estimated to average 1 hour per response, including the time for reviewing instructions, searching existing data sources, gathering and maintaining the data needed, and completing and reviewing this collection of information. Send comments regarding this burden estimate or any other aspect of this collection of information, including suggestions for reducing this burden to Washington Headquarters Services, Directorate for Information Operations and Reports, 1215 Jefferson Davis Highway, Suite 1204, Arlington, VA 22202-4302, and to the Office of Management and Budget, Paperwork Reduction Project (0704-0188), Washington, DC 20503

1. AGENCY USE ONLY (Leave blank)		2. REPORT DATE Final	3. REPORT TYPE AND DATES COVERED 07/01/98 - 06/30/02	
4. TITLE AND SUBTITLE Mechanisms of Crack Tip Hydrogen Embrittlement in High Strength Alloy Steels for Marine Application			5. FUNDING NUMBERS N00014-98-1-0740	
6. AUTHOR(S) R.P. Gangloff, J.R. Scully, E. Richey III, R.L.S. Thomas, D. Li and M.A. Switzer				
7. PERFORMING ORGANIZATION NAME(S) AND ADDRESS(ES) University of Virginia Office of Sponsored Programs P. O. Box 400195 Charlottesville, Virginia 22904-4195			8. PERFORMING ORGANIZATION REPORT NUMBER UVA 110723-101-GG10077-31340 (FAS #5-25522)	
9. SPONSORING / MONITORING AGENCY NAME(S) AND ADDRESS(ES) Office of Naval Research Ballston Centre Tower One 800 N. Quincy St., Arlington, VA 22217			10. SPONSORING / MONITORING AGENCY REPORT NUMBER N/A	
11. SUPPLEMENTARY NOTES N/A				
12a. DISTRIBUTION / AVAILABILITY STATEMENT Approved for public release, distribution unlimited.				12b. DISTRIBUTION CODE N/A
13. ABSTRACT (Maximum 200 Words) <p>The primary objective of this research was to characterize and understand: (a) the interaction of a range of bulk-dissolved hydrogen concentrations with the complex tempered martensitic microstructure of AerMet[®]100 ultra-high strength steel, (b) the effect of such trapped hydrogen on fracture resistance associated with internal hydrogen embrittlement (IHE), and (c) the levels of trapped and diffusible hydrogen achieved after cadmium plating and baking operations. Studies of hydrogen transport rates, trapping and redistribution after heating sought to correlate embrittlement-threshold levels with redistribution of diffusible hydrogen during IHE.</p> <p>A strong dependence of the threshold stress intensity (K_{TH}) for the onset of IHE in AerMet[®]100 on diffusible H concentration was measured and modeled in this project. H was trapped at the interfaces of M_2C precipitates that are responsible for strengthening of peak aged AerMet[®]100. Modeling showed that very high levels of H can redistribute within the crack tip process zone and promote transgranular fracture due to two factors; unexpectedly high crack tip normal and hydrostatic stresses, as well as substantial weak reversible H trapping at M_2C precipitates unique to AerMet[®]100. Upon stressing, H redistributes to the crack tip process zone due to lattice dilation from the crack tip stress field.</p> <p>Slow hydrogen transport rates, high trap densities and a variety of microstructural trap sites complicate the effectiveness of conventional baking procedures in AerMet[®]100. Hydrogen capacity is large due to a high trap density and transport rates are over one order of magnitude slower in AerMet[®]100 than seen in other tempered martensitic microstructures. H transport is, also, dependent on diffusible hydrogen concentration. Nevertheless, diffusible and reversible trapped hydrogen concentrations were significantly reduced by baking bare electrochemically precharged AerMet[®]100 at 190°C, but intensified during 0.5-30 h of baking of cadmium plated AerMet[®]100. In the latter case, H was released from the cadmium layer into the steel. Diffusible hydrogen was eventually out-gassed to approximately 50% of as-plated values at long baking times. However, baking times up to 200 h did not lower reversibly and deeply trapped hydrogen contents. As shown by modeling, this reservoir of residual reversibly trapped hydrogen can promote IHE.</p> <p>The second objective was to identify the extent to which occluded pit/crevice geometry and electrochemical conditions affect local hydrogen production and uptake in PH 13-8 Mo stainless steel exposed to aqueous environments. Localized corrosion scaling laws of the type x^2/gap, where x is the pit depth and gap is the crevice or pit diameter, were successfully exploited to rescale the sizes of model pits from micrometer to millimeter-scale dimensions. Such rescaling enabled successful hydrogen measurements on global and local length scales inside rescaled model pits. Severe local hydrogen uptake was observed in model pits under conditions where boldly exposed surfaces on planar electrodes were in the passive state.</p>				
14. SUBJECT TERMS				15. NUMBER OF PAGES
				16. PRICE CODE
17. SECURITY CLASSIFICATION OF REPORT Unclassified	18. SECURITY CLASSIFICATION OF THIS PAGE Unclassified	19. SECURITY CLASSIFICATION OF ABSTRACT Unclassified	20. LIMITATION OF ABSTRACT UL	

**TRAP-GOVERNED HYDROGEN DIFFUSIVITY AND
UPTAKE CAPACITY IN ULTRAHIGH-STRENGTH
AERMET 100 STEEL**

R.L.S. Thomas, D. Li, R.P. Gangloff, J.R. Scully

Department of Materials Science and Engineering
University of Virginia
Charlottesville, VA 22904-4745
USA

Trap-Governed Hydrogen Diffusivity and Uptake Capacity in Ultrahigh-Strength AERMET 100 Steel

RICHARD L.S. THOMAS, DAOMING LI, RICHARD P. GANGLOFF, and JOHN R. SCULLY

The hydrogen-uptake capacity and mobility in ultrahigh-strength AERMET 100 are characterized for various electrochemical charging and baking conditions. From thermal desorption spectroscopy, the apparent hydrogen diffusivity ($D_H < 3 \times 10^{-8} \text{ cm}^2/\text{s}$ at 23 °C) is over tenfold less than the values typical of tempered martensitic steels such as AISI 4130. The value of D_H decreases with decreasing temperature below 200 °C, with a relatively high apparent activation energy for diffusion of 17.7 to $18.8 \pm 0.2 \text{ kJ/mol}$ at the 95 pct confidence level. The value of D_H also decreases with decreasing diffusible H concentration from less-severe charging or increased baking. Potentiostatic charging in saturated Ca(OH)_2 produced total and diffusible H concentrations in AERMET 100 which increase with (H^+/H) overpotential and are significantly higher than results for AISI 4130 steel under the same conditions. A significant H concentration was produced by zero overpotential deposition. These characteristics are explained by extensive reversible and irreversible H trapping involving at least three unique trap states in the ultrafine AERMET 100 microstructure. The former likely include coherent M_2C carbides, soluble Ni, or precipitated austenite, and the latter include larger incoherent M_xC_y or martensite lathed-packet interfaces. Baking at 23 °C and 200 °C removes H from the lowest binding-energy sites, but results in reduced D_H levels to prolong outgassing time. Additionally, substantial H was retained in stronger trap states. These trapping effects are pertinent to hydrogen embrittlement of AERMET 100 steel.

I. INTRODUCTION

A. Effect of Trapping on H Diffusivity and Solubility in Steels

THE lattice diffusivity of hydrogen (H) in steel is impeded strongly by the presence of microstructural inhomogeneities including grain boundaries, dislocations, carbides, and nonmetallic particles, which are potential H trapping sites.^[1] Whether a microstructural feature can act as a trapping site is governed by a potential-energy well (and binding energy (E_b)) relative to normal interstitial positions in the Fe lattice. With increasing strength of trapping proportional to the energy well depth, traps are categorized as reversible then irreversible.^[2] In the absence of traps, H diffusion occurs by random-jump migration between interstitial lattice positions, with a very short residence time for a diffusing H atom.^[2] Hydrogen diffusion is then described by the ideal lattice diffusivity (D_L) and governed by the activation energy for diffusion associated with the energy barrier (or lattice migration energy (E_m)) between interstitial positions. In pure annealed Fe, D_L is $1.3 \times 10^{-5} \text{ cm}^2/\text{s}$ at 25 °C,^[3] and E_m is 7 kJ/mol (0.07 eV/atom).^[2] Reversible trap sites with $E_b > E_m$ create an "effectively" higher barrier to H movement. Consequently, trapping decreases the rate of transport of H through the lattice and increases the activation energy for diffusion. This trap-affected, or apparent, H diffusivity (D_H)

is up to three orders of magnitude lower than D_L , depending on the nature and extent of trapping.^[3,4]

The effect of each type of trap depends on dissolved H concentration. In a lattice containing only irreversible traps which can be saturated, H diffusivity decreases to D_H during H uptake, until the irreversible traps fill with H. Ideal irreversible traps are often saturable at a low lattice H concentration and, once filled, no longer interact with dissolved H; consequently, the apparent D_H value increases to D_L . In contrast, reversibly trapped H is in "dynamic equilibrium" with H dissolved in the lattice and represents a permanent "impedance" to H transport.^[5] Therefore, the apparent D_H value in a lattice containing reversible traps is always less than D_L , and the difference is intensified at a lower H concentration.^[5]

In a perfect lattice, solubility is governed by the heat of solution for the solute in an ideal dilute solution.^[6] For a heat of solution for H in Fe equal to 28.6 kJ/mol, the perfect lattice H solubility (C_0) in equilibrium with 10^5 Pa H_2 is $3 \times 10^{-4} \text{ wppm}$ at 25 °C.^[2] In steels, however, the apparent H solubility (C_H) is increased dramatically by traps, where H accumulation alters the local heat of solution.^[4,5,7] For example, at 25 °C, the H solubility in martensitic AISI 4135 steel $\sigma_{YS} = 1380 \text{ MPa}$ is 0.4 wppm,^[8,9] about four orders of magnitude greater than that in high-purity Fe, due to H trapping at dislocations, solute, and other microstructural inhomogeneities.

Numerous studies have shown that D_H decreases and C_H increases, relative to values for pure iron, with increasing trap density and trap strength in steels.^[10-15] Quenched and tempered ultrahigh-strength steel (UHSS) microstructures possess many potential trap sites, including dislocations, solutes, martensite lath and packet boundaries, prior-austenite grain boundaries, retained or precipitated austenite, and

RICHARD L.S. THOMAS, formerly Graduate Student, Department of Materials Science and Engineering, University of Virginia, is R&D Engineer, Medtronic Ave., Santa Rosa, CA 95403. DAOMING LI, Research Scientist, and RICHARD P. GANGLOFF and JOHN R. SCULLY, Professors, are with the Department of Materials Science and Engineering, University of Virginia, Charlottesville, VA 22904-4745. Contact e-mail: jrs8d@virginia.edu

Manuscript submitted October 4, 2001.

carbides.¹¹⁶⁻¹⁹¹ Tensile strength and trapping frequently correlate, because nanoscale features that strengthen often provide effective sites for H trapping.^{12,11,14,15,18,20,21} For example, grain boundaries in iron-based alloys are H traps with a binding energy ranging from 29 kJ/mol (0.3 eV/atom)^{118,221} to 58 kJ/mol (0.6 eV/atom).^{118,231} Dislocations exhibit a H binding energy of 29 kJ/mol (0.3 eV/atom) in ferrous-based materials,¹²⁴¹ and semicoherent and incoherent carbides were characterized as H traps with binding energies ranging from 34 to 97 kJ/mol (0.35 to 1 eV/atom), increasing as the degree of coherency of the carbide/matrix interface decreased.^{116,191} Uncertainties in E_b arise from differences in measurement method, as well as some reports that equate E_d to E_b rather than the sum of $E_b + E_m$, where E_d is the activation energy for H desorption.

The E_b below which trapping is termed reversible, depends on temperature (T). As T increases, dissolved H atoms possess more thermal energy, given by kT (k being the Boltzmann's constant) energy. The probability of H escape from a trap site increases with kT for a given trap binding energy. At room temperature, where $kT \approx 4 \times 10^{-21}$ J (0.025 eV), a binding energy of 29 kJ/mol (0.3 eV/atom) was determined to be the value below which trapping was reversible in Fe-M-C ($M = V, Nb$, and Ti) alloys.¹²⁵¹ A separate investigation reported a higher value of 77 kJ/mol (0.8 eV/atom) as the upper value, below which trapping was reversible in steel at room temperature.^{15,261}

B. Trap-Rich AERMET* 100 Microstructure

*AERMET is a trademark of Carpenter Technology Corp., Wyomissing, PA.

AERMET 100 is a martensitic secondary hardening UHSS in which a specific austenization, air quench, refrigeration, and temper-age procedure was developed for optimal fracture toughness and slightly overaged yield strength.^{127,281} Optimized tempering at 482 °C produces an extremely fine microstructure^{29,29a,301} with a large density of potential trap sites, including (1) less than 0.1- μ m-diameter incoherent carbides (*i.e.*, $(MoCr)_7C_3$, $(FeCr)_x C_y$, TiC , and $(TiCrMo)C$) which provide grain refinement, (2) martensite laths (or plates) on the order of 0.15- μ m thick, both twinned and untwinned, with interfaces that are qualitatively high angle and arrayed in packets, (3) prior-austenite grain boundaries, (4) dislocations in martensite and not recovered at this tempering temperature, (5) finely distributed and generally crystalline-coherent M_2C (where $M = 66$ at. pct Cr, 18 Fe, and 16 Mo) in martensite, averaging 3 nm in diameter \times 10 nm in length, (6) solute clusters preceding M_2C precipitation, (7) precipitated austenite, and (8) Ni, Cr, and Mo dissolved in martensite and austenite.^{129,29a,301} The amount of retained austenite is essentially nil due to refrigeration.¹²⁹¹ Precipitated austenite is present exclusively as a thin layer (~ 3 nm) at martensite lath interfaces based on electron microscopy, but the volume fraction from X-ray diffraction measurements is uncertain, ranging from an average vol pct of 0.8¹²⁹¹ to 4^{129a1} for the 482 °C temper. The martensite-lath interface area and the proportion covered by precipitated austenite are uncertain. The Ni, Co, Cr, and Mo contents of austenite and martensite solid solutions were not measured. Among these AERMET 100 microstructural features, some should trap H with a relatively low binding energy (*i.e.*,

coherent M_2C , solute zones, solute in martensite or austenite, dislocations, and low-misorientation martensite interfaces), while others should trap H with relatively high binding energies, such as high-misorientation interfaces (prior- γ boundaries and martensite lath/packet interfaces), dislocation cores, and incoherent carbides. The lattice solubility of H in fcc austenite is high compared to martensite.¹²¹ Consequently, both reversible and irreversible trapping may be extensive in AERMET 100 in the temperature range from 25 °C to 300 °C.

Although studies on H trapping in AERMET 100 are lacking, experiments with Fe-M-C (where $M = Ti, V, Nb$) alloys revealed that both reversible and irreversible traps were produced by the precipitation of finely distributed coherent TiC , VC , and NbC during tempering.¹²⁵¹ For quenched and tempered Fe-Mo-C, the effective H solubility was increased by one order of magnitude, relative to the as-quenched condition, due to precipitation of coherent Mo_2C .¹⁴¹ In such microstructures, the number of reversible traps was much greater than that of irreversible traps: 10^{-2} to 10^{-3} vs 10^{-5} to 10^{-8} mol/cm³, respectively. In H-charged specimens, a significant fraction of the total dissolved H, relative to the interstitial lattice H concentration, resides in reversible traps.¹²⁵¹ If this trend is obeyed in H-charged AERMET 100, the quantity of reversibly trapped, mobile H may be substantial, and D_H may be reduced, regardless of the extent of additional irreversible trapping.

C. Effect of H Trapping on Hydrogen Embrittlement of UHSS

Hydrogen trapping critically affects the resistance of a steel to hydrogen embrittlement (HE).^{15,18,31,321} First, H diffusion to the crack-tip fracture-process zone is a key step in hydrogen-induced cracking.^{132,331} A lower D_H value results in lower rates of internal hydrogen embrittlement (IHE) as well as hydrogen-environment embrittlement (HEE) in trap-rich steels. Second, strong reversible or irreversible H traps, connected in three dimensions and containing "in-place" bound H, may define a brittle-crack path and decrease resistance to HE. Third, the strength and distribution of traps alter the time-stress-dependent redistribution of H to microstructural features that constitute a brittle crack path. In a closed system (*i.e.*, a fixed quantity of total dissolved H), the quantity of H available to diffuse to brittle fracture sites depends on the strength and distribution of the H traps. Hydrogen trapped in a large population of low-binding energy traps will have a high probability of release from such traps at room temperature, and, therefore, a large population of weak traps provides a reservoir of highly mobile H. This mobile H could diffuse to areas of lower H chemical potential, such as the dilated region under triaxial tensile stress ahead of a crack tip, and exacerbate embrittlement.¹³⁴¹ For example, K_{TH} in AISI 4135 steel decreased as the concentration of predissolved-diffusible H increased.^{19,351} In contrast, a homogeneous distribution of irreversible or strong-reversible traps can prevent H from segregating to lower-interaction energy sites, such as prior-austenite and martensite-lath boundaries, which are susceptible to HE.^{136,37,381} A Mo addition to AISI 4130 steel caused a significant increase in resistance to HEE, attributed to strong H trapping at fine Fe_2MoC precipitates.¹³⁹¹ Strong irreversible H trapping at TiC carbides and $PdAl$ particles improved the HE resistance of an HSLA

Table I. Chemical Compositions (Weight Percent) of AERMET 100 and AISI 4130^[43]

	Fe	Co	Ni	Cr	Mn	Mo	Cu	Si	C	Ti	P	S	H (wppm)
AERMET 100	bal	13.43	11.08	3.00	—	1.18	—	—	0.23	0.009	0.003	0.0008	0.35
AISI 4130	bal	—	0.18	0.92	0.54	0.23	0.18	0.26	0.3	—	0.011	0.008	—

Table II. Mechanical Properties of AERMET 100

Hardness (Rockwell C)	σ_{YS} MPa (ksi)	σ_{UTS} MPa (ksi)	RA (Pct)	K_{IC} MPa \sqrt{m} (ksi \sqrt{in})
54	1765 (256)	1985 (288)	61	139 [LR] (120) 127 [CR] (116)

steel^[37] and PH 13-8 Mo stainless steel,^[40,41] respectively. Finally, H is often codeposited during electroplating of UHSS, necessitating subsequent baking to eliminate HE. While baking parameters are established for conventional steels such as AISI 4340, the novel, strong H trapping in new steels such as AERMET 100 will affect H outgassing. Information on C_H for a given plating process and D_H is required to mitigate HE by baking.

D. Objective

Trap-governed H diffusivity and solubility have not been characterized in AERMET 100, as required to understand the HE behavior of this new alloy and design optimal baking procedures. The goal of this research is to quantitatively characterize and understand the influence of H trapping in a UHSS, AERMET 100, on H transport and solubility. Trap-affected H capacity and H diffusivity are determined, and apparent activation energies for diffusion are calculated as a function of hydrogen concentration. The roles of unique microstructural features, such as coherent M_2C carbides, solute zones, and precipitated austenite, are assessed qualitatively by comparison of the H-trapping behaviors of AERMET 100 to quenched and tempered AISI 4130 steel.

II. EXPERIMENTAL PROCEDURES

A. Material

The material for study was AERMET 100. A 15.2-cm-diameter \times 30.5-cm-long forged bar, of the chemical composition shown in Table I, was obtained in the annealed condition. After machining, specimens were vacuum heat-treated (for optimal strength and toughness^[42]) as follows: solution treated at 885 °C for 1 hour, air cooled to room temperature in 2 hours, chilled at -73 °C for 1 hour, and aged at 482 °C for 5 hours. Table II shows the mechanical properties that resulted. These values are consistent with the tensile yield strength (σ_{YS}) of 1740 MPa, ultimate tensile strength (σ_{UTS}) of 1950 MPa, and plane-strain fracture toughness (K_{IC}) of 166 MPa \sqrt{m} reported for this processing condition.^[42] The expected microstructural features associated with these mechanical properties were detailed in the Introduction.^[29,29a,30]

In selected cases, comparisons are made to quenched and

tempered (2 hours at 300 °C) AISI 4130 steel with a martensitic microstructure and yield strength of 1330 MPa. Its chemical composition is listed in Table I.

B. Electrochemical H Charging

The H charging was performed at constant electrochemical potential under potentiostatic control. The charging solution was saturated with $Ca(OH)_2$ at a pH of ~ 12.1 in pre-electrolyzed, 18.2 M Ω deionized water. The reversible H oxidation/reduction potential ($E_{RH^+/H}$) in this solution was -1.33 V (vs Hg/Hg_2SO_4). Prior to charging, each specimen was ground to a 600-grit finish and degreased ultrasonically.

C. Determination of D_H

Specimens (12.7 \times 6.4 \times 1 mm) were H charged potentiostatically at several hydrogen overpotentials ($\eta_{chg} = E_{applied} - E_{RH^+/H}$) of -1.17, -0.62 or -0.07 V at 60 °C for 60 h. This time was determined using a solution to Fick's Second Law for one-dimensional diffusion in a plane sheet and a conservative estimate for D_H of 3×10^{-8} cm²/s at 60 °C,^[44] as necessary to produce a uniform H concentration across the 1 mm specimen thickness.^[45] After charging, samples were stored in liquid nitrogen or tested immediately.

Thermal desorption spectroscopy (TDS) was utilized to measure the H egress from each specimen at various constant temperatures between 60 °C and 200 °C. The TDS detects H by monitoring the increase in H_2 partial pressure (P_{H_2}) in a high-vacuum chamber with a quadrupole gas analyzer. The background P_{H_2} in the vacuum chamber was approximately 0.04 μ Pa, as determined by performing TDS experiments on uncharged specimens.^[46] To restore the vacuum in the chamber upon specimen installation, specimens were first held at room temperature for 30 to 40 min in an upper chamber, then dropped into a preheated lower chamber for isothermal TDS. This holding time is small compared to the 60-h charging time.

From the TDS data, the quantity of total H egressed at each temperature was determined by calculating the area under the P_{H_2} -time curve, after background P_{H_2} subtraction, using the trapezoidal integration method. The time needed to egress one-half of this quantity ($t_{1/2}$) was determined, as demonstrated in Figure 1, and D_H was calculated using^[47]

$$D_H = \frac{0.0492B^2}{t_{1/2}} \quad [1]$$

where B is the specimen thickness. Equation [1] assumes a hydrogen diffusion coefficient independent of the H-concentration profile during testing and is valid for flat-plate specimens. For temperature-dependent diffusion, $D_H(T)$ is determined by^[48]

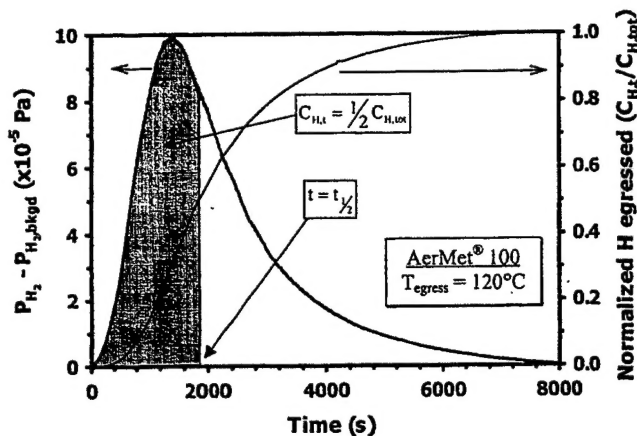


Fig. 1—Measured H_2 pressure and normalized-total H concentration egressed vs time for AERMET 100 at 120 °C, showing the determination of $t_{1/2}$ used in Eq. [1].

$$D_H(T) = D_0 \exp \left(-\frac{E_m^{app}}{RT} \right) \quad [2]$$

where D_0 is the pre-exponential diffusion coefficient, E_m^{app} is the apparent activation energy, R is the gas constant (8.31 J/mol-K), and T is the absolute temperature. The slope of a $\ln D_H(T)$ vs $1/T$ plot was determined by linear-regression analysis, and E_m^{app} was calculated. Slow H egress prevented the use of TDS to determine D_H at temperatures below 60 °C.

When H desorption is surface-reaction limited, H diffusivities determined from TDS data and Eq. [1] do not accurately represent D_H in the bulk specimen. Consequently, diffusion-limited desorption must be ensured during TDS experiments. The isothermal H desorption rate (dC_H/dt), (after a brief period of t_i), for solid-state diffusion-controlled desorption from a homogeneously charged specimen can be described by^[49]

$$\log \left(\frac{dC_H}{dt} \right) = \lambda - KD_H t \quad [3]$$

where K is a geometrical; C_H is the hydrogen evolved, which is expressed as a concentration such that $\int_0^t dC_H/dt \times$

$dt = C_{H,tot}$ ($C_{H,tot}$ = total H concentration); and λ is a constant. Equation [3] assumes that all of the H desorbed from the specimen is detected by the mass spectrometer. Diffusion-limited desorption during TDS experiments may be verified by ensuring linearity of the H desorption-rate data plotted as $\log (dC_H/dt)$ vs time.^[49]

An alternate expression that describes thermal desorption from a homogeneously charged specimen is^[50]

$$\frac{dX_d}{dt} = v_x (1 - X_d)^n \exp \left(\frac{-E_d}{RT} \right) \quad [4]$$

where v_x is a constant, X_d is the fraction of H desorbed, and E_d is the activation energy for desorption and may equal $E_b + E_m$ for egress by rate-limiting detrapping and lattice migration followed by nonrate-limiting surface desorption. If $n = 1$, then dX_d/dt vs $(1 - X_d)$ is linear and the desorption process is a first-order process controlled by H detrapping and diffusion. If $n = 2$, then dX_d/dt vs $(1 - X_d)^2$ is linear

and the H egress is surface-reaction-limited, a process governed by recombinative H desorption of dihydrogen (H_2). In these experiments, dP/dt was converted to dC_H/dt , and detrapping/diffusion-limited desorption was confirmed through Eqs. [3] and [4].

D. Determination of Diffusible H Capacity

The barnacle electrode method^[51] was used to measure the diffusible H concentration, ($C_{H,diff}$). Specimens ($12.7 \times 6.4 \times 0.6$ mm) were H charged at 23 °C for 48 hours to produce uniform H concentrations at various constant H overpotentials between -0.17 and -1.17 V. The $C_{H,diff}$ rate resulting from each charging potential was determined in the same cell without air exposure according to^[51]

$$C_{H,diff} = \frac{J_i}{zF} \left(\frac{D_H}{\pi t} \right)^{-\frac{1}{2}} \quad [5]$$

where J_i is the measured H-oxidation current density (A/cm^2) recorded at time t . Equation [5] assumes fixed $C_{H,diff} = 0$ at the steel surface at $t > 0$ and a uniform diffusible hydrogen concentration in the steel sample at $t = 0$. It is the first-term approximation of a complex expression and, therefore, requires that $B^2/D_H t \geq 4$. This condition was ensured for all experiments. Deaerated-saturated $Ca(OH)_2$ was used as the extraction solution for H oxidation. An extraction potential of -1.00 V (vs Hg/Hg_2SO_4) (~330 mV anodic to E_{H/H^+} and ~300 mV cathodic to the open-circuit potential (E_{OCP}) was maintained potentiostatically. The temperature was constant at 23 °C during extraction.

Use of the measured H oxidation currents to determine $C_{H,diff}$ requires that the experimental data adhere to Eq.[5].^[51] The majority of measured total oxidation current must result from H oxidation, and the oxidation current cannot be either raised or reduced by other electrochemical reactions such as oxygen reduction.

E. Determination of Total H Capacity

Specimens ($12.7 \times 6.4 \times 1$ mm) were H charged at 60 °C for 60 hours to produce uniform H concentrations at various constant H overpotentials between -0.07 and -0.47 V. Immediately following charging, the specimens were submerged in liquid nitrogen. The total H concentration ($C_{H,tot}$) in each specimen was determined using a modification of the LECO*/ASTME1447 melt-extraction method.^[52] Rather

*LECO is a trademark of LECO Corporation, St. Joseph, MI.

than melting, the specimen was heated to a temperature below the fusion temperature to extract the H into an inert carrier gas. This method produced less scatter in H-concentration data than the LECO fusion method.

III. RESULTS

A. Apparent Hydrogen Diffusivity

The TDS results yielded reproducible but H-concentration- and temperature-dependent D_H values for AERMET

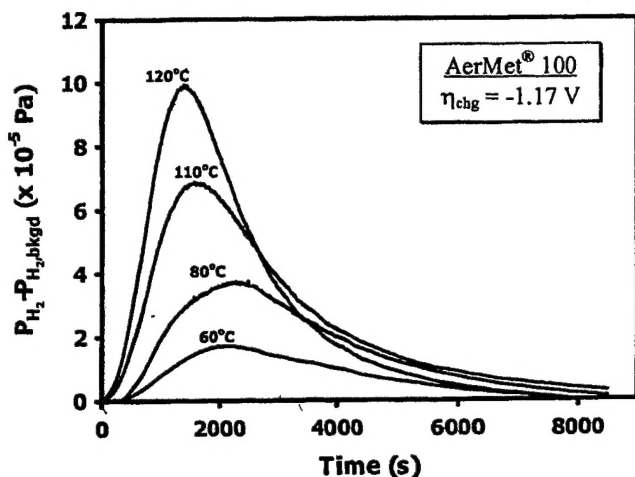


Fig. 2—Net H_2 pressure vs time at various temperatures for AERMET 100 specimens charged at $\eta_{chg} = -1.17$ V and 60 °C (background H_2 pressure, $P_{H_2,bkgd} \approx 0.04$ μ Pa).

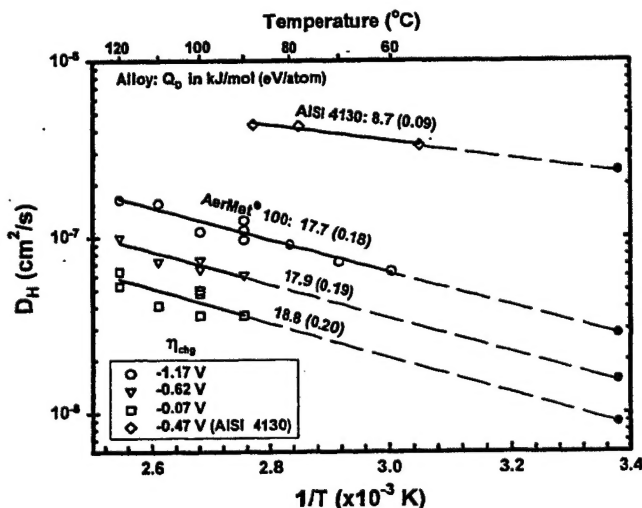


Fig. 3—Apparent hydrogen diffusivity, D_H , vs $1/T$ for AERMET 100 specimens charged at H overpotentials, η_{chg} , of -1.17 , -0.62 , and -0.07 V, compared with data for AISI 4130 at $\eta_{chg} = -0.47$ V. All specimens were H-charged at 60 °C. Filled data points were extrapolated based on regression analyses on TDS data. The value of D_H was not experimentally obtained at 23 °C.

100. Figure 2 shows H desorption data at several temperatures from specimens charged at $\eta_{chg} = -1.17$ V and 60 °C. The results for specimens charged at other H overpotentials and, hence, C_{Htot} show an identical trend. As the desorption temperature increases, the total quantity of desorbed H (the area under the P_{H_2} -time curve) increases. Apparent diffusivities of H between 120 °C and 60 °C for AERMET 100 charged at hydrogen overpotentials (η_{chg}) of -1.17 , -0.62 , and -0.07 V and 60 °C are shown in Figure 3. Linear-regression analyses of the data yielded apparent activation energies (E_m^{app}) of 17.7 kJ/mol (0.18 eV/atom), 17.9 kJ/mol (0.19 eV/atom), and 18.8 kJ/mol (0.20 eV/atom) ± 0.2 kJ/mol (± 0.002 eV/atom) for $\eta_{chg} = -1.17$, -0.62 , and -0.07 V, respectively. The H diffusivities at 23 °C were estimated to be 3.0×10^{-8} , 1.5×10^{-8} , and 9.5×10^{-9} cm^2/s by linear-regression analyses of these data (Figure 3).

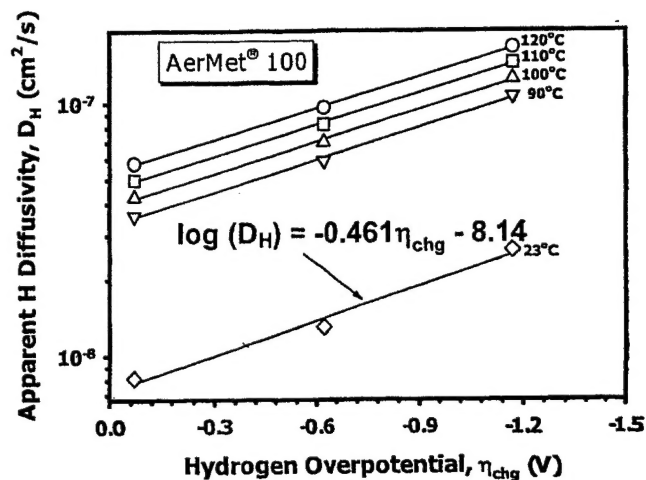


Fig. 4—Apparent H diffusivity vs hydrogen overpotential at various temperatures. The data shown for 23 °C were extrapolated from TDS data obtained at temperatures between 90 °C and 120 °C. Specimens were H-charged at 60 °C.

Figure 4 shows $\log D_H$ measurements vs charging overpotential at egress temperatures of 120 °C, 110 °C, 100 °C, and 90 °C. As shown, D_H increases with η_{chg} , and the slope of the $\log D_H$ vs η_{chg} relationship is similar for each egress temperature. The H diffusivities were extrapolated from the TDS results to 23 °C, preserving the $\log D_H$ - η_{chg} trend established by the elevated-temperature egress data. Linear-regression analysis of these extrapolated D_H values yielded the following empirical relationship between apparent D_H at 23 °C and charging overpotential in saturated $Ca(OH)_2$ at 60 °C for AERMET 100

$$\log(D_H) \left(\frac{cm^2}{s} \right) = -0.461 \eta_{chg}(V) - 8.14 \quad [6]$$

The TDS data in Figure 3 show that D_H for AISI 4130 charged at $\eta_{chg} = -0.47$ V is significantly greater than that in AERMET 100 for all η_{chg} values considered. The room-temperature value of $D_H = 2.5 \times 10^{-7}$ cm^2/s , extrapolated from the TDS data for AISI 4130, is in excellent agreement with literature results established by other methods, such as electrochemical permeation.^[13,35,32,53,54] Linear-regression analysis of the TDS data for AISI 4130 yielded an apparent activation energy of 8.7 kJ/mol in Eq. [2], about half the value determined for AERMET 100.

B. Effects of Baking on Diffusivity

Test specimens were first charged at $\eta_{chg} = -0.62$ V and 60 °C. Then isothermal TDS was performed to determine D_H for specimens that were as-charged, after 3 days of exposure at 23 °C (or 23 °C baking) and after baking at 200 °C for 2.3 h. The H desorption curves for each test condition are shown in Figure 5. In Figure 6, the apparent H diffusivity is plotted against the reciprocal of absolute temperature. As shown in Figure 6, the range of egress temperatures is extended (from 120 °C in Figure 3) to 200 °C. Comparing the value of E_m^{app} in Figure 6 for the as-charged specimens (18.0 kJ/mol or 0.187 eV/atom) with that in Figure 3 (17.9 kJ/mol or 0.186 eV/atom) after

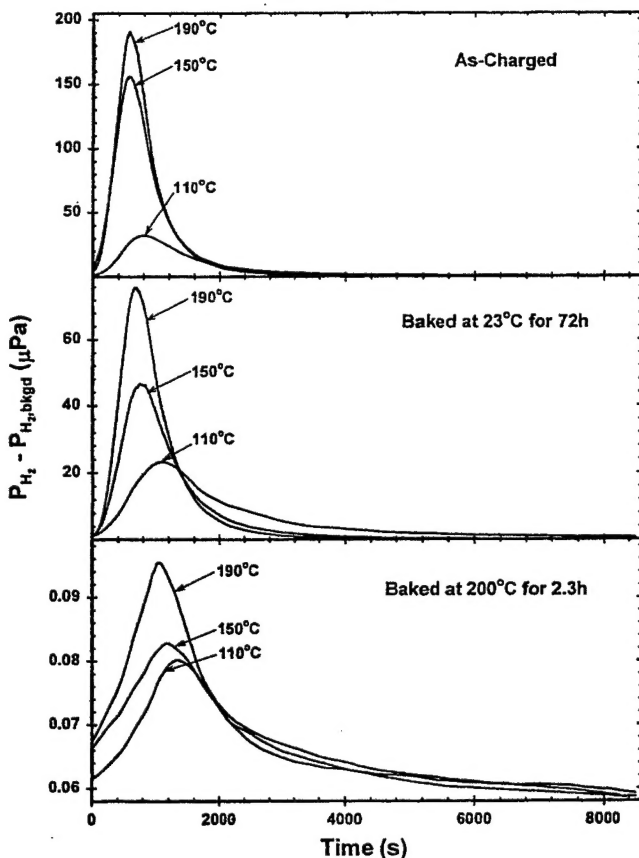


Fig. 5—Net H_2 pressure vs time at typical desorption temperatures for AERMET 100 specimens charged at $\eta_{\text{chg}} = -0.62$ V and 60 °C (background H_2 pressure, $P_{H_2,bkgd} \approx 0.04$ μPa). Conditions prior to the desorption are labeled on each plot.

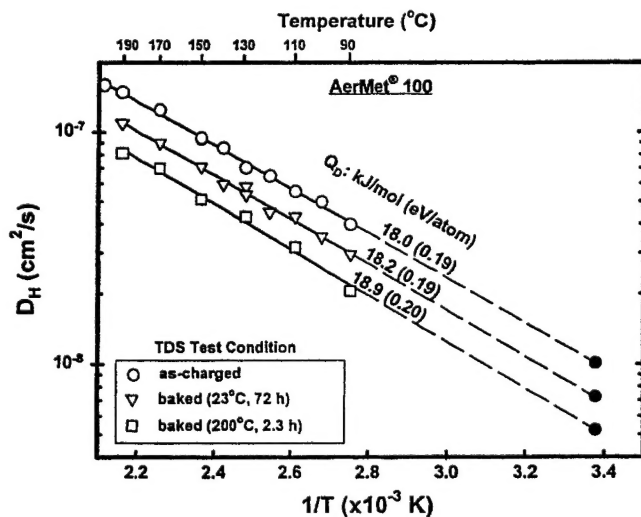


Fig. 6—Apparent hydrogen diffusivity, D_H , vs $1/T$ for specimens of AERMET 100 charged at a H overpotential of -0.62 V and 60 °C. Tests were performed in the as-charged condition and after two different baking conditions.

charging at the same overpotential of -0.62 V indicates good reproducibility in the method.

Notably, H diffusivity depends on the quantity of H remaining after electrochemical charging plus subsequent

Table III. Total H and Diffusible H in AERMET 100 Affected by Baking

Condition Prior to TDS	$C_{H,\text{total}}$ (wppm) (60 °C)	$C_{H,\text{diff}}$ (wppm) (23 °C)
As-charged ($\eta_{\text{chg}} = -0.62$ V)	27.4	7.5
Charged + baked at 23 °C for 72 h	20.2	0.34
Charged + baked at 200 °C for 2.3 h	9.67	*

*Not detectable by Barnacle cell methods, but some diffusible H remains as indicated by TDS results in Figs. 5 and 7.

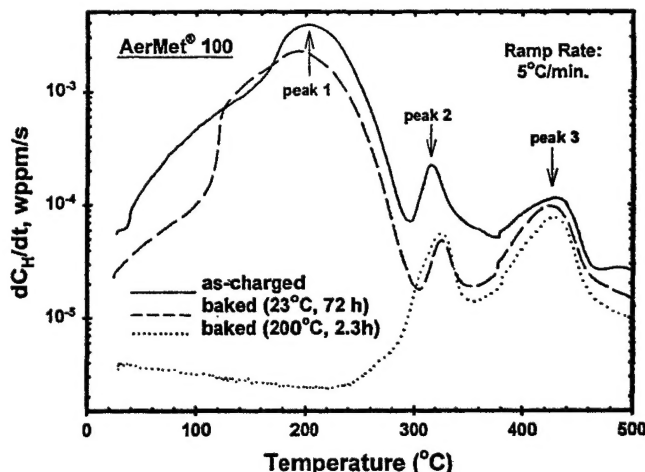


Fig. 7—The H desorption rate as a function of temperature, measured by TDS at a ramp heating rate of 5 °C/m, showing the effect of baking compared with the as-charged condition (charged at $\eta_{\text{chg}} = -0.62$ V and 60 °C). At least three peaks are observed, as indicated by the arrows.

outgassing exposure. As indicated in Figure 6, 23 °C baking causes a general decrease in the diffusivity at all temperatures, as compared with the as-charged condition. Increasing the baking temperature to 200 °C further decreases D_H at each egress temperature. For instance, at 90 °C, D_H decreases from $\sim 4 \times 10^{-8}$ cm^2/s for the as-charged sample to $\sim 3 \times 10^{-8}$ cm^2/s for the 23 °C baked sample, and then to $\sim 2 \times 10^{-8}$ cm^2/s for the 200 °C baked sample. However, the variation in the activation energy is marginal: almost no change in E_m^{app} after 23 °C baking and only a slight increase in E_m^{app} after 200 °C baking.

This slow-down in the apparent diffusivity is due to hydrogen-concentration-dependent diffusion behavior, as the gross H concentration is appreciably decreased upon baking prior to TDS, especially when baked at 200 °C. This latter point is confirmed by the decrease in the total H concentration (LECO results) as well as in the diffusible H concentration at 23 °C (results of the barnacle electrode technique) after baking is performed, as shown in Table III. Note that substantial total H remains after 200 °C baking compared to the H content of as-processed AERMET 100 (0.35 wppm in Table I), but $C_{H,\text{diff}}$ approaches zero.

To examine to what extent the baking processes affected the coverage of specific H trap sites, TDS analysis was conducted at a fixed rate of specimen heating. The results obtained for a heating-ramp rate of 5 °C/min are shown in Figure 7 for the specimens charged at the same H overpotential of -0.62 V and then subjected to the same baking

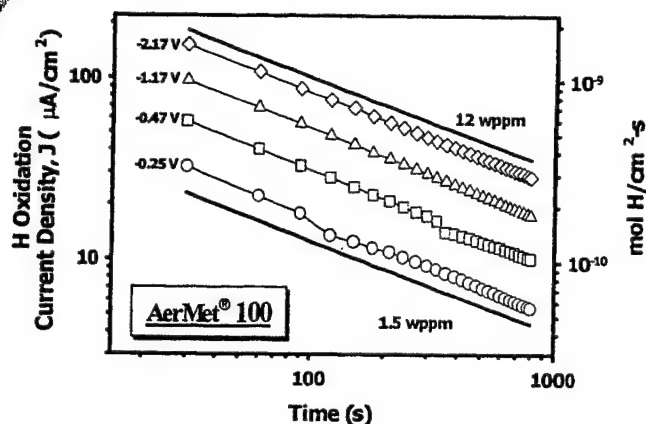


Fig. 8—Experimental and theoretical ($C_{H,diff} = 1.5$ and 12 wppm, and $D_H = 3.0 \times 10^{-8}$ cm²/s) H oxidation curves for egress of diffusible H in AERMET 100 at 23 °C. The hydrogen charging overpotentials are shown.

conditions as in Figure 6. Each peak on a H-desorption-rate curve signals a burst of H egress as a result of H release from a specific type of trap site when the thermal energy at the temperature exceeds the trap-H binding energy. At least three distinct trap states are seen in Figure 7. The desorption energy for the first peak (labeled “peak 1”) is estimated to be ~ 21 kJ/mol or ~ 0.2 eV/atom based on TDS ramp-test data, using a desorption-temperature maxima vs heating-rate relationship.^[54a,54b] Baking at 23 °C lowers the magnitude of the desorption rate vs temperature curve, especially between 23 °C and 200 °C. In contrast, baking at 200 °C substantially removes the first peak. As estimated from the dC_H/dt vs time curves obtained from TDS, the amount of H associated with the first peak in Figure 7 decreases by about 20 pct for the 23 °C baked specimen and by nearly 100 pct for the 200 °C baked specimen, compared to the as-charged case. It is indicated in Figure 7 that little additional H was released from trapping sites with desorption maxima temperatures above 200 °C for these baking conditions. The H egress after 200 °C baking was restricted to the remaining H associated with the first peak. Thus, trap states for the first peak likely correspond to diffusible hydrogen (made up of reversibly trapped H and lattice H) that is substantially removed by 23 °C and 200 °C baking.

C. Diffusible H Capacity

Large diffusible H concentrations are produced in AERMET 100 by H charging in saturated Ca(OH)_2 at modest overpotentials. Figure 8 illustrates $\log J$ vs $\log t$ data generated using the barnacle electrode technique, applied to specimens H charged at the four indicated H overpotentials and 23 °C. Equation [5] yields the solid lines which have a slope of -0.5 for $D = 3.0 \times 10^{-8}$ cm²/s and theoretical values of $C_{H,diff}$ of 1.5 or 12 wppm. The experimental data for each specimen also have a slope of -0.5 , indicating that the measurements are valid and well described by Eq. [5].

The diffusible H concentration produced vs charging overpotential is shown in Figure 9 for AERMET 100 and AISI 4130. The value of $C_{H,diff}$ was determined using Eq. [5] applied to the H-oxidation current density at $t = 300$ s.^[51] The specific H diffusivity used in Eq. [5] for each charging overpotential was determined from Eq. [6]. For AERMET

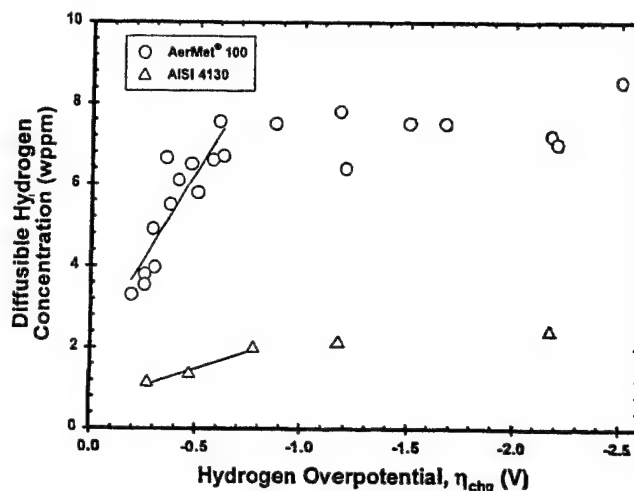


Fig. 9—Diffusible H concentration ($C_{H,diff}$) vs hydrogen overpotential for AERMET 100 and AISI 4130 charged in saturated Ca(OH)_2 at 23 °C. Hydrogen was extracted at 23 °C in saturated Ca(OH)_2 at an egress potential of -1.00 V_{Hg/Hg₂SO₄}. The value of D_H from Eq. [6] was used in the calculation of $C_{H,diff}$ with Eq. [5].

100 at charging overpotentials of -0.19 V $> \eta_{chg} > -0.62$ V, $C_{H,diff}$ increased linearly with increasingly cathodic overpotential. Linear-regression analysis of the calculated diffusible H concentrations between $\eta_{chg} = -0.19$ and -0.62 V at 23 °C yielded

$$C_{H,diff} \text{ (wppm)} = -8.66 \eta_{chg} \text{ (V)} + 2.01 \quad [7]$$

The value of $C_{H,diff}$ is extrapolated to equal 2.01 wppm at a hydrogen overpotential of 0.0 V and temperature of 23 °C.*

*A similar relationship was found after charging at 60 °C, except that the exact slope and intercept differed.

Charging at overpotentials more cathodic than -0.62 V produced a diffusible H concentration of approximately 8 wppm, independent of η_{chg} (Figure 9).

For identical charging conditions, substantially greater diffusible H concentrations are produced in AERMET 100 than in AISI 4130 in the microstructures tested, as demonstrated in Figure 9. Linear regression of the diffusible-H-concentration data for AISI 4130 between $\eta_{chg} = -0.19$ and -0.62 V yielded an extrapolated value of $C_{H,diff} = 0.8$ wppm at $\eta_{chg} = 0.0$ V, about one-third that produced in AERMET 100. Charging at more-cathodic overpotentials produced diffusible H concentrations in AISI 4130 steel as low as one-quarter the levels produced in AERMET 100.

D. Total H Capacity

The total H capacity, given as the sum of diffusible and deeply trapped H and characterized by the high-temperature LECO extraction measurements, is represented in Figure 10 for the two alloys studied. For AERMET 100 charged at 60 °C, total H concentrations ranged from approximately 14 wppm at $\eta_{chg} = -0.07$ V to ~ 30 wppm at $\eta_{chg} = -0.62$ V. Linear-regression analysis of the data in Figure 10 yielded

$$C_{H,tot} \text{ (wppm)} = -32.45 \eta_{chg} \text{ (V)} + 11.41 \quad [8]$$

The value of $C_{H,tot}$ is extrapolated to equal 11.41 wppm at a hydrogen overpotential of 0.0 V and temperature of 60 °C.

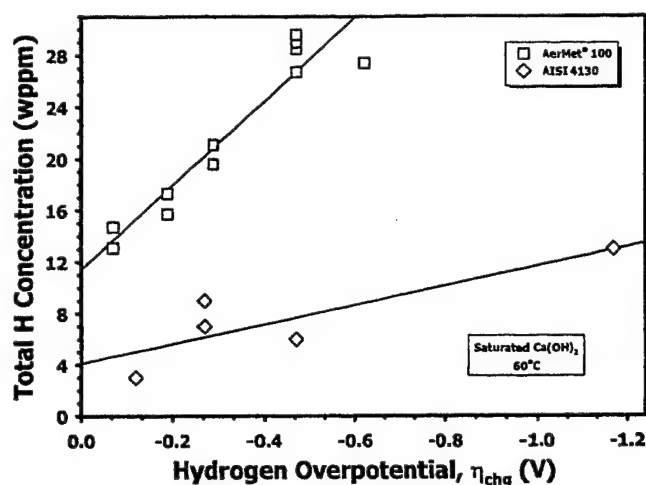


Fig. 10—Total H concentration vs H overpotential for AERMET 100 and AISI 4130 charged in saturated $\text{Ca}(\text{OH})_2$ at 60 °C.

The high total H concentrations measured in AERMET 100 (Figure 10) are consistent with the high diffusible H concentrations measured (Figure 9) and suggest that the H capacity of AERMET 100 is high, even for H overpotentials that approach zero and increase to positive values. The total H capacity of AERMET 100 in the microstructure is significantly greater than that of quenched and tempered AISI 4130 steel, as compared in Figure 10. Linear regression of the total-H-concentration data for AISI 4130 yielded an extrapolated value of $C_{\text{H,tot}} = 4.1$ wppm at a hydrogen overpotential of 0.0 V, less than half that produced in AERMET 100.

IV. DISCUSSION

A. General

The high H concentrations produced in AERMET 100 result from a high capacity for H trapping and are produced even by charging at modest hydrogen overpotentials. For example, charging AERMET 100 specimens in saturated $\text{Ca}(\text{OH})_2$ at $\eta_{\text{chg}} = -0.47$ V produced a total H concentration of 28 wppm, whereas charging AISI 4130 under identical conditions produced a total H concentration of only 6 wppm. As further evidence for the high H capacity of AERMET 100, H charging of specimens at the reversible H oxidation/reduction potential (i.e., $\eta_{\text{chg}} = 0$) in saturated $\text{Ca}(\text{OH})_2$ produced a total H concentration of 11.41 wppm. These results establish that substantial H, a fraction being mobile at room temperature, can be introduced to AERMET 100 by modest electrochemical conditions.

The slow H diffusivity in AERMET 100 must be considered in assessing the depth to which H penetrates during Cd electroplating for corrosion-resistant components. Furthermore, the slow H diffusivity and substantial H uptake in AERMET 100 must be considered in the design of thermal treatments to remove H dissolved during such processes.^[55,56] Substantially longer baking times may be necessary to completely remove H, which is dissolved during such processes. Furthermore, the H-concentration dependence of the apparent D_{H} in AERMET 100 must be considered in modeling of H diffusion and egress during baking. As the hydrogen content decreases during baking, D_{H} slows and

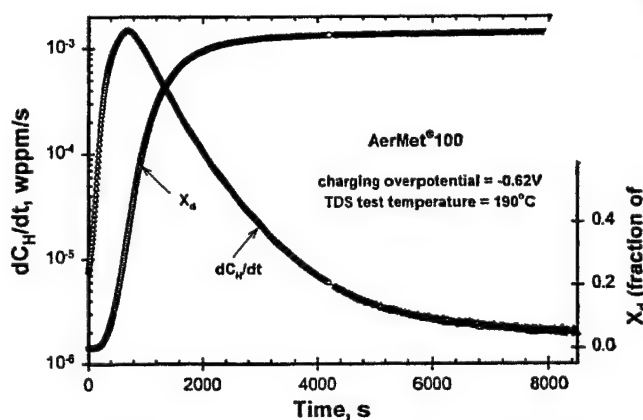


Fig. 11—Desorption rate, dC_{H}/dt , and the fraction of H egressed, X_d , vs desorption time during thermal desorption of H at 190 °C from the specimen charged at $\eta_{\text{chg}} = -0.62$ V.

longer time may be required to reduce $C_{\text{H,diff}}$ compared to that predicted using a single value of H diffusivity independent of $C_{\text{H,diff}}$. This issue is particularly important for AERMET 100, due to susceptibility to severe IHE.^[56a]

The behavior of H in AERMET 100 is likely to affect both IHE and HEE. The high fraction of mobile H could provide either a cracking-prone path or a source of H for partitioning to such a brittle crack path. The low D_{H} value could result in relatively slow kinetics of such hydrogen cracking,^[33] provided that the diffusion distance is large compared to the spacing of active trap sites in the microstructure.

B Evidence for Volume Diffusion-Limited H Desorption

Hydrogen desorption during TDS experiments was volume-diffusion limited, not surface-reaction limited. According to Eq. [3], this is confirmed by the linearity of the desorption rate vs time curve for AERMET 100 specimens charged at various H overpotentials and subjected to thermal desorption at different temperatures. Figure 11 shows one example of these data for verification, and Figure 12 shows dX_d/dt vs both X_d and $(1 - X_d)$ for H desorption at 120 °C from specimens charged at $\eta_{\text{chg}} = -0.62$ V and 60 °C. The linearity of the dX_d/dt vs X_d data in Figure 12 ($0.1 < (1 - X_d) < 0.5$) provides further evidence for diffusion-limited desorption during the TDS experiments, according to Eq. [4]. In all cases, $t_{1/2}$ (Figure 1) was greater than 1000 s, indicating that the depth of H egress from which D_{H} was determined was significantly greater than the trap spacing in AERMET 100. For $D_{\text{H}} = 10^{-8}$ cm²/s and $t = 1000$ s, $x = \sqrt{D_{\text{H}}t} = 32$ μm . This distance is more than 3 times the prior- γ grain size in AERMET 100 (11 μm) and orders of magnitude larger than the martensite interface, austenite film, and M_2C spacings.^[29,29a,30]

C. Concentration-Dependent Diffusion

Trap-sensitive hydrogen diffusion in AERMET 100, for $20 < T < 120$ °C, is concentration dependent. The combination of Eqs. [6] through [8] yields D_{H} at 23 °C:

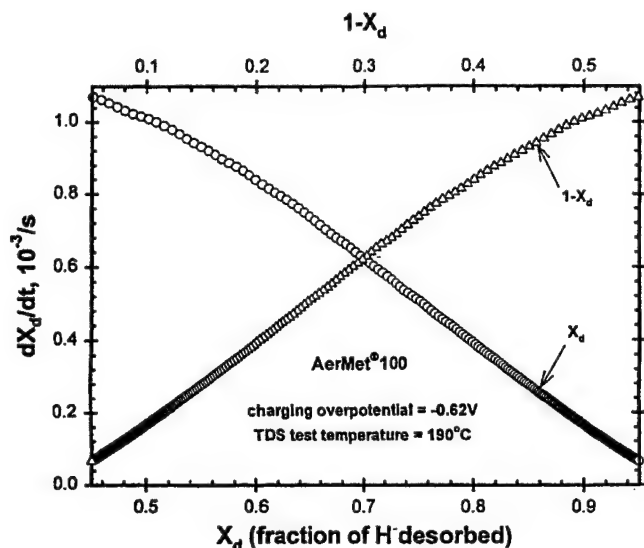


Fig. 12—The rate of H egress expressed as the derivative of X_d (the fraction of H desorbed), dX_d/dt , vs X_d and $(1 - X_d)$ during thermal desorption of H at 190 °C from the specimen charged at $\eta_{\text{chg}} = -0.62$ V. An approximately linear relationship is obtained.

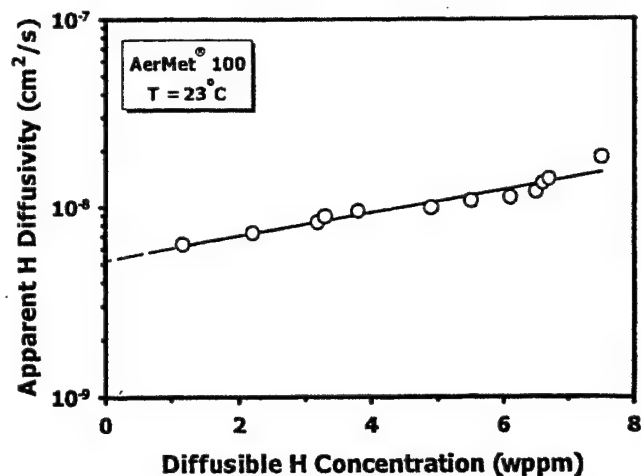
$$\log D_H (\text{cm}^2/\text{s}) = 0.057 C_{\text{H,diff}} (\text{wppm}) - 8.27 \quad [9a]$$

$$\log D_H (\text{cm}^2/\text{s}) = 0.012 C_{\text{H,tot}} (\text{wppm}) - 8.26 \quad [9b]$$

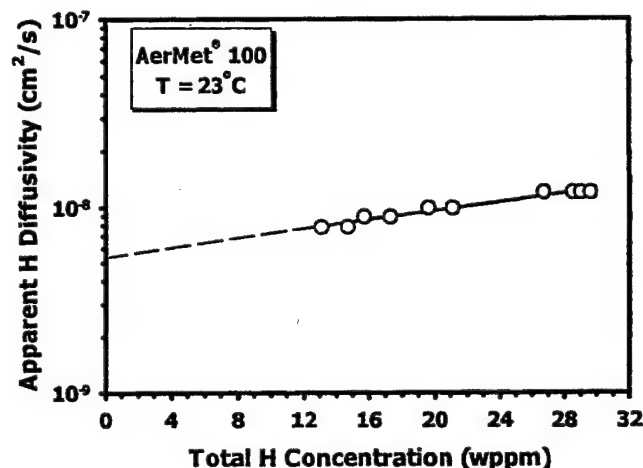
In these formulations, $C_{\text{H,diff}}$ was established by electrochemically charging at 23 °C and $C_{\text{H,tot}}$ was established by charging at 60 °C. Figure 13 shows plots of D_H (23 °C) vs $C_{\text{H,diff}}$ and $C_{\text{H,tot}}$, establishing that the apparent D_H value in AERMET 100 decreases with decreasing H concentration. These trends are consistent with concentration-dependent H diffusivity in iron and steel, as reported in the literature.^[15,57] It is also confirmed by the results on the effect of baking prior to TDS measurements, as shown in Figure 6. As indicated in Figure 7, baking at room temperature and 200 °C can change, to varying degrees, the status of trap occupancy.

The sensitivity of apparent D_H to H concentration is likely due to the variation of trap occupancy by H. As the perfect-lattice H concentration (C_0) increases, due to increasing η_{chg} or reduced baking, the coverage of trap sites in equilibrium within lattice sites increases. This leads to decreased interaction between lattice dissolved H and the more highly occupied trap sites and, therefore, results in an increase in apparent H diffusivity. For example, a diffusion-trapping model predicts that the apparent D_H in AISI 4340, with an estimated $2.1 \pm 0.5 \times 10^{18}$ reversible trap sites per cm^3 , increases by more than one order of magnitude when C_0 increases from 10^{-3} to 0.1 wppm.^[57] Similar calculations for a 3.5 pct Ni-Cr-Mo-V steel, with an estimated $4.9 \pm 0.6 \times 10^{18}$ reversible trap sites per cm^3 , showed an even greater increase in D_H for the same increase in lattice H concentration.^[57] In both calculations, a single reversible trap state with a H binding energy of 48.2 kJ/mol (0.5 eV/atom) was determined by fitting the trapping model to permeation transient data.

To establish the effect of reversible trapping on apparent D_H , Oriani assumed that dynamic equilibrium exists between the reversibly trapped H population and H in interstitial lattice sites.^[14] The constant interaction between diffusing H and lower-binding-energy reversible traps slows diffusion.



(a)



(b)

Fig. 13—Apparent H diffusivity at 23 °C vs (a) diffusible H concentration, $C_{\text{H,diff}}$, and (b) total H concentration, $C_{\text{H,tot}}$, showing concentration-dependent H diffusion in AERMET 100. The value of $C_{\text{H,diff}}$ was established by electrochemical charging at 23 °C and $C_{\text{H,tot}}$ at 60 °C.

In contrast, strong irreversible traps are not in equilibrium with the lattice H and, upon saturating, do not further interact with lattice H. Using this assumption, Oriani formulated an equation describing the apparent H diffusivity in a trap-containing alloy. Assuming a low reversible trap-site coverage and low C_0 , D_H is related to the number of reversible trap sites of each type per unit volume ($N_{R,i}$) with binding energy ($E_{b,i}$), according to^[14]

$$D_H = \frac{D_L}{1 + \sum_i \frac{N_{R,i}}{N_L} \exp\left(\frac{E_{b,i}}{RT}\right) (1 - \Theta_{T,i})} \quad [10]$$

where D_L is the ideal trap-free lattice H diffusivity (for steels, $D_L = D_{\text{H,pure Fe}}$), N_L is the number of ordinary interstitial sites available for H in the pure lattice (2.6×10^{29} octahedral sites per m^3 for bcc Fe^[40]), and $\Theta_{T,i}$ is the fractional site coverage. The value of D_H in AERMET 100 is over three orders of magnitude slower than H diffusivity in pure iron, $D_L \sim 10^{-5} \text{ cm}^2/\text{s}$ at 25 °C.^[3]

Assumptions of equilibrium between lattice and reversibly trapped H, and that $C_0/N_L \ll 1$, implies that an increase in

C_0 leads to a proportional increase in reversibly trapped H concentration, ($C_{T,r}$) for a single trap state:^[14,58]

$$C_{T,r} = \frac{N_{R,i}}{N_L} \exp\left(\frac{E_b}{RT}\right) C_0 \quad [11]$$

The effect of H concentration on apparent D_H for a single dominant trap state is given by^[14]

$$D_H = \frac{D_L C_0}{C_0 + C_{T,r}(1 - \Theta_T)} = \frac{D_L}{1 + \alpha(1 - \Theta_T)} \quad [12]$$

where $\alpha = N_{T,r}/N_L \exp(E_b/RT)$ and D_L is assumed to be independent of H concentration. Equation [12] is relevant to electrochemically charged AERMET 100 and suggests that an increase in apparent D_H with increasing η_{chg} and $C_{H,\text{diff}}$ is due to an increase in fractional reversible trap-site coverage, assuming $\alpha \neq f(\Theta_T)$. That is, Θ_T increases with increasingly cathodic η_{chg} or reduced postcharging baking concurrent with increasing $C_{H,\text{diff}}$. However, D_H never approaches D_L (Figures 3, 6, and 13), since Θ_T never approaches 1 in Eq. [12] for a high density of low-strength reversible traps.

The low solubility of H in Fe^[2] and the high diffusible-H capacity of AERMET 100 (Figure 9) suggest that $C_{T,r}$ is significantly larger than C_0 , and both are small compared to the concentration associated with unity coverage. As such, $\Theta_T \ll 1$ and $C_0 \ll C_{T,r}(1 - \Theta_T)$, and, from Eq. [12],

$$\frac{D_H}{D_L} \approx \frac{C_0}{C_{T,r}} \quad [13]$$

From Eq. [13], it can be seen that the ratio of D_H/D_L is approximately equal to that of $C_0/C_{T,r}$. The ratio of D_H/D_L is on the order of 4×10^{-4} if D_L is taken as $\sim 10^{-5} \text{ cm}^2/\text{s}$ ^[3] and D_H is calculated to equal $4 \times 10^{-9} \text{ cm}^2/\text{s}$ from Eq. [6] at $\eta_{\text{chg}} = 0$ and 23 °C. Therefore, the ratio of $C_0/C_{T,r}$ should also be about 4×10^{-4} , if the trap theory expressed in Eqs. [11] through [13] describes the data for AERMET 100. This is indeed the case. Recognizing that $C_{H,\text{diff}} = C_0 + C_{T,r}$ and that $C_0 \ll C_{T,r}$, then $C_{T,r}$ can be estimated from Eq. [7]. The value of $C_{H,\text{diff}} = 2.2 \text{ wppm}$ at $\eta_{\text{chg}} = 0$. The value of C_0 can be estimated from the relationship between the equilibrium concentration of hydrogen in a perfect lattice and effective hydrogen pressure, recognizing that the partial pressure of hydrogen equals 1 atm $\eta_{\text{chg}} = 0$.^[59] Under this condition, C_0 is approximately 10^{-4} wppm . The numerical value of the ratio $C_0/C_{T,r}$ ($10^{-4}/2.2 = 5 \times 10^{-5}$) is, thus, found to equal D_H/D_L (4×10^{-4}) to a reasonable, albeit not perfect, approximation. Uncertainty arises because the solid-solution composition of AERMET 100 is not equal to that of pure iron, such that C_0 and D_L should differ. However, errors in D_L and C_0 may be roughly offsetting.

D. Apparent Activation Energy for Diffusion During Egress

Linear-regression analysis of the TDS data for AERMET 100 yielded an apparent activation energy for H diffusion (E_m^{app}) in the narrow range of 17.7 to 18.8 kJ/mol (0.18 to 0.19 eV/atom), quite insensitive to diffusible H concentration for the levels examined. For AISI 4130, similar analysis revealed that $E_m^{\text{app}} = 8.7 \text{ kJ/mol}$ (0.09 eV/atom). Previous studies indicate that the apparent activation energy for H

diffusion increases with increasing strength and density of reversible traps.^[11] The approximately twofold increase in E_m^{app} in AERMET 100, relative to that for AISI 4130, implies that reversible H trapping is more extensive in AERMET 100 and is consistent with the diffusible H concentration and H diffusivity data for each steel (Figures 3 and 9).

The E_m^{app} values for AERMET 100 and AISI 4130, determined from TDS data, are lower than those determined from electrochemical permeation studies for other quenched and tempered steels, but higher than E_m^{app} for pure Fe ($\sim 7 \text{ kJ/mol}$ or $\sim 0.07 \text{ eV/atom}$ ^[2]). Hydrogen permeation studies of quenched and tempered UHSS typically result in apparent activation energies between 30 and 40 kJ/mol (0.31 to 0.41 eV/atom).^[4,40,54,60] In all these studies, diffusion was volume, and not surface, controlled. For example, for quenched and tempered microstructures, E_m^{app} is 37 kJ/mol (0.38 eV/atom) for H diffusion in Fe-Mo-C,^[41] $\sim 32 \text{ kJ/mol}$ ($\sim 0.33 \text{ eV/atom}$) for AISI 4130 steel (yield strengths not specified),^[54,60] and 30.7 kJ/mol (0.32 eV/atom) for PH 13-8 Mo stainless steel.^[40] As shown in Figure 3, E_m^{app} values for both AERMET 100 and AISI 4130, determined from TDS experiments, are significantly less than these reported energies. However, despite differences in E_m^{app} for TDS and permeation data, the room-temperature value of D_H for AISI 4130 extrapolated from TDS data is consistent with D_H values determined using permeation methods.^[35] Similarly, the extrapolated room-temperature D_H values for AERMET 100 (from TDS) are consistent with limited estimations of D_H made from permeation data.^[44]

The discrepancy between the E_m^{app} values from TDS experiments and those determined for other quenched and tempered steels through permeation studies is unexpected, since the room-temperature D_H values are similar. Several permeation methods, each with various boundary conditions, are utilized to determine D_H in steels; these include rise time, time lag, breakthrough, and decay transient methods.^[61] Under certain conditions, a permeation method may exhibit some differences in H-concentration profile from the TDS, which may cause a difference in E_m^{app} thus measured.^[62] It is not known, however, whether the experimental differences between TDS and electrochemical permeation can fully account for the discrepancy mentioned. Further investigations are needed to understand the underlying causes.

E. Reversible H Trapping

Figures 3, 9, and 10 show that apparent H diffusivity is slower and H capacity is higher in AERMET 100, with a secondary-hardening martensitic microstructure and precipitated austenite, compared to quenched and tempered AISI 4130 with a martensitic microstructure and Fe_3C . Similarly, the apparent H diffusivity, even after irreversible traps are filled, is one order of magnitude slower in AERMET 100 than in other quenched and tempered high-strength steels with a similar high strength and dislocation substructure.^[35,63] Diffusible H concentrations produced during electrochemical charging are also significantly higher in AERMET 100 than in such steels. These observations suggest that reversible H trapping is significantly more extensive in AERMET 100 than in older quenched and tempered steels.

The high diffusible H concentrations measured in AERMET 100 also support the notion of high H concentrations

associated with a population of H at low trap binding-energy states. This fact, and Eqs. [10] and [13], suggest a large concentration of reversible traps in AERMET 100. This is confirmed by the results shown in Figure 7, which reveal that the occupancies of trap sites (especially those to be energetically activated at around 200 °C) decrease with room-temperature baking and are essentially eliminated with 200 °C baking.

The data in the present study are not sufficient to produce systematic binding-energy values to identify the exact type(s) of trapping in AERMET 100. A variety of microstructural features may act as reversible H traps in AERMET 100. Based on studies of H trapping in other steels,^[14-16,18,19,24,44,64] candidate reversible H traps in AERMET 100 are dislocations, coherent M_2C carbides, solute zones and substitutional elements, precipitated austenite, low-angle boundaries, and coherent interfaces.

1. Dislocations

The dislocation density in AERMET 100 is large due to the unrecovered martensitic microstructure which is promoted by the high level of C_0 in this steel.^[65] The H trapping at dislocations in steel, first discussed by Darken and Smith,^[15] has been confirmed through the use of H-permeation transient and internal friction measurements.^[14,21,66] A trap binding energy of ~29 kJ/mol (~0.3 eV/atom) is commonly reported for H trapping in the elastic-strain field of a dislocation, while higher binding energies, ~58 kJ/mol (~0.6 eV/atom), are reported for trapping at mixed dislocation cores.^[2,23] Reversible H trapping in the elastic-strain field of dislocations and at low-misorientation dislocation sub-boundaries is typically considered to be the major cause for the decrease of apparent D_H in quenched and tempered steels, relative to that of annealed Fe.^[67] Large dislocation densities are produced in such steels during the austenite-to-martensite transformation.

The decrease of apparent D_H for AERMET 100, relative to that of iron, is due to some extent to reversible H trapping at these sites. However, the dislocation density in AERMET 100 is likely on the same order of magnitude as that in other quenched steels tempered at lower temperatures for similar high strength, yet the apparent D_H in AERMET 100 is one order of magnitude slower than that reported for such steels and confirmed for AISI 4130 in Figure 3. The binding energy (E_b) for H traps associated with the first peak in Figure 7 is estimated to be 8 to 9 kJ/mol (0.08 to 0.09 eV/atom), less than the values for typical dislocation structures cited previously. These observations suggest that the low apparent D_H value in AERMET 100 cannot be entirely attributed to reversible H trapping at dislocations and dislocation sub-boundaries.

2. M_2C Carbides

The M_2C carbides formed in AERMET 100 during the 482 °C/5-hour heat treatment are coherent, with some fraction existing as precursor solute zones.^[29,29a] The H binding energies of 67.5 to 96.5 kJ/mol (0.7 to 1 eV/atom) were reported for various incoherent particles in Fe.^[68] However, the binding energy of H to precipitates in steels decreases with increasing precipitate coherency,^[69] and the H-coherent M_2C binding energy will be less than these values. For a secondary-hardening Fe-Mo-C steel,^[4] the apparent H diffusivity was slowest and the diffusible H capacity was at a maximum when the microstructure contained a fine distribution of

coherent M_2C carbides in the peak-hardened condition. This suggests that these particles are reversible H traps in Fe-Mo-C alloys. Hydrogen- M_2C binding energies between 22 and 28 kJ/mol (0.23 and 0.29 eV/atom) were reported,^[4] values that are slightly lower than those typically reported for H-dislocation binding energies,^[36,70] but higher than the binding energy associated with the first peak (Figure 7) in this study. Permeation studies revealed that coherent VC carbides in a Fe-V-C alloy were reversible H traps with a binding energy of 17.4 kJ/mol (0.18 eV/atom).^[25] The apparent H diffusivity in the Fe-V-C alloy was more than one order of magnitude slower than recrystallized Fe, due to reversible trapping at the coherent VC carbides.

It is likely that the M_2C carbides in AERMET 100, like the M_2C carbides in Fe-Mo-C alloys and VC carbides in Fe-V-C alloys, are reversible H traps and a major contributor to the low H diffusivities measured and the high diffusible H concentrations. As estimated according to the volume fraction and dimensions of M_2C in the peak-hardened AERMET 100, the coverage of H on the M_2C /matrix interface can be high, with up to 5×10^{20} atom-center sites/cm³, which is about 7 to 8 times the corresponding value reported for the TiC-TiN/ferrite interface in an Fe-Ti alloy.^[71] As a reference, the total available ordinary interstitial lattice sites for H occupancy (N_L in Eq. [10]) is estimated to be 2.6×10^{23} /cm³.^[40]

3. Substitutional Alloy Elements

Substitutional alloy elements can reversibly trap H and affect apparent D_H and C_H . Cobalt dissolved in ferrite has little effect on D_H in steels.^[44] In contrast, the apparent D_H in single-phase Fe-4.7 Cr (wt pct) was two orders of magnitude slower than that for pure Fe.^[64] Bernstein and Pressouyre^[68] reported a H binding energy of 9.7 kJ/mol (0.10 eV/atom) to Cr substitutional atoms in Fe, suggesting that the H associated with Cr solute atoms in AERMET 100 may contribute to $C_{H,diff}$. The effect of Ni on D_H in bcc Fe alloys is smaller than that of Cr, although still significant.^[63] The D_H value in Fe-10 Ni (wt pct) is approximately one order of magnitude less than the D_H value in Fe.^[63] The binding energy of H to Ni atoms in Fe was estimated to be 7.7 kJ/mol (0.08 eV/atom).^[68]

In view of the chemical composition, it is probable that Cr and Ni contribute to the slow D_H value in AERMET 100, although the magnitudes are not known. Cr^[64] and Ni^[63] additions to Fe cause a substantial increase in H solubility. The H trapping at Cr may be limited by the low amount (<3 pct) of this alloy addition, particularly after M_2C precipitation.^[29] Since Ni is not present in M_2C , Ni solute atoms are likely the more important reversible H traps. Although some of the 11 wt pct Ni in AERMET 100 partitions to austenite, the nil retained austenite and low volume fraction of precipitated austenite (~0.8 to 4 vol pct) upon aging at 482 °C^[29] suggest a significant Ni content in the martensite matrix, particularly compared to older quenched and tempered steels such as AISI 4340 with a very low Ni content.

4. Precipitated Austenite

In the standard-aged condition, precipitated austenite represents about 0.8 to 4 vol pct of the AERMET 100 microstructure and could affect D_H .^[29,29a] The H diffusivity in austenite is about three orders slower of magnitude than that in ferritic iron.^[63] Thus, the presence of austenite could slow H diffusivity. Ritchie *et al.*^[72] observed a considerable

decrease in Stage II crack growth rates during HEE of 300M and attributed the decrease to the slowing of D_H by the presence of 12 vol pct retained austenite. The extent to which precipitated austenite affects H diffusivity in AERMET 100 is not known. Its thin-film morphology increases the likelihood that H atoms must cross austenite layers during diffusion. However, since the austenite layer is only ~ 3 -nm thick (equivalent to 30 H atom diameters), its effect on D_H may be small.

5. Interfaces

A variety of interfaces in AERMET 100 may affect H trapping. Pressouyre and Bernstein^[18] reported binding energies between 29 and 97 kJ/mol (0.3 and 1 eV/atom) for interfaces including the particle/matrix, grain boundaries, and internal free surfaces. The most significant effect of precipitated austenite on diffusible H capacity may result from the increased interface area with the surrounding martensite laths. The precipitated austenite/martensite lath interface in AERMET 100 has not been characterized. If the H binding energy of this interface is ~ 30 to 40 kJ/mol (~ 0.3 to 0.4 eV/atom), then the interface could act as a reversible H trap. The same argument can be applied to the other interfaces in the microstructure, *i.e.*, lower misorientation in segments of martensite lath boundaries. In contrast, high-misorientation interfaces, such as prior-austenite grain boundaries and martensite lath segments or packet interfaces, have higher binding energies and are likely stronger, irreversible H traps.

A binding energy of 27 kJ/mol (0.28 eV/atom) was reported for martensite lath boundaries in AISI 4130.^[33] High-resolution microautoradiography revealed that H preferentially concentrated on martensite lath interfaces in a quenched Fe-Cr alloy.^[70] The fineness of the AERMET 100 microstructure creates a large number of martensite lath interfaces. If trapping at these interfaces is reversible in AERMET 100, then their presence will contribute significantly to the low apparent D_H and high diffusible H capacity in this steel. However, it is unclear why lath interfaces in AERMET 100 would produce behavior radically different than in other quenched and tempered alloys.

F. Irreversible H Trapping in AERMET 100

Unlike the diffusible H content, the total H concentration includes the concentration of irreversibly trapped H that releases during near-melt extraction. Furthermore, the total H concentration contains H which exists in the strongest reversible traps and could not escape under the conditions (*i.e.*, temperature and surface-electrode potential) at which the diffusible H concentration was measured. Traps with binding energies greater than 77 kJ/mol (0.8 eV/atom) were found to irreversibly trap H at room temperature in steel.^[51] In a separate study, traps with a binding energy greater than 55 kJ/mol (0.57 eV/atom) irreversibly trapped H in Fe-M-C (where M = V, Nb, Ti) alloys.^[125] In martensitic steels, traps with sufficiently high binding energies for classification as either irreversible or strong-reversible are likely interfaces such as prior-austenite grain boundaries, high-misorientation martensite lath and packet boundaries, and the matrix/carbide interface of incoherent carbides.^[16,17,19,23] Of these, incoherent carbides are reported to have the highest binding energies, up to 97 kJ/mol (1 eV/atom).^[12,16,18,36,70] The high

total H capacity of AERMET 100, shown in Figure 10, indicates that extensive reversible trapping (implied by the low apparent D_H and high diffusible H concentrations, Figures 3 and 9) is accompanied by widespread irreversible and strong-reversible trapping.^[17,23,34] A comparison of data in Figures 9 and 10 (*e.g.*, $(C_{H,tot} - C_{H,diff})$ provide an estimate of the irreversible H) suggests that the quantity of irreversibly trapped H in AERMET 100 is much greater than that in AISI 4130 steel.

Solutionizing AERMET 100 at 885 °C dissolves virtually all of the metal carbides (*i.e.*, $(MoCr)_7C_3$, $(FeCr)_x C_y$, TiC, and $(TiCrMo)C$).^[30] However, for grain refinement, a small fraction of these carbides remain. Also, a small fraction of the M_2C carbides in peak-hardened AERMET 100 are incoherent.^[29] The H-incoherent carbide binding energy in AERMET 100 has not been determined; however, the binding energies of other incoherent carbides in steels have been reported. A binding energy of 95 kJ/mol (0.98 eV/atom) was reported for TiC in an Fe-Ti-C alloy.^[18] Chromium carbides in an Fe-9 Cr alloy trapped H with a binding energy of approximately 68 kJ/mol (0.7 eV/atom).^[70] A similar binding energy was determined for ϵ -carbides in an Fe-23Ni-0.4C martensitic alloy.^[67] These high values reported for incoherent carbides in several Fe alloys suggest that the binding energies of the incoherent complex-metal and M_2C carbides in AERMET 100 are similarly high and that they are likely irreversible H traps.

Trapping at martensite lath boundaries in AERMET 100 may occur with a stronger binding energy than that in older quenched and tempered steels. Binding energies ranging from less than 29 to 59 kJ/mol (0.3 to 0.61 eV/atom) have been reported for H/grain-boundary interactions in steels.^[36,70] Transmission electron microscopy investigations revealed that a significant fraction of the martensite lath interfaces in AERMET 100 were highly misorientated.^[29] In contrast, Krauss reported that small laths in a model Fe-C steel, sized similarly to those in AERMET 100 with a mean width of about 0.15 μm , are arrayed on a single dominant $\{557\}$, habit plane and should, accordingly, exhibit a low-boundary misorientation.^[73] The crystallographic orientations of martensite laths in the austenite of AERMET 100^[29,29a,30] or other complex UHSSs^[73] were not reported to determine if such boundaries are uniquely disordered. If so, however, then the H-trapping strength of these interfaces is expected to increase with increasing misorientation, and, therefore, a significant fraction of the martensite lath interfaces in AERMET 100 may be irreversible traps. The high total H concentrations measured in AERMET 100 are consistent with irreversible and/or strong-reversible trapping at these abundant microstructural interfaces.

V. CONCLUSIONS

1. Extensive reversible H trapping significantly slows the apparent volume-controlled H diffusivity in ultrahigh strength AERMET 100 at temperatures between 20 °C and 200 °C. The room-temperature D_H value of $< 3 \times 10^{-8}$ cm²/s is at least ten-fold slower, and the activation energy for diffusion (17.7 to 18.8 ± 0.2 kJ/mol at the 95 pct confidence level) is three-fold higher for AERMET 100 compared to tempered martensitic AISI 4130 steel.

- The apparent H diffusivity in AERMET 100 is concentration dependent, increasing with increasing diffusible-H concentration according to

$$\log D_H (\text{cm}^2/\text{s}) = 0.057 C_{H,\text{diff}} (\text{wppm}) - 8.27$$

As $C_{H,\text{diff}}$ increases, the fractional coverage of reversible trap sites increases and local impedance to H migration is reduced which explains the rising D_H value. During baking to lower $C_{H,\text{diff}}$, the converse is true.

- The diffusible and total H capacities of AERMET 100 are significantly higher than those of AISI 4130 under equal H charging conditions, due to the more extensive reversible and irreversible H trapping in AERMET 100. Potentiostatic charging at various potentials in saturated $\text{Ca}(\text{OH})_2$ (23 °C) produces diffusible H concentrations between 3.9 and 10.5 wppm in AERMET 100, with 2.0 wppm achieved by zero-overpotential hydrogen deposition. Identical charging produces diffusible H concentrations between 1.1 and 2.4 wppm in AISI 4130. Similarly, such charging at 60 °C produces total H concentrations in AERMET 100 that are three-fold greater than those produced in AISI 4130.
- Extensive reversible H trapping in AERMET 100 likely occurs at three or more distinct trap states; coherent M_2C carbides, dissolved Ni, and precipitated γ interfaces may be particularly unique reversible trap sites. Extensive irreversible trapping occurs at high-misorientation interfaces likely associated with grain-refining incoherent metal carbides and martensite lath structures. The fineness of the AERMET 100 microstructure creates a large number of both types of trapping sites.
- Baking at 23 °C and particularly 200 °C leads to reduced diffusible and total H, substantially reducing the quantity of hydrogen associated with the lowest-energy trap state. Substantial H remains in two or more higher-energy states, even after 200 °C baking.
- The D_H value for H in baked AERMET 100 is reduced due to both strong trapping and H egress from lattice and reversible trap sites. Baking parameters and considerations of HE of AERMET 100 must account for reduced H mobility and strong trapping.

ACKNOWLEDGMENTS

Financial Support from the Office of Naval Research (Grant No. N00014-98-1-0740) under the direction of contract monitor, Dr. A. John Sedriks, is gratefully acknowledged. We acknowledge contributions of the electrochemical instrumentation by Perkin Elmer Corporation and Scribner Associates, Inc. and the experimental results by Mr. Hakan Dogan.

REFERENCES

- A. Turnbull, M.W. Carroll, and D.H. Ferriss: *Acta Metall.*, 1989, vol. 37, pp. 2039-46.
- J.P. Hirth: *Metall. Trans. A*, 1980, vol. 11A, pp. 861-90.
- A.J. Kurnick and H.H. Johnson: *Metall. Trans.*, 1974, vol. 5, pp. 1199-1206.
- S. Hinotani, Y. Ohmori, and F. Terasaki: *Mater. Sci. Engineer.*, 1985, vol. 76, pp. 57-69.
- G.M. Pressouyre and F.M. Faure: in *Hydrogen Embrittlement: Prevention and Control*, ASTM STP 962, L. Raymond, ed., ASTM, Philadelphia, PA, 1988, pp. 353-71.
- C.A. Wert: in *Topics in Applied Physics—Hydrogen in Metals II*, G. Alefeld and J. Volkl, editors, Springer-Verlag, New York, NY, 1978, pp. 305-30.
- R. Valentini and A. Solina: *Mater. Sci. Technol.*, 1994, vol. 10, pp. 908-14.
- P.K. Subramanyan: in *Comprehensive Treatise of Electrochemistry Volume 4: Electrochemical Materials Science*, J.O.M. Bockris et al., eds., Plenum Press, New York, NY, 1981, pp. 411-62.
- R.P. Gangloff: in *Corrosion Prevention and Control*, M. Levy and S. Isserow, eds., United States Army Materials Technology Laboratory, Watertown, MA, 1986, pp. 64-111.
- C.D. Kim and A.W. Loginow: *Corrosion*, 1968, vol. 24, pp. 313-18.
- H.H. Johnson and R.W. Lin: in *Hydrogen Effects in Metals*, I.M. Bernstein and A.W. Thompson, eds., TMS, Warrendale, PA, 1980, pp. 3-25.
- G.M. Evans and E.C. Rollason: *J. Iron Steel Institute*, 1969, vol. 207, pp. 1591-98.
- M. Wang and P.G. Shewmon: in *Hydrogen Embrittlement: Prevention and Control*, ASTM STP 962, L. Raymond, ed., ASTM, Philadelphia, PA, 1988, pp. 117-24.
- R.A. Oriani: *Acta Metall.*, 1970, vol. 18, pp. 147-57.
- L.S. Darken and R.P. Smith: *Corrosion*, 1949, vol. 5, pp. 1-16.
- G.M. Pressouyre: in *Current Solutions to Hydrogen Problems in Steels*, C.G. Interrante and G.M. Pressouyre, eds., ASM INTERNATIONAL, Materials Park, OH, 1982, pp. 18-34.
- G.M. Pressouyre: *Metall. Trans. A*, 1983, vol. 14A, pp. 2189-93.
- G.M. Pressouyre and I.M. Bernstein: *Metall. Trans. A*, 1978, vol. 9A, pp. 1571-80.
- A.W. Thompson: in *Environmental Degradation of Engineering Materials*, M.R. Louthan and R.P. McNitt, eds., Virginia Polytechnic Institute, Blacksburg, VA, 1977, pp. 3-17.
- T. Asaoka, G. Lapasset, M. Aucouturier, and P. Lacombe: *Corrosion*, 1978, vol. 34, pp. 39-47.
- A.J. Kurnick and H.H. Johnson: *Acta Metall.*, 1980, vol. 28, pp. 33-39.
- G.M. Pressouyre and I.M. Bernstein: *Corrosion Sci.*, 1978, vol. 18, pp. 819-33.
- R. Gibala and A.J. Kurnick: in *Hydrogen Embrittlement and Stress Corrosion Cracking*, R. Gibala and R.F. Hehemann, eds., ASM INTERNATIONAL, Materials Park, OH, 1984, pp. 61-77.
- J.K. Tien, A.W. Thompson, I.M. Bernstein, and R.J. Richards: *Metall. Trans.*, 1976, vol. 7A, pp. 821-29.
- F. Gehrman, H.J. Grabke, and E. Riecke: in *Hydrogen Transport and Cracking in Metals*, A. Turnbull, ed., The University Press, London, 1995, pp. 216-26.
- G.M. Pressouyre: *Metall. Trans. A*, 1979, vol. 10A, pp. 1571-72.
- P.M. Novotny and T.J. McCaffrey: *Aerotech '92*, Society of Automotive Engineers, Inc., Warrendale, PA, 1992.
- P.M., Novotny: *Gilbert R. Speich Symp.—Fundamentals of Aging and Tempering in Bainitic and Martensitic Steel Products*, ISS, Warrendale, PA, 1992, pp. 215-36.
- R. Ayer and P.M. Machmeier: *Metall. Trans. A*, 1993, vol. 24A, pp. 1943-55.
- C.H. Yoo, H.M. Lee, J.W. Chan, and J.W. Morris: *Metall. Mater. Trans.*, A, 1996, vol. 27A, pp. 3466-72.
- C.J. Kuehmann: Ph.D. Dissertation, Northwestern University, Evanston, IL, 1994.
- G.M. Pressouyre: in *Hydrogen Effects in Metals*, I.M. Bernstein and A.W. Thompson, eds., TMS, Warrendale, PA, 1981, pp. 27-36.
- W.W. Gerberich, T. Livne, X.-F. Chen, and M. Kaczorowski: *Metall. Trans. A*, 1988, vol. 19A, pp. 1319-34.
- R.P. Gangloff: in *Hydrogen Effects on Material Behavior*, N.R. Moody et al., eds., TMS, Warrendale, PA, 2001, in press.
- R.A. Oriani: *Fundamental Aspects of Stress Corrosion Cracking*, NACE, Houston, TX, 1969, pp. 32-50.
- K. Yamakawa, S. Yonezawa, and S. Yoshizawa: *Int. Congr. on Metallic Corrosion*, National Research Council, Toronto, 1984, pp. 254-61.
- G.M. Pressouyre and I.M. Bernstein: *Acta Metall.*, 1979, vol. 27, pp. 89-100.
- M.F. Stevens and I.M. Bernstein: *Metall. Trans. A*, 1985, vol. 16A, pp. 1879-86.
- M.J. Morgan and C.J. McMahon Jr.: *Hydrogen Degradation of Ferrous Alloys*, R.A. Oriani, J.P. Hirth, and M. Smailowski, eds., Noyes Publications, Park Ridge, NJ, 1985, pp. 608-40.
- B.D. Craig: *Metall. Trans. A*, 1982, vol. 13A, pp. 1099-1102.
- J.R. Scully, J.A. Van Den Avyle, M.J. Cieslak, J. Romig, and C.R. Hills: *Metall. Trans. A*, 1991, vol. 22A, pp. 2429-43.

41. J.R. Scully, M.J. Cieslak, and J.A. Van Den Avyle: *Scripta Metall. Mater.*, 1994, vol. 31, pp. 125-30.
42. *Alloy Data-AerMet® 100 Alloy*, Carpenter Technology Corporation, Reading, PA, Carpenter Steel Division, 1992.
43. R.P. Gangloff: *Metall. Trans. A*, 1985, vol. 16A, pp. 953-69.
44. B.P. Pound: *Acta Metall.*, 1998, vol. 46, pp. 5733-43.
45. J. Crank: *The Mathematics of Diffusion*, Oxford University Press, Inc., New York, NY, 1975, p. 414.
46. M.A. Gaudett: Ph.D. Dissertation, University of Virginia, Charlottesville, VA, 1997.
47. F. Iacoviello, J. Galland, and M. Habashi: *Corr. Sci.*, 1998, vol. 40, pp. 1281-93.
48. P. Shewmon: *Diffusion in Solids*, The Minerals, Metals, & Materials Society, Warrendale, PA, 1989, pp. 9-51.
49. M.L. Hill and E.W. Johnson: *Acta Metall.*, 1955, vol. 3, pp. 566-71.
50. D.P. Woodruff and T.A. Delchar: *Modern Techniques of Surface Science*, Cambridge University Press, Cambridge, United Kingdom, 1986, p. 284.
51. J.J. DeLuccia and D.A. Berman: in *Electrochemical Corrosion Testing*, ASTM STP 727, F. Mansfeld and U. Bertocci, eds., ASTM, Philadelphia, PA, 1981, pp. 256-73.
52. *1999 Annual Book of ASTM Standards Vol. 3.06*, ASTM, Philadelphia, PA, 1999, pp. 398-400.
53. M.R. Louthan Jr., R.G. Derrick, J.A. Donovan, and G.R. Caskey, Jr.: in *Effect of Hydrogen on Behavior of Materials*, A.W. Thompson and I.M. Bernstein, eds., TMS, Warrendale, PA, 1976, pp. 337-47.
54. W.J. Kass: in *Effect of Hydrogen on Behavior of Materials*, A.W. Thompson and I.M. Bernstein, eds., TMS, Warrendale, PA, 1976, pp. 327-36.
- 54a. H.E. Kissinger: *Analytical Chem.*, 1957, vol. 29, pp. 1702-06.
- 54b. E.V. Kornelsen and A.A. van Gorkum: *Vacuum*, 1981, vol. 31, pp. 99-111.
55. J.B. Boodey and V.S. Agarwala: *Corrosion* 87, NACE, Houston, TX, 1987.
56. D.A. Berman: *Mater. Performance*, 1985, vol. 24, pp. 36-41.
- 56a. R.L.S. Thomas: Masters Thesis, 2000, University of Virginia, Charlottesville, VA.
57. A.J. Griffiths and A. Turnbull: *Corr. Sci.*, 1995, vol. 37, pp. 1879-81.
58. H.H. Johnson, N.R. Quick, and A.J. Kumnick: *Scripta Metall.*, 1979, vol. 13, pp. 67-72.
59. N.R. Quick and H.H. Johnson: *Acta Metall.*, 1978, vol. 26, pp. 903-07.
60. H.G. Nelson and J.E. Stein: *Report No. NASA TN D-7265*, National Aeronautics and Space Administration, Washington, DC, 1973.
61. M.A.V. Devanathan and Z. Stachurski: *Proc. R. Soc. London*, 1962, vol. 270A, pp. 90-102.
62. R.S. Lillard, D.G. Enos, and J.R. Scully: *Corrosion*, 2000, vol. 56, pp. 1119-32.
63. W. Beck, J.O.M. Bockris, M.A. Genshaw, and P.K. Subramanyan: *Metall. Trans.*, 1971, vol. 2, pp. 883-88.
64. J.O.M. Bockris, M.A. Genshaw, and M. Fullenwider: *Electrochimica Acta*, 1970, vol. 15, pp. 47-60.
65. G.R. Speich, D.S. Dabkowski, and L.F. Porter: *Metall. Trans.*, 1973, vol. 4, pp. 303-15.
66. A. Zielinski, E. Lunarska, and M. Smialowski: *Acta Metall.*, 1977, vol. 25, pp. 551-56.
67. P. Kedzierzawski: in *Hydrogen Degradation of Ferrous Alloys*, R.A. Oriani, J.P. Hirth, and M. Smialowski, eds., Noyes Publications, Park Ridge, NJ, 1985, pp. 271-320.
68. I.M. Bernstein and G.M. Pressouyre: in *Hydrogen Degradation of Ferrous Alloys*, R.A. Oriani, J.P. Hirth, and M. Smialowski, eds., Noyes Publications, Park Ridge, NJ, 1985, pp. 641-711.
69. D.L. Johnson, G. Krauss, J.K. Wu, and K.P. Tang: *Metall. Trans. A*, 1987, vol. 18A, pp. 717-21.
70. C. Paes de Oliveira, M. Aucouturier, and L. Lacombe: *Corrosion*, 1980, vol. 36, pp. 53-59.
71. R. Valentini, F. D'Errico, D.M. De Micheli, and A. Solina: in *Hydrogen Transport and Cracking in Metals*, A. Turnbull, ed., The University Press, London, 1995, pp. 312-19.
72. R.O. Ritchie, V.F. Castro Cedeno, V.F. Zackay, and E.R. Parker: *Metall. Trans. A*, 1978, vol. 9A, pp. 35-40.
73. G. Krauss: *Steels: Heat Treatment and Processing Principles*, ASM INTERNATIONAL, Materials Park, OH, 1990, pp. 57-77.

**DIFFUSION CONTROL OF HYDROGEN ENVIRONMENT
EMBRITTLEMENT IN HIGH STRENGTH ALLOYS**

R.P. Gangloff

Department of Materials Science and Engineering
University of Virginia
Charlottesville, VA 22904-4745
USA

DIFFUSION CONTROL OF HYDROGEN ENVIRONMENT EMBRITTLEMENT IN HIGH STRENGTH ALLOYS

R.P. Gangloff

Department of Materials Science and Engineering
University of Virginia
Charlottesville, VA 22903-2442
USA

Abstract

The objective of this research is to examine critically the importance of hydrogen diffusion in the crack tip process zone during intergranular hydrogen environment embrittlement of high strength alloys. The fastest rates of K-independent Stage II cracking are directly proportional to hydrogen diffusivity, with each changing over five orders of magnitude for a wide range of nickel, aluminum, iron, and titanium-based alloys. Hydrogen diffusion rate limits such cracking, however, surface-reaction limitation can occur for weak-H producing environments and high-H diffusivity alloys. Models predict that the critical distance for H-diffusion limited intergranular cracking is small, but different, for high strength alloys in H-producing gases (5-10 nm) and electrolytes ($\sim 0.7 \mu\text{m}$). This critical distance is not understood based on classical micromechanical concepts. Rather, high-H concentration localized within $1 \mu\text{m}$ of an electrochemically active crack tip, high stresses from restricted crack tip plasticity, and intense-H trapping could focus HEE damage very near to the growing crack tip. These factors enrich concentration such that hydrogen effectively embrittles high strength alloys.

R.P. Gangloff, *Diffusion Control of Hydrogen Environment Embrittlement in High Strength Alloys*, in Hydrogen Effects in Materials, N.R. Moody and A.W. Thompson, eds., The Minerals, Metals & Materials Society, Warrendale, PA, in press (2002).

Introduction

High strength alloys based on Fe, Ni, Al, or Ti are prone to severe hydrogen environment embrittlement (HEE) when stressed in a gas or electrolyte that produces atomic hydrogen (H). The H production is localized on the crack tip surface, and enters the fracture process zone (FPZ) to promote stress-based damage that is often intergranular (IG) and ascribed to interface decohesion from H (plus segregated impurity) interaction [1,2]. Extensive fracture mechanics data on the threshold stress intensity factor (K_{TH}) and rates of subcritical crack growth (da/dt) for HEE were followed by micromechanical and chemical models [3,4]. Modeling is complicated by the need to integrate: (1) mass transport and electrochemical reactions in the occluded crack, (2) H diffusion and distribution between microstructural-trapping features in the FPZ, (3) stresses and plastic strains proximate to the crack tip, and (4) a failure criterion based on the unproven mechanism of embrittlement. These factors change sharply over distances on the order of 0.1-50 μm in the FPZ [5]. Equilibrium models of K_{TH} , with the onset or arrest of H cracking at a combination of local-tensile stress and enriched-critical H concentration (C_{CRIT}) [6,7], provide a basis for more complex modeling of the kinetics of HEE.

Wei and coworkers modeled the K-independent Stage II crack growth rate (da/dt_{II}) as proportional to the rate of supply of H to the FPZ; enabled by a sequence of environment-mass transport, surface reaction to produce H, and H diffusion to competing fracture sites in the FPZ [8,9]. The contribution of each process depends on temperature, environmental-H activity, and material-kinetics parameters; but regimes exist where one step is HEE-rate limiting [9]. For high strength steels, da/dt_{II} is rate limited by surface-reaction for water vapor and perhaps H_2 [10,11], gas-phase transport for low pressure H_2S [11,12], and H diffusion in the FPZ for higher-pressure H_2S [11,12] and H_2 [13-15] environments. Identification of the rate-limiting step for a gas was based on comparisons between measured vs. predicted pressure and temperature dependencies of da/dt_{II} . However, these conclusions are not absolute because of modeling assumptions and unknown material-environment parameters. Additionally, the rate limiting steps for cracking in electrolytes and a variety of alloys have not been established [16]. Surface reaction has not been integrated with 2-dimensional H diffusion in the FPZ [17].

Internal hydrogen embrittlement (IHE) from H predissolved prior to loading does not involve crack environment and surface reactions, and growth kinetics have been modeled as governed by H diffusion to the crack tip FPZ [18-26]. Such models were used to describe HEE, from the concentration of H on the crack tip surface and in equilibrium with the local environment (C_o for H in stress and strain-free metal) [14,17,25-32]. The C_o depends on environmental parameters such as temperature, resulting in the need to model coupled surface reaction and H diffusion to describe da/dt_{II} [15,17,32]. Diffusion-based models include two important parameters: the critical distance ahead of the crack tip surface where H damage nucleates (χ_{CRIT}) and the trap-sensitive diffusivity of H in the metal (the apparent diffusivity, D_H). None of the H-diffusion models were confirmed by a range of data and important uncertainties persist, including: (1) the time dependence and level of C_o on the strained crack surface, (2) χ_{CRIT} from the crack tip surface, (3) the distribution of stress and plastic strain at the IG crack tip, (4) D_H in the trap-rich FPZ, and (5) the magnitude of trapped H. The objective of this research is to examine these unresolved issues by analyzing a broad range of literature data on the kinetics of HEE, and compared to new probes of H uptake and damage local to the FPZ.

Results: Correlation and Analysis

HEE in Aqueous Chloride Solutions

Extensive crack growth rate data were obtained from the literature [9,18,33-40] and produced at

the University of Virginia [41-51]. Only high strength alloys were examined, as listed in Table I and exhibiting a wide range of D_H . The environment was aqueous chloride solution of varying pH and electrode potential at 25°C. Crack growth was essentially intergranular for each alloy-environment system and likely occurred by HEE, with a high overpotential for cathodic H production at the strain-bared crack tip enabled by hydrolytic acidification and reduced crack tip potential [52,53]. Crack growth rates were within Stage II and independent of applied K for each case tabulated. (While modest-K dependencies (viz, $da/dt \propto K^{0.1-1}$) were sometimes reported, the crack growth rates presented in the following plots were outside of the strongly K-dependent Stage I regime and at K levels well above K_{TH} .) Literature values of D_H were typically obtained from H-permeation measurements, and approximate the H trapping typical of complex microstructures but not of the plastically strained state of the crack tip [22,54,55].

Table I High Strength Materials Investigated for Aqueous HEE

Alloy	σ_{YS} (MPa)	D_H @ 25°C (cm ² /s)
Nickel-based Superalloy: IN-718 [39,41]	1125	$9-14 \times 10^{-12}$ [56,57]
Precipitation Hardened Al: 7050-T6, 7079-T6 [9,38,42,43,46,47]	500	1×10^{-9} [38,44,46]
18Ni Maraging Steel [33,58]	> 1700	2.5×10^{-9} [33,34]
Tempered Martensitic Steel: H-11 [35]	1650	4×10^{-9} [35]
Tempered Martensitic Steel: AerMet 100, AF1410 [40]	1700	2×10^{-8} [51]
Tempered Martensitic Steel: AISI 4340-type [36]	1650	1×10^{-8} to 1×10^{-7} [36]
Tempered Martensitic Steel: AISI 4340-type [37]	> 1500	$1-2 \times 10^{-7}$ [18,35,51]
Tempered Martensitic Steel: AISI 4340 [18,35]	> 1500	$1-2 \times 10^{-7}$ [18,35,51]
Tempered Martensitic: ASTM A723 [39,40]	>1150	$1-2 \times 10^{-7}$ [18,35,51]
$\beta+\alpha$ Ti: Ti-8V-6Cr-4Mo-4Zr-3Al, 15Mo-3Nb-3Al [45,48-50]	1150	5×10^{-7} in β [45]

Fastest-Reported Rates of HEE in Chloride Solution Since extensive data exist for each alloy in Table 1, it is possible to select the fastest-reported rates of HEE as representing minimal surface reaction limitation. For each alloy-chloride environment examined, the fastest-measured da/dt_{II} is directly proportional to D_H as shown in Fig. 1. The Ni-based superalloy was cracked in NaCl that was either acidified (pH 0.3 – 1) NaCl [41] or contained a H recombination poison (As_2O_3) with cathodic polarization [39]; aluminum alloys in acidified chromate-chloride solution [38,42,43,47]; steels in neutral NaCl [33,35-37], H_2S -bearing acidified chloride (NACE) [37], or concentrated H_2SO_4/H_3PO_4 acid [40]; and Ti alloys in neutral chloride solution [45,49,50]. AA7079-T6 is the only aluminum alloy ever reported to exhibit crack growth rates in chloride solution that exceed about 0.1 $\mu m/s$ [38]. The correlation in Fig. 1 is particularly strong for the alloy steels of widely varying D_H . Reduced D_H , from 10^{-7} cm²/s for conventional tempered martensitic steels to 10^{-8} cm²/s for precipitation hardened AerMet 100 and 10^{-9} cm²/s for 18Ni Maraging steels, resulted in a 2 order of magnitude reduction in da/dt_{II} for essentially identical environment chemistry and fracture mechanics conditions. Silicon addition to martensitic AISI 4340-type steel reduced da/dt_{II} from 25 $\mu m/s$ to 0.6-2 $\mu m/s$, ascribed to reduced H mobility from the presence of low- D_H austenite [59,60].¹

¹ Note added in proof: Underwood and coworkers recently reported that ASTM A723 Gr 2 steel ($\sigma_{YS} = 1310$ MPa) exhibits an unexpectedly high da/dt_{II} of 600 $\mu m/s$ when stressed in pure H_2SO_4 [61] compared to previous experiments with H_2SO_4/H_3PO_4 solutions [39,40]. This point, plotted in Fig. 1 (A723), reflects substantially faster HEE compared to other tempered martensitic steels and all alloys in the general correlation. Much like AA7079, the abnormally severe HEE in A723 steel in H_2SO_4 is not understood.

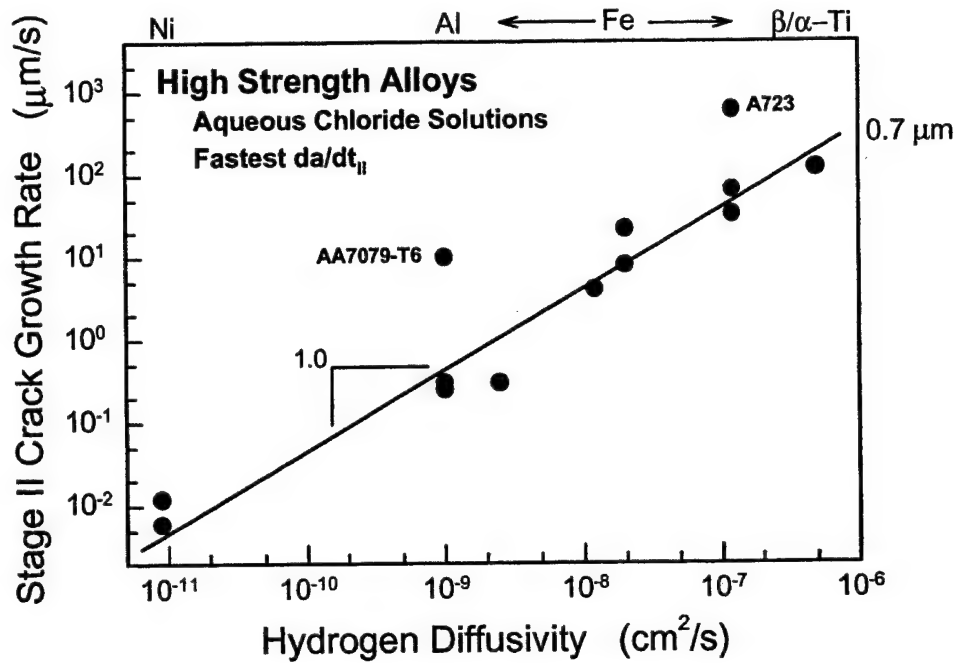


Figure 1 The dependence of the fastest-measured da/dt_{II} on D_H from permeation measurements for a variety of high strength alloys that exhibit HEE in aqueous chloride solutions at 25°C. Specific alloys and references are identified by the H diffusivity values presented in Table I.

For HEE, rate limited by H diffusion in the FPZ, da/dt_{II} is modeled as equaling the ratio of χ_{CRIT} to the time required for H to diffuse over this distance and reach C_{CRIT} . Models are of varying complexity depending on whether the Hs-diffusion field is: (a) concentration and/or stress driven, (b) transient or steady state, (c) ahead of a stationary or moving crack, (d) modeled in one or two dimensions (e) emanating from environment-sensitive C_o , (f) microstructure-trap affected, (g) plastic strain-trap affected, and (h) coupled with a H-failure criterion [7-9,14,17-32,61-63]. The results of 1-dimensional modeling are of the general form:

$$\frac{da}{dt_{II}} = \frac{D_H}{\chi_{CRIT}} \left[\xi \left(\frac{C_o}{C_{CRIT}}, D_H, \chi_{CRIT}, \sigma_{YS}, t \right) \right] \quad (1)$$

where ξ is a function of the indicated variables and was predicted to equal:

4.0 for H diffusion in a concentration gradient and at steady state without a failure criterion involving C_o/C_{CRIT} [14,32].

2.9 obtained from $\{4.5\sigma_{YS}V_H/RT\} \{C_o/(C_{CRIT} + C_o)\}$ for stress enhanced H diffusion at steady state with cracking at a fixed value of C_o/C_{CRIT} [18,19]. V_H is the partial molar volume of H in Fe, C_o/C_{CRIT} is assumed to equal 0.5, R is the gas constant, temperature (T) = 23°C, and σ_{YS} = 1600 MPa.

2.8 for transient-H diffusion under concentration and stress-gradient control, where ξ is estimated from the results of a numerical solution for $C_o/C_{CRIT} = 0.5$ and $\chi_{CRIT} = 25 \mu m$ [23].

0.35 to 2.3 for stress enhanced H diffusion in the concentration gradient ahead of a crack tip moving at steady state [29,30]. The exact value of ξ depends on the length-scale of H diffusion ahead of the crack tip, given by $D_H/(\chi_{CRIT} da/dt_{II})$.

0.01 to 0.3 for H diffusion in the concentration gradient ahead of a crack tip moving at steady state and for $C_0/C_{\text{CRIT}} = 3.3$ coupled with $D_H/(da/dt_{II}) = 2 \times 10^{-5}$ cm from the correlation in Fig. 1 [28]. ($C_0 > C_{\text{CRIT}}$ for models that do not include stress enhancement of H solubility.)

The observed and predicted direct proportionality between Stage II crack growth rate and D_H supports H-diffusion control of HEE. An upper bound of χ_{CRIT} can be determined from the data in Fig. 1. The highest-reasonable value of ξ is 3 and constant, provided that the fastest rates of HEE in Fig. 1 are not sensitive to differences in C_0 for the various chloride solutions and if cracking is governed by constant C_{CRIT}/C_0 of order 2 [37]. These assumptions result in $\chi_{\text{CRIT}} = 0.7 \mu\text{m}$ for the trend line in Fig. 1, and independent of alloy. Smaller values of ξ result in smaller χ_{CRIT} ; for example Johnson's model for a moving crack tip [28] suggests that χ_{CRIT} is between 0.01 and 0.06 μm for the trend line in Fig. 1.

The correlation and associated χ_{CRIT} in Fig. 1 are sensitive to the values of D_H employed, and such diffusivities are variable due to substantial H trapping from microstructural features that confer high strengths [8,14,23,54,55]. The effective D_H is reduced well below values typical of H transport in pure-annealed metals as the density of reversible trap sites increases [64,65], and for such cases, D_H increases as the concentration of lattice-soluble H increases due to increasing environmental severity [64-66]. This behavior was modeled for the Ni-based alloys [57] and demonstrated experimentally for the ultra-high strength steels [51] represented in Fig. 1. The dilemma that H trapping presents to a broad correlation with da/dt_{II} (Fig. 1) is clear and uncertainties are particularly associated with the crack tip. For example, the permeation experiment should employ an environment that approximates the occluded crack tip [66], and a microstructural and strain based trap density similar to the FPZ condition [22,62,63]. Microstructures are likely similar for permeation and crack growth experiments. However, the crack environment is typically more aggressive with regard to H production, favoring increased D_H compared to a permeation result. A 10-fold increase in the lattice H associated with increasing environmental severity produces a 3-fold [51] to 10-fold [66] increase in D_H for steel; the exact dependence depends on specific trapping parameters for a given alloy. High plastic strain about the crack tip may enhance trapping to slow D_H [22,62,63], but could enable dislocation transport that raises effective D_H [54,67]. A small χ_{CRIT} could involve H-diffusion distances that are small compared to the bulk length typical of a permeation experiment. If important traps are spaced above χ_{CRIT} , then D_H could approach faster lattice values compared to the permeation measurements plotted in Fig 1 [26]. Experimental D_H can be in error due to surface-reaction rate limitation of permeation, particularly for passivated alloy surfaces in the aluminum and titanium systems [44]. The trend shown in Fig. 1, and agreement with diffusion-based models, suggest that these complications are offsetting or not primarily important in the context of a broad correlation. This is speculative; the χ_{CRIT} of 0.7 μm could be in error by up to an order of magnitude.

All Reported Rates of HEE in Chloride Solution Refined modeling of da/dt_{II} is complicated because ξ depends on C_{CRIT} and C_0 , with the former dependent on microstructure and σ_{YS} , and the latter on environment chemistry. To examine this behavior, all da/dt_{II} are correlated with D_H in Fig. 2. The vertical arrows represent the range of growth rates reported for a given material and in response to electrochemical or metallurgical variables. The increases in da/dt_{II} for IN 718 and AA7050 were produced by changing-applied electrode potential [41,43]; for the 18Ni Maraging steel due to steel composition and strength change from the 250 to 350 grades [33,58]; for 4340-type steels due to sulfide addition to the chloride solution (Δ) [37], for Ni-Cr-Mo ASTM A723 steel due to increasing σ_{YS} from 1150 to 1380 MPa (\square) [40], and for β -Ti alloys due to crack tip strain rate increase [45].

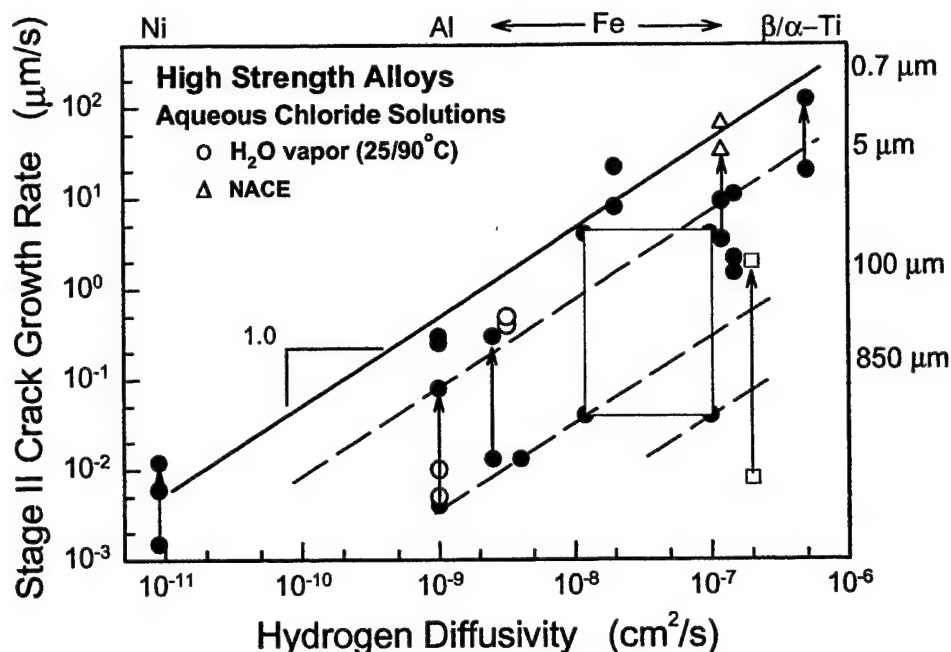


Figure 2 The dependence of da/dt_{II} on D_H for a wide variety of high strength alloys that exhibit HEE in various chloride solutions at 25°C.

The results in Fig. 2 show that da/dt_{II} can be 1-3 orders of magnitude less than the upper-bound trend from Fig. 1. With $\xi = 3$, larger χ_{CRIT} (5 to 850 μm) are associated with the dashed lines for $da/dt_{II} \propto D_H$. Analysis of limited data below the upper bound leads to large χ_{CRIT} above 1 μm that is incorrect due to three situations that reduce da/dt_{II} below the fastest levels reported. These include reduced-equilibrium C_o due to chemical factors [32], the intervention of environmental mass transport or crack-surface reaction rate-control that reduces the surface-H concentration to below the equilibrium C_o [8], and strength or metallurgy effects on C_{CRIT} . Essentially, ξ depends on C_o and C_{CRIT} , and is reduced below the value of 3.0 used to analyze the data in Fig. 1. Stated alternately, $da/dt_{II} \propto D_H C_o / \chi_{CRIT}$ [8] and environmental conditions that lower C_o will lower da/dt_{II} for constant χ_{CRIT} . Estimation of χ_{CRIT} from these data is complicated because C_o or ξ are unknown.

The data in Fig. 2 illustrate chemically limited C_o and reduced da/dt_{II} . First, consider the large amount of data for steels ($10^{-8} < D_H < 10^{-7} \text{ cm}^2/\text{s}$) cracked in neutral NaCl solution at the free corrosion potential [18,35-37,39,40]. Electrochemical conditions (e.g., cathodic polarization) that increase C_o will increase da/dt_{II} toward the upper bound line with χ_{CRIT} between 5 and 0.7 μm . This is supported by data for high strength AISI 4340-type steel cracked in neutral NaCl solution (\bullet at $D_H = 1.0\text{-}1.2 \times 10^{-7} \text{ cm}^2/\text{s}$) and H_2S -saturated acidified chloride (NACE solution, Δ) [37]. The latter promoted H uptake in steel and the da/dt_{II} increased substantially to the upper-bound. The large amount of steel HEE data reviewed by Carter, Fig. 3, further illustrates this behavior [68]. The da/dt_{II} span the range from 0.007 to 40 $\mu\text{m}/\text{s}$, with the fastest rates fitting the upper-bound trend line and $\chi_{CRIT} = 0.7 \mu\text{m}$ in Figs. 1 and 2. For lower D_H steels ($10^{-9} < D_H < 10^{-8} \text{ cm}^2/\text{s}$), da/dt_{II} for the lower- C_o neutral chloride solution correlates with the higher upper bound trend line. Since D_H and da/dt_{II} are lower, reaction rate control is less likely to affect H uptake. Turnbull and coworkers modeled coupled surface reaction and H diffusion to predict that H is lost through crack walls adjacent to the tip for high D_H materials such as alloy steels ($D_H \sim 10^{-7} \text{ cm}^2/\text{s}$); C_o is limited to less than the equilibrium level [17]. This H loss reduces da/dt_{II} , consistent with the data in Figs. 2 and 3.

The data for steels in Figs. 2 and 3 illustrate the effect of alloy strength on HEE; da/dt_{II} increases with increasing σ_{YS} [3]. An example is provided for ASTM A723 (\square in Fig. 2), where the vertical arrow shows increasing da/dt_{II} for σ_{YS} from 1150 to 1380 MPa and HEE in NaCl solution [39,40]. Similar strength dependence is apparent for the 18Ni Maraging steels in Fig. 2 ($D_H = 2.5 \times 10^{-9} \text{ cm}^2/\text{s}$) [33,58] and suggested in Fig. 3 (e.g., AISI 4340 in water, \bullet). The adverse effect of strength on da/dt_{II} is due to increasing crack tip stress, proportionate to σ_{YS} for a given K and achieving the H-failure condition at reduced C_{CRIT} [1,6,7,18,19,23,24,32]. In H diffusion models (Eq. 1), reduced C_{CRIT} results in increased ξ and da/dt_{II} at fixed C_o .

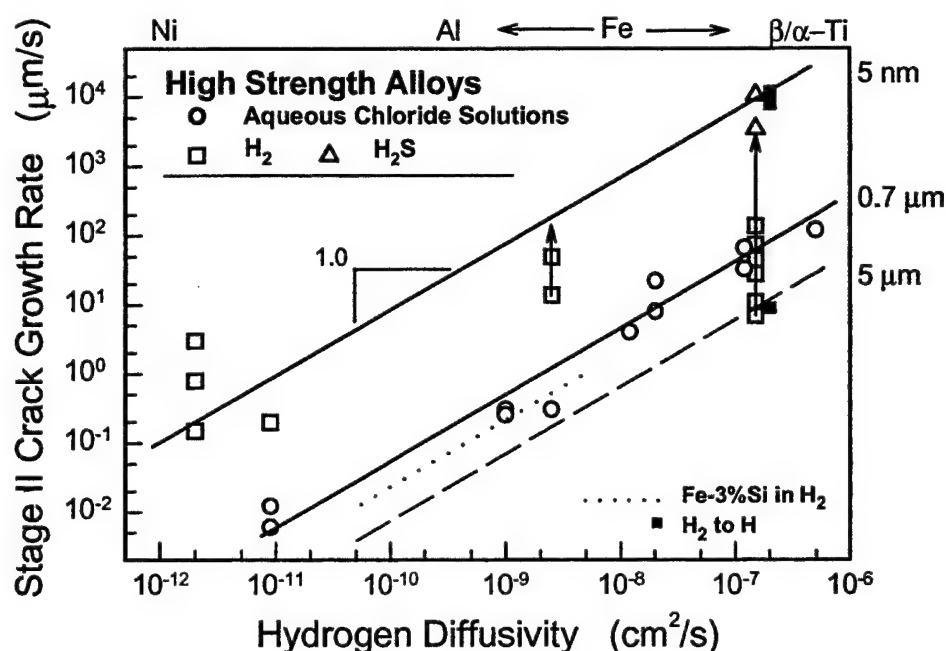
The complexities associated with environment-sensitive equilibrium C_o , kinetic limitation of surface H production, and strength dependent C_{CRIT} are minimized through the use of the fastest-reported da/dt_{II} in Fig. 1. It is reasonable to conclude that fast da/dt_{II} is proportional to D_H , as predicted by H-diffusion limitation, and that χ_{CRIT} is less than $1 \mu m$.

Hydrogen diffusion control of HEE is further established by correlating D_H with da/dt_H for IG cracking of high strength alloys in gaseous H_2 and H_2S environments. Data are plotted in Fig. 4 for the alloys listed in Table II. High strength austenitic stainless steel and nickel superalloys were cracked in high pressure (100–200 MPa) H_2 , while maraging and tempered-martensitic steels were cracked in low pressure (~ 100 kPa) H_2 . The dotted line represents TG cracking of Fe-3%Si single crystal, exposed to 100 kPa H_2 at 0°C to 125°C [14].

Figure 3 The dependence of da/dt_{II} on σ_{YS} for high strength steels in distilled water or chloride solution [68].

Table II High Strength Materials Investigated for Gaseous HEE

Alloy	σ_{YS} (MPa)	D_H @ 25°C (cm ² /s)
Fe-3%Si Single Crystal [14]	300	1.4×10^{-10} [14]
Precipitation Hardened Austenitic Stainless: JBK-75 [69]	850	2×10^{-12} [71]
Nickel-based Superalloy: IN-903, IN-718 [70,71]	1125	$9-14 \times 10^{-12}$ [56,71]
18Ni (250) Maraging Steel [13]	1700	2.5×10^{-9} [34]
Tempered Martensitic Steels: AISI 4340 type [8,10,11,18,35,37,72]	> 1500	$1-2 \times 10^{-7}$ [18,35,51]

Figure 4 The dependence of da/dt_{II} on D_H for a wide variety of high strength alloys that exhibit HEE in various gases and electrolytes at 25°C.

The fastest Stage II crack growth rates in H_2 and H_2S are reasonably proportional to D_H , paralleling the correlation from Fig. 1 for chloride solutions and suggesting that H diffusion limits crack growth. The results for 4340-type steels at high D_H (\square , 1.5×10^{-7} cm²/s), and to a lesser extent 18Ni Maraging steels (\square , 2.5×10^{-9} cm²/s), are consistent with a C_o reduced by either surface reaction-rate limitation [8,9] or reduced environmental activity at equilibrium [13,32]. This effect on C_o is prominent at the faster D_H and da/dt_{II} , where rate limitation is more likely, and for these cases where lower pressures of hydrogen were used. For HEE in pure H_2 , C_o and da/dt_{II} increase with H_2 pressure raised to powers between 0.5 and 1 [11,13]. The vertical arrows in Fig. 4 reflect this influence of increasing hydrogen pressure and hence C_o . While the alloy steels have not been studied in high pressure H_2 , faster da/dt_{II} were reported for HEE in H_2S (Δ in Fig. 4 [37,68]) where surface reaction is not likely to rate limit crack growth and efficient-H uptake leads to a high-equilibrium level of C_o . Compelling support for this argument is provided by da/dt_{II} data reported for AISI 4130 steel tested in either low pressure H_2 (lowest \blacksquare at $D_H = 2.0 \times 10^{-7}$ cm²/s in Fig. 4) or thermally dissociated H (highest two values of da/dt_{II} , \blacksquare) [73]. Crack growth is low for the molecular gas case, but increases in response to predissociation of H_2 to H and the resultant substantial increase in C_o . It is likely that da/dt_{II} for the maraging steels increases for higher H_2 pressures, H_2S , or dissociated-H environmental

conditions, and approaches the upper-bound line drawn in Fig. 4. The behavior of Fe-3%Si may similarly be raised towards the upper bound by increasing H_2 pressure. Notably, da/dt_{II} values measured at elevated temperatures were below the dotted-trend line because surface reaction became rate limiting over H diffusion [14]. Similar behavior was reported for high strength alloy steels [13]. The D_H values for the face-centered cubic stainless steel and Ni-based alloys were estimated to reflect the trapping typical of such precipitation hardened microstructures [56,57,71], but are subject to the uncertainties discussed in a previous section. The variation in da/dt_{II} for the A-286 type stainless steel (JBK-75) is due to changes in grain boundary precipitation [69], and likely reflects changing C_{CRIT} .

An extremely low critical distance, $\chi_{CRIT} = 5$ nm, is suggested for the H-producing gases based on the diffusion analysis of the trend line using $\xi = 3$ in Eq. 1. This distance is 150 times lower than the value calculated for the upper bound for the electrolytes, contradicting the notion that χ_{CRIT} should be independent of environment and C_0 . The correlations in Fig. 4 suggest an intriguing possibility. Corrosion could produce a high concentration of vacancies localized to within a short distance of the crack-tip surface [74-77]. Hydrogen is trapped at vacancies or vacancy clusters that are not annihilated by self-diffusion [44,54], suggesting that H transport in this near-surface layer is characterized by a reduced D_H . The correlations in Fig. 4 show that D_H must be reduced 200-fold to superpose the gas and electrolyte data.

Discussion

The correlations in Figs. 1, 2 and 4 strongly support H-diffusion control of the fastest rates of intergranular hydrogen environment embrittlement of high strength alloys. Important insights are obtained regarding recurring uncertainties that hinder modeling, including: (1) χ_{CRIT} , (2) stress and plastic strain about the IG crack tip, and (3) the magnitude of crack-tip surface and fracture process zone hydrogen concentrations.

Critical Distance for HEE

Critical distance is centrally important to modeling hydrogen embrittlement. The χ_{CRIT} has been equated to the location of highest tensile stress ahead of a crack tip [6,18,19,23], microstructural features such as grain size or precipitate spacing [8,18,20,25,26,60,78,79], strain-generated H-trap sites [22,25,26,62,63], or the crack-tip surface [6,32,80-82]. The correlations in Figs. 1, 2 and 4 suggest that χ_{CRIT} for Stage II HEE in high strength alloys is extremely small, less than 1 μm and as small as 5 nm. For the alloys represented, grain size ranged from 20 to 100 μm ; this distance does not correlate with χ_{CRIT} . Fracture mechanics modeling locates the maximum in crack tip tensile and hydrostatic stresses at 1 to $4\delta_T$ where $\delta_T = K^2/2\sigma_{YS}E$ for a blunted crack tip [4,83,84], well inside of the crack tip plastic zone. For the alloys and stress intensities at the onset of Stage II HEE in Figs. 1 to 4, this location ranges from 2 – 6 μm to as high as 24 – 96 μm (Table III). Typically, da/dt_{II} was sustained for K levels 2 to 4 times higher than used in these calculations, resulting in distances that are 4 to 16 times higher than listed in Table III. These comparisons suggest that H damage occurs much closer to the crack tip than expected based on elastic-plastic stress control.

Several studies concluded that χ_{CRIT} is very small for HEE. Circumstantial evidence suggested that, when H diffusion was rate limiting for steel in H_2S or H_2 , the FPZ was well within one austenite grain diameter [11]. For transgranular HEE in low strength Fe-3%Si, acoustic emission and crack-surface arrest markings suggested that χ_{CRIT} was less than 1 μm [14]. Measurements of rapid change in da/dt , with changing H_2 pressure [6,85-87] or temperature [13] suggested a near-surface FPZ for HEE with χ_{CRIT} less than 0.1 to 1 μm . Ficalora and

Table III Calculated Blunted Crack Tip Opening Displacement, $\delta_T = K^2/2\sigma_{YS}E$

Alloy	σ_{YS} (MPa)	Applied K (MPa \sqrt{m})	1 to 4 δ_T (μm)
Fe-3%Si Single Crystal	300	30	10 to 40
Precipitation Hardened Austenitic Steel	850	90	24 - 96
Nickel Based Superalloy	1125	50	6 - 22
Precipitation Hardened Aluminum	500	15	3 - 12
18Ni Maraging Steel	1700	30	2 - 6
Tempered Martensitic Steel	1600	40	3 - 10
$\beta + \alpha$ Ti Alloy	1150	30	4 - 14

coworkers argued that a surface reaction-limiting model effectively describes HEE in the steel/H₂ system, and by default, the process zone must be near to the crack tip to enable rapid H diffusion [82]. Vehoff and coworkers modeled da/dt_{II} as controlled by surface adsorption-limited supply of H, with χ_{CRIT} assumed to be less than 1 nm [80,81,86,87]. Gerberich and coworkers predicted the temperature dependence of da/dt_{II} for HEE of high strength steels cracked in H₂, with adjustable values of χ_{CRIT} in the range from 50 to 400 nm providing the best fit of experiment and a H-diffusion model [32]. The observed independence of the rising-K growth-initiation threshold on applied dK/dt between 10^{-3} and 10^{-4} MPa $\sqrt{m/s}$ is consistent with χ_{CRIT} less than 1 μm for nickel-based superalloy X-750 in high pressure H₂ [79]. The same experimental method, applied to β/α -Ti alloys cracked in NaCl (Fig. 1), established that K_{IH} was independent of dK/dt over the wide range from 10^{-4} to 4 MPa $\sqrt{m/s}$ [45]. Severe intergranular HEE was sustained in this Ti alloy at a loading rate that is 3-4 orders of magnitude faster than the highest rate used for X-750, consistent with the 10^5 -times faster D_H for β -Ti compared to a Ni-based alloy.

A consensus is emerging that χ_{CRIT} is small for HEE, but large for IHE in the same microstructure. Predicted χ_{CRIT} values were 10–100 μm for IHE of tempered martensitic steels [18,20,32], nickel based X-750 [79], and nickel-based IN-903 (in Stage I) [25,26,78]. These larger values of χ_{CRIT} were related to grain size, particle spacing, or the boundary of the crack tip plastic zone (or at least 5 to 10 δ_T). HEE and IHE experiments were conducted with notched specimens to better determine the controlling length scale in the FPZ, as suggested by Rice [88,89]. While IHE nucleated just before the elastic-plastic boundary and well ahead of the notch root, HEE in the same high strength steel occurred at or 0.1–10 μm ahead of the notch surface in contact with the environment [90–92]. The exact distance was not resolved. The χ_{CRIT} is likely controlled by a different crack-tip H distribution for IHE vs. HEE. For example, calculations indicate that H is lost from the near-crack tip region during IHE, since the specimen is typically cracked in moist air, resulting in a large χ_{CRIT} [17,79]. In contrast the near-surface H concentration is high for HEE [92], in a location where crack tip plastic strain is presumably large and associated trapping is significant [22,62,63], resulting in a small χ_{CRIT} .

Extensive results for slow- D_H nickel-based superalloys demonstrate that the critical distance is affected by interactions of microstructure, FPZ-H concentration, fracture mechanism, K level, and the source of H [24–26,78,93–95]. For some systems (18Ni Maraging steel [96] and small grain superalloys [93] in H₂) HEE is intergranular for all K levels, while a transgranular to IG transition occurred as K increased from Stage I to II for other alloys (IN-718 in NaCl [41] and large grain superalloys in H₂ [93]). A fracture path change is likely accompanied by a change in the governing critical distance [24–26]. For example, the Stage I threshold for HEE in IN-

903 in high pressure H_2 increased with increasing grain size, coincident with a change from IG to transgranular H-enhanced cracking [93]. This behavior was predicted by a change from stress-based IG cracking, with χ_{CRIT} equaling the grain size of 20-50 μm [78,94], to strain based transgranular cracking, with χ_{CRIT} equaling the spacing (35 μm) of carbides within large ($> 100 \mu m$) grains [93]. These critical distances are orders of magnitude larger than the values inferred from the intergranular Stage II da/dt_{II} data and H-diffusion analysis associated with Fig. 4. Specifically, da/dt_{II} for intergranular HEE of IN-903 in high pressure H_2 [71], included in Fig. 4, is well described by H diffusion over χ_{CRIT} of ~ 5 nm. For transgranular IHE in the same alloy, Moody and coworkers conclude that χ_{CRIT} is large (20-40 μm) and dictated by carbide spacing from strain-based modeling of Stage I cracking [78,95]. Here, H diffusion is not important since equilibrium redistribution of H to the FPZ is enabled over a relatively large distance by low da/dt and long time [78,95]. This model distance is reduced to $\sim 0.8 \mu m$ for transgranular Stage II, based on the assumption that da/dt_{II} is controlled by the much shorter time associated with short-range H redistribution from γ' -precipitate trap sites to crack nuclei at slip band intersections of a 0.8 μm spacing [25,26]. A similar analysis has not been conducted for intergranular HEE where the boundary condition of the starting-H source is very different compared to IHE. None-the-less, these results suggest that a small χ_{CRIT} may govern Stage II cracking and this critical distance may increase to a large value typical of a larger-scale microstructure length at low crack growth rates within Stage I.

Intergranular-Crack Tip Mechanics

Crack tip stresses are central to understanding the critical distance and damage during HEE. The calculated δ_T values in Table III are based on a continuum-plasticity theory solution for a smoothly blunting crack [4,83,84,97]. However, experimental results in Fig. 5 show that intergranular cracking typical of HEE exhibits a reduced-tip opening for a high strength $\beta+\alpha$ Ti alloy (Ti-8V-6Cr-4Mo-4Zr-3Al) [45,48]. A transgranular crack produced by fatigue loading (lower-left image) and an intergranular crack from prior HEE in NaCl solution (lower-right image showing the crack tip at a grain-boundary triple point, TP) were loaded in the vacuum stage of a scanning electron microscope. Crack-surface displacement in the Mode I direction (CDSI at a distance of 3 μm behind the crack tip) was measured as a function of applied K. The K dependence of δ_T for the stationary-blunted TG crack in Fig. 5 is consistent with the Hutchinson-Rice-Rosengren (HRR) model [83,97]. However, this model over-predicts CSDI for the crack, as reported for transgranular fatigue cracks in other alloys [98]. Critically, both the data on CDSI vs. applied K and the SEM images, obtained at the same magnification for $K = 33$ $MPa\sqrt{m}$, show that the opening of the intergranular HEE crack is substantially less than that of the TG crack. For example in Fig. 5, the HRR-calculated δ_T is 3.9 μm for $K = 33$ $MPa\sqrt{m}$, while the measured CDSI is 1.3 μm for the TG crack and 0.3 μm for the IG TP crack.

Restricted opening of an intergranular crack should shift H-damage sites nearer to the crack tip compared to $1 - 4\delta_T$ from the blunted crack analysis (Table III), contributing to small χ_{CRIT} . Crack tip stresses are bounded by a singular $1/(\text{distance})^{1/2}$ distribution for elastic deformation, and a nonsingular distribution maximized at $3 - 5\sigma_{YS}$ and located at $1 - 4\delta_T$ from the blunted crack tip subjected to elastic-plastic deformation [4,83,84,88,97]. It is reasonable to speculate that stresses near the tip of the very sharp IG crack tend to the singular-elastic distribution and high values. Oriani [6,850] and van Leeuwen [23] so speculated to fit models of K_{TH} with experimental measurements. Such stresses were ascribed to local irregularities in the stress state, perhaps associated with restricted plastic deformation on a sub- μm length scale.

Advances have been recorded in modeling near-singular stress levels at crack tips in deformable metals. Shih and coworkers modeled such high stresses based on a hypothesized thin-elastic

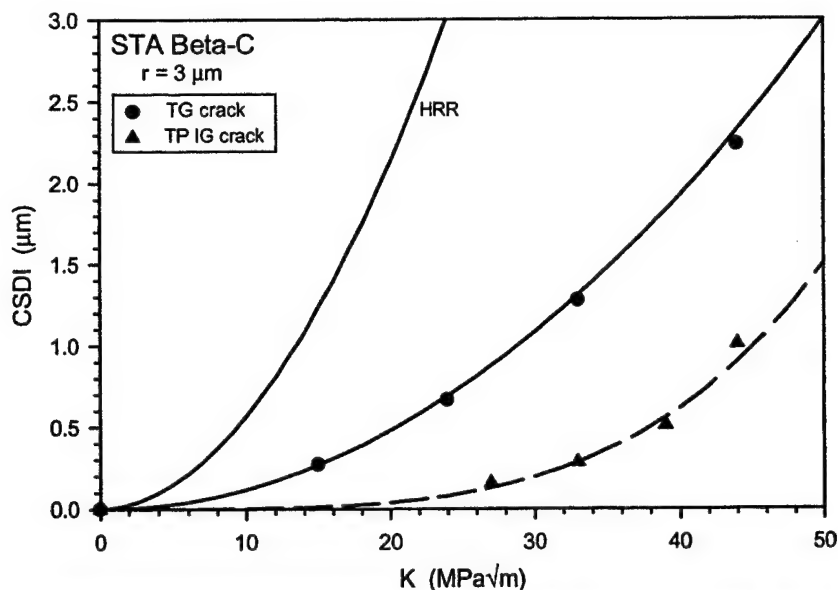


Figure 5 *In situ* SEM measurements of the Mode I crack tip opening vs. applied K for a transgranular fatigue precrack (left image and “TG crack”) and HEE-intergranular crack (right image and “TP IG crack”) in a high strength $\beta+\alpha$ Ti alloy (Ti-8V-6Cr-4Mo-4Zr-3Al) [45,48]. The marker bar represents a distance of 20 μm and each specimen imaged was loaded in the vacuum chamber of an SEM to an applied K of 33 $\text{MPa}\sqrt{\text{m}}$.

zone embedded about a crack tip and surrounded by elastic-plastic deformation [99]. Chen and Gerberich predicted very high stresses in a single crystal [14], using a model of the interaction of elastic stress fields about shielding dislocations arrayed in a pileup standing-off from the tip of a sharp crack [100-102]. In this work with Fe-Si ($\sigma_{\text{YS}} = 300 \text{ MPa}$), the blunt-crack model predicted that the mean of the opening-direction tensile stresses was 600 MPa, maximized at $2\delta_{\text{T}} = 10 \mu\text{m}$ ahead of the crack tip for $K = 20 \text{ MPa}\sqrt{\text{m}}$. The dislocation model predicted that this hydrostatic stress equaled 22,000 MPa, maximized 20 nm ahead of the sharp tip. Crack tip dislocation configurations in the complex microstructures of high strength alloys are uncertain.

Continuum-plasticity models provide an alternate approach to understanding crack tip deformation. Consider an explanation at the meso-length scale. Lee and Kim demonstrated that both the opening-mode tensile and hydrostatic stresses ahead of a crack tip along an interface are increased by up to 50% at a given K due to differences in elastic properties as well

as the yield strength and work hardening capacity of the two bounded materials [103]. The plastic zone size is reduced dramatically (up to 15 times) in the hard material and increased modestly ($\sim 15\%$) in the softer material. This effect could be exacerbated due to hardening by an elevated dislocation density [104] and compatibility stresses from anisotropic deformation local to the grain boundary [105]. This stress elevation and restricted crack tip plasticity in 1 of the 2 crystals could be manifest as a restricted crack tip blunting. Similar differences could occur locally in the polycrystals proximate to a grain boundary, but the effect would be countered for an array of randomly oriented grains along a crack front. This behavior has not been modeled.

A strain gradient mechanism for crack tip stress elevation could operate at the dislocation-length scale. Experiment and theory show that plastic flow is hindered by a strain gradient that is substantial over a restricted and material-constant length on the order of $0.5 - 5 \mu\text{m}$ [106]. Geometrically necessary dislocations result in added hardening, with the density of necessary-extra dislocations scaling with the magnitude of the strain gradient. Continuum models that capture this hardening in various problems in deformation and fracture predict lower crack opening displacements and higher stresses compared to classical plasticity theory [106-110]. For example, Hutchinson and coworkers reformulated crack tip stress and strain fields, using gradient plasticity, and demonstrated a factor of 3 reduction in δ_T and large increases in crack tip stresses (from $4\sigma_{YS}$ to $10\sigma_{YS}$) within the first 2-4% of the plastic zone diameter [107,109]. This situation is illustrated schematically in Fig. 6. Jiang and coworkers used an alternate formulation of strain gradient plasticity to confirm that crack tip stresses are increased several times above the predictions of classic theory, in the region within 30% of the characteristic-material dimension for storage of necessary dislocations in a strain gradient [108]. Effectively, a zone of material is gradient hardened, adjacent to the crack tip surface and embedded well within the plastic zone. Crack tip stress elevation increases as the ratio of the gradient length scale to plastic zone increases [110]. High levels of gradient hardening are therefore expected when the material length is large or the extent of plasticity ahead of the crack tip is restricted.

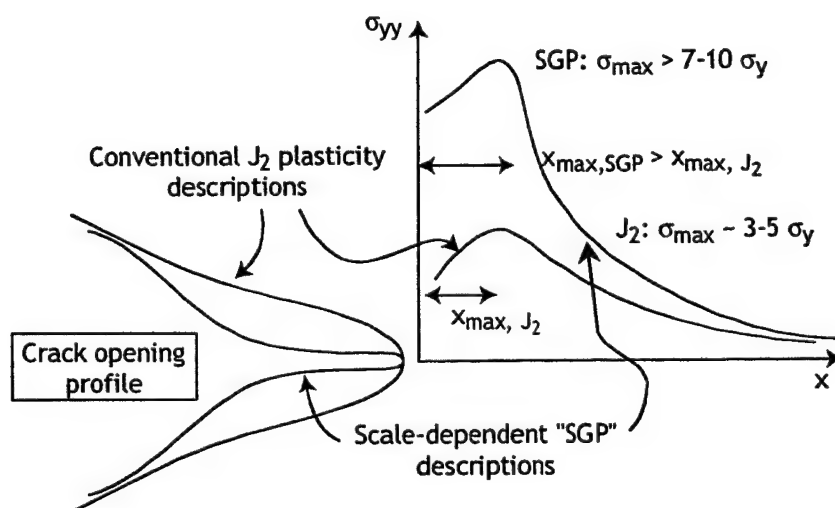


Figure 6 Schematic diagram of the effect of enhanced hardening at the crack tip due to strain gradient plasticity (SGP) effects, based on results from Wei and Hutchinson [109]. After Begley [111].

Increased stresses are important to a damage process localized to the scale of strain-gradient hardening [106-109]. When the crack tip plastic zone, and included FPZ associated with the work of fracture separation, extend over ~ 25 to $500 \mu\text{m}$, as in microvoid fracture, then strain

gradient effects on the crack tip stresses and strains that drive this damage are not important [106,107]. However, when the intrinsic plastic zone and FPZ damage distances are small, less than ~ 5 to $10\ \mu\text{m}$ and only 2 to 3 times the gradient distance for altered hardening, then stress elevation and reduced plastic dissipation are likely to be important. This should be the case for HEE, given the very small χ_{CRIT} inferred from hydrogen diffusion modeling. For such situations, crack tip stresses are elevated and damage sites are shifted close to the crack tip.

The issue is whether this mechanism is promoted for a HEE crack along a boundary between deformable grains in a complex alloy. If H is trapped at the grain boundary, then fracture is localized there and strain gradient plasticity will be important. Wei and Hutchinson show that gradient plasticity elevates the stresses in a thin-deformable layer deposited on a nondeformable substrate, and this process is exacerbated when a crack is present along the interface [107]. Interface fracture is promoted by this hardening when there is either an elastic zone about the boundary [14,99] or plastic deformation in the metal [107]. If the plastic zone size is reduced by differences in elastic and plastic flow between the bounded grains [103,105], or by reduced boundary-fracture resistance, then the length scale of the crack tip strain gradient is a more significant fraction of the plastic zone at fixed K and crack tip stresses rise. If large H concentrations are present in one or both grains, in a layer above and below the crack wake and tip, then deformation may be restricted and stresses rise due to the elastic singularity [14,99] as well as strain gradient hardening [107]. There are a variety of scenarios by which gradient plasticity could promote intergranular HEE, however, modeling and experimental probes of such effects are nonexistent.

Consider the crack tip images in Fig. 5 based on these concepts. The TG crack was extended by fatigue in moist air at a K level ($15\ \text{MPa}\sqrt{\text{m}}$) below the range employed for the *in situ* SEM experiment. The IG TP crack was extended by HEE in NaCl at a K level of about $40\ \text{MPa}\sqrt{\text{m}}$. Each specimen was machined to produce a smaller specimen and H was likely lost prior to loading in the vacuum of the SEM. These results should not reflect an influence of H on deformation about the crack tip. A likely hypothesis is that this deformation was restricted by elastic and plastic property differences between adjacent grains for the IG crack. For a given applied K, the crack opening was reduced by this restricted deformation, the length for strain gradient plasticity was a larger fraction of this plastic zone, the crack tip opening was further decreased, and crack tip tensile stresses were increased. For the more complex HEE case, if H in the IG process zone affects damage at a lower K, or hinders plastic deformation in either grain, then strain gradient hardening and stress elevation are further amplified.

Process Zone H Enrichment

Model Predictions In addition to critical distance and local stress concentration, H enrichment about the crack tip is critical to understanding HEE and IHE [1,6,7,14,18-24,27,32,79,112]. The total concentration of H at damage sites within the stressed FPZ (C_H) is affected interactively by the lattice concentration of H (C_o), hydrostatic stress (σ_H), and the strength of H trapping at one or more sites. The C_o in equilibrium with the crack tip environment is determined by the local overpotential for H production. The enhancing effect of σ_H on lattice-H concentration, $C_{H\sigma}$, is approximated by the elastic solution [23,113]:

$$C_{H\sigma} = C_o \exp [\sigma_H V_H / RT] \quad (2)$$

The amplifying effect of trapping on C_o and $C_{H\sigma}$, to yield C_H , is given by [64,65,114]:

$$C_H = \frac{C_{H_0} \exp \left[\frac{H_T}{RT} \right]}{1 + C_{H_0} \exp \left[\frac{H_T}{RT} \right]} \quad (3)$$

for the case where C_{H_0} is small and H_T is the binding energy of H to a dominant-single trap site.

The amount of H associated with process zone failure has been controversial, in large part due to uncertainties with the magnitudes of C_0 and σ_H [23,85]. For example, McMahon argued that intergranular IHE and HEE only occur in steels if impurities such as S and P co segregate because C_H is orders of magnitude smaller than the concentrations of other embrittling-boundary solute [1,115]. In this interpretation, C_0 was calculated from a solubility relationship for low pressure H_2 without trapping and σ_H was modeled to equal $2.4\sigma_{YS}$. The K_{TH} for HEE of high strength steels correlated with a composition parameter equaling $(10^4 C_0 + Mn + Si/2 + P + S)$ in weight pct. The origin of the 10^4 multiplier of C_0 was not specified, and precise levels of P and S responsible for intergranular embrittlement of high strength steels were not measured [1,115]. This analysis is suspect; results show that high levels of H can accumulate about the crack tip, particularly in high strength alloys.

One or more factors promote high-H content in the FPZ. (1) *H Trapping*: Symons showed that H trapping at boundary carbides ($H_T = 26$ kJ/mol) in a nickel superalloy, combined with stress enhancement typical of a blunted crack ($\sigma_H = 4.5\sigma_{YS}$) resulted in predicted C_{H_0} of 0.6-0.9 atom fraction at intergranular fracture sites and in equilibrium with 140 kPa H_2 at an applied K of ~ 40 MPa \sqrt{m} [79]. Trapping of H at microstructural features in high strength steels produces orders of magnitude increase in C_H , inferred from trapping theory and permeation measurements [3]. (2) *Stress*: The previous discussion of intergranular crack tip mechanics shows that there are several mechanisms for elevation of the crack tip tensile stresses to the level where $\sigma_H = 10$ to $20\sigma_{YS}$. If C_{H_0} is proportional exponentially to σ_H (Eq. 2), then a 5-fold increase in crack tip σ_H , from 2.5 to $12.5\sigma_{YS}$, results in a 10^4 to 10^5 increase in C_0 to C_{H_0} . This effect was recognized by Oriani, Gerberich, van Leeuwen, and coworkers who argued that "elastic" levels of σ_H that were of order $E/10$ resulted in $C_{H_0} \sim 30,000 C_0$ [6,14,23,85]. (3) *(Electro)Chemistry*: Expectations of the magnitude of low C_0 in equilibrium with a H-producing gas or electrolyte are based largely on the results of measured-H fluxes in permeation experiments. However, high fugacities are predicted for H production on bare metal surfaces [53]. While the enhancing effects of aggressive electrochemical factors and plastic deformation on H uptake have been considered broadly, it is difficult to simulate the situation at a crack tip. Such work supports substantial H uptake at a crack tip in Al, Ti, and Ni based alloys in chloride solution [38,41,43,47,53,116,117], as well as for aluminum alloys in water vapor [9,46].

Experimental Measurement Progress in modeling HEE is hindered by the lack of direct measurements of C_H in the FPZ of a high strength alloy. Dissolved H is difficult to measure due to small atomic size, high mobility, small χ_{CRIT} , and strong concentration gradient. Thermal desorption spectroscopy provided evidence of extreme-H enrichment in the wake of an intergranular HEE crack in AA7050-T6 stressed in acidified chromate-chloride solution [43,47]. The TDS spectra in Fig. 7 show this enrichment from 0.03 ppm to 0.10 and 0.29 ppm, the integrated amount of H evolved during ramp heating of 1-mm thick crack-wake specimens, for HEE at 2 applied-electrode potentials. A C_H above the bulk-measured concentration of 0.045 ppm was not observed for the wake of the transgranular corrosion fatigue precrack, grown at a lower electrode potential, or a fracture produced in liquid nitrogen (LN_2) after the

specimen was removed from solution. The increase in C_H with decreasing electrode potential shown in Fig. 7 correlated with increasing da/dt_{II} , consistent with electrochemical considerations of H production at the occluded crack tip [43].

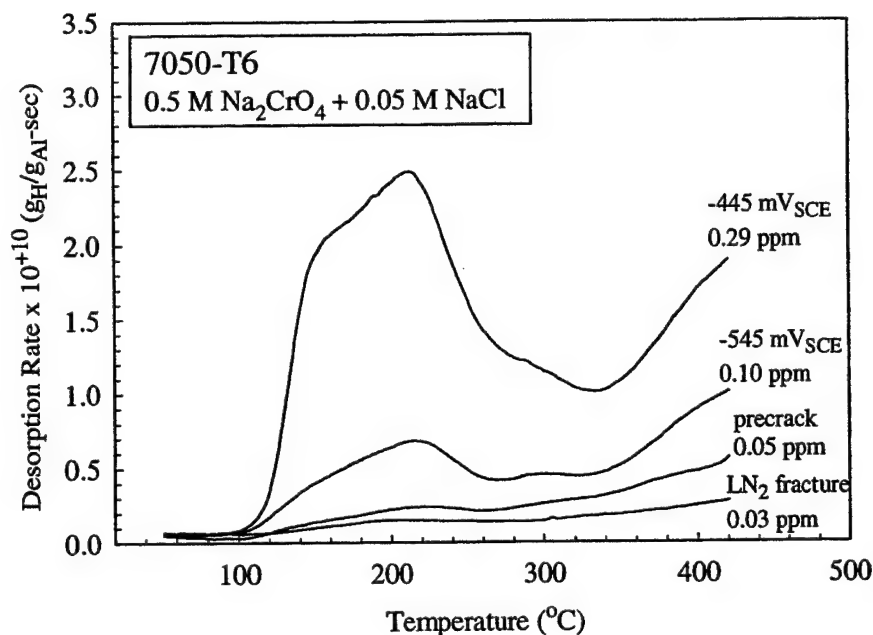


Figure 7 Thermal Desorption Spectroscopy results for 1-mm thick specimens from the wakes of a HEE crack grown at 2 different potentials, a corrosion-fatigue precrack, and a solution-exposure free rapid-LN₂ fracture surface in AA7050-T6 stressed in aqueous chromate-chloride solution [43,47].

The result in Fig. 7 is unexpected since TDS measured the total amount of H dissolved in a relatively large specimen that extended 1000 μm below the crack surface. If H is enriched within 1 μm of the crack surface, then thick-specimen dilution should cloak the amount dissolved during HEE. Results of neutron activation analysis (NRA) of the same crack surface provide an explanation [47]. As shown in Fig. 8, the amount of H retained in the wake of the HEE crack in AA7050-T6 stressed in chloride is massive, between 600 and 6000 ppm by weight or 3 to 15 H atoms per 100 Fe atoms, localized within 0.2 μm of the crack surface. This H profile explains the average amount of H resolved by the TDS measurements (Fig. 7) in spite of dilution. Young measured even larger amounts of H dissolved in the crack wake for AA7050 stressed in water vapor saturated air at 90°C [46]. TDS and NRA experiments represented in Figs. 7 and 8 have not been conducted with other material-environment systems, and must be replicated due to the complexity of the measurements.

Based on the time and temperature associated with NRA-specimen preparation, the H profile in Fig. 8 should only be retained if D_H is of order $10^{-13} \text{ cm}^2/\text{s}$ [47], or 4 orders of magnitude slower than measured in permeation experiments with 7000-series aluminum alloys [44]. This suggests that H is trapped strongly by a high dislocation density or vacancies from dissolution. Shifting the point in Fig. 4 for AA7050-T6, from $D_H = 10^{-9} \text{ cm}^2/\text{s}$ to $10^{-13} \text{ cm}^2/\text{s}$ at the same da/dt_{II} of 0.1 $\mu\text{m}/\text{s}$, results in good agreement with the upper bound for HEE in H₂, as hypothesized previously based on vacancy trapping of H in the FPZ.

A high level of H in the first μm of a HEE crack surface can explain the near tip fracture process zone derived from the correlations in Figs. 1, 2 and 4. Speculatively, if a crack surface

is reactive due to electrochemistry or plastic strain, then near-monolayer-H coverage and high C_0 could form quickly. This H penetrates by diffusion over a micrometer-scale distance and is retained by trapping. High H eliminates the need for longer range diffusion to the region of highest crack tip stresses, if such stresses are maximized more deeply beneath the surface, as suggested in Fig. 6 for both conventional and strain gradient plasticity models. Crack advance is governed by a small volume of hydrogenated material of weakened bond strength and subjected to crack tip stresses of yield level. While tensile stress is required for cracking, the distribution of crack tip stress does not establish χ_{CRIT} . If crack stresses are high due to restricted plasticity, then the embrittling effect of high C_H is exacerbated.

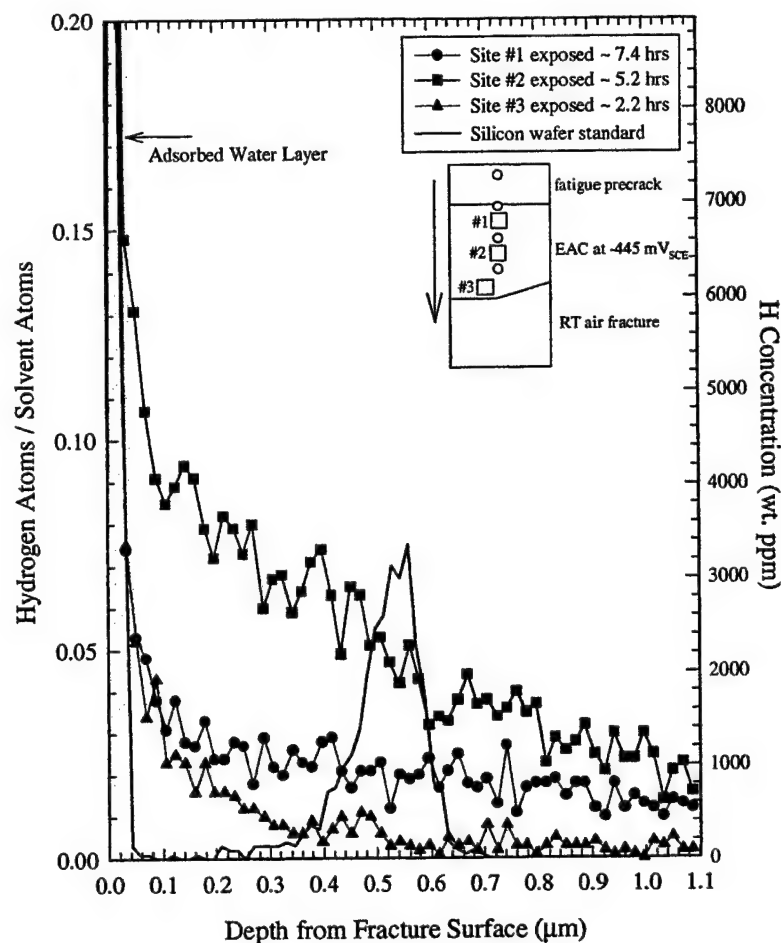


Figure 8 NRA measurements from the wake of a HEE crack in AA7050-T6 stressed in aqueous chromate-chloride solution [47]. The Si standard is used to calibrate the amount of H dissolved at a known depth.

Conclusions

1. The fastest rates of Stage II intergranular hydrogen environment embrittlement are directly proportional to hydrogen diffusivity for a wide range of high strength alloys in the nickel, aluminum, iron, and titanium classes. Hydrogen diffusion about the crack tip appears to rate limit this brittle cracking, however, surface-reaction limitation may occur in these alloy-environment systems depending on chemical (low-H production) and material variables (high-H diffusivity).
2. The critical distance ahead of the crack tip for H-diffusion control and intergranular embrittlement is small, less than 1 μm and perhaps as small as 5-10 nm, for high strength alloys in H-producing electrolytes and gases, respectively. This small-critical distance is not understood based on classical micromechanical and electrochemical modeling.
3. Extraordinarily high hydrogen concentration localized within 1 μm of an electrochemically active crack tip, coupled with high crack tip stresses from strain gradient plasticity or elastic shielding as well as H trapping at microstructural sites, focus HEE damage very near to the growing crack tip. With these amplifying factors to enrich concentration, hydrogen is an effective embrittler of high strength alloys.

Acknowledgements

The Office of Naval Research supported this research and many of the cited-graduate studies at the University of Virginia under Grant N00014-91-J-4164, with Dr. A. John Sedriks as the Scientific Monitor.

References

1. C.J. McMahon, Jr., Engng. Frac. Mech., 68 (2001), 773.
2. R.A. Oriani, Corrosion, 43 (1987), 390.
3. R.P. Gangloff, Corrosion Prevention and Control, ed. M. Levy and S. Isserow (Watertown, MA: US Army Laboratory Command, 1986), 64.
4. R.P. Gangloff, Matls. Sci. Engng., A103 (1988), 157.
5. Embrittlement by the Localized Crack Environment, ed. R.P. Gangloff (Warrendale, PA: The Minerals, Metals & Materials Society, 1984).
6. R.A. Oriani and P.H. Josephic, Acta Metall., 22 (1974), 1065.
7. W.W. Gerberich, Engng. Frac. Mech., 68 (2001), 619.
8. M. Gao and R.P. Wei, Metall. Trans. A, 16A (1985), 2039.
9. R.P. Wei, Hydrogen Effects in Metals, ed. I.M. Bernstein and A.W. Thompson (Warrendale, PA: The Minerals, Metals & Materials Society, 1981), 677.
10. G.W. Simmons, P.S. Pao, and R.P. Wei, Metall. Trans. A, 9A (1978), 1147.
11. M. Gao, M. Lu and R.P. Wei, Metall. Trans. A, 15A (1984), 735.
12. M. Lu, P.S. Pao, T.W. Weir, G.W. Simmons and R.P. Wei, Metall. Trans. A, 12A (1981), 805.
13. R.P. Gangloff and R.P. Wei, Metall. Trans. A, 8A (1977), 1043.
14. X. Chen and W.W. Gerberich, Metall. Trans. A, 22A (1991), 59.
15. R.P. Gangloff (PhD Dissertation, Lehigh University, Bethlehem, PA, 1974).
16. A. Turnbull, Corrosion, 57 (2001), 175.
17. A. Turnbull, D.H. Ferriss, and H. Anzai, Matls. Sci. Engng., A206 (1996), 1.
18. W.W. Gerberich, Hydrogen in Metals, ed. I.M. Bernstein, and A.W. Thompson (Materials Park, OH: ASM International, 1974), 115-147.
19. W.W. Gerberich, Y.T. Chen, and C. St. John, Metall. Trans. A, 6A (1975), 1485.
20. W.W. Gerberich, T. Livne, X.F. Chen, and M. Kaczorowski, Metall. Trans. A, 19A (1988), 1319.
21. W.W. Gerberich, P.G. Marsh, and J.W. Hoehn, Hydrogen Effects in Metals, ed. A.W. Thompson, and N.R. Moody (Warrendale, PA: The Minerals, Metals & Materials Society, 1996), 539.
22. A.H.M. Krom, R.W.J. Koers, and A. Bakker, J. Mech. Phys. Solids, 47 (1999), 971.
23. H.P. van Leeuwen, Review on Coatings and Corrosion, V (Haifa, Israel: Technion, 1979), 5.
24. N.R. Moody, S.L. Robinson and W.M. Garrison, Jr., Res Mech., 30 (1990), 143.
25. N.R. Moody, S.L. Robinson, J.E. Angelo and M.W. Perra, Hydrogen Effects in Materials, ed., A.W. Thompson and N.R. Moody (Warrendale, PA: The Minerals, Metals & Materials Society, 1996), 967.
26. N.R. Moody, M.I. Baskes, S.L. Robinson and M.W. Perra, Engng. Frac. Mech., 68 (2001), 731.
27. H.P. van Leeuwen, Corrosion, 31 (1975), 42.
28. H.H. Johnson, Hydrogen in Metals, ed. I.M. Bernstein and A.W. Thompson (Materials Park, OH: ASM International, 1974), 35.
29. J. Toribio and V. Kharin, Intl. J. Frac., 88 (1997), 233.
30. J. Toribio and V. Kharin, Intl. J. Frac., 88 (1997), 247.
31. P. Doig and G.T. Jones, G.T., Metall. Trans. A, 8A (1977), 1993.

32. W.W. Gerberich, T. Livne and X. Chen, Modeling Environmental Effects on Crack Growth Processes, ed. R.H. Jones and W.W. Gerberich (Warrendale, PA: The Minerals, Metals & Materials Society, 1986), 243.
33. D.P. Dautovich and S. Floreen, Stress Corrosion Cracking and Hydrogen Embrittlement of Iron Alloys, ed. R.W. Staehle, et al. (Houston, TX: NACE, 1977), 798.
34. D.P. Dautovich and S. Floreen, Met. Trans., 4 (1973), 2627.
35. G.E. Kerns, M.T. Wang and R.W. Staehle, Stress Corrosion Cracking and Hydrogen Embrittlement of Iron Alloys, ed. R.W. Staehle, et al. (Houston, TX: NACE, 1977), 700.
36. C.S. Kortovich and E.A. Steigerwald, Engng. Frac. Mech., 4 (1972), 637.
37. A.N. Kumar and R.K. Pandey, Engng. Fract. Mech., 20 (1984), 289.
38. N.J.H. Holroyd, Environment-Induced Cracking of Metals, ed. R.P. Gangloff and M.B. Ives (Houston, TX: NACE, 1990), 311.
39. G.N. Vigilante, J.H. Underwood and D. Crayon, Fatigue and Fracture Mechanics: 28th Volume, ASTM STP 1321, ed. J.H. Underwood, B.D. MacDonald and M.R. Mitchell (West Conshohocken, PA: ASTM, 1998), 602.
40. G.N. Vigilante, J.H. Underwood and D. Crayon, "Use of the Instrumented Bolt and Constant Displacement Bolt-Loaded Specimen to Measure In Situ Hydrogen Crack Growth in High Strength Steels", Technical Report ARCCB-TR-98015, (Watervliet, NY: Benet Laboratories, 1998).
41. J.A. Lillard (PhD Dissertation, University of Virginia, Charlottesville, VA, 1998).
42. L.M. Young and R.P. Gangloff, James T. Staley Honorary Symposium on Aluminum Alloys, ed. M. Tiryakioglu (Materials Park, OH: ASM International, 2002), 135.
43. K.R. Cooper, L.M. Young, R.P. Gangloff and R.G. Kelly, Matls. Sci. Forum, 331-337 (2000), 1625.
44. J.R. Scully, G.A. Young, Jr. and S.W. Smith, Matls. Sci. Forum, 331-337 (2000), 1583.
45. B.P. Somerday, L.M. Young and R.P. Gangloff, Fatg. Fract. Engng. Matls. Struct., 23(2000), 39.
46. G.A. Young (PhD Dissertation, University of Virginia, Charlottesville, VA, 2000).
47. L.M. Young (PhD Dissertation, University of Virginia, Charlottesville, VA, 1999).
48. B.P. Somerday (PhD Dissertation, University of Virginia, Charlottesville, VA, 1998).
49. B.P. Somerday and R.P. Gangloff, Matls. Sci. Engng. A, A254 (1998), 166.
50. L.M. Young, G.A. Young, J.R. Scully and R.P. Gangloff, Metall. Trans. A, 26A (1995), 1257.
51. R.L.S. Thomas, D. Li, R.P. Gangloff and J.R. Scully, "Trap Affected Hydrogen Diffusivity and Hydrogen Capacity in Ultrahigh-Strength AerMet[®]100", Metall. Matls. Trans. A, in press (2002).
52. R.P. Gangloff and A. Turnbull, Modeling Environmental Effects on Crack Initiation and Propagation, ed. R.H. Jones and W.W. Gerberich (Warrendale, PA: The Minerals, Metals & Materials Society, 1986), 55.
53. D.G. Kolman and J.R. Scully, Effects of the Environment on the Initiation of Crack Growth, ASTM STP 1298, ed. W.A. Van der Sluys, R.S. Piascik and R. Zawierucha (West Conshohocken, PA: ASTM, 1998), 61.
54. J.P. Hirth, Metall. Trans. A, 11A (1980), 861.
55. G.M. Pressouyre and I.M. Bernstein, Hydrogen Degradation of Ferrous Alloys, ed. R.A. Oriani, J.P. Hirth and S. Smialowska (Park Ridge, NJ: Noyes Publications, Park Ridge, NJ, 1985), 641.
56. W.A. Robertson, Metall. Trans. A, 8A (1977), 1709.
57. N.R. Moody, S.L. Robinson, S.M. Myers and F.A. Greulich, Acta Metall., 37 (1989), 281.
58. C.S. Carter, Metall. Trans., 2 (1971), 1621.

59. R.O. Ritchie, M.H. Castro Cedeno, V.F. Zackay and E.R. Parker, Metall. Trans. A, 9A (1978), 35.s
60. R. Padmanabhan and W.E. Wood, Metall. Trans. A, 14A (1983), 2347.
61. E. Troiano, G.N. Vigilante and J.H. Underwood, "Experiences and Modeling of Hydrogen Cracking in a Thick Walled Pressure Vessel", Fatigue and Fracture Mechanics: 33rd Volume, ASTM STP 1417, ed. W.G. Reuter and R.S. Piascik (West Conshohocken, PA: ASTM, 2002), in press.
62. P. Sofronis and A. Taha, Environmentally Assisted Cracking: Predictive Methods for Risk Assessment and Evaluation of Materials, Equipment and Structures, ASTM STP 1401, ed. R.D. Kane (West Conshohocken, PA: ASTM, 2000), 70.
63. A. Taha and P. Sofronis, Engng. Frac. Mech., 68 (2001), 803.
64. R.A. Oriani, Acta Metall., 18 (1970), 147.
65. H.H. Johnson, Metall. Trans. A, 19A (1988), 2371.
66. A.J. Griffiths and A. Turnbull, Corrosion Science, 37 (1995), 1879.
67. J.K. Tien, S.V. Nair and R.R. Jensen, Hydrogen Effects in Metals, ed. I.M. Bernstein and A.W. Thompson (Warrendale, PA: The Minerals, Metals & Materials Society, 1981), 37.
68. C.S. Carter, "Stress Corrosion Cracking and Corrosion Fatigue of Medium-Strength and High-Strength Steels", (Seattle, WA: Boeing Commercial Aircraft Company, 1980), unpublished-unnumbered report.
69. M.W. Perra and R.E. Stoltz, Hydrogen Effects in Metals, ed. I.M. Bernstein and A.W. Thompson (Warrendale, PA: The Minerals, Metals & Materials Society, 1981), 645.
70. R.J. Walter and W.T. Chandler, Environmental Degradation of Engineering Materials, ed. M.R. Louthan and R.P. McNitt (Blacksburg, VA: VPI Press, 1977), 513.
71. N.R. Moody, unpublished research, Sandia National Laboratories, Livermore, CA, 2002.
72. P. McIntyre, Stress Corrosion Cracking and Hydrogen Embrittlement of Iron Alloys, ed. R.W. Staehle, et al. (Houston, TX: NACE, 1977), 788.
73. H.G. Nelson, D.P. Williams and A.S. Tetelman, Met. Trans., 2 (1971), 953.
74. H.W. Pickering, and C. Wagner, J. Electrochem. Soc., 114 (1967), 698.
75. T. Magnin, R. Chieragatti, and R. Oltra, Acta Metall., 38 (1990), 1313.
76. R.W. Revie, and H.H. Uhlig, Acta Metall., 22 (1972), 69.
77. D.A. Jones, A.F. Jankowski and G.A. Davidson, "Diffusion of Anodically Induced Vacancies in Cu/Ag Thin-Film Couples", Paper No. 188, Corrosion 97 (Houston, TX: NACE, 1997).
78. N.R. Moody, M.W. Perra and S.L. Robinson, Hydrogen Effects on Material Behavior, ed. N.R. Moody and A.W. Thompson, (Warrendale, PA.: The Minerals, Metals & Materials Society, 1990), 625.
79. D.M. Symons, Engng. Frac. Mech., 68 (2001), 751.
80. H. Vehoff, Hydrogen in Metals III: Properties and Applications, (Berlin, Germany Springer-Verlag, 1997), 215.
81. H. Vehoff and P. Neumann, Hydrogen Degradation of Ferrous Alloys, ed. R.A. Oriani, J.P. Hirth and S. Smialowska (Park Ridge, NJ: Noyes Publications, 1985), 686.
82. R.W., Pasco, K. Sieradzki and P.J. Ficalora, Embrittlement by the Localized Crack Environment, ed. R.P. Gangloff (Warrendale, PA: The Minerals, Metals & Materials Society, 1984), 375.
83. J.R. Rice and G.R. Rosengren, J. Mech. Phys. Solids, 16 (1968), 1.
84. J.R. Rice and M.A. Johnson, Inelastic Behavior of Solids, ed. M.F. Kannin, W.G. Adler, A.R. Rosenfield and R.I. Jaffee (New York, NY: McGraw Hill, 1970), 641.
85. R.A. Oriani, Stress Corrosion Cracking and Hydrogen Embrittlement of Iron Alloys, ed. R.W. Staehle, et al. (Houston, TX: NACE, 1977), 351.
86. H. Vehoff and H.-K. Klameth, Acta Metall., 33, (1985), 955.

87. H. Vehoff and W. Rothe, Acta Metall., 31 (1983), 1781.
88. J.R. Rice, Stress Corrosion Cracking and Hydrogen Embrittlement of Iron Based Alloys, ed. R.W. Staehle, et al. (Houston, TX: NACE, 1977), 11.
89. J.R. Rice, Corrosion, 32 (1976), 22.
90. R.A. Page and W.W. Gerberich, Metall. Trans. A, 13A (1982), 305.
91. T.D. Lee, T. Goldenberg and J.P. Hirth, Metall. Trans. A, 10A (1979), 439.
92. O. Onyewuenyi and J.P. Hirth, Metall. Trans. A, 14A (1983), 259.
93. B.P. Somerday and N.R. Moody, Advances in Fracture Research, Proceedings of ICF10, ed. K. Ravi-Chandar, B.L. Karihaloo, T. Kishi, R.O. Ritchie, A.T. Yokobori, Jr. and T. Yokobori, CD version (Oxford, UK: Elsevier Science, 2001), Paper No. ICF108920R.
94. N.R., Moody, M.W. Perra and S.L. Robinson, Scripta Metall., 22 (1988), 1261.
95. N.R., Moody, R.E. Stoltz and M.W. Perra, Metall. Trans., 18A (1987), 1469.
96. R.P. Gangloff and R.P. Wei, Fractography in Failure Analysis, ASTM STP 645, (West Conshohocken, PA: ASTM, 1978), 87.
97. J.W. Hutchinson, J. Mech. Phys. Solids, 16 (1968), 13.
98. K.S. Chan, Metall. Trans. A, 21A (1990), 69.
99. Z. Suo, C.F. Shih and A.G. Varias, Acta Metall., 41 (1993), 1551.
100. X. Chen, T. Foeche, M.J. Lii, Y. Katz and W.W. Gerberich, Engng. Frac. Mech., 35 (1990), 997.
101. H. Huang and W.W. Gerberich, Acta Metall., 42 (1994), 639.
102. W. Zielinski, M.J. Lii, P.G. Marsh, H. Huang and W.W. Gerberich, Acta Metall., 40 (1992), 2883.
103. H. Lee and Y-J. Kim, Engng. Frac. Mech., 68 (2001), 1013.
104. T.H. Courtney, Mechanical Behavior of Materials, 2nd Edition, (New York, NY: McGraw-Hill Companies, Inc., 2000), 210.
105. R.E. Hook and J.P. Hirth, Acta Metall., 15 (1967), 525.
106. J.W. Hutchinson, Intl. J. Solids and Struct., 37 (2000), 225.
107. Y. Wei and J.W. Hutchinson, "Models of Interface Separation Accompanied by Plastic Dissipation" Report No. Mech. 341 (Cambridge, MA: Harvard University, 1998).
108. H. Jiang, Y. Huang, Z. Zhuang and K.C. Hwang, J. Mech. Phys. Solids, 49 (2001), 979.
109. Y. Wei and J.W. Hutchinson, J. Mech. Phys. Solids, 45 (1997), 1253.
110. M.R. Begley and J.W. Hutchinson, J. Mech. Phys. Solids, 46 (1998), 2049.
111. M.R., Begley, unpublished research, University of Virginia, Charlottesville, VA, 2002.
112. R.L.S. Thomas, J.R. Scully and R.P. Gangloff, "Internal Hydrogen Embrittlement of Ultrahigh-Strength AerMet[®]100 Steel", Metall. Matls. Trans. A, in review (2002).
113. J.C.M. Li, R.A. Oriani and L.S. Darken, Phys Chem. Z, 49 (1966), 271.
114. D. McLean, Grain Boundaries in Metals, (Oxford, UK: Oxford University Press, 1957).
115. N. Bandyopadhyay, J. Kameda and C.J. McMahon, Jr., Metall. Trans. A, 14A (1983), 881.
116. D.G. Kolman and J.R. Scully, Metall. Trans. A, 28A (1997), 2645.
117. D.G. Kolman and J.R. Scully, Phil. Mag. A, 79 (1999), 2313.

EMBRITTLEMENT OF HIGH STRENGTH β -TI ALLOYS

R.P. Gangloff

**Department of Materials Science and Engineering
University of Virginia
Charlottesville, VA 22904-4745
USA**

Embrittlement of High Strength β -Ti Alloys

R.P. Gangloff

Department of Materials Science and Engineering, University of Virginia, SEAS-Thornton Hall,
Charlottesville, VA 22903-2442, USA

ABSTRACT

The outstanding strength of α -precipitation hardened β -Ti alloys is compromised by low plane strain fracture toughness, hydrogen embrittlement and perhaps elemental segregation. Solution treated all- β alloys are immune to hydrogen cracking for low to moderate H concentrations, but critical aging to form α triggers transgranular internal hydrogen embrittlement (TG IHE, along α/β interfaces) and intergranular hydrogen environment embrittlement (IG HEE, along β -grain boundaries). Increased strength does not explain this deleterious effect of aging. Rather, the aging dependence of TG IHE appears to be related to H enrichment in β and microscopic stress intensification at α/β interfaces arrayed continuously through β grains. Intergranular HEE is not explained by either grain boundary α formation or deformation localization due to aging. HEE persists when all α is dissolved, suggesting that elemental segregation of Si or impurities may be the requisite for IG cracking, but the offending species have not been resolved.

KEYWORDS

Titanium alloys, fracture toughness, hydrogen embrittlement, fracture mechanics, embrittlement.

INTRODUCTION

Titanium alloys based on a bcc (β) matrix that is hardened by fine precipitates of the hcp- α phase exhibit high strength to weight, excellent formability, and hardenability properties that enable high performance aerospace, marine, and land-based applications [1,2]. For example, a martensitic alloy steel must exhibit a tensile yield strength (σ_{YS}) of about 2400 MPa to exceed the strength-to-density ratio of the strongest β -Ti alloys ($\sigma_{YS} \sim 1600$ MPa). Results suggest, however, that fracture toughness and resistance to hydrogen (H)-assisted cracking are degraded substantially in concert with α strengthening of metastable β . The objective of this work is to examine the effect of α formation on the fracture resistance of modern β/α -Ti alloys, emphasizing deleterious hydrogen embrittlement and the crack tip damage mechanisms that govern damage tolerant properties.

EXPERIMENTAL PROCEDURES

Several β -Ti alloys were examined, including Ti-15-3 (Ti-15V-3Cr-3Sn-3Al in weight pct) [3-5], LCB (Low Cost Beta, Ti-7Mo-4.5Fe-1.5Al) [3], Beta-21S (Ti-15Mo-3Nb-3Al) [4,6], and Beta-C (Ti-8V-6Cr-4Mo-4Zr-3Al) [6-8]. Each alloy contained a total-dissolved H content of $C_H = 25$ -200 ppm (parts-per-million by weight). High strength microstructures were developed by solution treatment (ST) above the β transus, air cooling to retain β only, and heating isothermally to precipitate α . This solution treated and aged (STA) microstructure is shown in Figure 1 for Ti-15-3 sheet where up to 60-volume pct of sub-micrometer α needles precipitate in the Burger's orientation of $\{110\}_\beta \parallel \{0001\}_\alpha$, $\langle 111 \rangle_\beta \parallel \langle 11\bar{2}0 \rangle_\alpha$ [9]. In addition to α , $(\text{Ti,Zr})_5\text{Si}_3$ can precipitate at high aging temperatures and ω may be produced at low aging temperatures [9,10].

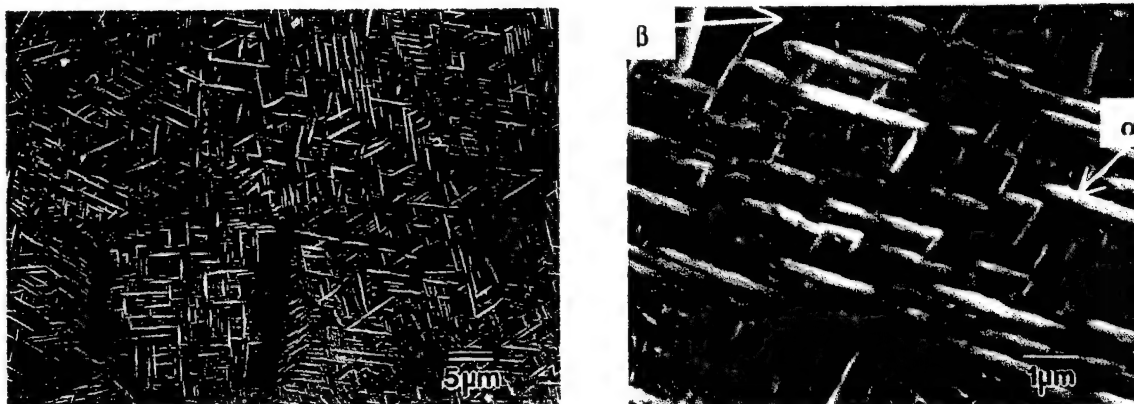


Figure 1: Optical (left) and scanning electron (right) micrographs of the deeply etched microstructure of STA Ti-15-3 sheet showing fine α needles precipitated with long axes that intersect to make angles of 0° , 60° and 90° depending on the sectioning plane and consistent with the Burger's relationship.

Crack growth resistance was measured with a fatigue precracked specimen subjected to increasing crack mouth opening displacement (δ) at a fixed rate and using elastic-plastic J-integral fracture mechanics [11]. For cracking in moist air, the plane strain initiation toughness ($K_{JIC} \sim K_{IC}$ [11]) was obtained for specimens with as-processed levels of H and the threshold K (K_{JTH} or K_{TH}) for the onset of H-assisted subcritical cracking was obtained for specimens electrochemically precharged to C_H of 100 to 10,000 ppm [3]. For specimens in aqueous chloride solution without H precharging, K_{TH} and stable crack growth rate (da/dt) were measured vs dK/dt [4,6].

RESULTS AND DISCUSSION

Fracture Toughness

The plane strain fracture toughness of high strength β/α -Ti alloys is deficient compared to martensitic steels at similar high strengths. The data compiled in Figure 2 show that the benefit of the 30% lower density typical of a β -Ti alloy is insufficient to compensate for the very high toughnesses achieved in steels such as AerMet 100 ($K_{IC} \sim 120$ -170 $\text{MPa}\sqrt{\text{m}}$ at $\sigma_{YS} \sim 1800$ MPa). Such steels exhibit up to an order of magnitude higher fracture toughness compared to K_{IC} approaching 25 $\text{MPa}\sqrt{\text{m}}$ for very high strength β -Ti alloys.

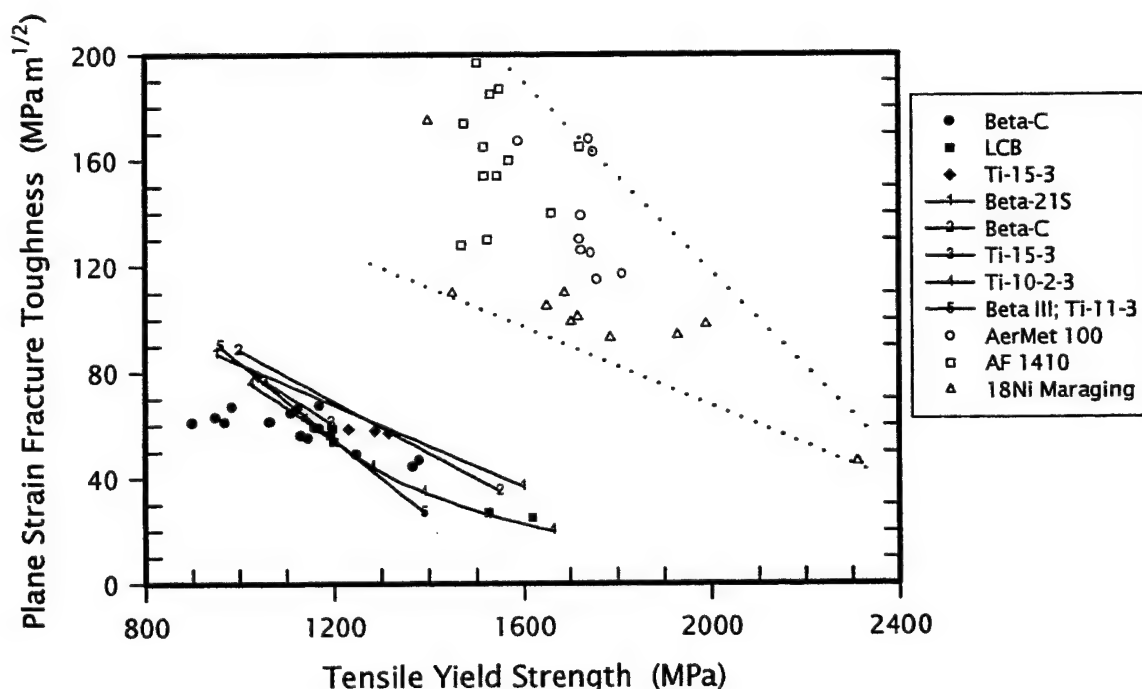


Figure 2: The yield strength dependence of plane strain fracture toughness for a variety of high strength β/α -Ti alloys and martensitic steels fractured in moist air at 25°C .

Low fracture toughness in β -Ti is traced to the size and location of deformable α that localizes plastic strain and tensile stress to exacerbate microvoid nucleation, growth and coalescence [12-16]. For the lower strengths, α films or colonies precipitate heterogeneously at β -grain boundaries and large needles of α precipitate intragranularly; each provides preferred sites for microvoid damage and reduced K_{IC} [3,12,13,15]. To produce high strength, the size of α is reduced and the distribution is homogenized by low temperature aging with added nucleation sites such as dislocations, vacancies, or ω . The toughnesses of such microstructures are, however, low due to deformation banding and microvoid coalescence associated with the particularly high work hardening of fine α relative to β [14-16]. The dependencies of work hardening on α and β size and composition must be better understood, and local stresses from cooperative deformation in α and β must be incorporated into micromechanical models of fracture toughness [17].

Internal Hydrogen Embrittlement

Atomic hydrogen can dissolve in titanium during processing, fabrication, or service to degrade fracture resistance during subsequent deformation, so-called internal hydrogen embrittlement (IHE). Modern STA β/α -Ti alloys are prone to severe IHE for the tensile strengths in Figure 1 [3,5,8,18-20]. For example, experiments with H-precharged STA LCB ($\sigma_{YS} = 1180$ MPa) and Ti-15-3 ($\sigma_{YS} = 1200$ MPa) sheet showed that K_{TH} for IHE under rising- δ loading ($dK/dt = 0.008$ MPa $\sqrt{m/s}$) was reduced to 50% of K_{IC} at C_H levels of 400–500 ppm, and to 25% of K_{IC} at $C_H = 750$ –900 ppm [3]. Absolute values of K_{TH} as low as 12 MPa \sqrt{m} were measured [3].

Aging and/or precipitation of α in β are a requisite for IHE in the moderate- C_H regime (< 2500 ppm) [5,8,18-20]. Figure 3 shows the aging time and strength dependencies of K_{JIC} for as-processed ST Ti-15-3 with 60 ppm H, and K_{JTH} for IHE of ST Ti-15-3 that was H-precharged electrochemically ($C_H = 1300$ ppm) [3]. ST Ti-15-3 is immune to IHE that only occurs for aging in excess of 5–6 h at 510°C. The reduction in K_{JTH} below K_{JIC} is accompanied by a change from dimpled rupture to transgranular-faceted cracking, as shown in Figure 3. Hydrogen cracking was likely along the interface between α needles and the β matrix, with facet surfaces reflecting the Burger's relationship between α and the multiple variants of $\{110\}$ in β [3]. Intergranular (IG) cracking was never observed for IHE of STA LCB and Ti-15-3 for conditions typical of the data in Figure 3 [3].

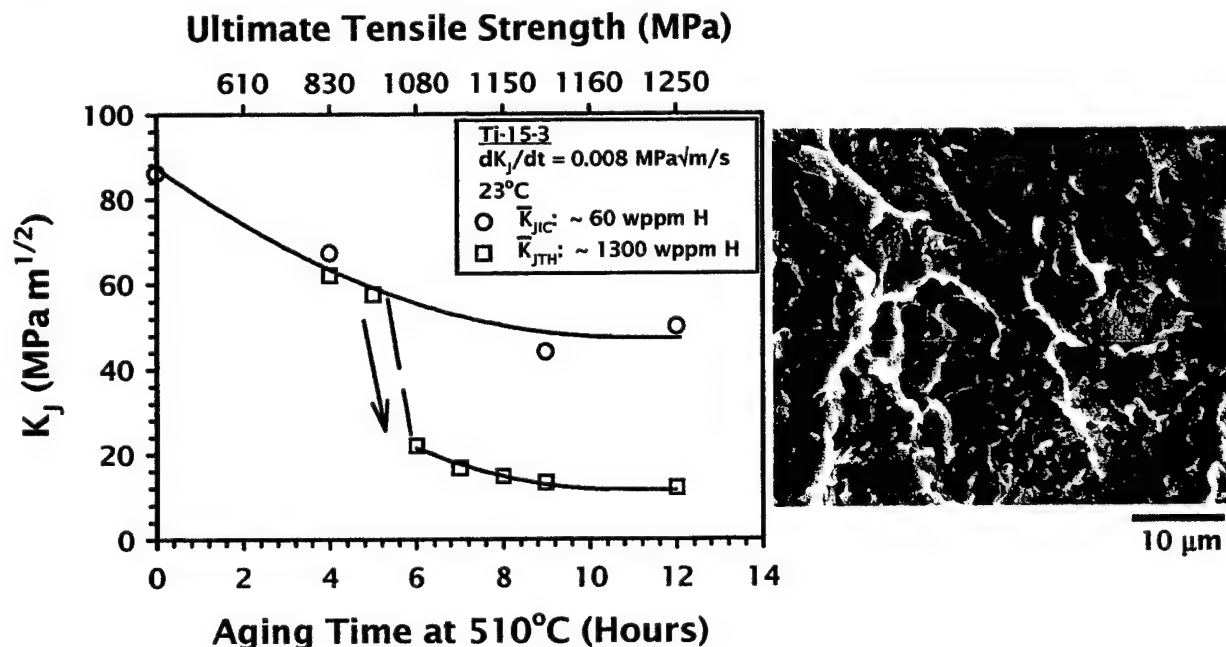


Figure 3: The isothermal-aging time and yield strength dependencies of plane strain fracture toughness at the as-processed H content of 60 ppm and the threshold stress intensity for IHE of H-precharged ($C_H = 1300$ ppm) ST Ti-15-3 stressed in moist air at 25°C. The SEM fractograph shows the morphology of transgranular IHE for the 12 h age case [3]. (The subscript, J, denotes K calculated from the J-integral and the bar indicates the average of 1st initiation and blunting-line offset definitions of crack growth [3,11].)

Generally, IHE of STA β -Ti alloys involves a variety of fracture modes depending on C_H , α/β microstructure, dK/dt , and constraint. The crack path in STA Beta-C changed from microvoid-based at low C_H , to intergranular along β boundaries (at 1300 ppm H), to crystallographic cleavage (2200 ppm H), to α/β -interface cracking at 3300 ppm H [8,19,20]. Intergranular cracking (1000 ppm H), slip plane cracking (4000 ppm H), and cleavage (5600 ppm H) were associated with IHE in Beta-21S [5,18]. ST β -Ti is susceptible to IHE by cleavage at very high C_H [21].

Hydrogen Environment Embrittlement in Aqueous Chloride Solutions

STA β/α -Ti alloys are susceptible to severe intergranular cracking when stressed in aqueous-NaCl solution [4,6,22-25] and the cracking mechanism was established with substantial certainty to be hydrogen environment embrittlement (HEE) [6,7,26,27]. H is produced exclusively at crack tip sites where the passive film is breached by concurrent plastic deformation and diffuses into the process zone to cause embrittlement. Locally large amounts of H can be introduced into Ti by this electrochemical scenario, provided that an occluded crack tip exists and crack tip strain rate conditions are favorable for H production and uptake [25-29]. Under such conditions, K_{TH} for HEE is as low as 15-20 MPa \sqrt{m} and da/dt is as high as 200 $\mu m/s$ for STA alloys such as Beta-C and Beta-21S [22-25].

Aging and/or precipitation of α in β is a requisite for IG HEE. Figure 4 shows the strength and isothermal-aging time dependencies of K_{JIC} and K_{TH} for ST Beta-C stressed under rising δ ($dK/dt = 0.004$ MPa $\sqrt{m/s}$) in moist air and neutral-aqueous chloride solution, respectively [6,22]. ST Beta-C is immune to HEE that only occurs for aging in excess of 3-4 h at 500°C. The reduction in K_{TH} below K_{JIC} is accompanied by a change from microvoid to 100% IG cracking, as shown in Figure 4 and with no evidence of the brittle-transgranular cracking mode typical of IHE (Figure 3).

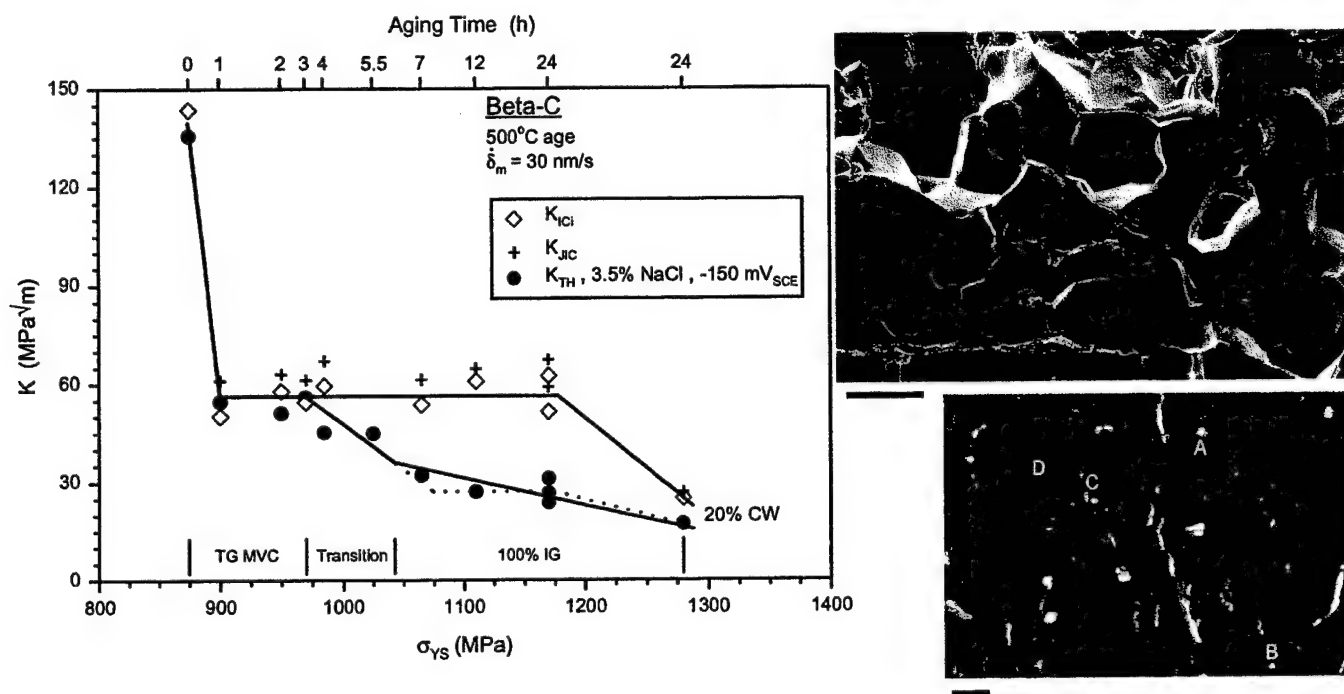


Figure 4: The strength and isothermal-aging time dependencies of fracture toughness and the threshold K for HEE of ST Beta-C stressed in moist air and aqueous-chloride solution at 25°C [6,22]. The highest strength and lowest K_{JIC} were achieved by 20% cold work prior to aging to stimulate fine- α precipitation. SEM fractographs show the morphology of 100% intergranular HEE for the 6 to 24 h age cases (top, 100 μm bar) and the high magnification view of an IG facet surface in these STA microstructures (bottom, 250 nm bar) [36].

Hydrogen Damage Mechanism and Metallurgical Culprit

Both IHE and HEE can be promoted by increasing yield strength since the magnitude of crack tip stresses increases proportionate to 3 to 5 σ_{YS} and H-damage mechanisms are exacerbated [30,31]. However, it is unlikely that strengthening explains the deleterious effect of aging on IHE (Figure 3) and HEE (Figure 4). For Beta-C, the ST β microstructure was immune to HEE for prior cold work levels from 0 to 80 pct, causing strength increases over the range typical of age hardening in Figs. 3 and 4 [22,23]. Experiments with notched-tensile specimens showed that cold worked Beta-C was also immune to IHE [19,20]. Yield strength increases are of secondary importance, perhaps because work hardening decreases with aging to offset the effect of rising σ_{YS} , and blunted crack solutions that equate crack tip stresses to 3-5 σ_{YS} may not be accurate for hydrogen embrittlement due to unique aspects of tip deformation for a crack localized to an interface or grain boundary [32].

Rather than strength, a metallurgical factor that changes during aging is responsible for the occurrence of IHE and HEE in β/α -Ti. Determination of the culprit is complicated by the multiple changes and fine scale of the α microstructure that evolve during aging of ST β -Ti. Additionally, the damage mechanism for hydrogen embrittlement is controversial, with possible contributions from hydride-phase transformation, hydrogen enhanced-localized plasticity, and interface decohesion [30,31,33].

IHE: Considerations of the kinetics of K_{TH} and da/dt vs dK/dt for IHE in Ti-15-3 suggest that H diffuses rapidly during loading and over a short distance (0.5-5 μm) through β in the fracture process zone to reach the α/β interface [3]. While brittle TiH may form in α [34], hydrides are less important in β alloys due to the high solubility of H in bcc Ti (~15,000 ppm at 25°C) [19,20]. H is enriched in β when α precipitates are present; local hydriding of α , at the interface with β , should occur for total C_H above 2500 ppm [19,20]. This hydriding was not observed experimentally and is not a likely cause of cracking at the C_H levels in Figure 3. The effect of locally high interface stresses on hydride precipitation is uncertain and this mechanism cannot be discounted. Fracture without H occurs at α/β interfaces in STA alloys such as Ti-15-3. It is reasonable to speculate that this fracture mode is promoted by H, trapped at this interface and with locally high tensile stresses, as envisioned in classic decohesion theory [30,31].

The aging dependence of TG IHE may be understood based on the need for a critical amount of intragranular α . Considering Figure 3, α precipitation was restricted to β -grain boundaries during 0-5 h of aging (α volume fraction of 0 to 0.48) and when Ti-15-3 was immune to IHE. H cracking correlated with α precipitation within many β at the 6 h age (0.52 α) and within all grains at 10-12 h (0.68-0.80 α) [3]. A critical amount of α in β may be required for: (1) a connected path for H cracking [35], (2) locally high tensile stresses from microscopic constraint adjacent to the α/β interface, or (3) H enriched in β and trapped at the interface with α . A connected crack path is not sufficient for IHE since the immune microstructures in Figure 3 exhibited α on all grain boundaries, but IG cracking did not occur.

HEE: Metallurgical variables could promote intergranular HEE by enhancing H production and uptake near β -grain boundaries at the crack tip, and by enabling brittle cracking of H-enriched boundaries within the process zone. Two factors constrain the governing metallurgical variable. The fully-IG fracture mode observed for susceptible STA Beta-C (Figure 4) dictates that the HEE mechanism and variable must operate at essentially every grain boundary, at least for some β -Ti alloys. Second, since H damage appears to occur within 0.1-1 μm of the crack tip surface contacting NaCl solution, the metallurgical variable must be sized and interconnected on this length scale [25,32]. Three microstructural factors may be consistent with these constraints and change during isothermal aging of the ST- β phase: grain boundary α , slip localization, and elemental segregation.

A study isolated these candidate explanations of aging-dependent HEE for the situation represented in Figure 4, but the results were not conclusive [36]. Two features, grain boundary α and H-enhanced slip localization, are not the cause of IG HEE in Beta-C stressed in NaCl solution. TEM and SEM analyses showed that α decorated less than 5% of the β -grain boundaries, but HEE was nearly-100% IG. High magnification examination of matching surfaces of IG facets, using an SEM with a field-emission gun and dual detectors to optimize topographic contrast and resolution, failed to evidence localized plasticity of the sort reported for IG IHE of β/α -Ti [19,20] and hydrogen embrittlement in general [33]. As illustrated by the high-magnification SEM fractograph in Figure 4, the only features resolved were perturbations of the cracked β -grain boundary surface by intersection of occasional α plates. The predominant feature was mildly undulating and featureless grain surfaces, consistent with interface decohesion.

Circumstantial evidence suggested that solute segregation to β -grain boundaries during aging, combined with trapped H, explained the onset of IG HEE in β/α -Ti (Figure 4). A similar explanation was adopted for IG IHE of STA Beta-C [20] and H embrittlement of steels [31]. Results implicated segregated Si as reducing boundary cohesion in β -Ti without H [37]. Experiments, where STA Beta-C was aged at higher temperatures to progressively dissolve α and remove segregation, support the importance of elemental segregation [36]. For example, a double aged and α -free microstructure was susceptible to IG HEE, confirming that grain boundary α and intragranular α are not required for embrittlement. Double aging at higher temperatures and longer times eliminated IG HEE in the all- β microstructure and restored the original ST immunity to cracking. The hypothesis was that HEE was precluded by elimination of boundary segregation, due to either reduced thermodynamic driving force or formation of $(\text{Ti,Zr})_3\text{Si}_3$. Boundaries in HEE-immune and susceptible single and double ages of Beta-C were examined by small-probe STEM. No segregant was observed to correlate with the IG cracking tendency. Auger spectroscopy of intergranular facets produced by *in situ* fracture of H-precharged STA Beta-C failed to resolve segregation that correlated with severe IG IHE in long time single-aged specimens [20].

Similar aging times and α precipitation are required to trigger IHE and HEE of ST β -Ti, as shown by the similar K_{TH} relationships in Figures 3 and 4. As such, the mechanisms for these aging dependencies of TG vs IG H embrittlement may share a common feature. Elemental segregation to α/β interfaces during aging has not been considered for TG IHE, and enhanced-H trapping from enrichment in β or stress localization due to the presence of α have not been considered for IG HEE.

CONCLUSIONS

1. The outstanding strength capability of α -precipitation hardened β -Ti alloys is compromised by low plane strain fracture toughness compared to martensitic steels, and by both IHE and HEE.
2. All- β alloys are immune to hydrogen embrittlement for low to moderate H concentrations, but transgranular IHE (along α/β interfaces) and intergranular HEE (along β -grain boundaries) are triggered by a critical amount of aging to form α .
3. Increased strength does not explain the deleterious effects of aging on H embrittlement. The onset of TG IHE appears to be related to H enrichment in β and stress intensification at α/β interfaces continuous through β grains. For IG HEE, neither grain boundary α nor deformation localization explain the effect of aging. Segregation may be the requisite for IG cracking, but offending species were not resolved.

ACKNOWLEDGEMENT

This research was supported by the Office of Naval Research (Grant N00014-91-J-4164), with Dr. A. John Sedriks as Scientific Monitor. The author acknowledges the critical contributions of B.P. Somerday, S.P. Hayes and L.M. Young, as well as the collaboration with J.R. Scully.

REFERENCES

1. Boyer, R.R. and Rosenberg, H.W. (1984). *Beta Titanium Alloys in the 80's*, TMS, Warrendale, PA.
2. Eylon, D., Boyer, R.R. and Koss, D.A. (1993). *Beta Titanium Alloys in the 90's*, TMS, Warrendale, PA.
3. Hayes, S.P. (2000). PhD Dissertation, University of Virginia, Charlottesville, VA.
4. Young, L.M. (1993). MS Thesis, University of Virginia, Charlottesville, VA.
5. Young, G.A. (1993). MS Thesis, University of Virginia, Charlottesville, VA.
6. Somerday, B.P. (1998). PhD Dissertation, University of Virginia, Charlottesville, VA.
7. Kolman, D.G. (1995). PhD Dissertation, University of Virginia, Charlottesville, VA.
8. Gaudett, M.A. (1997). PhD Dissertation, University of Virginia, Charlottesville, VA.
9. Headley, T.J. and Rack, H.J. (1979) *Metall. Trans. A* 10A, 909.
10. Shen, G.Q., Wang, S.H., Liang, T.M., Luo, G.Z. and Xie, L.Y. (1996) *Trans. Metal Heat Treatment* 17, 10.
11. Haynes, M.J. and Gangloff, R.P. (1997) *J. Testing Eval.* 25, 82.
12. Froes, F.H., Chesnutt, J.C., Rhodes, C.G. and Williams, J.C. (1978). In: *Toughness and Fracture Behavior of Titanium*, STP 651, pp. 115-153, ASTM, West Conshohocken, PA.
13. Williams, J.C., Froes, F.H., Chesnutt, J.C., Rhodes, C.G. and Berryman, R.G. (1978). In: *Toughness and Fracture Behavior of Titanium*, STP 651, pp. 64-114, ASTM, West Conshohocken, PA.
14. Terlinde, G.T., Duerig, T.W. and Williams, J.C. (1983) *Metall. Trans. A* 14A, 2101.
15. Terlinde, G.T. and Schwalbe K.-H. (1987). In: *Microstructure, Fracture Toughness and Fatigue Crack Growth in Titanium Alloys*, pp. 97-109, Chakrabarti, A.K. and Chesnutt, J.C. (Eds.). TMS, Warrendale, PA.
16. Terlinde, G.T., Rathjen, H.-J. and Schwalbe K.-H. (1988) *Metall. Trans. A* 19A, 1037.
17. Haynes, M.J. and Gangloff, R.P. (1998) *Metall. Trans. A* 29A, 1599.
18. Young, G.A. and Scully, J.R. (1994) *Corrosion* 50, 919.
19. Gaudett, M.A. and Scully, J.R. (1999) *Metall. Trans. A* 30A, 65.
20. Gaudett, M.A. and Scully, J.R. (2000) *Metall. Trans. A* 31A, 81.
21. Nelson, H.G. (1992). *NASP Government Work Package #92*, NASA Ames Research Center, Moffett Field, CA.
22. Somerday, B.P. and Gangloff, R.P. (1998) *Mats. Sci. Engr. A* A254, 166.
23. Somerday, B.P. and Gangloff, R.P. (1998) *Mats. Sci. Engr. A* A254, 179.
24. Young, L.M., Young, G.A., Scully, J.R. and Gangloff, R.P. (1995) *Metall. Trans. A* 26A, 1257.
25. Somerday, B.P., Young, L.M. and Gangloff, R.P. (2000) *Fatg. Fract. Engr. Mats. Struct.* 23, 39.
26. Kolman, D.G. and Scully, J.R. (1998). In: *Effects of the Environment on the Initiation of Crack Growth*, ASTM STP 1298, pp. 61-73, Van der Sluys, W.A., Piascik, R.S. and Zawierucha, R. (Eds.). ASTM, West Conshohocken, PA.
27. Kolman, D.G. and Scully, J.R. (1997) *Metall. Trans. A* 28A, 2645.
28. Kolman, D.G. and Scully, J.R. (1999) *Phil. Mag. A* 79, 2313.
29. Kolman, D.G., Gaudett, M.A. and Scully, J.R. (1998) *J. Electrochem. Soc.* 145, 1829.
30. Oriani, R.A. (1987) *Corrosion* 43, 390.
31. McMahon, C.J., Jr. (2001) *Engr. Frac. Mech.* 68, 773.
32. Gangloff, R.P. (2001). "Diffusion Control of Hydrogen Environment Embrittlement in High Strength Alloys", In: *Hydrogen Effects on Material Behavior*, Moody, N.R. et al. (Eds.). TMS, Warrendale, PA, in review.
33. Robertson, I.M. (2001) *Engr. Frac. Mech.* 68, 671.
34. Nelson, H.G. (1973) *Metall. Trans. A* 4, 364.
35. Scully, J.R. (2000). In: *Environmentally Assisted Cracking*, STP 1401, pp. 40-69, Kane, R.D. (Ed.). ASTM, West Conshohocken, PA.
36. Somerday, B.P., Wilson, A.W., Howe, J.M. and Gangloff, R.P. (2001) "Microstructural Cause of Intergranular Hydrogen Environment Embrittlement of Aged Beta-Ti Alloys", *Metall. Trans. A*, in review.
37. Graham, D.E. and Koss, D.A. (1978) *Metall. Trans. A* 9A, 1435.

**STRAIN RATE DEPENDENT ENVIRONMENT ASSISTED CRACKING
OF α/β -TI ALLOYS IN CHLORIDE SOLUTION**

E. Richey III and R.P. Gangloff

Department of Materials Science and Engineering
University of Virginia
Charlottesville, VA 22904-4745
USA

Edward Richey III and Richard P. Gangloff¹

Strain Rate Dependent Environment Assisted Cracking of α/β -Ti Alloys in Chloride Solution

Reference: Richey, E. and Gangloff, R. P., "Strain Rate Dependent Environment Assisted Cracking of α/β -Ti Alloys in Chloride Solution," *Environmentally Assisted Cracking: Predictive Methods for Risk Assessment and Evaluation of Materials, Equipment, and Structures, ASTM STP 1401*, R. D. Kane, Ed., American Society for Testing and Materials, West Conshohocken, PA, 2000.

Abstract: Environment assisted cracking (EAC) occurs in annealed- α/β Ti-6Al-4V (ELI) and Ti-6Al-2Zr-2Sn-2Cr-2Mo in aqueous chloride solution, as evidenced by rising-displacement threshold stress intensity factors well below K_{IC} and a mode transition from ductile fracture to transgranular cleavage of α . The acicular- α/α_2 microstructure of Ti-6-2222 is susceptible to severe cracking in 3.5% NaCl compared to the equiaxed- α/α_2 structure of Ti-6-4. Thresholds and growth rates depend on loading rate, and appear most environment sensitive at intermediate crack tip strain rates. EAC is sustained to high loading rates ($dK/dt = 0.3 \text{ MPa}\sqrt{\text{m/s}}$ for Ti-6-4 and above $10 \text{ MPa}\sqrt{\text{m/s}}$ for Ti-6-2222) and crack growth rates are rapid ($10 \text{ }\mu\text{m/s}$). The hydrogen environment embrittlement mechanism is consistent with such rapid cracking kinetics, but only if the process zone is within 0.001 to $1 \text{ }\mu\text{m}$ of the crack tip surface. A near-tip process zone may be promoted by high H produced electrochemically on active areas of the crack surface, or by a sharp crack tip.

Keywords: Hydrogen embrittlement, stress corrosion cracking, titanium alloy, fracture mechanics, crack tip strain rate, crack propagation

Introduction

Two-phase α/β titanium alloys are susceptible to transgranular (TG) environment assisted cracking (EAC) when stressed in aqueous solutions with halide anions including Cl^- [1-5]. Embrittlement is promoted by an existing crack [6, 7] and occurs at a fraction of the fracture toughness with subcritical crack growth rates approaching $50 \text{ }\mu\text{m/s}$. The likely mechanism is hydrogen environment embrittlement (HEE) [8], where atomic hydrogen (H) uptake is localized from the crack tip surface into the process zone [9]. Transgranular H damage is in the hexagonal-close packed α phase, and involves lattice decohesion or brittle-hydride formation leading to near-basal plane cracking and slip-

¹Graduate Research Assistant and Professor, respectively; Department of Materials Science and Engineering, University of Virginia, Charlottesville, VA 22903.

based tubular microvoiding [2, 4, 8, 10]. Cracking along α/β interfaces is promoted at high levels of H [11]. The body-centered β phase in metastable β -Ti alloys is susceptible to intergranular HEE in chloride solution [12] and cleavage at high dissolved H contents [13], but may act as a crack arrestor during TG EAC in α/β -Ti alloys [2, 8, 11].

Stress intensity factor (K) and crack tip strain rate ($\dot{\epsilon}_{CT}$) interactively govern EAC propagation in α/β -Ti alloys. The K controls process zone tensile and hydrostatic stresses [14]. $\dot{\epsilon}_{CT}$ affects the stability of the crack tip passive film that governs cathodic H production and uptake [15-20], as well as the time for H transport in the process zone. Experimental results are contradictory. Embrittlement appears to be maximized at intermediate $\dot{\epsilon}_{CT}$ for loading in an electrolyte and eliminated under static or very slow-rate loading [21-23]. Other data suggest that EAC is increasingly severe as dK/dt decreases to quasi-static levels for chloride solution [3, 24] and H_2 [8, 25]. Comparisons are complicated by subtle differences in prestressing of a cracked specimen prior to hydrogen exposure; conditions that promote crack tip creep and reduced $\dot{\epsilon}_{CT}$ may retard HEE [26, 27]. EAC is generally eliminated at high loading rates, but the levels of environmental crack growth rate (da/dt) and applied stress intensity rate (dK/dt) where brittle cracking persists in α/β -Ti alloys are high [21, 25, 28]. The process that rate limits HEE was speculated to be either dislocation transport of H in equiaxed α [21], short-range diffusion of H in α/TiH for low H concentration-continuous α microstructure conditions [11, 25], or long range diffusion of H in β for high crack tip H levels and a continuous β phase [28]. The details of these rate-sensitive processes are not understood.

Crack tip strain rate effects on HEE in Ti alloys are uncertain because quantitative fracture mechanics methods have not been employed [8, 11, 21, 25]. Experimentation to characterize the effect of $\dot{\epsilon}_{CT}$ on the threshold K for the onset of EAC and subsequent da/dt must precisely monitor crack growth, and systematically vary loading rate and format to probe a range of $\dot{\epsilon}_{CT}$. Modeling must define $\dot{\epsilon}_{CT}$ to establish the factors that rate limit crack tip damage; particularly film rupture, electrochemical hydrogen adsorption, and H transport into the crack tip process zone. Such understanding is a critical element of life prediction to control EAC in a high performance component [29].

The objectives of this research are to characterize the aqueous-EAC resistance of two α/β -Ti alloys as a function of crack tip strain rate and to understand the crack tip damage mechanism. Fracture mechanics threshold K and crack growth rate measurements are interpreted to: (1) better characterize alloy susceptibility to EAC, (2) determine if EAC kinetics correlate with crack tip strain rate, and (3) identify the H transport process capable of sustaining high-rate cracking to test the HEE mechanism. Experiments utilize a precracked specimen stressed at a constant crack mouth opening displacement rate ($\dot{\delta}_m$) in neutral NaCl solution at 23°C.

Experimental Methods

Materials

Two α/β -Ti alloys were studied, Ti-6.2Al-4.3V-0.12O (Ti-6-4; extra-low interstitial, ELI) and Ti-5.6Al-1.9Zr-2.0Sn-2.1Cr-2.2Mo-0.11O (Ti-6-2222) in weight pct. Ti-6-4 was obtained as a 12.7 mm thick plate that was α/β rolled, mill-annealed (MA) for 8 h at 760°C, and vacuum-furnace cooled. The optical micrograph in Fig. 1a

shows that the microstructure consists of about 7 volume pct of retained β (dark phase) in a continuous-equiaxed α matrix (light), with an average α grain diameter of 20 to 25 μm .

Ti-6-2222 plate (6.6 mm thick) was hot rolled in the $\alpha + \beta$ phase field, air cooled, heated at 900°C for 2 h and furnace cooled at 3°C/min. The beta transus (β_T) for Ti-6-2222 is near 950°C. Figure 1b shows that the resulting microstructure consists of coarse acicular α (dark) phase in a continuous β (light) matrix. Globular-recrystallized α is arrayed parallel to the rolling direction (RD) in Fig. 1b. The β phase in each alloy is free of secondary α precipitates [30], while silicides are present in the β of Ti-6-2222 but not Ti-6-4 [31]. Slow cooling precipitated Ti_3Al (α_2) in the α of both Ti-6-2222 [32] and Ti-6-4 [33].

Yield strength (σ_{YS} in the T orientation) and plane strain fracture toughness (K_{JIC} in the TL orientation) are 940 MPa and 66 $\text{MPa}\sqrt{\text{m}}$ for Ti-6-2222, and 940 MPa (L) and 79 $\text{MPa}\sqrt{\text{m}}$ (LT) for Ti-6-4.²

HEE Characterization

Compact tension (CT) specimens were machined from the mid-planes of the plates. For Ti-6-4, specimens were 6.4 mm thick (B), 63.5 mm wide (W), and in the LT orientation. For Ti-6-2222, B equaled 6.1 mm, W was 50.0 mm, and the orientation was TL.² Crack length was determined from measured crack-mouth opening displacement (δ_m) during fatigue cracking and thermal-corrected direct current electrical potential (dcPD) during EAC. The details of compliance and electrical potential measurements are presented elsewhere [30], and standard equations were employed to calculate crack length and K [34].

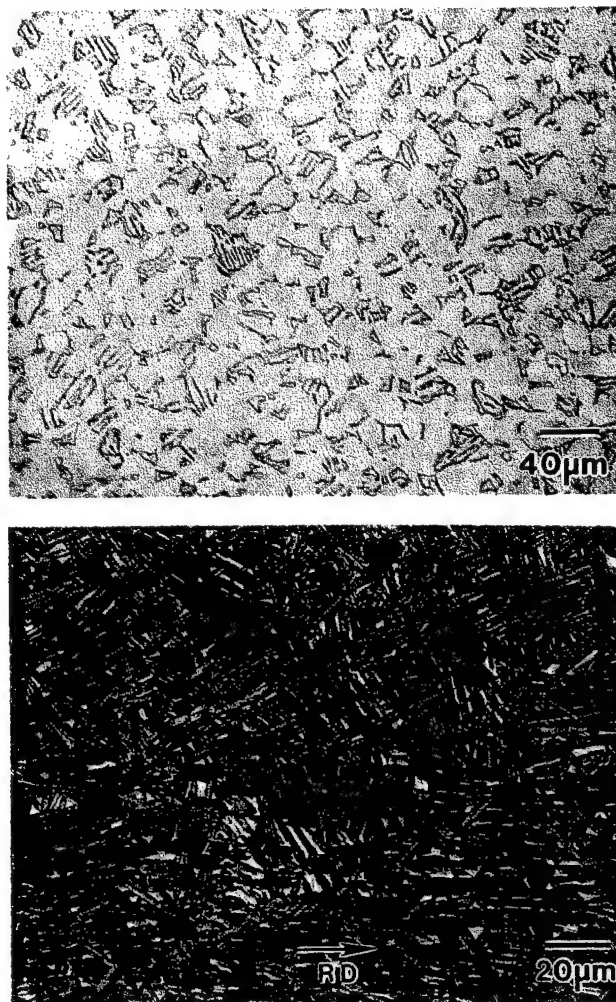


Figure 1 - Optical micrographs of annealed and furnace cooled Ti-6-4 (top) and Ti-6-2222 plates.

² The long axis of the tensile specimen was parallel to the transverse (T) or longitudinal (L) direction in the plate, while the Mode I crack was stressed in the first direction with growth parallel to the second direction.

Environment assisted cracking experiments were conducted at 23°C in a near-neutral (pH 6 to 7) and quiescent chloride solution [30]. A polymethyl methacrylate environmental cell, was used to selectively immerse the crack tip in 3.5 weight pct NaCl dissolved in deionized water. Elastomeric tubing was inserted in the notch to seal the cell and solution was circulated through the notch at 0.5 ml/s. The grounded CT specimen was maintained at fixed electrode potential with a potentiostat, platinum-mesh counter electrode, and two Ag/AgCl reference electrodes located adjacent to each broad face of the specimen. The counter electrode was positioned in a separate 2-liter reservoir. The electrode potential difference across the specimen notch was always less than 10 mV, as monitored with the two reference electrodes. The selected potential of -500 mV (vs. saturated calomel, SCE) is the value where EAC of several α/β -Ti alloys in chloride was most severe [2, 35]. The open circuit potential was -300 mV_{SCE} for ELI Ti-6-4 and -200 mV_{SCE} for Ti-6-2222.

Each specimen was fatigue precracked in the aqueous chloride environment to a final crack length (a) to W ratio of 0.50 utilizing a closed loop servohydraulic test machine operated in load control, a stress ratio ($R = K_{min}/K_{max}$) of 0.1, and frequency of 5-10 Hz. The precracked specimen, controlled with a crack mouth displacement gauge, was loaded at a constant- δ_m rate in aqueous solution to determine the stress intensity at the onset (or threshold) of EAC and subsequent subcritical crack growth rates. Similar experiments in moist air provided a measure of the initiation-fracture toughness at the onset of stable crack growth, K_{JICi} [36]. Prior to crack-growth initiation, a fixed δ_m produced constant dK/dt that was determined by linear regression of K vs. time data. For the CT specimen and fatigue crack length, δ_m of 2.3×10^{-6} and 1.2×10^{-2} mm/s produced dK/dt levels of 2.0×10^{-4} and 1.0 MPa $\sqrt{m/s}$; the relationship between these two rates is linear [30].

An elastic-plastic analysis was used to account for uncracked-ligament plasticity [36]. The plastic part of the J integral was determined using the area method with compliance calculated from the dcPD-measured crack length; the specimen was not unloaded during an experiment. The effective modulus used in this calculation was determined from the δ_m vs. P data prior to crack extension and the measured-final fatigue crack length. Plane strain constraint was substantial at crack initiation, as evidenced by a lack of shear lips, and the crack was in the Mode I orientation without branching. Crack growth rate was calculated as a function of the elastic K from J (K_J) using a modified incremental polynomial method [30].

Results

Determination of Environment Assisted Cracking Resistance

Measured load, δ_m , and dcPD were analyzed to characterize the fracture resistance of each Ti alloy in moist-laboratory air and NaCl. For CT specimens loaded at fixed δ_m in air, and in aqueous chloride at faster loading rates, the dcPD signal increased steadily by up to 1 pct prior to crack-growth initiation [30]. This rise, due to crack tip plasticity and crack opening, dictated that the δ_i level at the onset of crack growth be determined objectively by regression analysis of pre and post-initiation data [36]. For specimens loaded at slower dK/dt in NaCl, δ_i was defined clearly by a sharp increase in dcPD and

decrease in load. These analyses of dcPD vs. δ_m yielded crack length and K vs. time (Fig. 2), as well as da/dt vs. K . The air-initiation fracture toughness was indicated by either K_{JIC} at δ_i or K_{JIC} at the K level after 0.2 mm of crack extension. For EAC, K_{JTH} and K_{JTH} were defined similarly.

Two propagation behaviors were observed. For moist air and faster loading rates in NaCl, crack length increased monotonically with increasing K during fixed- δ_m loading (Fig. 2b). For slow-rate loading in NaCl, subcritical crack growth occurred with oscillating periods of slow and faster da/dt . As shown in Fig. 2a, each period of slow growth occurred under rising K , while more rapid extension resulted in decreasing K due to falling load.

Both Ti-6-4 and Ti-6-2222 were embrittled by rising- δ_m loading in NaCl solution. The threshold stress intensity for crack growth, crack growth rate, and the microscopic cracking path each depended on applied δ_m and dK/dt .

Threshold Stress Intensity for EAC

The threshold stress intensity for EAC in both Ti-6-4 and Ti-6-2222 exposed to 3.5% NaCl solution is less than K_{JIC} and depends on dK/dt , particularly for the latter α/β -Ti alloy, as shown in Figs. 3 and 4.

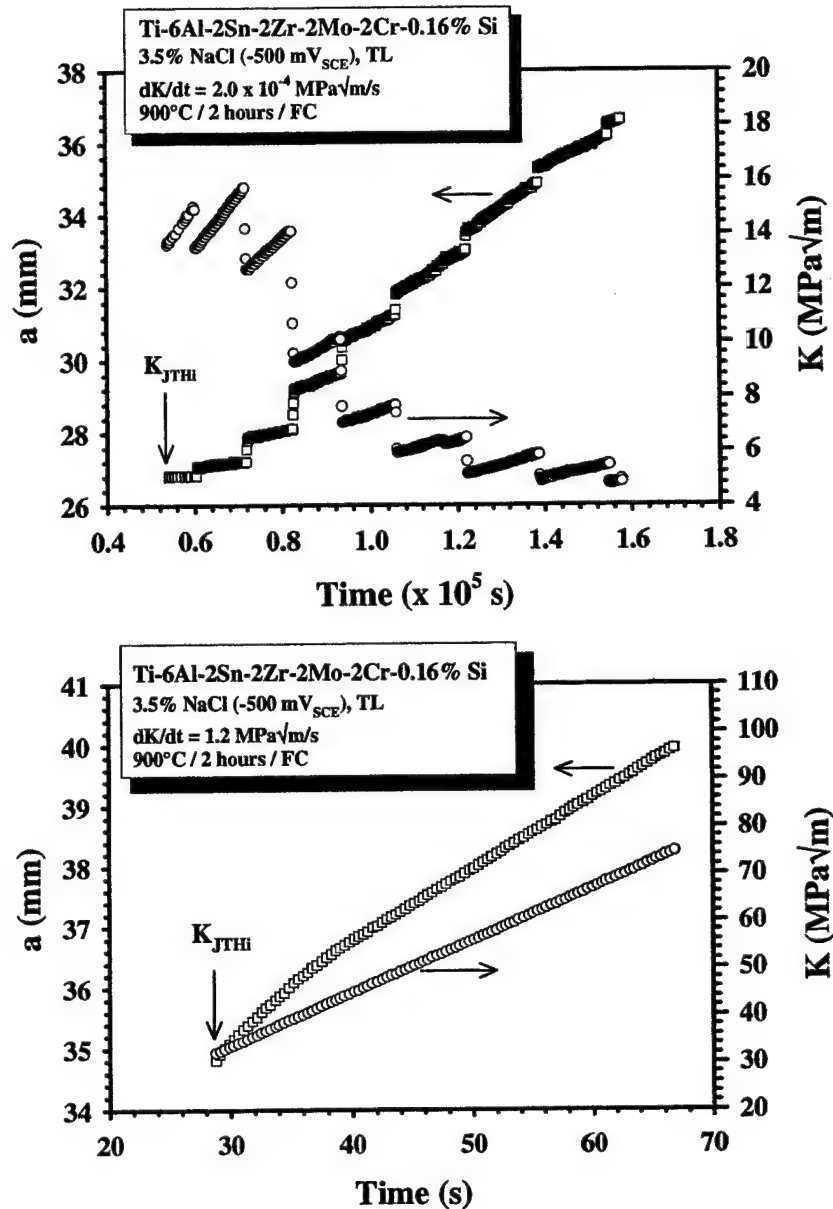


Figure 2 - Crack length and K vs. time for Ti-6-2222 plate in 3.5% NaCl (-500 mV_{SCE}) for: (a) initial dK/dt of $2.0 \times 10^{-4} \text{ MPa}\sqrt{\text{m/s}}$ (top) and (b) $1.2 \text{ MPa}\sqrt{\text{m/s}}$ (bottom).

Mill-annealed Ti-6-4 (ELI, LT) plate exhibits moderate EAC susceptibility. In Fig. 3, K_{JIC} (■) is independent of dK/dt between 4×10^{-3} and $0.1 \text{ MPa}\sqrt{\text{m/s}}$, and is $79 \text{ MPa}\sqrt{\text{m}}$. K_{JICi} equals $66 \text{ MPa}\sqrt{\text{m}}$. K_{JTHi} is below K_{JIC} for loading rates below 0.1 to $0.3 \text{ MPa}\sqrt{\text{m/s}}$, indicating EAC. K_{JTHi} (o) and K_{JTH} (•) depend on applied dK/dt and are a minimum of $56 \text{ MPa}\sqrt{\text{m}}$ at 10^{-2} to $0.1 \text{ MPa}\sqrt{\text{m/s}}$.

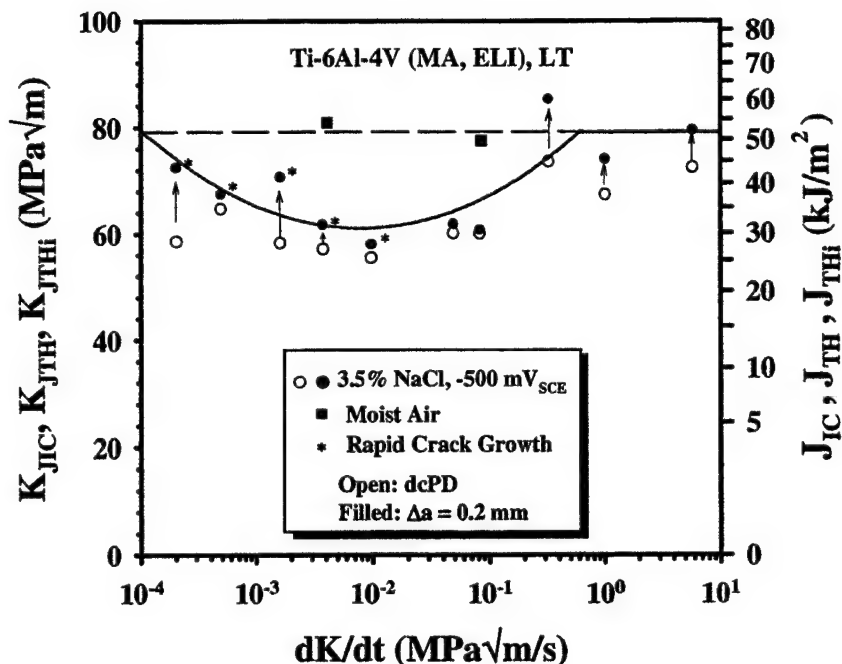


Figure 3 - K_{JTHi} (o) and K_{JTH} (•) vs. loading rate for Ti-6-4 (ELI, LT) plate in aqueous chloride, compared to K_{JIC} (■).

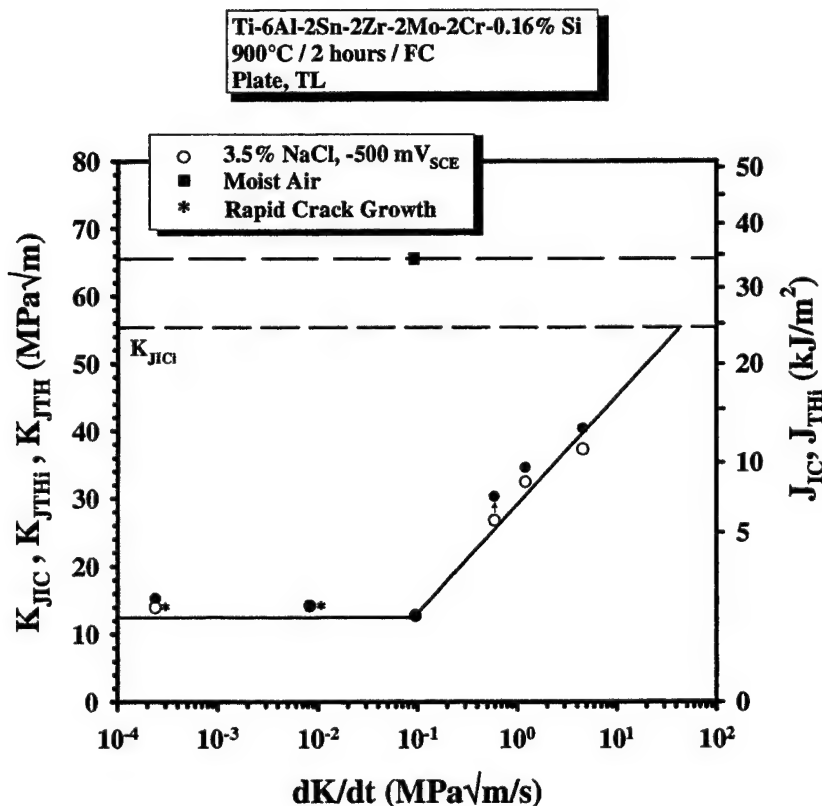


Figure 4 - K_{JTHi} (o) and K_{JTH} (•) vs. loading rate for Ti-6-2222 plate (TL) in aqueous chloride, compared to K_{JIC} (■).

The trend in Fig. 3 suggests that fast and slow loading rates eliminate EAC of Ti-6-4 in NaCl. As dK/dt decreases below $10^{-2} \text{ MPa}\sqrt{\text{m/s}}$, threshold stress intensities increase toward the moist air fracture toughness. For dK/dt above $0.3 \text{ MPa}\sqrt{\text{m/s}}$, mechanical crack tip damage occurs coincident with the onset of EAC, as suggested by equal K_{JTHi} and K_{JICi} . The difference between K_{JTHi} and K_{JTH} is highest at the extreme high and low loading rates. Values of the plane strain

tearing modules over the initial Δa of 0.5 mm [30] (10.7, 1.1, 3.1, 2.8, 1.2, 2.5, 0.1, 2.2, 2.8, and 7.0 for the 10 levels of increasing dK/dt in Fig. 3) confirm that the susceptibility to environmental propagation is maximized at the intermediate dK/dt of 0.1 MPa $\sqrt{m/s}$.

Ti-6-2222 plate exhibits significantly greater EAC susceptibility than Ti-6-4, as indicated by the lower K_{JTHi} values in Fig. 4. While K_{JIC} (■) is 66 MPa \sqrt{m} and K_{JICi} is 56 MPa \sqrt{m} , K_{JTHi} is as low as 13 MPa \sqrt{m} over a range of dK/dt from 2×10^{-4} to 0.1 MPa $\sqrt{m/s}$. K_{JTHi} rises sharply to 37 MPa \sqrt{m} as dK/dt increases to 5 MPa $\sqrt{m/s}$. The trend line suggests that EAC is eliminated by fast loading rates ($dK/dt \approx 40$ MPa $\sqrt{m/s}$). The threshold stress intensity does not increase with decreasing dK/dt , and the difference between K_{JTHi} and K_{JTH} is small indicating limited resistance to initial-crack growth.

Crack Growth Rate

For both alloys in air, crack growth under rising δ_m was stable, consistent with finite crack growth resistance and positive tearing modulus. Similar behavior was observed for each alloy stressed in NaCl solution, but only at dK/dt levels above 10^{-2} MPa $\sqrt{m/s}$. For slower loading rates, cracking in NaCl oscillated between periods of slow-stable and faster-stable growth, as illustrated in Fig. 2a. Loading rates that produced slow-fast da/dt are designated by * in Figs. 3 and 4.

The absence of the rapid da/dt regions for dK/dt values greater than 10^{-2} MPa $\sqrt{m/s}$ suggests that specimen-compliance may cause this phenomenon. A CT specimen of Ti-6-2222 was loaded in NaCl at a constant δ_m , producing a dK/dt of 6.5×10^{-4} MPa $\sqrt{m/s}$. The measured K_{JTHi} was 12.9 MPa \sqrt{m} and stable crack growth was oscillatory. The

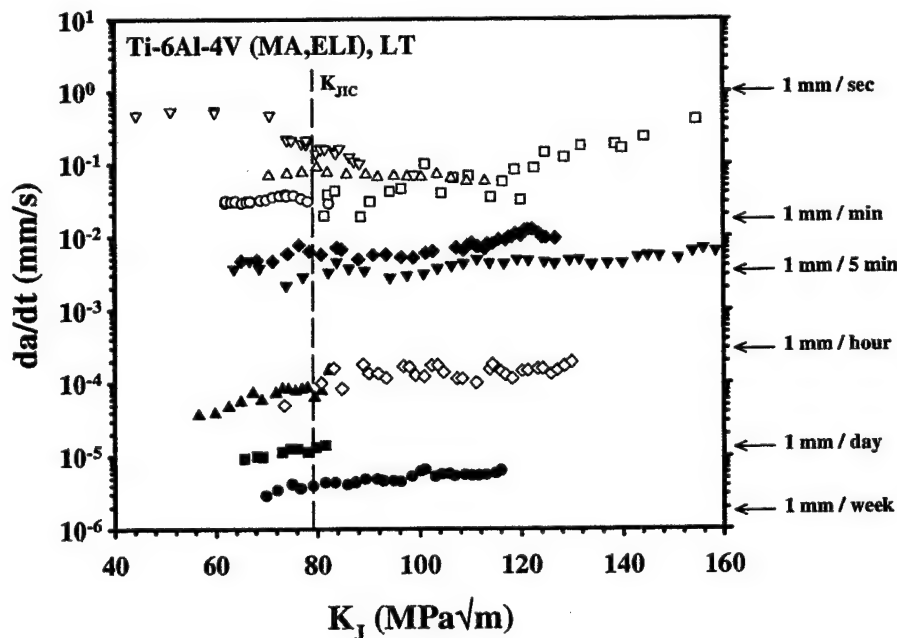


Figure 5 - da/dt vs K_J for Ti-6-4 (ELI, LT) plate in 3.5% NaCl (-500 mV_{SCE}) and moist air for various loading rates. Values of dK/dt are: 0.2 (●), 0.5 (■), 1.6 (▲), 53 (▼), 82 (○), 320 (□), 1000 (△), and 5800 (▽) $\times 10^{-3}$ MPa $\sqrt{m/s}$ for NaCl; and 4.1 (◇) and 85 (◆) $\times 10^{-3}$ MPa $\sqrt{m/s}$ for loading in moist air.

specimen was then stressed in load (P) control at a constant dP/dt that produced an initial dK/dt of 7.2×10^{-4} MPa $\sqrt{m/s}$. The resulting K_{JTHi} was 14.4 MPa \sqrt{m} and crack growth above K_{JTHi} did not oscillate. Rather, crack length and K increased steadily with increasing time.

Figure 5 shows da/dt vs. K_I for Ti-6-4 (ELI, LT) in moist air and NaCl. Data were included for both subcritical crack growth ($K < K_{JIC}$) and stable crack growth above K_{JIC} . The regions of rapid-stable crack extension were not plotted. For all loading rates and both environments, da/dt was independent of K_I for the regions of slow-stable crack extension. As dK/dt increased, the average crack growth rate increased, as shown by the open (NaCl) and filled-circle (moist air) symbols in Fig. 6 for K_I of 60 (\square), 70 (\circ), and 80 (\triangle) $\text{MPa}\sqrt{\text{m}}$, as well as the average da/dt (\bullet) for moist air. The trend line in Fig 6 is

$$da/dt = 0.1 (dK/dt)^{1.13} \quad (1)$$

for the units shown.

The da/dt corresponding to rapid crack extension in NaCl are included (\blacksquare) for comparison and were calculated by linear regression of a vs. t data, Fig. 2a. The average da/dt for rapid EAC was $7 \mu\text{m/s}$, independent of dK/dt . Below $10^{-1} \text{ MPa}\sqrt{\text{m/s}}$, these rates were one to three orders of magnitude faster for chloride solution vs. moist air. The NaCl crack growth rates observed for dK/dt above $10^{-1} \text{ MPa}\sqrt{\text{m/s}}$ were equal to the air growth rates and cracking did not oscillate.

Similar crack growth behavior was observed for Ti-6-2222, as shown in Fig. 7. The average value of da/dt during rapid-stable crack extension was $11 \mu\text{m/s}$, independent of dK/dt . Crack growth rates during the regions of rapid crack extension below $10^{-1} \text{ MPa}\sqrt{\text{m/s}}$ were orders of magnitude faster than the likely crack growth rates in moist air. The NaCl growth rates observed for loading rates above $10^{-1} \text{ MPa}\sqrt{\text{m/s}}$ are consistent with the expected air crack growth rates. The average-fast NaCl growth rate for Ti-6-2222 was 60% higher than that observed for Ti-6-4, but similar and environment-independent growth rates were observed for each alloy at dK/dt above $0.1 \text{ MPa}\sqrt{\text{m/s}}$.

Fracture Mode

Environment and loading rate effects on the microscopic fracture mode were established by SEM analysis. In all fractographs presented, the crack growth direction is

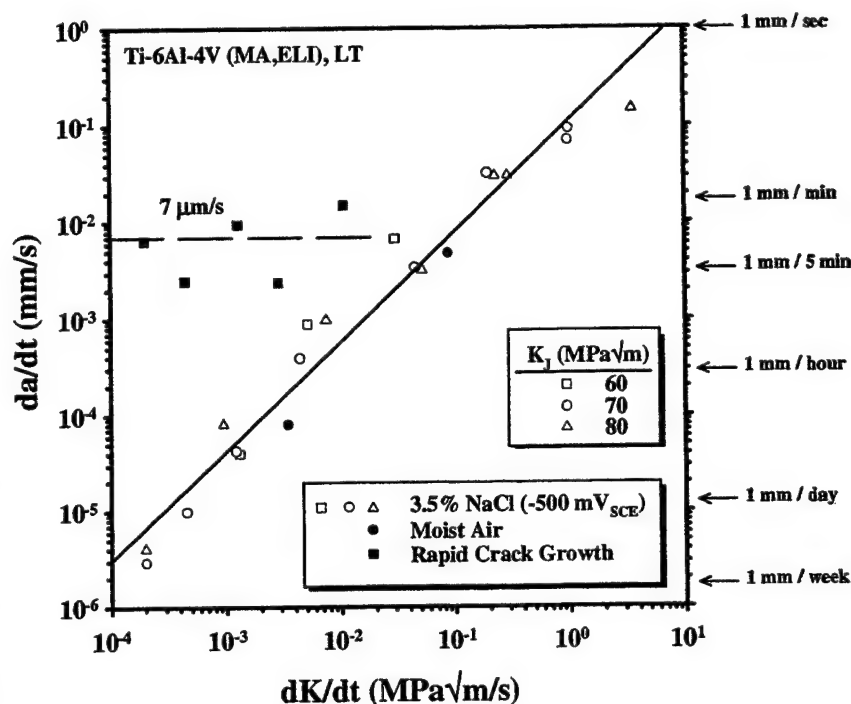


Figure 6 - da/dt vs. dK/dt for Ti-6-4 (ELI, LT) plate in 3.5% NaCl (-500 mV_{SCE}) and moist air for various loading rates and K_I levels.

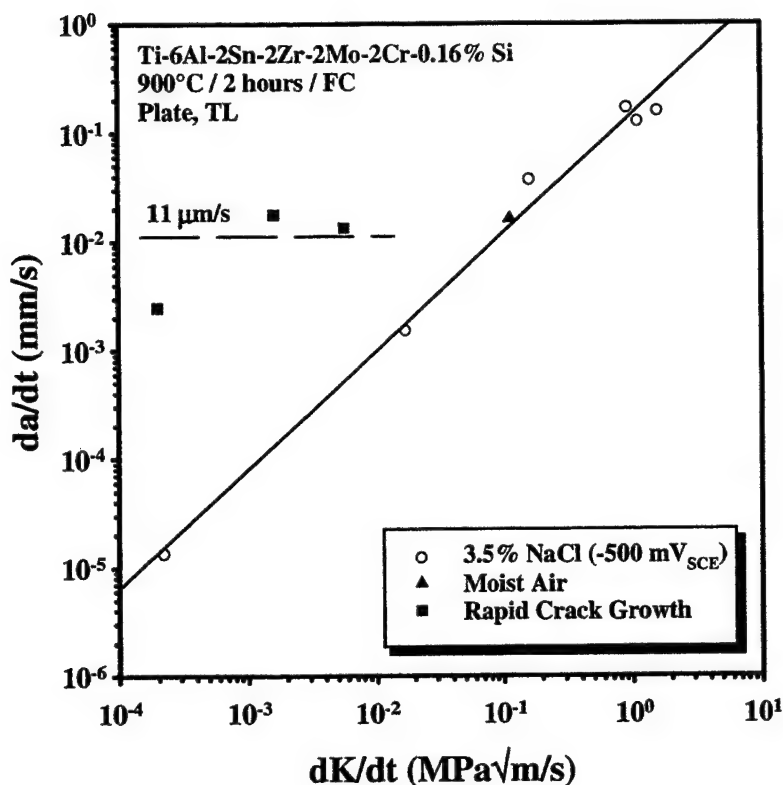


Figure 7 - da/dt vs. dK/dt for annealed Ti-6-2222 plate (TL) in 3.5% NaCl (-500 mV_{SCE}) and moist air for various loading rates. For slow-stable cracking in NaCl, K was 13 $\text{MPa}\sqrt{\text{m}}$ for loading rates below 10^{-1} $\text{MPa}\sqrt{\text{m/s}}$ and 35 $\text{MPa}\sqrt{\text{m}}$ above 10^{-1} $\text{MPa}\sqrt{\text{m/s}}$.

and grain boundaries. A small amount of cleavage-like features (D) is present on the air fracture surface.

Chloride solution exposure affected a fracture mode change in Ti-6-4, consistent with reduced K_{JTHi} vs. K_{JIC} . Figure 8b shows the Ti-6-4-NaCl fracture surface for a dK/dt of 4×10^{-3} $\text{MPa}\sqrt{\text{m/s}}$, corresponding to the maximum EAC susceptibility in Fig. 3. Compared to fracture in air, cracking in NaCl involved a substantial amount of cleavage (D). Metallographic sectioning confirmed that EAC in the equiaxed- α microstructure of Ti-6-4 was transgranular [30], consistent with literature results [8]. Presumably this cleavage is along a high index plane in α , nearly parallel to $\{0001\}$ [2, 10, 37-39]. SEM examination showed that the amount of cleavage decreased with increasing K_{JTHi} as dK/dt both increased and decreased from the minimum in Fig. 3 [30]. The crack surfaces created by stressing in NaCl at the fastest and slowest dK/dt levels contained a substantial amount of features A, B, and C. Figure 9 contains the fractograph typical of Ti-6-4 stressed in NaCl at the slowest dK/dt examined. Since microvoid-based features are not environment sensitive, this result confirms that the susceptibility to EAC is reduced at slow loading rates. Similar fractographic results were obtained for fast dK/dt .

Rising- δ_m loading of Ti-6-2222 in NaCl solution produced a fracture mode change corresponding to reduced K_{JTHi} vs. K_{JIC} (Fig. 4). Air fracture was by TG MVC, similar to that for Ti-6-4 (Fig. 8a). Figure 10 shows NaCl fracture surfaces for rapid-stable and

from bottom to top. The fractographs were taken of regions immediately following the fatigue precrack.

Air fracture of Ti-6-4 was by TG-microvoid coalescence (MVC), as illustrated in Fig. 8. Higher magnification analyses established that four features, A through D, constituted this fracture [30]. Region A represents the dominant feature of spherical microvoids. Region B is reminiscent of void sheeting linking two regions of different elevation. Region C shows elongated voids probably caused by the intersection of intense-planar slip bands or the intersection of slip bands

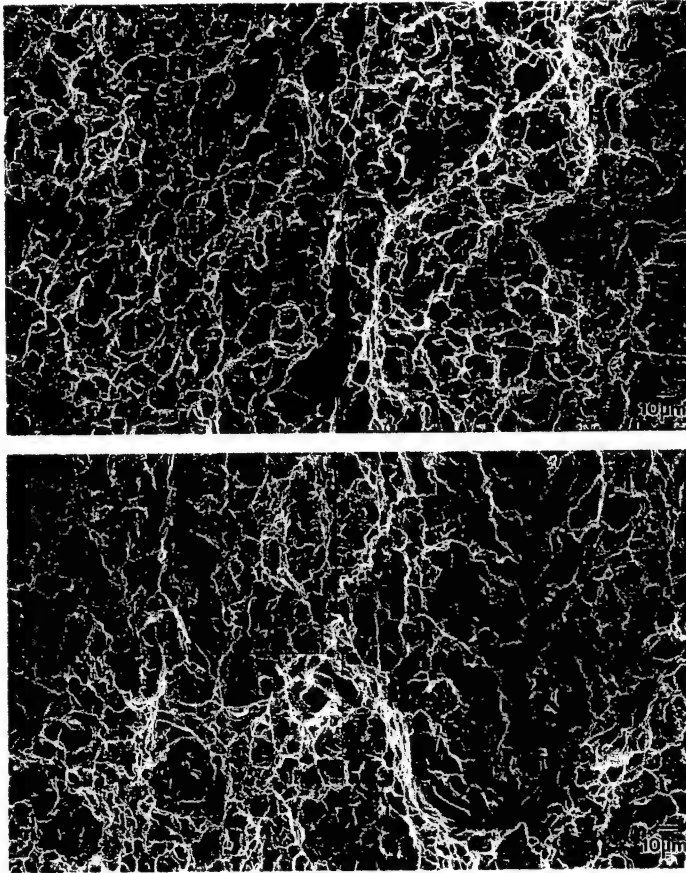


Figure 8 - Scanning electron fractographs of crack surfaces in Ti-6-4 (LT) produced by rising- δ_m loading in (a-top) moist-laboratory air and (b-bottom) 3.5% NaCl solution at dK/dt of $4 \times 10^3 \text{ MPa}\sqrt{\text{m/s}}$.

Discussion

EAC Resistance of Ti-6-2222

The modern α/β -Ti alloy, Ti-6-2222, is susceptible to severe transgranular EAC in chloride solution, as established by the results in Figs. 4, 7, 10, and 11. The threshold stress intensity for the onset of EAC, K_{JTH} , is reduced to 25% of K_{JIC} , subcritical crack growth rates are as high as $20 \mu\text{m/s}$ (or one-third of a prior β -Ti grain per second), and a fracture mode

slow-stable EAC in Ti-6-2222. The environmental fracture mode contained extensive TG α -cleavage. This morphology was produced for all loading rates examined, as illustrated by the fractograph of fast- dK/dt EAC in Fig. 11.

Fractographic and metallographic examinations showed that the transition from slow to rapid-stable cracking in NaCl was not accompanied by a crack mode change for either α/β -Ti alloy in NaCl. The fractographs in Fig. 10 show the regions of slow and rapid-stable EAC in Ti-6-2222/NaCl (Fig. 2a). Each regime involved extensive α -cleavage, without a resolvable transition in the crack path when da/dt changed from fast to slow or from slow to fast. Similar results were obtained for Ti-6-4 [30].

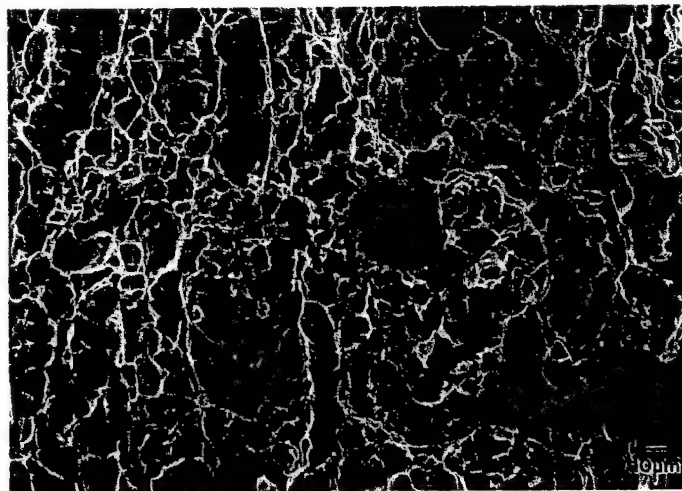


Figure 9 - SEM fractograph of the NaCl fracture surface of annealed Ti-6-4 (ELI, LT) plate loaded at a slow dK/dt of $2.0 \times 10^4 \text{ MPa}\sqrt{\text{m/s}}$.

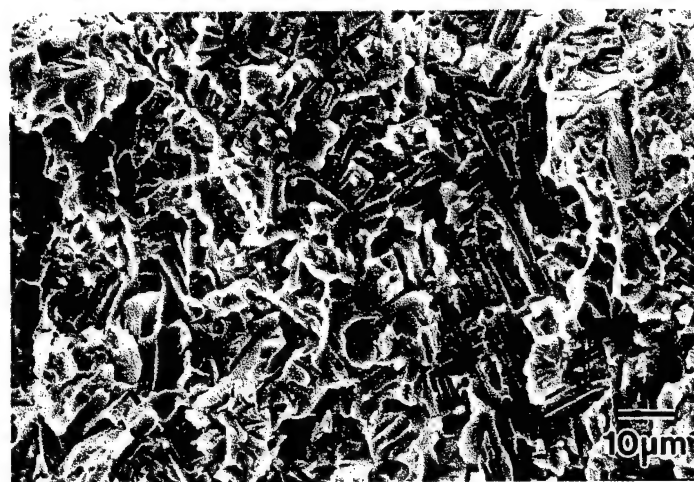
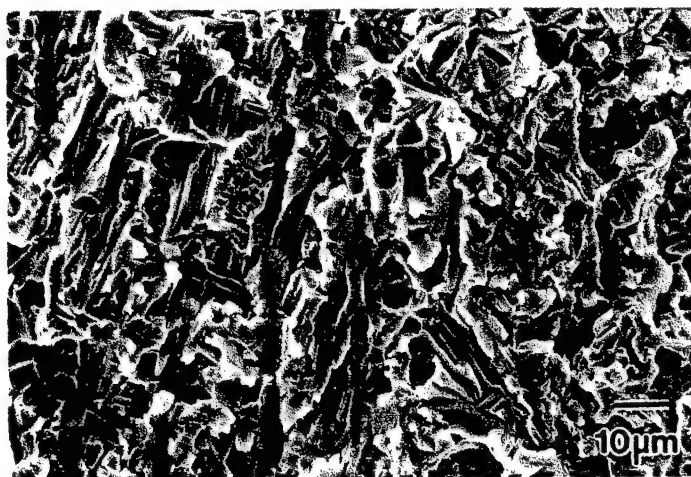


Figure 10 - Ti-6-2222 (TL) NaCl fracture surfaces depicting regions of (a-top) rapid and (b-bottom) slow-EAC at dK/dt of 2.0×10^{-4} MPa $\sqrt{m/s}$.

well as Ti-5Al-2.5Sn, Ti-6Al-6V-2Sn, Ti-6Al-2Sn-4Zr-2Mo, and Ti-6Al-2Sn-4Zr-6Mo [21, 40]).

The microstructure of the α/β -hot rolled plate of Ti-6-2222 (Fig. 1b) was not optimized for yield strength and air-fracture toughness. A so-called Triplex thermomechanical process (solution treat at $\beta_T + 28-42^\circ\text{C}$ for 0.5 h and cool at $20-67^\circ\text{C/min}$; anneal at $\beta_T - 28-$

transition is affected by concurrent stress and chloride exposure. Severe EAC persisted over a wide range of applied dK/dt from 2×10^{-4} MPa $\sqrt{m/s}$ (or lower) to 0.01 MPa $\sqrt{m/s}$. Less severe EAC continued to dK/dt levels at least as high as 5 MPa $\sqrt{m/s}$, and the trend line in Fig. 4 suggests that EAC may be sustained in Ti-6-2222 for dK/dt levels up to 40 MPa $\sqrt{m/s}$.

EAC may be significant for some applications of Ti-6-2222. The susceptibility of Ti-6-2222 is substantially higher than that exhibited by the ELI grade of Ti-6-4 for identical test conditions. The EAC of Ti-6-2222 was similar in terms of absolute K_{JTHi} to α/β -Ti alloys with high Al and Sn contents, and heat treated to precipitate α_2 (Ti-8Al-1Mo-1V and Ti-7Al-4Mo [3, 40], as



Figure 11 - SEM fractograph of the environmental fracture surface for annealed Ti-6-2222 (TL) loaded at dK/dt of 1.2 MPa $\sqrt{m/s}$ in NaCl.

50°C for 1.0 h and cool at 20-67°C/min; age at 496-538°C for 8h and air cool) optimized σ_{YS} (minimum 910 MPa) and plane strain fracture toughness (minimum 77 MPa \sqrt{m}) [41]. The lower toughness of the Ti-6-2222 microstructure in Fig. 1b ($K_{JIC} = 56$ MPa \sqrt{m}) is likely due to globular-aligned α (Fig. 1b) as well as silicides and α_2 formed during slow cooling from the α/β annealing temperature [31, 42].

Ti-6-2222 is generally susceptible to severe TG EAC [30]. Several microstructures of both plate and extrusion, including that subjected to the Triplex treatment, were prone to brittle cracking when exposed to NaCl solution under rising δ_m . The effect of microstructure on EAC resistance is considered in detail elsewhere [43], where it is established that the critical factor that controls TG EAC is α_2 precipitation in α . This phase formed during furnace cooling of both Ti-6-2222 [32, 42] and Ti-6-4 (ELI) [33] in the present study. The EAC susceptibility of Ti-6-2222 relative to Ti-6-4 was speculatively ascribed to enhanced α_2 -precipitation kinetics due to Si [43].

Mechanistic Implications

Each annealed α/β -Ti alloy and aged-metastable β -Ti alloy listed in Table 1 is susceptible to severe environmental cracking for similar chloride solution and cracked-specimen loading conditions. The β -Ti alloys are susceptible to intergranular (IG) cracking, while TG- α cleavage occurs in α/β Ti-6-4 and Ti-6-2222.

Table 1 - *Titanium Alloys Susceptible to EAC in Aqueous Chloride Solution Under Rising Crack-Mouth-Opening Displacement Loading*

	Microstructure	EAC Mode	Minimum K_{JTH}/K_{JIC}	Maximum dK/dt	Maximum da/dt	H Penetration (μm)	
			(MPa \sqrt{m})	(MPa $\sqrt{m/s}$)	($\mu m/s$)	dK/dt	da/dt
Ti-6Al-4V (ELI)	Equiaxed α/α_2 + retained β	TG; α cleavage	56/79	0.1-0.5	7	0.4	0.0004
Ti-6Al-2Zr-2Sn-2Cr-2Mo	Coarse-acicular α/α_2 in β/Ti_xSi_y	TG; α cleavage	14/66	4-40	11	0.03 (α)	0.0003 (α)
						7 (β)	0.02 (β)
Ti-8V-6Cr-4Mo-4Zr-3Al [12, 70]	Fine α precipitates in β	IG; along β bounds	24/64	>40	20-100	15	0.01
Ti-15Mo-3Nb-3Al [12, 65]	Fine α precipitates in β	IG; along β bounds	40/70	0.2-2	≈ 20	95	—

Background: Hydrogen Environment Embrittlement Mechanism-A body of evidence establishes that both TG EAC in α/β -Ti alloys [8] and IG EAC in β/α -Ti alloys [9, 12] are caused by HEE local to the crack tip. Qualitatively, EAC in α/β alloys is similar for stressed exposure in H_2 and aqueous-halogen solutions [8]. Quantitatively for the β/α -electrolyte system, crack acidification and lowered electrode potential favor electrochemical H production and entry, establishing a crack tip surface H concentration of C_{HS} [6, 9]. This H is transported into the process zone where damage occurs when the local tensile stress exceeds a critical level that decreases with increasing concentrated H content. The process zone is typically hypothesized to be located where tensile and hydrostatic stresses are maximum, within the first 20% of the plastic zone [14, 44]. Process zone H promotes near-basal cleavage-like cracking through α in α/β -Ti alloys [2, 4, 10] and IG cracking along β grain boundaries in β/α -Ti alloys [12], Table 1.

Three elements must be understood to model the threshold and kinetics of HEE in Ti alloys; crack electrochemistry, crack tip strain rate, and process zone H diffusion.

Crack Electrochemistry-While bare titanium is extremely reactive, passivity is a critical element of HEE because the surface oxide hinders H supply to damage sites [17, 45, 46]. As such, HEE is focused at the crack tip where plastic deformation ruptures the passive film to expose the active and H-diffusion barrier-free alloy [9, 45, 47, 48]. Titanium fractured in simulated crack solution repassivates in less than 10^{-3} s [45], but net-anodic current transients, with a prolonged decay time of 2 to 20 s, emit from surface reactions on a straining-electrode surface in chloride solution [47]. These long-time transients were modeled as comprised of numerous and overlapping-discrete dissolution events, each caused by oxide destabilization due to a superdislocation composed of many single dislocations arriving at the oxide/metal interface in a distribution of time and space [48]. Experiments with smooth and notched tensile specimens of a β/α -Ti alloy in NaCl showed that both finite plastic strain and an average strain rate in excess of 10^{-5} s $^{-1}$ were required to produce discrete depassivation events that overlapped to produce a long-term transient [48].

From these results, it is hypothesized that the H production step in HEE only occurs above a critical crack tip strain rate that is necessary to mechanically destabilize the tip-passive film for H uptake. It is further speculated that, above a critical strain rate and on average at K_{JTHi} , crack tip deformation conditions are sufficient to provide a quasi-steady state level of film destabilization and H production. Essentially, deformation at this level causes a continued and constant destabilization of a portion of the straining crack tip; as such, a quasi-steady state hydrogen concentration, C_{HS} , is developed. This view is supported by experimental measurements of net-anodic current transients of many seconds duration emitted from a chloride-laden crack subjected to rising K. Such prolonged transients began at about half of K_{JTHi} and increased in frequency to overlap as K approached this threshold [47]. The actual H production condition will likely vary about the perimeter of the crack tip due to strain and strain rate variations with position, as well as noncontinuum microscopic plasticity. This model of passive film destabilization should be relevant to α/β -Ti alloys that contain α_2 precipitates that exacerbate localized-planar slip via the particle cutting mechanism and produce large slip offsets at a free surface [26, 49].

The rate of supply of electrolyte from the bulk to support crack tip reactions, as well as the removal of ionic reaction products from this region, could rate limit HEE at high loading or crack growth rates [18]. For Ti in bulk-neutral chloride solution, the cracking rate limited by Faradic dissolution of a fully-bare crack tip surface is orders of magnitude faster than those encountered in the present study [50]. Two uncertainties exist. The limiting rate can be reduced by electrolyte-mass transport that is impeded by either the occluded crack-opening geometry or a precipitated-salt film near the crack tip [51]. The anodic and cathodic currents local to the crack tip, and the amount of salt formed, depend on the passive current density vs. crack-solution volume and area of passive surface that is bared by slip step formation. This active area is unknown for Ti alloys in chloride solution [9, 47, 48, 50].

Hydrogen Diffusion-If C_{HS} is established rapidly, then the amount of H transported to crack tip damage sites (C_H) should limit the kinetics of HEE. For a stationary-infinite planar surface, maintained at constant C_{HS} , the one-dimensional H-penetration distance is

$$x = A\sqrt{D_H t} \quad (2)$$

where x is distance ahead of the surface, A is a constant that depends on the selected level of C_H/C_{HS} , D_H is the diffusivity of H in α or β Ti, and t is time. For a propagating crack, H penetration distance is estimated from steady-state C_H vs. x profiles for different ratios of da/dt to D_H and with the crack tip acting as a moving line source of H in two dimensions [52]. More complex solutions account for stress and plastic strain effects on H diffusion [53]. Several issues confound H-transport analysis. The diffusion distance into the process zone is not known [54]. Second, H diffusion in a complex α/β -Ti microstructure may occur by parallel lattice and interface paths [11, 28]. Third, H may be transported by dislocation sweeping into the process zone [55], until H breaks from moving dislocations in α -Ti at a critical strain rate of order 0.01 s^{-1} [21, 55].

Crack Tip Strain Rate-In the HEE scenario, $\dot{\epsilon}_{CT}$ represents a tensile or shear-strain rate component local to the crack tip. Time derivatives of elastic-plastic continuum solutions for strain ahead of a stationary crack show that each component of strain rate depends on alloy deformation properties, position in the crack tip process zone (x ahead of the crack tip and θ above the crack plane), K , and dK/dt [56-58]. For the tensile-flow properties of Ti-6-4 (ELI) and Ti-6-2222

$$\dot{\epsilon}_{CT} = \lambda \left[\frac{1}{E\sigma_o x} \right]^\gamma K^\theta \left(\frac{dK}{dt} \right) \quad (3)$$

where $\lambda = 0.04$, $\gamma = 1.0$, and $\theta = 1.0$ for a solution based on a small-strain description of the crack tip field [57], and $\lambda = 0.20$, $\gamma = 2.2$, and $\theta = 3.4$ derived from a large-strain finite element analysis of crack tip tensile strains [59]. Solutions for a propagating crack include an additional term to account for the effect of da/dt on strain rate [60]. The crack tip opening displacement rate in the Mode I loading direction, $\dot{\delta}_{CT}$, approximates $\dot{\epsilon}_{CT}$. A J-integral based description of $\dot{\delta}_{CT}$ is [60]

$$\dot{\epsilon}_{CT} \propto \dot{\delta}_{CT} = 2\alpha \frac{dK}{dt} \frac{K(1-\nu^2)}{E\sigma_{ys}} + \beta \frac{da}{dt} \frac{\sigma_o}{E} \ln \left(0.2 \frac{K^2(1-\nu^2)}{\sigma_{ys}^2 r} \right) \quad (4)$$

where $\alpha = 0.7$ for low-strain hardening α/β -Ti alloys, $\beta = 5$, r is the distance behind the crack tip, and σ_o is the yield strength or Ramberg-Osgood reference stress.

Crack tip strain rate is difficult to determine. Equation 3 predicts an infinite tip-surface strain rate as x approaches 0, and different strain rate distributions ahead of the crack tip depending on the model chosen. From Eq. 4, $\dot{\epsilon}_{CT}$ at the blunted-crack tip surface is estimated from $\dot{\delta}_{CT}$ using an uncertain gauge geometry (shear band vs. crack opening displacement) and gauge length [58, 61]. The relevant value of r behind this surface is unknown and Eq. 4 does not describe the gradient of $\dot{\epsilon}_{CT}$ ahead of the crack tip. The continuum approach may not describe $\dot{\epsilon}_{CT}$ adequately if microscopic deformation is heterogeneous due to slip localization in the two-phase α/β microstructure, accentuated by α_2 precipitates. Equations 3 and 4 do not include a creep contribution. Nonetheless, Eqs. 3 and 4 provide the best available description of crack tip strain rate for use in interpreting EAC data and trends.

Hypothesis-The kinetics of EAC of alloys are established by the effect of $\dot{\epsilon}_{CT}$ on quasi-steady C_{HS} and coupled H diffusion ahead of the crack tip. This notion was considered for IG HEE of aged β/α -Ti alloys [12] and is tested here for TG HEE of α/β -Ti alloys of two distinctly different microstructures.

Oscillating Environmental Crack Growth-Each of the alloys in Table 1 exhibited EAC that oscillated between periods of slow-stable and fast-stable growth. Analysis of cracking in β -Ti alloys (Table 1) established that this behavior was due to an extrinsic effect of specimen compliance on K and $\dot{\epsilon}_{CT}$ [12] rather than an intrinsically-discontinuous hydrogen embrittlement mechanism [62, 63]. The experimental results confirm this conclusion for TG HEE in α/β Ti-6-4 and Ti-6-2222. Each regime of slow or rapid EAC occurred over thousands of micrometers (Fig. 2), well in excess of a typical process zone in a discontinuous cracking process. Crack growth did not arrest during slow growth and occurred at a finite rate during fast- da/dt cracking. Oscillatory EAC was eliminated by either fast dK/dt loading at fixed $\dot{\delta}_m$ (Figs. 2-4) or by load-control at fixed dP/dt . The TG fracture mode was identical for the slow- da/dt and fast- da/dt regions of EAC in Ti-6-4 and Ti-6-2222 (Fig. 10). There was no evidence for striation markings on the fracture surface, or crack-wake ligaments that ruptured by ductile fracture after the environmental crack passed.

Oscillating crack growth and the dK/dt dependence of da/dt (Figs. 6 and 7) are explained by H production governed by crack tip strain rate. Equation 4 shows that the strain rate for a propagating crack depends on dK/dt and da/dt . For slow da/dt or high dK/dt , the loading rate term in Eq. 4 dominates $\dot{\epsilon}_{CT}$, and da/dt increases with increasing dK/dt , as shown in Figs. 6 and 7 for the regions of slow crack growth. In contrast the growth rates during rapid crack extension are independent of dK/dt . Here, increasing specimen compliance creates negative dK/dt (Fig. 2) and the da/dt term in Eq. 4 controls $\dot{\epsilon}_{CT}$, independent of the applied $\dot{\delta}_m$ rate. The crack tip strain rates are similar resulting in

crack growth rates that are independent of the initial-applied dK/dt . The rapidly growing crack generates a self-sustaining crack tip strain rate, and rapid crack growth continues until a lower K level is reached which arrests EAC.

Although Eq. 4 qualitatively explains the effect of dK/dt on EAC kinetics, the predicted deformation rates are not consistent with the measured effect of loading on da/dt . During slow crack growth, the calculated da/dt term in Eq. 4 is larger than the dK/dt term for the range of applied displacement rates examined. As concluded for the β -Ti alloys in Table 1 [12], existing continuum descriptions of crack tip strain rate with known input parameters are inadequate to explain the experimental observations of HEE in Ti alloys. From the practical perspective, rising crack mouth opening displacement loading is an effective method to characterize the threshold stress intensity for the onset of EAC, but is a complex loading condition for crack growth rate measurement.

HEE at Quasi-Static Crack Tip Strain Rates-Early studies suggested that EAC does not occur in α/β -Ti alloys under either static load [21-23] or if crack-tip creep occurs prior to solution exposure [26, 27]. The implication is that uptake of H ceases below a critical crack tip strain rate (10^{-5} s^{-1}) due a stable crack tip oxide. The reduction of HEE at low crack tip strain rates was demonstrated for the β -Ti alloys in Table 1 [12].

Results suggest that HEE is nearly eliminated in Ti-6-4 at the lower dK/dt examined (Figs. 3, 8 and 9), but not for Ti-6-2222 (Fig. 4). For a slow-applied dK/dt of $10^{-4} \text{ MPa}\sqrt{\text{m/s}}$, calculated crack tip strain rates are $2 \times 10^{-6} \text{ s}^{-1}$ (Eq. 3 with $\lambda = 0.04$, $\gamma = 1.0$, and $\theta = 1.0$), $6 \times 10^{-6} \text{ s}^{-1}$ (Eq. 3 with $\lambda = 0.20$, $\gamma = 2.2$, and $\theta = 3.4$), and $7 \times 10^{-5} \text{ s}^{-1}$ (Eq. 4 with $da/dt = 0$); all for $x = r = 1 \text{ }\mu\text{m}$ and $K = 60 \text{ MPa}\sqrt{\text{m}}$ relevant to Ti-6-4. These strain rates are, with the exception of the propagating crack result, less than the strain rate ($1 \times 10^{-5} \text{ s}^{-1}$) necessary to stimulate passive film destabilization in the presence of significant plastic strain, as established based on tensile-straining electrode experiments [47, 48]. It is reasonable to expect that HEE would not occur in Ti-6-4 at the lowest loading rates examined because crack tip passivity hinders hydrogen uptake.

Considering Ti-6-2222, for dK/dt of $10^{-4} \text{ MPa}\sqrt{\text{m/s}}$, $\dot{\epsilon}_{CT}$ is between $5 \times 10^{-7} \text{ s}^{-1}$ (Eq. 3 with $\lambda = 0.04$, $\gamma = 1.0$, and $\theta = 1.0$), $2 \times 10^{-7} \text{ s}^{-1}$ (Eq. 3 with $\lambda = 0.20$, $\gamma = 2.2$, and $\theta = 3.4$), and $2 \times 10^{-5} \text{ s}^{-1}$ (Eq. 4 with $da/dt = 0$); all for $x = r = 1 \text{ }\mu\text{m}$ and $K = K_{JTH} = 14 \text{ MPa}\sqrt{\text{m}}$. These strain rates are lower than those predicted for Ti-6-4 due to the lower K at the onset of cracking and suggest that HEE should not occur in Ti-6-2222 at low dK/dt . Since EAC was produced, the strain rate predictions from Eq. 3 and 4 are inconsistent with experimental observations.

The different low- $\dot{\epsilon}_{CT}$ responses of Ti-6-4 and Ti-6-2222 are not understood quantitatively. The parameters used in the crack tip strain rate equations are uncertain, particularly the distances (x and r). Strain rate models do not account for localized-planar slip at a crack tip. It is reasonable to speculate that the $\dot{\epsilon}_{CT}$ associated with enhanced-slip localization in Ti-6-2222 vs. Ti-6-4 [30] exceeds the continuum predictions to explain severe HEE at the slow dK/dt represented in Fig. 5; even lower dK/dt would be required to mitigate embrittlement in Ti-6-2222.

HEE at Rapid Rates-HEE in α/β -Ti alloys is sustained at high rates, Table 1. If the HEE scenario is correct, then the kinetics of the elemental steps outlined previously must support these rapid environmental cracking kinetics.

Threshold for HEE—It is reasonable to speculate that a quasi-steady level of C_{HS} is produced at the deforming crack tip in Ti-6-4 and Ti-6-2222 stressed in neutral-aqueous chloride at dK/dt of 10^{-2} MPa \sqrt{m}/s and faster, conditions that produced severe EAC. Predicted values of crack tip strain rate are between $8 \times 10^{-5} s^{-1}$ (Eq. 3 with $\lambda = 0.04$, $\gamma = 1.0$, and $\theta = 1.0$), $5 \times 10^{-5} s^{-1}$ (Eq. 3 with $\lambda = 0.20$, $\gamma = 2.2$, and $\theta = 3.4$), and $3 \times 10^{-3} s^{-1}$ (Eq. 4 with $da/dt = 0$); for $K = 20$ MPa \sqrt{m} , $dK/dt = 0.01$ MPa \sqrt{m}/s , and $x = r = 1 \mu m$. Each value exceeds the strain rate of $10^{-5} s^{-1}$ that is necessary for crack tip H production. Faster dK/dt should favor constant or increasing C_{HS} to sustain HEE, and H production and uptake should not be rate limiting for the range of dK/dt considered. It is further assumed that neither electrolyte-mass transport for ion renewal and removal, nor crack-potential drop, limit the cracking kinetics. This speculation is based on the results of occluded-crack electrochemical studies performed on a β/α -Ti alloy [7, 50].

The K_{JTH} vs dK/dt data in Figs. 3 and 4 provide insight into the location of crack tip damage sites; above a critical dK/dt , HEE is eliminated because time is insufficient for H transport. This location is estimated from the maximum distance of H penetration ahead of the stationary-crack tip surface (x_c) during the time to load to K_{TH} at the maximum dK/dt that produced TG cracking. For diffusion, penetration distances are estimated from Eq. 2. Since the critical level of C_H is not known, C_H/C_{HS} is assumed to equal 0.5 ($A = 1.0$). Differences in C_H/C_{HS} over a reasonable range exert a second-order effect on the calculation that follows. The time for H transport is less than the duration of solution exposure prior to K_{TH} because H uptake only occurs during film rupture. Assuming that film rupture starts at 50% of K_{TH} [48], the time for H diffusion ahead of the crack tip is 170 s for Ti-6-4 (HEE terminates at $dK/dt \geq 0.2$ MPa \sqrt{m}/s where $K_{JTH} = K_{JIC} = 68$ MPa \sqrt{m}), and 1 s for Ti-6-2222 ($dK/dt > 20$ MPa \sqrt{m}/s , $K_{JTH} = K_{JIC} = 52$ MPa \sqrt{m}). Assuming that HEE is controlled by H diffusion in α , with an associated D_H of 1×10^{-11} cm $^2/s$ at 25°C [64], Eq. 2 shows that x_c is 0.4 μm for Ti-6-4 and 0.03 μm for Ti-6-2222.

These calculated H penetration distances are smaller than the estimated size of the process zone. Continuum modeling of a blunted-stationary crack tip demonstrates that tensile stresses are several times higher than σ_{YS} over a distance from the tip that equals two to four times the blunted crack tip opening displacement (δ_t), where $4\delta_t$ equals $2K^2/\sigma_{YS}E$ [14]. This distance is 70 μm for Ti-6-4 and 3 μm for Ti-6-2222, both stressed to K_{JTH} . Hydrogen trapping by dislocations generated by high crack tip plastic strain may reduce D_H ; x_c is further reduced 10-fold for each 100-times decrease in the apparent D_H (Eq. 2). The exact effect of dislocation density on D_H in α -Ti is unknown. These comparisons suggest that diffusion in the α lattice cannot supply H to the location of maximum tensile stress predicted from the blunt-crack model.

Each CT specimen was fatigue cracked in chloride solution prior to rising- δ_m testing. Hydrogen, introduced to the process zone during fatigue, could affect K_{JTH} . The effect of precrack environment was not defined for Ti-6-4 or Ti-6-2222. Similar experiments with cast Ti-6-2222 in NaCl produced severe transgranular EAC emanating from an air fatigue crack.³ This cracking exhibited all of the characteristics observed for the plate microstructure of Ti-6-2222 (Figs. 2, 4, 7, 10 and 11). Identically severe IG EAC was produced for air and NaCl-fatigue precracked specimens of a β -Ti alloy [65]. Typically, 1 to 12 h elapsed between NaCl fatigue cracking and the beginning of the

³ Edward Richey III, Unpublished research, University of Virginia, Charlottesville, VA, 1999.

rising- δ_m EAC experiment. The specimen was maintained without stress in the solution during this transition, but H uptake would not occur since crack tip deformation was nil. From Eq. 2, a typical H diffusion distance is 2-7 μm , suggesting that H from fatigue precracking dispersed sufficiently within the process zone, with the residual amount being small compared to C_{HS} produced during rising δ_m . Possible H trapping in the process zone, and the effect of lapsed time between solution-precracking and rising displacement EAC testing, were not studied.

Crack Propagation Kinetics-The fast rates of TG cracking observed for α/β -Ti alloys in NaCl solution provide further insight into the H-embrittlement site. The ratio of $(da/dt)/D_H$ controls the maximum-H penetration distance [52]. For Ti-6-4 (maximum $da/dt = 7 \mu\text{m/s}$ from Fig. 3, an assumed critical C_H/C_S ratio of 0.5, and a D_H of $1.0 \times 10^{-11} \text{ cm}^2/\text{s}$ [64]), the maximum penetration distance is $4 \times 10^{-4} \mu\text{m}$. For Ti-6-2222, the maximum da/dt is $11 \mu\text{m/s}$ (Fig. 4) and the maximum penetration distance is $3 \times 10^{-4} \mu\text{m}$.

The opening of a propagating crack tip is less than δ_t estimated for the stationary crack due to elastic unloading of material in the wake. The tip opening predicted from the moving-crack analysis that yielded Eq. 4 is $\delta_t = \{\beta\sigma_o r/E\} \ln\{0.2 K^2/\sigma_o^2 r\}$ [60]. Four times this distance, for $r = 1 \mu\text{m}$ behind the crack tip, is $1.0 \mu\text{m}$ for Ti-6-4 and $0.60 \mu\text{m}$ for Ti-6-2222, both stressed to the threshold K for HEE. If this multiple of δ_t defines the location of the maximum tensile stresses and process zone ahead of a propagating crack tip, then lattice diffusion cannot supply H at the observed rates of EAC.

Discrepancy between Predicted and Expected Process Zone Distances- Of the four cases in Table 1, the continuum-predicted process zone distance equals the lattice-H diffusion distance only for the static crack in the two β/α Ti alloys. For the static crack in each α/β -Ti alloy, as well as for the propagating cracks in the α/β and β/α -Ti alloys, the calculated H-diffusion distance is substantially smaller than a classic process zone size based on the location of the stress maximum ahead of a blunted crack tip. For HEE to be the correct mechanism, this discrepancy must be explained.

Rapid-Path H Transport-A rapid-path H transport mechanism could augment lattice diffusion of H over the predicted $4\delta_t$. Considering the static crack, D_H for β -Ti is rapid ($5 \times 10^{-7} \text{ cm}^2/\text{s}$ at 25°C ⁴) and H transport distances are 90 and $7 \mu\text{m}$, respectively, for Ti-6-4 and Ti-6-2222 at the fastest dK/dt that produced TG EAC. While these distances are comparable to the static process zone located at $4\delta_t$, the β phase is sufficiently discontinuous in Ti-6-4 and not a fast-path for H diffusion. The β is sufficiently continuous in Ti-6-2222 to supply H embrittlement of α/β interfaces [11]. However, TG- α cleavage is the cracking mechanism for α/β -Ti alloys in chloride solution (Figs. 8, 10 and 11 and Ref. [8]). Since the α -plate width is much larger than the lattice diffusion distance, it is unclear how rapid H diffusion in β would supply H to a process zone that is within α . The similar cracking kinetics and transgranular modes for Ti-6-4 and Ti-6-2222 in NaCl solution, in spite of the microstructural differences, suggests that fast-path

⁴ George A. Young, Unpublished research, University of Virginia, Charlottesville, VA, 1996.

diffusion does not explain the low K_{JTHi} at the relatively high dK/dt levels represented in Figs. 3 and 4.

If dislocation transport of H is possible in the equiaxed and acicular morphologies of α , then H can be transported rapidly over the distance necessary to reach the blunted crack tip process zone⁵ [21]. Assuming a density of mobile and H-carrying dislocations of 10^{10} cm^{-2} , H will dissociate from dislocations at a critical velocity of $0.4 \text{ } \mu\text{m/s}$, corresponding to a critical strain rate of 0.01 s^{-1} . For a static crack and values of x and r in the range from 1 to $10 \text{ } \mu\text{m}$, Eqs. 3 and 4 suggest that this strain rate is achieved at applied dK/dt levels between 0.3 and $20 \text{ MPa}\sqrt{\text{m/s}}$. Above these rates, H is not carried by dislocations and HEE should not occur. These estimates are of the same order as the loading rates necessary to preclude HEE emanating from the static crack tip. Nonetheless, these calculations are suspect because of the uncertain values of the model parameters [21, 55]. Additionally, the simple model of H association with a dislocation is probably not relevant to the localized-heterogeneous slip structure in α_2 -bearing α . Finally, if the α/β interface is a H trap site with a higher binding energy compared to the dislocation, then H could be deposited at the interface as dislocations moved from α to β and fast-path H transport would be mitigated.

Process Zone Location-Stress-based estimates of process zone size, from blunt-crack continuum analyses, may not be relevant to HEE in α/β -Ti alloys. *In situ* SEM measurements showed that the opening of an IG environmental crack tip in the β/α -Ti alloy/NaCl system was less than that of a TG fatigue crack, that was in turn less than the predicted δ_t for a stationary crack at equal K [12]. As such, the location of high tensile stresses should be closer to the tip of a sharp IG crack, consistent with a short diffusion distance. High-elastic stresses may exist adjacent to the sharper crack tip [54,66]. The origin of the small opening for the IG crack was not understood, but microstructure appears to alter the continuum prediction of crack tip opening and stresses. Considering TG cracking in α/α_2 , Curtis *et al.* argued that planar slip constrains blunting to favor a sharper tip with a higher local stress concentration [26]. Additionally, interactions between heterogeneous slip bands and α/β boundaries could produce local stress concentrations. In these cases a stress-based process zone distance could be less than a continuum mechanics prediction of δ_t for a stationary or propagating crack.

High C_{HS} -Extremely high levels of H, produced on the crack tip surface, could define the location of the damage zone independent of local tensile stress. The continuum crack tip tensile and hydrostatic stress distributions rise from one to about four times σ_{YS} with distance from the crack tip surface to $4\delta_t$. The C_H decreases from C_{HS} , but is enhanced by hydrostatic tension, and microcracking is usually projected to occur at the subsurface point where stresses are maximized [14, 44]. Alternately, C_{HS} may be orders of magnitude higher than expected, as measured for a crack tip in the aluminum alloy/neutral NaCl system and attributed to the high fugacity of H produced on bared Al in contact with an acidified electrolyte [67]. It is reasonable to expect a similar high level

⁵ Using reasonable parameters in the equations that describe dislocation transport of H [21], $D_H = 10^{-11} \text{ cm}^2/\text{s}$ [64], and strain rate from Eq. 4, the calculated transport distance is $160 \text{ } \mu\text{m}$ for Ti-6-4 and $90 \text{ } \mu\text{m}$ for Ti-6-2222 at the dK/dt levels where EAC was eliminated.

of C_{HS} adsorbed at slip-step bared regions of the crack tip surface for the Ti alloy/chloride system. Embrittlement could occur essentially at the crack tip surface, controlled by high C_{HS} and consistent with very short process zone distances.

Environmental cracking under fast dK/dt and da/dt rule out HEE based on TiH fracture. This brittle phase forms by nucleation and growth from a supersaturated solid solution of H in α -Ti, rather than martensitically [68]. The growth of TiH on α -Ti contacting H_2 above $100^\circ C$ was rate limited by H diffusion through the growing hydride; the extrapolated thickening rate was 0.002 to $0.02 \mu m/s$ at $25^\circ C$ [69]. This rate is orders of magnitude slower than the EAC rates (7 to $100 \mu m/s$) in Table 1, suggesting that sufficient TiH cannot form during environmental crack propagation. If HEE is the mechanism for environmental cracking in α/β -Ti alloys, then the damage process is reasonably presumed to be lattice or interface decohesion.

Conclusions

1. Annealed Ti-6Al-4V (ELI) and Ti-6Al-2Zr-2Sn-2Cr-2Mo are susceptible to environment assisted cracking (EAC) when stressed under rising crack-opening displacement in aqueous chloride solution. The threshold K_{JTH} is less than K_{JIC} and the ductile-fracture mode transitions to transgranular cleavage of α .
2. The acicular- α/α_2 microstructure of Ti-6-2222 is susceptible to severe cracking in chloride solution compared to the resistant equiaxed- α structure of Ti-6-4 (ELI).
3. EAC in α/β -Ti alloys depends on loading rate and may be most severe at intermediate crack tip strain rates.
4. EAC is sustained at high loading rates ($dK/dt = 0.3 \text{ MPa}\sqrt{m/s}$ for Ti-6-4 and greater than $10 \text{ MPa}\sqrt{m/s}$ for Ti-6-2222) and crack growth rates are rapid ($10 \mu m/s$).
5. The hydrogen environment embrittlement mechanism is consistent with rapid cracking kinetics in α/β -Ti, but only if the process zone is within 0.001 to $1 \mu m$ of the crack tip surface.
6. A near-tip process zone may be promoted by very high H produced on electrochemically active areas of the crack surface, or by a sharp crack tip.
7. Apart from the TG vs. IG crack path, the phenomenological and mechanistic aspects of environmental cracking are similar for annealed α/β and aged-metastable β -Ti alloys stressed actively in aqueous chloride solution.

Acknowledgments

This research was sponsored by the Boeing Company with R. L. Lederich as program monitor, and by the Office of Naval Research (Grant N00014-91-J-4164) with A. John Sedriks as Scientific Officer. Informative discussions were conducted with J. R. Scully and B. P. Somerday.

References

- [1] Speidel, M. O., Blackburn, M. J., Beck, T. R. and Feeney, J. A., in *Corrosion Fatigue: Chemistry, Mechanics and Microstructure*, O. Devereaux, A. J. McEvily and R. W. Staehle, Eds., NACE, Houston, TX, 1972, pp. 324-345.

- [2] Wanhill, R. J. H., *British Corrosion Journal*, vol. 10, pp. 69-78, 1975.
- [3] Czyrklis, W. F. and Levy, M., in *Environment-Sensitive Fracture of Engineering Materials*, Z. A. Foroulis, Ed., TMS-AIME, Warrendale, PA, 1979, pp. 303-313.
- [4] Hardie, D., in *Environment-Induced Cracking of Metals*, R. P. Gangloff and M. B. Ives, Eds., NACE, Houston, TX, 1990, pp. 347-361.
- [5] Simbi, D. J., *Corrosion Reviews*, vol. 14, pp. 343-374, 1996.
- [6] Brown, B. F., in *Materials Research and Standards*, pp. 129-133, 1966.
- [7] Kolman, D. G. and Scully, J. R., in *Effects of the Environment on the Initiation of Crack Growth*, ASTM STP 1298, W. A. Van der Sluys, R. S. Piascik and R. Zawierucha, Eds., ASTM, West Conshohocken, PA, 1998, pp. 61-73.
- [8] Nelson, H. G., in *Hydrogen in Metals*, I. M. Bernstein and A. W. Thompson, Eds., ASM International, Materials Park, OH, 1974, pp. 445-464.
- [9] Kolman, D. G. and Scully, J. R., *Metallurgical and Materials Transactions A*, vol. 28A, pp. 2645-2656, 1997.
- [10] Wanhill, R. J. H., *Corrosion*, vol. 29, pp. 435-441, 1973.
- [11] Nelson, H. G., *Metallurgical Transactions*, vol. 4, pp. 364-367, 1973.
- [12] Somerday, B. P., Young, L. M. and Gangloff, R. P., *Fatigue and Fracture of Engineering Materials and Structures*, vol. 23, pp. 3s9-58, 2000.
- [13] Gaudett, M. A. and Scully, J. R., *Metallurgical and Materials Transactions A*, vol. 30A, pp. 65-79, 1999.
- [14] Gangloff, R. P., *Materials Science and Engineering A*, vol. A103, pp. 157-166, 1988.
- [15] Kolman, D. G., Gaudett, M. A. and Scully, J. R., *Journal of the Electrochemical Society*, vol. 145, pp. 1829-1840, 1998.
- [16] Scully, J. C., *Corrosion Science*, vol. 20, pp. 997-1016, 1980.
- [17] Scully, J. R. and Moran, P. J., *Journal of the Electrochemical Society*, vol. 135, pp. 1337-1348, 1988.
- [18] Ford, F. P., in *Environment-Induced Cracking of Metals*, R. P. Gangloff and M. B. Ives, Eds., NACE, Houston, TX, 1990, pp. 139-165.
- [19] Parkins, R. N., in *Stress Corrosion Cracking - The Slow Strain-Rate Technique*, ASTM STP 665, G. M. Ugiansky and J. H. Payer, Eds., ASTM, West Conshohocken, PA, 1979, pp. 5-25.
- [20] Evans, J. T., *Acta Metallurgica*, vol. 25, pp. 805-808, 1977.
- [21] Moskovitz, J. A. and Pelloux, R. M., *Corrosion*, vol. 35, pp. 509-514, 1979.
- [22] Buhl, H., in *The Slow Strain Rate Technique*, ASTM STP 665, G. M. Ugiansky and J. H. Payer, Eds., ASTM, West Conshohocken, PA, 1979, pp. 333-346.
- [23] Bomberger, H. B., Meyn, D. A. and Fraker, A. C., in *Titanium Science and Technology*, G. Lutjering, U. Zwickler and W. Bunk, Eds., Dt Gesellschaft fur Metallk., Germany, vol. 4, 1985, 2435-2454.

- [24] Anderson, D. R. and Gudas, J. P., in *Environment-Sensitive Fracture: Evaluation and Comparison of Test Methods*, ASTM STP 821, S. W. Dean, E. N. Pugh, and G. M. Ugiansky, Eds., ASTM, West Conshohocken, PA, 1984, pp. 98-113.
- [25] Nelson, H. G., Williams, D. P. and Stein, J. E., *Metallurgical Transactions*, vol. 3, pp. 469-475, 1972.
- [26] Curtis, R. E., Boyer, R. R. and Williams, J. C., *Transactions of the ASM*, vol. 62, pp. 457-469, 1969.
- [27] Leckie, H. P., *Corrosion*, vol. 23, pp. 187-191, 1967.
- [28] Williams, D. P. and Nelson, H. G., *Metallurgical Transactions*, vol. 3, pp. 2107-2113, 1972.
- [29] Andresen, P. L., Gangloff, R. P., Coffin L. F. and Ford, F. P., in *Fatigue 87*, vol. III-A, R. O. Ritchie and E. A. Starke, Jr., Eds., EMAS, West Midlands, UK, 1987, pp. 1723-1751.
- [30] Richey, E., *Microstructure and Strain Rate Effects on the Environment Assisted Cracking of α/β -Ti Alloys in Aqueous Chloride*, PhD Dissertation, University of Virginia, Charlottesville, VA, 1999.
- [31] Evans, D. J., Broderick, T. F., Woodhouse, J. B. and Hoenigman, J. R., *Materials Science and Engineering A*, vol. A213, pp. 37-44, 1996.
- [32] Zhang, X. D., Wiezorek, J. M. K., Baeslack, W. A., Evans, D. J. and Fraser, H. L., *Acta Metallurgica*, vol. 46, pp. 4485-4495, 1998.
- [33] Briggs, R. D., in *Advances in the Science and Technology of Titanium Alloy Processing*, TMS-AIME, Warrendale, PA, 1996, pp. 413-420.s
- [34] E647-95a *Standard Test Method for Measurement of Fatigue Crack Growth Rates*, in *Annual Book of ASTM Standards*, vol. 03.01, ASTM, West Conshohocken, PA, 1999, pp. 577-613.
- [35] Blackburn, M. J., Feeney, J. A. and Beck, T. R., in *Advances in Corrosion Science and Technology*, M. G. Fontana and R. W. Staehle, Eds., Plenum Publishing, New York, NY, 1972, pp. 67-292.
- [36] Haynes, M. J. and Gangloff, R. P., *Journal of Testing and Evaluation*, vol. 25, pp. 82-98, 1997.
- [37] Mauney, D. A. and Starke, E. A., *Corrosion*, vol. 25, pp. 177-179, 1969.
- [38] Fager, D. N. and Spurr, W. F., *Transactions of the ASM*, vol. 61, pp. 283-292, 1968.
- [39] Aitchison, I. and Cox, B., *Corrosion*, vol. 28, pp. 83-87, 1972.
- [40] Schutz, R. W., in *Stress Corrosion Cracking*, R. H. Jones, Ed., ASM International, Materials Park, OH, 1992, pp. 265-297.
- [41] Ginter, T. J., Cornell, B. L. and Bayha, T. D., *Characterization of Ti-6Al-2Sn-2Zr-2Mo-2Cr*, Report No. WL-TR-4128, Air Force Research Laboratory, Wright Patterson Air Force Base, OH, 1997.
- [42] Wilson, A. W. and Howe, J. M., *Metallurgical and Materials Transactions A*, vol. 29A, pp. 1585-1592, 1998.
- [43] Richey, E and Gangloff, R. P., "Microstructure-Dependent Environment Assisted Cracking of α/β Ti-6Al-2Sn-2Mo-2Zr-2Cr-Si", *Metallurgical and Materials Transactions*, in review, 2000.

- [44] Akhurst, K. N. and Baker T. J., *Metallurgical Transactions. A*, vol. 12A, 1059-1070, 1980.
- [45] Kolman, D. G. and Scully, J. R., *Journal of the Electrochemical Society*, vol. 143, pp. 1847-1860, 1996.
- [46] Shah, K. K. and Johnson, D. L. in *Hydrogen in Metals*, I. M. Bernstein and A. W. Thompson, Eds., ASM International, Materials Park, OH, 1974, pp. 475-481.
- [47] Kolman, D. G., Gaudett, M. A. and Scully, J. R., *Journal of the Electrochemical Society*, vol. 145, pp. 1829-1840, 1998.
- [48] Kolman, D. G. and Scully, J. R., *Philosophical Magazine A*, vol. 79, pp. 2313-2338, 1999.
- [49] Blackburn, M. J. and Williams, J. C., *Transactions of the ASM*, vol. 62, pp. 398-409, 1969.
- [50] Kolman, D. G., *Passivity and Bare Surface Electrode Kinetics on β -Titanium Alloys in Aqueous Chloride Solution and Their Relevancy to Environmentally Assisted Cracking*, Ph.D. Dissertation, University of Virginia, Charlottesville, VA, 1995.
- [51] Simonen, E. P., Jones, R. H. and Danielson, M. J., *Corrosion Science*, vol. 34, pp. 899-914, 1993.
- [52] Johnson, H. H., in *Hydrogen in Metals*, I. M. Bernstein and A. W. Thompson, Eds., ASM International, Materials Park, OH, 1974, pp. 35-49.
- [53] Toribio, J. and Kharin, V., *Fatigue and Fracture of Engineering Materials and Structures*, vol. 20, pp. 729-745, 1997.
- [54] Pasco, R. W., Sieradzki, K. and Ficalora, P. J., in *Embrittlement by the Localized Crack Environment*, R. P. Gangloff, Ed., TMS-AIME, Warrendale, PA, 1984, pp. 375-381.
- [55] Tien, J. K., Nair S. V and Jensen, R. R., in *Hydrogen Effects in Metals*, I. M. Bernstein and A. W. Thompson, Eds., TMS-AIME, Warrendale, PA, 1981, pp. 37-56.
- [56] Hutchinson, J. W., *Journal of the Mechanics and Physics of Solids*, vol. 16, pp. 13-31, 1968.
- [57] Rice, J. R. and Rosengren, G. F., *Journal of the Mechanics and Physics of Solids*, vol. 16, pp. 1-12, 1968.
- [58] Lidbury, D. P. G., in *Embrittlement by the Localized Crack Environment*, R. P. Gangloff, Ed., TMS-AIME, Warrendale, PA, 1984, pp. 149-172.
- [59] McMeeking, R. M., *Journal of the Mechanics and Physics of Solids*, vol. 25, pp. 357-381, 1977.
- [60] Rice, J. R., Drugan W. J.s and Sham T-L., in *Fracture Mechanics: 12th Conference, ASTM STP 700*, P.C. Paris, Ed., ASTM, West Conshohocken, PA, 1980, pp. 189-221.
- [61] Mayville, R. A., Warren T. J. and Hilton, P. D., in *Fracture Mechanics: Perspectives and Directions (Twentieth Symposium)*, ASTM STP 1020, R. P. Wei and R. P. Gangloff, Eds., ASTM, West Conshohocken, PA, 1989, pp. 605-614.
- [62] Sanderson, G., Powell, D. T and Scully, J. C., in *Fundamental Studies of Stress Corrosion Cracking*, R. W. Staehle, A. J. Forty and D. van Rooyen, Eds., NACE, Houston, TX, 1967, pp. 638-649.

- [63] Webb, T. W. and Meyn, D. A., in *Fracture Mechanics: 26th Volume, ASTM STP 1256*, W.G. Rueter, J. H. Underwood and J. C. Newman, Eds., ASTM, West Conshohocken, PA, 1997, pp. 678-712.
- [64] Tsai, M. M., *Lengthening Kinetics of (0110) γ Hydride Precipitates in α Titanium*, M.S. Thesis, University of Virginia, Charlottesville, VA, 1994.
- [65] Young, L. M., *Environment Assisted Cracking in β -Titanium Alloys*, M.S. Thesis, University of Virginia, Charlottesville, VA, 1993.
- [66] Oriani, R. A. and Josephic, P. H., *Acta Metallurgica*, vol. 22, pp. 1065-1074, 1974.
- [67] Young, L. M., *Crack Growth and Hydrogen Uptake in Environment Assisted Cracking in AA 7050*, PhD Dissertation, University of Virginia, Charlottesville, VA, 1999.
- [68] Tsai, M. M., *Determination of the Growth Mechanism of γ TiH in α -Ti Using High Resolution and Energy Filtered Transmission Electron Microscopy*, PhD Dissertation, University of Virginia, Charlottesville, VA, 1997.
- [69] Efron, A., Lifshitz, Y. and Lewkowicz, I., *Journal of the Less Common Metals*, vol. 153, pp. 23-34, 1989.
- [70] Somerday, B. P., *Metallurgical and Crack Tip Mechanics Effects on Environment Assisted Cracking of Beta-Ti Alloys in Aqueous Chloride*, Ph.D. Dissertation, University of Virginia, Charlottesville, VA, 1998.

**INTERNAL HYDROGEN EMBRITTLEMENT OF ULTRAHIGH
STRENGTH AERMET[®] 100 STEEL**

R.L.S. Thomas, J.R. Scully and R.P. Gangloff

Department of Materials Science and Engineering
University of Virginia
Charlottesville, VA 22904-4745
USA

Internal Hydrogen Embrittlement of Ultrahigh Strength AerMet[®]100 Steel

Richard L.S. Thomas, John R. Scully and Richard P. Gangloff

Center for Electrochemical Science and Engineering
Department of Materials Science and Engineering
University of Virginia
Charlottesville, VA 22904-4745
USA

ABSTRACT

Near-peak aged AerMet[®]100 is susceptible to severe internal hydrogen embrittlement (IHE) at 23°C, if a sufficient-diffusible hydrogen content is present, compromising the high toughness of this ultrahigh strength steel. Evidence includes the threshold stress intensity for subcritical IHE (K_{TH}) as low as 10% of the plane strain fracture toughness (K_{IC}), and a fracture mode transition from microvoid coalescence to brittle-transgranular cracking apparently along martensite lath interfaces and cleavage planes. The K_{TH} decreases from K_{IC} of 132-143 MPa \sqrt{m} to 12 MPa \sqrt{m} , and the amount of brittle-transgranular fracture increases to near 100%, as the concentration of diffusible H increases from essentially 0 to 8 wppm, with severe embrittlement in the 0-2 wppm H regime. IHE is time dependent, evidenced by increasing K_{TH} with increasing dK/dt and K -independent subcritical crack growth rates, and attributed to diffusional-H repartition from reversible trap sites to the stressed crack tip. The partition distance is $\sim 1 \mu m$, consistent with the fine-scale microstructure of AerMet[®]100. The causes of the susceptibility of AerMet[®]100 to TG IHE are very high crack tip stresses and a reservoir of mobile H trapped reversibly at $(Fe,Cr,Mo)_2C$ precipitates. These factors enable repartition of H to misoriented martensite lath interfaces and interstitial sites near cleavage planes, with each prone to decohesion along a connected path. Predissolved H also reduces the ductile-fracture toughness of AerMet[®]100 at high loading rates, perhaps due to reduced void growth caused by H trapped strongly at undissolved metal carbides.

INTRODUCTION

AerMet[®]100, a secondary hardening quenched and tempered martensitic steel, was developed for high performance aerospace applications [1-5]. Composition and heat treatment were optimized for ultrahigh tensile yield strength ($\sigma_{YS} \sim 1750$ MPa) and outstanding plane strain fracture toughness ($K_{IC} \sim 130$ MPa \sqrt{m}) [6-12]. An electroplated coating is used for corrosion resistance, but atomic hydrogen (H) can be co-deposited in the plating and steel substrate [13-14]. Thermal treatment ("baking") may reduce this dissolved H; however, the effectiveness was questioned for steels such as AISI 4340 [13-15]. The dissolved H content increases in the early stage of baking and a considerable amount remains in the steel substrate after prolonged heating. The 1-5 wppm level of dissolved H typical of Cd electroplating and subsequent baking embrittles high strength AISI 4340 [15]. To exploit the high σ_{YS} - K_{IC} properties of AerMet[®]100, it is necessary to understand and control H uptake, outgassing, and embrittlement.

Hydrogen Embrittlement of Ultrahigh Strength Steels

Ultrahigh strength steels (UHSS) are susceptible to severe internal hydrogen embrittlement (IHE), as well as hydrogen environment embrittlement (HEE), from precharged and environmental sources of H, respectively [16-39]. This time dependent subcritical cracking in martensitic steels such as AISI 4340 is typically intergranular (IG) along prior austenite grain boundaries, at apparent threshold stress intensity (K_{TH}) levels approaching 10 MPa \sqrt{m} , and crack growth rates (da/dt) up to 10^4 $\mu\text{m/s}$ [34,36,39]. The K_{TH} for IG IHE and HEE decreases, and da/dt increases, in response to increasing steel σ_{YS} [23,24,32,34], dissolved-H concentration [19,21,26,27,32,34], and impurity content [28-31]. The da/dt is directly proportional to the trap-sensitive effective diffusivity of H (D_H) for IHE and HEE in a wide range of high strength alloys, but crack tip diffusion distances are different and surface reaction kinetics can dominate rates of HEE [36]. The mechanism for IG hydrogen cracking likely involves reduced boundary cohesion due to segregated H and impurities such as S, P, Sb, or Sn [21,22,28,29].

Modern UHSS may resist IG hydrogen embrittlement through composition control. Olson speculated that IG hydrogen cracking is eliminated by rare-earth element additions that reduce grain boundary impurity segregation in UHSS [40,41]. However, micromechanical models of grain boundary decohesion suggest that H trapping and high stress at a crack tip are sufficient to promote hydrogen embrittlement without a dominant impurity contribution [21,23,24,32,36,42]. For example, 18Ni Maraging steels contain only trace levels of P, S, Si and Mn, but are susceptible to

severe IG IHE and HEE [19,20,35]. AerMet[®]100 is produced by double-vacuum melting to yield ultra-low S and P levels, and neither Mn nor Si are added, in contrast to AISI 4340 or 300M. Data suggest that AerMet[®]100 is prone to only limited IG HEE in acids and near-neutral chloride solutions with cathodic polarization, certainly much less so than less pure UHSS [43-51]. The susceptibility of AerMet[®]100 to IG IHE is not established.

Time dependent IHE and HEE can occur along transgranular (TG) paths in steels [20,24,37,38], including martensite interfaces [29,33,52,53] and cleavage planes [54-56]. Interface cracking may be governed by decohesion and cleavage cracking may occur due to a reduction in the work of fracture, both traced to dissolved H [54]. Changing environmental variables and predissolved-H content affect an IG to TG crack path change, as illustrated by the effect of temperature on HEE of 18Ni Maraging steel [33] and H-partitioning modeling [57]. Subcritical TG cracking occurs in high purity steels, but at K_{TH} levels higher than those for IG H-cracking, at least in moderate strength steels [29,30]. Substantial TG HEE was reported for peak aged AerMet[®]100 at low K_{TH} [43-51]. The susceptibility of AerMet[®]100 to TG IHE is not established.

In addition to subcritical cracking, dissolved H can reduce the initiation-fracture toughness of steel (K_{IC} and K_C), without affecting a change in the ductile-fracture mode [28,58,59]. The mechanism involves H-enhanced particle-matrix interface decohesion for enhanced microvoid nucleation [59], H-enhanced flow localization for enhanced microvoid growth and coalescence [60-62], and/or slip plane decohesion [28,53]. This H damage is characterized for moderate strength steels [58], but has not been investigated for UHSS such as AerMet[®]100.

Effect of H Trapping on IHE in UHSS

Research paralleling the present study established that H trapping is extensive in AerMet[®]100, as evidenced by an order of magnitude lower and H-concentration dependent D_H at 20-200°C, as well as 5-fold higher H uptake, compared to martensitic AISI 4130 [63]. Considering the complex microstructure of peak aged AerMet[®]100, reversible-H trapping is likely at coherent M_2C interfaces, dislocations, and low-misorientation martensite interfaces; and H could trap at Ni or Co solute (clusters) if present in martensite. Strong-reversible and irreversible trapping occurs at incoherent alloy carbides and highly misoriented interfaces. Precipitated austenite at martensite lath interfaces could further slow H transport and increase total-dissolved H content. The binding energies for H trapping in AerMet[®]100 are approximate due to the multiplicity of possible microstructural sites [63].

Extensive H trapping can increase or decrease the hydrogen susceptibility of steel [64,65]. Embrittlement was reduced by strong H trapping at TiC particles in HSLA steel [66], VC in 2¼-1Mo-0.3V [67] and PdAl in PH 13-8 Mo stainless steel [68,69]. In general a homogeneous distribution of strong (irreversible) traps may increase resistance to cracking by shielding H segregation to the crack tip stress field and lower H-binding energy sites that are interconnected and susceptible to decohesion. This is particularly true if a finite quantity of H is available, as typical of IHE [67]. In contrast weak (reversible) traps can provide a reservoir of mobile (or “diffusible”) H to supply the crack tip fracture process zone (FPZ) and decrease resistance to IHE. For example, K_{TH} for IHE in AISI 4135-type steels decreased as the concentration of diffusible H increased [27,34]. Crack growth along prior-austenite grain boundaries occurred at a finite rate, indicating that H repartitioning to the FPZ was required. The importance of these competing contributions of H trapping in AerMet®100 has not been established for IHE and HEE, but the large concentrations of diffusible and total H achieved in this steel subjected to modest electrochemical charging conditions and presumably Cd electroplating are cause for concern [63].

Research Objective

The objective of this research is to characterize and understand the effects of predissolved and trapped H on the cracking resistance of modern UHSS, particularly AerMet®100. Fracture mechanics methods are utilized to measure the threshold stress intensity for the onset of subcritical crack growth in H-precharged specimens stressed in air at 23°C. Loading rate is varied to probe the kinetics of cracking. Scanning electron microscopy (SEM) is employed to characterize the fracture mode as a function of dissolved H concentration and loading rate. The results are interpreted based on microstructure-dependent reversible and irreversible H trapping [63], coupled with micromechanical modeling [36].

MATERIAL AND PROCEDURE

Material

Forged bar (15.2 cm diameter and 30.5 cm long) of AerMet®100 was obtained in the annealed condition with the composition shown in Table I. Specimens were vacuum heat-treated to optimize strength and toughness [7,70]: solution treat at 885°C for 1 h, air cool to room temperature in 2 h or less, chill at -73°C for 1 h, and age at 482°C for 5 h. The total H content and mechanical properties resulting from this heat treatment are given in Tables I and II, respectively,

and are typical of commercial practice [70,71].

Table I. Chemical Composition of AerMet®100 (wt%)

Fe	Co	Ni	Cr	Mo	C	Ti	P	S	H (wppm)	
Bal.	13.43	11.08	3.00	1.18	0.23	0.009	.003	.0008	0.26	0.35 ⁺

⁺ Replicate measurements of total H content, $C_{H,tot}$, using vacuum extraction at 600°C

Table II. Mechanical Properties of AerMet®100

HRC	σ_{YS} MPa	σ_{UTS} MPa	RA (%)	Strain Hardening Exponent ⁺ (1/n)	E GPa	σ_0 MPa	K_{JIC} ¹ MPa√m
54	1765	1985	61	0.03	194.4	1985	132 143 [LR] 127 [CR]

⁺ 1/n was determined by fitting true stress, σ , vs. true-total strain, ϵ , with the Ramberg-Osgood equation:

$$\frac{\epsilon}{\epsilon_0} = \frac{\sigma}{\sigma_0} + \alpha \left(\frac{\sigma}{\sigma_0} \right)^n; \text{ where } \alpha = 1.0, \epsilon_0 \text{ is reference strain } (\epsilon_0 = \sigma_0/E), E \text{ is elastic modulus, and } \sigma_0 \text{ is reference stress.}$$

Extensive transmission electron microscopy (TEM) has been conducted relevant to this condition of AerMet®100 [7-12], and results by Ayer and Machmeier provide the microstructural basis for the present study [7].² Specifically, prior austenite grain size was 11 μm with all resolvable-retained austenite eliminated by cryogenic treatment. Spherical carbides $\{(\text{MoCr})_7\text{C}_3, (\text{FeCr})_x\text{C}_y, \text{TiC}, (\text{TiCrMo})\text{C}\}$ sized between 40 and 85 nm in diameter} were present after solution treatment and not affected by aging [7,8]. The proportion of each carbide is uncertain for the present study since the former two compositions are promoted by solution treatment at 875°C and the latter two by heating at 900°C [8]. The martensite was reported to contain 0.15 μm thick laths separated by highly misoriented boundaries and not recovered [7]. Aging resulted in a homogeneous distribution of coherent $(\text{Cr,Fe,Mo})_2\text{C}$ rods (3 nm x 8 nm at ~1 volume pct), without

¹ In the LR orientation, the Mode I stress is parallel to the longitudinal (L) axis of the forged bar and crack growth is in the radial (R) direction. For CR, stress is parallel to the bar circumference (C) and crack growth is in the R direction. K_{JIC} was determined by elastic-plastic analysis and is not necessarily equal to K_{IC} from standardized-elastic analysis; however, differences are likely small for this specimen geometry of AerMet®100 [72,73].

² The AerMet®100 composition, product form and heat treatment employed by Ayer and Machmeier are identical to those of the present study with the following minor exceptions [7]. Their forged bar was rolled to a thickness of 2.1 cm compared to 15.2 cm, solution treatment was at 843°C vs 885°C, and quenching was in oil rather than air. The σ_{YS} - K_{JIC} combination was 1740 MPa and 168 MPa√m [7] compared to 1760 MPa and 132-143 MPa√m for the present study. Higher solution treatment temperature should produce higher K_{JIC} [8] rather than the lower value in Table II. The reason for this difference is not known, but may be traced to measurement variability.

cementite but with some solute zones [7,71]. A thin (~3 nm) layer of precipitated austenite likely formed along lath interfaces, but the amount between 0.5 and 4 volume pct is controversial [7,12].

Determination of K_{TH}

Compact tension (CT) specimens were machined in the LR orientation, with a width (W) of 38.1 mm, notch length of 15.2 mm, and thickness (B) of 2.8 mm. Each specimen was heat treated, ground to a 600-grit surface finish, and fatigue precracked in moist air under decreasing-maximum stress intensity, K_{max} , from 27 MPa \sqrt{m} to 11 MPa \sqrt{m} at constant stress ratio ($R = K_{max}/K_{min}$) of 0.10 and final crack length-to-width (a/W) ratio of 0.50.

In preparation for IHE testing, each CT specimen was precracked in moist air then H-charged for 360 h at 60°C in deionized and preelectrolyzed water (18.2 M Ω resistivity) saturated with Ca(OH)₂ at pH 12.1. Cathodic overpotential for H production (η_{chg}) was varied to produce a range of diffusible and total H concentrations. For calibration, electrochemical experiments established that the total H concentration ($C_{H,tot}$), measured by hot-vacuum extraction at 600°C, depended on applied η_{chg} according to [63]:

$$C_{H,tot} \text{ [wppm]} = -32.5 \eta_{chg} + 11.4 \text{ [V]} \quad (1)$$

for $-0.62 < \eta_{chg} < -0.07$ V and a charging temperature of 60°C. Electrochemical extraction measurements using the Barnacle Cell and presented in Fig. 1 establish the relationship between diffusible H concentration ($C_{H,diff}$) at 23°C and η_{chg} for AerMet[®]100 exposed in saturated Ca(OH)₂ solution at 60°C (o) compared to extensive data (•) for charging at 23°C [63]. Environment temperature has a nil to small effect on $C_{H,diff}$, and all data between $-0.7 < \eta_{chg} < -0.2$ V in Fig. 1 were used to calibrate the 23°C-diffusible H content vs applied overpotential:

$$C_{H,diff} \text{ [wppm]} = -10.8 \eta_{chg} + 0.8 \text{ [V]} \quad (2)$$

For $\eta_{chg} < -0.7$ V, $C_{H,diff}$ was essentially constant at 7.6 wppm for charging at 23°C and presumably also at 60°C. All H concentrations for CT specimens charged at 60°C were calculated using applied η_{chg} in conjunction with Eq. 1 and 2, or the limiting-horizontal trend line in Fig. 1.³

³ The H detection limits of the vacuum (~0.1 wppm) and electrochemical (0.3 wppm) extraction methods are governed by spurious background signals such as material-environment sensitive oxygen reduction in the Barnacle Cell. The diffusible H content of uncharged AerMet[®]100 is not measurable since this cathodic background current obscures the anodic signal produced by oxidation of a diffusible H content of 0.3 wppm or less. The $C_{H,diff}$ is most probably 0 since such mobile H is lost to the surroundings when the alloy is aged in air at 482°C for 5 h [63], consistent with the low $C_{H,tot}$ of 0.26-0.35 wppm, Table 1.

Each fatigue cracked and H-precharged CT specimen was stressed under rising crack-mouth opening displacement (δ) to determine the K_{TH} at the initiation of stable crack growth. This K_{TH} likely equals the apparent threshold values measured in decreasing K or constant load experiments, provided that the alloy is susceptible to hydrogen embrittlement and the effect of stress intensity rate (dK/dt) is considered, as demonstrated for IHE of steels with $\sigma_{YS} > 1000$ MPa [74] and HEE of AerMet[®]100 [43,48,51]. Testing was performed with a closed-loop servoelectric tensile machine operated in δ -feedback control at a constant δ rate varied between 1.8×10^{-6} and 0.18 mm/s. This range corresponded to dK/dt between 2.2×10^{-4} and 27 MPa $\sqrt{m/s}$ for the precrack used and prior to the onset of crack growth. The δ was measured using a displacement gage across the notch mouth. Crack length was measured using the direct current potential difference (dcPD) technique [75]. The applied current was maintained constant at 2.000 ± 0.002 A and voltage across the crack plane was amplified by 10^4 with very low noise. Current-polarity switching eliminated thermal voltages and electrically isolated grips eliminated current diversion from the specimen. An uncracked reference-CT specimen of AerMet[®]100 was used to minimize changes in the dcPD signal unrelated to crack growth. Discrete values of dcPD, load (P), time (t), and δ were acquired continuously during testing by a computer, and typical results are presented in Fig. 2a. Crack length, a , was calculated from dcPD using an established calibration for the CT specimen [75] and corrected based on post-test measurements.

The elastic-plastic J-integral was determined for each crack length using the P vs. δ relationship (Fig. 2a) and unloading-elastic compliance calculated from dcPD-measured crack length without actual unloading [72,73]. The plastic component of J ($J_{plastic}$) at initiation was small for all H-charged samples and elastic stress intensity analysis was sufficient for K_{TH} . $J_{plastic}$ was significant for H-free CT samples, and the elastic-plastic fracture toughness (K_{JIC}) was determined using the 0.2 mm-offset blunting line [72,73]. K_{TH} was defined as the stress intensity at which hydrogen-induced crack growth initiated using the convention demonstrated in Fig. 2b. The regions of dcPD data prior to (baseline) and after the approximate crack-growth initiation (crack growth) were fit by linear regression and the intersection was defined as initiation. This initiation point from dcPD was always consistent with that given by the first-resolved deviation from linearity in the elastic part of the P vs. δ curve (vertical arrow in Fig. 2b).

RESULTS

Effect of Dissolved H on K_{TH} in AerMet[®]100

Predissolved H degrades the subcritical fracture resistance of AerMet[®]100. Figure 3 compares crack growth resistance data for CT specimens with $C_{H,diff} \sim 0$ vs. 7.6 wppm stressed initially at $dK/dt = 0.2$ and 2.2×10^{-4} MPa $\sqrt{m/s}$, respectively. For the as-received case with $C_{H,diff} \sim 0$ wppm (footnote 3), the plane strain K_{JIC} equals 143 MPa \sqrt{m} , followed by stable tearing under rising K. In contrast for $C_{H,diff} = 7.6$ wppm, cracking initiates at $K_{TH} < 15$ MPa \sqrt{m} and the resistance to stable growth is essentially zero.

The IHE resistance of AerMet[®]100 decreased substantially with increasing H content. The results of slow-rising δ ($dK/dt = 2.2 \times 10^{-4}$ MPa $\sqrt{m/s}$) experiments in Figs. 4a and b show K_{TH} as a function of diffusible and total-dissolved H concentrations, respectively. The stress intensity at the onset of crack growth decreased strongly, from K_{JIC} of 132-143 MPa \sqrt{m} to K_{TH} less than 30 MPa \sqrt{m} for $C_{H,diff}$ between 0 and 1 wppm ($C_{H,tot}$ between 0.26-0.35 and 10 wppm). K_{TH} decreased to less than 15 MPa \sqrt{m} as $C_{H,diff}$ increased to 7.6 wppm ($C_{H,tot} = 55$ wppm). Testing with replicate specimens containing $C_{H,diff}$ of 0, 0.5, 3.9-4.0, 5.9, and 7.6 wppm confirmed experimental reproducibility. The two lowest diffusible H concentrations plotted in Fig. 4a (0.8 wppm at applied η_{chg} of 0 V from Eq. 2, and 0.5 wppm at $\eta_{chg} = +0.13$ V) are estimates because the calibration measurements in Fig. 1 were limited to overpotentials less than -0.2 V. For underpotential deposition of H at $\eta_{chg} = +0.13$ V, Eq. 2 predicts that $C_{H,diff}$ is < 0 wppm, a physical impossibility. This lowest concentration is assumed to equal 0.5 wppm based on an upper bound trend line parallel to the regression line in Fig. 1.

Effect of Dissolved H Concentration on the IHE Fracture Mode in AerMet[®]100

Dissolved H in AerMet[®]100 caused a microscopic-fracture mode transition that paralleled decreasing K_{TH} . Figure 5 shows SEM images of the fracture surfaces corresponding to the data in Fig. 3. Fracture in H-free AerMet[®]100 at high K_{JIC} occurred by microvoid coalescence (MVC) over the entire crack surface (Fig. 5a). Two void-size populations are present (arrow), suggesting primary void nucleation at large particles coupled with void sheeting at small particles [76]. In contrast the reduction in crack growth resistance due to $C_{H,diff}$ of 7.6 wppm correlates with a brittle transgranular crack path, with limited IG features and no microvoids, as shown in Fig. 5b.

The brittle-TG character of the crack in AerMet[®]100 intensified with increasing hydrogen content, correlating with decreasing K_{TH} . This trend is illustrated in Fig. 6. The amount of MVC

declined to 0 as $C_{H,diff}$ increased from 0 to 0.8 wppm, corresponding to the sharp decline in K_{TH} from K_{JIC} in Fig. 4a. Limited brittle-transgranular features (arrows) were distributed with a majority of MVC for the specimen containing $C_{H,diff}$ of ~ 0.5 wppm (Fig. 6a), and conversely, microvoids were not apparent on the fracture surface of the 0.8-wppm case, Fig. 6b. Brittle-transgranular features are arrowed and voids of the sort shown in Fig. 5a are not observed. The TG H-crack morphology is unchanged with further increases in $C_{H,diff}$, as illustrated in Figs. 6c and 6d for the 2.1 and 5.9 wppm diffusible H cases. Intergranular cracking occurred only for $C_{H,diff}$ above 4 wppm and in a limited amount.

Brittle-transgranular cracking typical of the low- K_{TH} plateau regime in Fig. 4 is complex and involves at least 2 H-promoted processes. Figure 6c shows arrowed regions suggestive of martensite lath interface cracking; this type of feature is shown in higher magnification in Fig. 7a. While laths are about $0.15 \mu m$ thick, width and length are unclear [7], and cracking may involve multiple lath interfaces in a similar orientation to explain the μm -level features in Figs. 6 and 7a. The lower magnification images in Figs. 6b-6d show large faceted regions suggestive of crystallographic or cleavage-like cracking through prior austenite grains and martensite packets. Such features are shown (arrows) in Fig. 7b along with IG facets, and a TG facet is imaged at high magnification in Fig. 7c. Substructure is not apparent on TG facet surfaces.

Effect of dK/dt on K_{TH} in AerMet[®]100

Brittle H-enhanced TG fracture persists in precharged AerMet[®]100 over a wide range of loading rates. The effect of the initial-applied dK/dt on K_{TH} in AerMet[®]100 with $C_{H,diff} = 3.9$ wppm is shown in Fig. 8. Measured K_{TH} was similarly low, below $22 \text{ MPa}\sqrt{m}$ or 15% of K_{JIC} , for all dK/dt from 0.0002 to $0.3 \text{ MPa}\sqrt{m/s}$. This low K_{TH} at $dK/dt < 0.3 \text{ MPa}\sqrt{m/s}$ correlated with brittle TG fracture, identical to that in Figs. 6 and 7 and unaffected by applied dK/dt .

For H-precharged AerMet[®]100 stressed at higher dK/dt , to $25 \text{ MPa}\sqrt{m/s}$, K_{TH} increased abruptly to $55 \text{ MPa}\sqrt{m}$, but less than K_{JIC} for H-free steel. The K_{TH} values at high dK/dt in Fig. 8 appear independent of loading rate, typical of time-independent H damage.⁴ At $dK/dt > 0.6 \text{ MPa}\sqrt{m/s}$, brittle TG fracture was replaced by MVC fracture correlating with increasing K_{TH} . Figure 9 shows SEM images of the fracture surface of H-charged and H-free AerMet[®]100 stressed

⁴ Recent results show that the K for the onset of stable crack growth continues to be substantially less than K_{JIC} for H-precharged specimens subjected to dK/dt up to $2000 \text{ MPa}\sqrt{m/s}$ [77]. However, considering this larger range of loading rates and additional data, the critical K increases monotonically with increasing dK/dt rather than the plateau suggested in Fig. 8.

at high dK/dt . Microvoid size is substantially smaller for high- dK/dt loading of the H-precharged microstructure (Fig. 9b) compared to the H-free case (Fig. 9a). The large voids typical of H-free steel were not observed for fast- dK/dt ($> 0.6 \text{ MPa}\sqrt{\text{m/s}}$) cracking in H-precharged AerMet[®]100. For MVC at high dK/dt in Fig. 8, the K at the onset of stable crack growth is reasonably viewed as H-lowered K_{JIC} rather than K_{TH} for time dependent subcritical cracking.

Explanation of the time dependence and mechanism of H-enhanced MVC in AerMet[®]100 is beyond the scope of the present study. Solution treatment at 885°C dissolves all strengthening carbides and only a fine distribution of spherical carbides $\{(\text{MoCr})_7\text{C}_3, (\text{FeCr})_x\text{C}_y, \text{TiC}, (\text{TiCrMo})\text{C}\}$ sized between 40 and 85 nm in diameter remains [7,8]. In uncharged AerMet[®]100, only the largest carbides likely initiate microvoids. Growth and coalescence of these voids require significant plastic strain, consistent with the high K_{IC} of H-free AerMet[®]100 and the large voids shown in Fig. 9a. The more numerous voids in the H-charged case (Fig. 9b) suggest that trapped H enhanced void nucleation at smaller-sized carbide particles. H-stimulated nucleation of small voids, as well as possible H-enhanced plastic-flow localization [60-62,78], appear to cause intravoid-strain localization that reduces stable-void growth in AerMet[®]100. Localization results in void coalescence at lower strain and fracture at lower applied K [76]. As-charged “in-place” H appears to contribute to reduce the fracture resistance of AerMet[®]100, since cracking by H sensitive MVC occurs in 2 s at dK/dt of $30 \text{ MPa}\sqrt{\text{m/s}}$ (Fig. 8) and 40 ms at $2000 \text{ MPa}\sqrt{\text{m/s}}$ [77]. This is reasonable since the incoherent metal carbides are strong sites for H trapping during precharging [63] and are preferred locations for microvoid nucleation in AerMet[®]100. If diffusion during stressing is necessary for additional H segregation to microvoid sites, then the transport distance is 1 μm or less, as estimated using the approach in an ensuing section. Precharged H promoted lower toughness and reduced void size in ultra-high strength 18Ni Maraging steel, but the damage kinetics and causal mechanism were not established [79].

IHE Test Method Qualification

Characterization of internal hydrogen embrittlement requires control of the crack tip stress state, initial H distribution, and H loss to the surroundings during loading. Results confirm the accuracy and relevance of the present method, and demonstrate that IHE is reversible.

Crack Tip Stress State

Crack growth initiated under plane strain constraint for H-free and H-charged AerMet[®]100.

Finite element and experimental results suggest that crack tip constraint is high and independent of specimen thickness when B exceeds $\beta J_{\text{Applied}}/\sigma_{\text{Flow}}$, where σ_{Flow} is the average of the yield and ultimate tensile strengths and β is a constant [72,73,80]. For ultra-high strength AerMet®100, the thickness necessary for dominant plane strain constraint increases from 0.024 mm for $K = 20$ MPa $\sqrt{\text{m}}$ to 1.0 mm for $K = 130$ MPa $\sqrt{\text{m}}$ using the standard value of $\beta = 25$ [72]. These thicknesses are doubled for the more conservative β of 50 [80]. Since the CT specimen used was 2.8 mm thick, all K_{TH} and K_{JIC} results in Figs. 3, 4, and 8 (as well as in Figs 10 through 12 to follow) were obtained for plane strain crack tip deformation.

Plane strain cracking in AerMet® 100 is supported by experimental observations. The fracture surface, proximate to the center of the CT specimen at the location of crack growth initiation, was always flat and normal to the Mode I load axis as shown by the insert in Fig. 10. The fracture toughnesses obtained from the K vs. Δa data in Fig. 3 are 130 MPa $\sqrt{\text{m}}$ at the first detection of crack extension (K_{JICi} as defined in [73]), and 143 MPa $\sqrt{\text{m}}$ from the offset-blunting line definition, K_{JIC} [72]. A duplicate test yielded $K_{\text{JICi}} = 100$ MPa $\sqrt{\text{m}}$ and $K_{\text{JIC}} = 132$ MPa $\sqrt{\text{m}}$. These K_{JIC} values bracket the typical plane strain fracture toughness for AerMet®100 at this strength level and measured using a standard K_{IC} method [2,70].

These results demonstrate that ductile fracture and IHE are characterized effectively using a thin specimen of UHSS coupled with modern fracture mechanics. Elastic-plastic mechanics are of secondary importance due to the small values of J_{plastic} , particularly when H cracking occurs at K below 50 MPa $\sqrt{\text{m}}$. Accurate K_{TH} and K_{JIC} characterization requires precise determination of the onset of crack growth [73]. When K vs Δa rises steeply as in Fig. 10, small uncertainty in initiation determination results in substantial error in K_{TH} or K_{JICi} . The dcPD method effectively detects crack initiation. As such, the K_{TH} and K_{JIC} results in Figs. 3, 4, and 8 are accurate, and relevant to IHE in thick geometries. It is likely that an even thinner CT specimen (~1 mm thick) will exhibit high constraint and facilitates uniform-H charging.

Specimen Charging Time

Trap-affected H diffusivity for peak aged AerMet®100 is slow and prolonged exposure time is required to establish a uniform distribution of dissolved H in a CT specimen. The D_{H} in AerMet®100 at 60°C decreased from 7×10^{-8} cm²/s to 2×10^{-8} cm²/s as $C_{\text{H,diff}}$ decreased from 8 wppm to 2 wppm [63]. These values represent H diffusivity during H egress, after irreversible traps are filled and governed by H interaction with reversible traps. The D_{H} with unfilled

irreversible traps, typical of H uptake during charging, may be lower; $\sim 5 \times 10^{-9} \text{ cm}^2/\text{s}$ at 60°C .

With this slow diffusivity, the charging time required to produce uniform H concentration in a 2.8-mm thick AerMet[®]100 CT specimen is long. Assuming H uptake only from specimen faces, this time is given by $t = 0.73 (B^2/D_H)$ [27] and equals 130 days. An exposure of 360 h was chosen based on the assumption that the $\text{Ca}(\text{OH})_2$ solution penetrated the fatigue precrack such that H absorption occurred on crack surfaces up to the tip. Crack acidification during charging was assumed negligible given the buffering capability of saturated $\text{Ca}(\text{OH})_2$. For 1-dimensional diffusion into a plane sheet from a fixed-surface concentration (C_S), 360 h produces a H concentration equal to $0.9C_S$ at a depth of $150 \mu\text{m}$ in a direction perpendicular to the fatigue precrack front. This penetration distance is 10-100 times longer than the governing crack tip fracture process distance defined in an ensuing section and the H charging employed is thus sufficient for accurate K_{TH} determination.

The low D_H for AerMet[®]100 resulted in a non-uniform H concentration across the CT specimen thickness, consistent with diffusion calculations. Figure 10 shows a crack growth resistance curve and low magnification SEM fractograph of a specimen charged to a near-surface $C_{H,\text{diff}}$ of 2.1 wppm. Cracking initiated at $K_{TH} = 24 \text{ MPa}\sqrt{\text{m}}$, well below K_{JIC} of 132-143 $\text{MPa}\sqrt{\text{m}}$, and resulted in brittle transgranular fracture of the sort illustrated in Fig. 6c. This TG cracking extended $400 \mu\text{m}$ ahead of the fatigue crack front, and $500 \mu\text{m}$ inward from the specimen surfaces that contacted the solution, as indicated by the white-dashed line in the insert of Fig. 10. As the crack propagated into the central region where H concentration was reduced by limited diffusion during the 360 h charging exposure, the resistance to crack growth increased and the fracture mode changed to MVC. The K vs. Δa curve is intermediate between the two results presented in Fig. 3. The lack of crack-growth resistance for the specimen with $C_{H,\text{diff}} = 7.6 \text{ wppm}$ (Fig. 3) is consistent with uniform charging of H across a larger distance since D_H increases by 5 to 10 times as $C_{H,\text{diff}}$ increases [63].

Since CT specimens were not charged uniformly, it was not possible to determine the effect of hydrogen concentration on subcritical crack growth rate. The high- $C_{H,\text{diff}}$ case in Fig. 3 is an exception and the da/dt vs. K data are presented in Fig. 11 for crack growth within $1,500 \mu\text{m}$ of the fatigue crack tip. The da/dt depends strongly on K in Stage I and is K independent in Stage II. The average Stage II crack growth rate (da/dt_{II}) is $1.6 \times 10^{-5} \text{ mm/s}$ for the applied dK/dt that was employed.

Hydrogen Loss and IHE Reversibility

The slow D_H in AerMet®100 limits H loss during testing. Since a similar-low K_{TH} is apparent for loading times of 0.02 to 20 h (Fig. 8), H loss was not important at even the lowest dK/dt examined for $C_{H,diff}$ of 3.9 wppm and stressing at 23°C.

Measurement of total H concentration in 2.8 mm thick specimens, both immediately after charging and after 60 h in moist air at 23°C, evidenced a reduction in $C_{H,tot}$ of less than 1 wppm. The H egress experiments summarized in Table III provide additional insight pertaining to H loss from AerMet®100. Here, $C_{H,tot}$ in a 1 mm thick specimen declined by 7.2 wppm during a 72 h exposure at 23°C. This loss is from lattice-soluble H and H in lower-binding energy reversible traps [63], as shown by the reduction in $C_{H,diff}$, from 7.5 wppm to an average of 0.45 wppm, accounting for the 7.2 wppm loss in total-dissolved H. Assuming that diffusion distance is proportional to the square root of D_H and exposure time, this degree of H loss in a 1 mm thick specimen is achieved in a 2.8 mm thick CT specimen after a 560 h exposure. This result is qualitatively consistent with the measured 1 wppm H loss from a 2.8 mm thick CT specimen after 60 h at 23°C. These results and a diffusion approximation suggest that the loss of diffusible H shown in Table III is achieved over a distance on the order of the crack tip plastic zone ($\sim 100 \mu m$ at K of 50 MPa \sqrt{m}) in 1 h. However, as H is lost through crack surfaces, it is replenished from the surrounding microstructure. The distribution of H about the crack tip must be established by diffusion modeling that considers trap states interacting with the crack tip stress field [81-83].

Table III. Loss of Total H and Diffusible H from AerMet®100 at 23°C

Condition	$C_{H,tot}$ (wppm) ⁺	$C_{H,diff}$ (wppm) ⁺⁺
As-charged	27.4	7.5
Charged + baked at 23°C for 72 h	20.2	0.1, 0.2, 0.4, 1.1 ⁺⁺⁺

⁺ H was precharged at 60°C and measured by hot-vacuum extraction at 600°C with a 1 mm thick specimen.

⁺⁺ H was precharged at 23°C and measured by electrochemical extraction at 23°C with a 0.6 mm thick specimen.

⁺⁺⁺ Calculated based on the reduced D_H at 23°C and corresponding to $C_{H,tot} = 20.2$ wppm [63].

The internal hydrogen embrittlement of UHSS is generally reversible if dissolved H is removed by outgassing at elevated temperature [17,18]. For maraging steel, K_{TH}/K_{IC} was 0.3 after H charging but 1.0 after charging plus baking at 150°C [19]. The IHE of AerMet®100 is similarly reversible, as demonstrated by Fig. 12. The specimen that was H-charged ($\eta_{chg} = -0.3$ V and $C_{H,diff}$

= 4.0 wppm from Eq. 2) exhibited severe TG embrittlement with $K_{TH} = 15.9 \text{ MPa}\sqrt{\text{m}}$ consistent with the data in Figs. 4a and 8. A similarly charged specimen was heated in moist air at 190°C for 24 h to essentially eliminate all diffusible H, as established by electrochemical extraction and thermal desorption spectroscopy experiments [63]. The fracture resistance of this specimen was restored to that of uncharged AerMet®100 with $K_{JIC} = 123 \text{ MPa}\sqrt{\text{m}}$, or perhaps higher due to variability in dcPD signal that obscured the precise onset of crack growth and magnitude of $J_{Plastic}$.

DISCUSSION

Technological Implications

The results establish that AerMet®100, heat treated for ultra-high strength and optimal fracture toughness, is susceptible to: (1) severe time dependent TG IHE at K_{TH} values well below the H-free K_{IC} for steel stressed at slow to moderate dK/dt , and (2) H-reduced K_{IC} for microvoid fracture at fast loading rates. If H is dissolved in the steel by a manufacturing process or in-service corrosion at a coating breach, then subcritical crack growth could be stimulated and/or ductile fracture resistance reduced, at least locally. Subcritical IHE cracking is the focus of this discussion.

The H-uptake capacity of AerMet®100 is significant for Cd-plated parts. While data are not available for AerMet®100, $C_{H,tot}$ greater than 2 wppm was absorbed by AISI 4130 during Cd-plating [14]. The $\text{Ca}(\text{OH})_2$ solution and polarization conditions that produce this H concentration in martensitic AISI 4130 produce $C_{H,tot} \sim 12 \text{ wppm}$ in AerMet®100 [63]. AerMet®100 is embrittled severely by this level of H; with $K_{TH} < 30 \text{ MPa}\sqrt{\text{m}}$ for a wide range of H concentration (Fig. 4) and dK/dt (Fig. 8). Slow D_H minimizes H penetration in AerMet®100 during electroplating [63], but thermal-outgassing could enhance penetration of H co-deposited in the Cd layer [13-15].

Subcritical IHE Susceptibility of AerMet®100 vs. Other UHSS

The threshold stress intensities for IHE and HEE of quenched and tempered alloy steels generally approach $10 \text{ MPa}\sqrt{\text{m}}$ with increasing σ_{YS} above 1400 MPa, and cracking is intergranular with respect to prior austenite boundaries [34]. The low values of K_{TH} for IHE of near-peak aged AerMet®100 parallel this behavior, but cracking is transgranular as summarized in Table IV. IHE at 23°C is severe in AISI 4340 and 300M steels, with $K_{TH} \sim 8\text{-}20 \text{ MPa}\sqrt{\text{m}}$ at relatively low $C_{H,tot}$. The IHE in the maraging steel is less severe, with $K_{TH} = 30\text{-}38 \text{ MPa}\sqrt{\text{m}}$ at $C_{H,tot} = 2 \text{ wppm}$ and 23°C . Values of hydrogen diffusivity are tabulated since lower D_H correlates with increased-reversible trapping of H that affects IHE, as developed in an ensuing section.

Table IV. Internal Hydrogen Embrittlement of Ultra-High Strength Steels at 23°C

	D_H @ 23°C cm ² /s	σ_{YS} MPa	Mn + Si/2 + P + S Wt %	K_{TH} @ $C_{H,tot}$ (MPa√m, wppm)	Fracture Path	Reference
AerMet®100	2×10^{-8}	1750	< 0.01	28 @ 10 18 @ 20	TG TG	Fig. 4
AISI 4340	2×10^{-7}	1600	0.9	20 @ 3-6 ⁺	IG	[24]
300M	< 10^{-7}	1700	1.7	8 @ 1-2 ⁺	IG	[19,20,84]
18Ni Maraging	2×10^{-9}	1750	< 0.01	38 @ 2 ⁺	IG	[19,20]
		2000	< 0.01	30 @ 2 ⁺	IG	[19,20]

⁺ Assumed measured by hot or melt extraction, representative of $C_{H,tot}$, but not specified [19,20,24,84].

Studies show that AerMet®100 is susceptible to severe hydrogen environment embrittlement [43-51], consistent with the demonstrated IHE severity. Threshold stress intensities were 17-27 MPa√m for specimens subjected to 10,000 h constant displacement or rising-step loading in a 3.5% NaCl solution at open circuit potential [43,45,48,51]. Such cracking was most likely by HEE and occurred by a brittle transgranular mode similar to that shown in Figs. 5b, 6 and 7, with limited regions of IG cracking. A mixture of brittle TG + IG cracking was produced by constant displacement loading of AerMet®100 in concentrated 50% H₂SO₄ + 50% H₃PO₄ (pH = 1), with $K_{TH} = 14$ MPa√m [44].

Approaches to produce H-cracking resistant UHSS by improving the purity of prior austenite grain boundaries are not sufficient [28,40,41,52,53,85]. McMahon argued that segregants such as P, S, Sn and Sb are a requisite for IG cracking because H alone cannot localize sufficiently in the FPZ to enable low- K_{TH} IHE or HEE [28,29]. A correlation showed that HEE is eliminated if a bulk composition parameter ($\psi = \text{Mn} + \text{Si}/2 + \text{P} + \text{S} + 10^4 C_H$) is less than about 0.5 atom pct, at least for moderate strength steels of $800 \text{ MPa} < \sigma_{YS} < 1400 \text{ MPa}$ and tempered martensitic microstructures heated through the temper embrittlement regime [28,29]. Severe IG IHE in AISI 4340 and 300M steels in Table IV is consistent with a high value of ψ . However, ψ is essentially 0 for AerMet®100 and 18Ni Maraging steels, but hydrogen cracking is severe. These results, and the mechanistic scenario in an ensuing section, establish that both IG and TG IHE can occur apart from a dominant impurity effect. The ψ -composition correlation is not accurate.

The explanation for the TG crack path of IHE in AerMet®100 compared to the IG path in 18Ni Maraging steel is uncertain. Each steel exhibits a similar prior austenite grain size (10-20

μm), low-bulk ψ , and strong-H trapping.⁵ The identifiable differences are: (a) martensite laths are larger (0.5-2 μm) in the maraging steel [87,88], compared to a 0.1-0.3 μm average thickness for AerMet®100 [7], (b) the bulk S content of the maraging steel is about 10 times higher than that of modern AerMet®100, and (c) H precharged AerMet®100 was cracked under slow-rising K, while the maraging steel was loaded at fixed δ and falling K. Speculatively, rising- δ loading favors the TG crack path in AerMet®100 because, while the highly stressed process zone is small as K increases from 0 through low K_{TH} levels, a large area of susceptible martensite lath interface is at risk for H embrittlement due to the very small size of the laths. Prior austenite grain boundaries are less likely included in the small FPZ. For maraging steel, the areas of austenite and martensite interface in a small FPZ are more likely of the same order of magnitude, and both could provide a viable crack path. IG cracking would be exacerbated if boundary segregation was pronounced due to the higher S content in maraging steel, but boundary compositions were not measured for either steel. The IHE path in the maraging steel was TG at the initial-high K, but transitioned to IG as K decreased to near K_{TH} [19]. The brittle TG crack path did not change during crack growth in AerMet®100. Research is required to understand the TG and IG crack paths in these steels.

H-Uptake Capacity Dependence of Subcritical IHE

The threshold for IHE of UHSS declines with increasing dissolved H concentration [19,24,26,27,34]. AerMet®100 exhibits this behavior, as shown in Fig. 3 and plotted logarithmically in Fig. 13 as the basis for the following regression relationships:

$$K_{TH} (\text{MPa}\sqrt{\text{m}}) + 40 C_{H,\text{diff}}^{-0.54} (\text{wppm}) \quad (3a)$$

$$K_{TH} (\text{MPa}\sqrt{\text{m}}) + 100 C_{H,\text{tot}}^{-0.49} (\text{wppm}) \quad (3b)$$

Yamakawa reported the trend in Fig. 13a for IG IHE of quenched and tempered AISI 4135 steel ($1300 < \sigma_{YS} < 1600 \text{ MPa}$) with $C_{H,\text{diff}}$ between 0.3 and 16 wppm calculated from the permeation flux of H [27,89]. AerMet®100 and AISI 4135 exhibit approximately the same K_{TH} vs. $C_{H,\text{diff}}$ for concentrations greater than about 5 wppm. At lower $C_{H,\text{diff}}$, K_{TH} for AerMet®100 increases more

⁵ Trapping likely occurs at coherent strengthening precipitates in AerMet®100 ((Mo,Cr,Fe)₂C [7]) and 18Ni Maraging steels (Ni₃Mo + Ni₃Ti [20]), and perhaps at solute (clusters) [63]. The strength of reversible H trapping is higher in the maraging steel, as indicated by the 10-fold lower D_H at 25°C (Table IV), perhaps due to the higher Ni plus Co content of the C-free martensite [63,86].

strongly than that of AISI 4135. The cause of this improved IHE resistance of AerMet® 100 is not established. The Yamakawa correlation used K_{TH} for specimens that were H precharged and stressed in the charging solution, constituting a worst-case combination of IHE and HEE, and an uncertain H distribution at the crack tip [36]. A single K_{TH} (o in Fig. 13a) was reported for IHE only; the result is higher than the threshold for combined IHE and HEE, but less than that for precharged AerMet®100.

The dependence of K_{TH} on the total-dissolved H concentration in AerMet®100 is compared to that for 18Ni Maraging steels in Fig. 13b [19]. AerMet®100 appears more resistant to IHE compared to maraging steel, however this comparison may be compromised. Higher H concentrations are achieved in AerMet®100 compared to those in the maraging steel due to two factors. First, H recombination to benign H_2 is poisoned in $Ca(OH)_2$ to a greater degree than in NaOH, and H uptake is enhanced for a given overpotential [90]. Second, the microstructure of AerMet®100 contains a high density of several H trapping states and large amounts of dissolved H were produced by low to moderate η_{chg} [63]. However, H trapping is even more severe in maraging steel (footnote 5) and $C_{H,tot}$ should be proportionately larger compared to AerMet®100. The lower $C_{H,tot}$ data for the 18Ni Maraging steel in Fig. 13b are opposite to this expectation and raise the concern that H concentration measurements were inaccurate.⁶ Experiments are required using a common electrolyte with accurate measurement of $C_{H,tot}$ and $C_{H,diff}$.

Mechanism of Transgranular Subcritical IHE in Ultra-high Strength Steel

The threshold stress intensity for hydrogen embrittlement of high strength alloys has been modeled micromechanically based on damage by decohesion [21,32,91,92]. Hydrogen concentrates in the crack tip fracture process zone, at locations of high tensile stress and trapping, and lowers the fracture resistance of interfaces or cleavage planes proportionate to the amount of H present [42]. The threshold is the K level required to elevate crack tip stress above the H-reduced fracture strength, over a critical distance [32]. Hydrogen is provided by an environment-specific crack surface concentration for HEE, or the initial-dissolved distribution for IHE, and the kinetics of each is governed by stress driven diffusion of H to damage sites [24,36]. Crack tip stresses are

⁶ 1.3 mm-thick specimens of maraging steel were precharged in 0.1N NaOH at a cathodic current density of 50 mA/cm² for 1 to 20 days, Cd electroplated, baked at 150°C, fatigue precracked, and loaded at fixed displacement to define K_{TH} at crack arrest [19]. The H concentration was calculated from measurements (presumably $C_{H,tot}$ from hot extraction) of precharged cubes that were presumably not Cd plated. The H introduced from the Cd plate during baking, and H loss during testing, were not quantified [14,15].

estimated from continuum or dislocation mechanics [36,42,91,92], and H segregation is inferred from trapping theory [64,78,93-95]. This modeling was applied predominantly to IG hydrogen cracking [28].

Brittle-H cracking in AerMet[®]100 is transgranular at low K for both precharged and environmental sources of H, however, the precise paths are not established. The fractographs in Figs. 6 and 7 suggest that IHE proceeds along martensite lath and packet interfaces, as well as cleavage planes through martensite laths. Martensite interfaces trap H [24,96,97] that could decrease fracture strength by the decohesion mechanism [29,33,52,53]. H promotes cleavage-like cracking parallel to {100} planes in ferrite [54,55], and {110} and {112} in martensite [56]. Cleavage planes were continuous across many laths in a martensite colony due to the crystallographic coincidence of such laths [56], however, laths in AerMet[®]100 are highly misoriented and colonies are not well developed [7].

Figure 14 illustrates the hypothesized factors that promote time-dependent transgranular IHE of UHSS. During charging without stress, H partitions among interstitial sites and reversible plus irreversible traps of varying binding-energy strength [63]. On loading, H drains from these trap states, and repartitions to martensite interface and cleavage fracture sites within the FPZ. This segregated H lowers the intrinsic strength of these features that fracture due to crack tip opening stress. The length scales involved are established by the crack tip stress distribution, H-binding energies and spacings of trap sites, and loading time. These considerations are detailed.

H Accumulation at Equilibrium

At equilibrium, the concentration of H at damage sites in the FPZ (C_H) is established interactively by the lattice concentration of H (C_0), crack tip hydrostatic stress (σ_H), and the binding energy of H trapping at one or more sites.

Stress Enhancement: Hydrostatic tension about the Mode I crack tip lowers the chemical potential of H relative to that dissolved in the unstressed surroundings and creates a driving force for diffusion to the FPZ. Classic-continuum modeling locates the maximum tensile and hydrostatic stresses at 1 to $4\delta_T$ ahead of the crack tip surface, where δ_T is the blunted crack tip opening displacement equaling $K^2/2\sigma_{YS}E$ [42,98-100]. The maximum opening mode stress (σ_{YY}) is $3.4\sigma_{YS}$ [98-100] and σ_H is $2.5\sigma_{YS}$ [32] for a low work-hardening UHSS. For K_{TH} between $15 \text{ MPa}\sqrt{\text{m}}$ and $30 \text{ MPa}\sqrt{\text{m}}$ in Fig. 3, this modeling suggests that the FPZ is located at 1 to $3 \mu\text{m}$ ahead

of the crack tip (based on $2\delta_T$) and σ_H equals 4.4 GPa. The $1-4\delta_T$ distance is illustrated in Fig. 14 for $K = 30 \text{ MPa}\sqrt{\text{m}}$. This FPZ envelops a small volume of the microstructure, less than one prior austenite grain, but a large amount of the martensite and secondary hardening carbides.

The blunt crack solution may not be relevant to an IG or TG crack tip in a hydrogen embrittled alloy; rather, stresses appear to be higher and the FPZ is closer to the crack tip [36]. Gerberich et al. predicted high stresses in an Fe-Si single crystal ($\sigma_{YS} = 300 \text{ MPa}$) [23], using a model of the interaction of elastic stress fields about dislocations in a pileup standing-off from the tip of a sharp crack [101-103]. For $K = 20 \text{ MPa}\sqrt{\text{m}}$, this model predicted that $\sigma_H = 22 \text{ GPa}$ maximized at 20 nm ahead of the tip. Hutchinson and others predicted stress elevation due to hardening by excess and geometrically necessary dislocations that accommodate the strain gradient at the crack tip [104-107]. This work predicted a factor of 3 reduction in the blunted δ_T , increases in σ_{YY} (from $4\sigma_{YS}$ to $10\sigma_{YS}$), and σ_H up to $8\sigma_{YS}$ [105,107]. An alternate formulation of strain gradient plasticity confirmed that crack tip stresses are increased several times above the classic theory, within 30% of the characteristic-material dimension for storage of necessary dislocations in a strain gradient [106]. These modern analyses suggest that σ_H may be as high as 14-22 GPa for IHE of AerMet®100, as recognized qualitatively in the early decohesion theory [21,91].

The lattice-H concentration (C_0) is enhanced by lattice dilation due to σ_H [108]:

$$C_{H\sigma} = C_0 \exp \left[\frac{\sigma_H V_H}{RT} \right] \quad (4)$$

for small elastic strains, an elastically-isotropic lattice that is expanded equally in all directions by dissolved H, and a negligible effect of dissolved H on elastic constants. $C_{H\sigma}$ is the stress enhanced lattice H concentration, V_H is the partial molar volume of H in Fe, $2.0 \text{ cm}^3/\text{mol}$ [58], and R and T have the usual meaning. The effect of hydrostatic tension on H accumulation at a crack tip in an UHSS is substantial. The ratio, $C_{H\sigma}/C_0$, is between 35 and 2×10^5 for σ_H between 4.4 and 15 GPa at 298K. The $V_H\sigma_H$ term in Eq. 4 equals between 9 kJ/mol and 30 kJ/mol for σ_H between 4.4 and 15 GPa. The hypothesis is that H is drained from moderate strength reversible trap sites, with H-binding energies less than these values of $V_H\sigma_H$, and attracted to this crack tip stress field.

H Trapping: Considerable attention has focused on the effect of H trapping on IHE in steel [66,68,69,93,96,109]. The details of H trapping in AerMet®100 were reported in a companion paper and recent report [63,110]. Three trap states were resolved by thermal desorption

spectroscopy (TDS) of H charged AerMet[®]100, with H-to-trap binding energies (E_B) estimated to be 12 kJ/mol, 62 kJ/mol, and 90 kJ/mol [63,110]. It is challenging to identify the microstructural feature corresponding to each binding energy due to the complex microstructure of AerMet[®]100, the possibility that different microstructural features exhibit similar E_B , the uncertain energy of H migration in the alloyed-steel lattice, and the accuracy of desorption energy determinations by TDS. The two high energy states suggest irreversible or strong-reversible trapping associated with undissolved metal carbides as well as highly misoriented prior austenite and martensite (lath and packet) interfaces. The low energy state was ascribed to H trapping at the relatively coherent interfaces of the (Fe,Cr,Mo)₂C strengthening phase, simple dislocation structures, and perhaps individual or clustered solute (Co and Ni) [110]. The dominant site for weak reversible H trapping is critical to IHE. Binding energies were reported to equal 8-10 kJ/mol for Ni and Cr in Fe [93], 18 kJ/mol for coherent VC particles [111,112], and 30 kJ/mol atom for dislocations [113,114]. A systematic study shows that the preexponential term in the temperature dependence of D_H is reduced by solute (Cr, Co, Ni, Mo) addition to Fe, but E_B is not changed [115]. This result suggests that solute is not a trap state, as confirmed by the lack of low E_B trapping in as-quenched AerMet[®]100 with solute but without M₂C precipitates [110]. AerMet[®]100 is unique since the dislocation structure does not recover during aging [7,8,12]. However, a similar high dislocation density is likely present in older UHSS by virtue of low temperature tempering and the lowest-measured E_B for AerMet[®]100 is substantially less than that reported for dislocations (12 vs. 30 kJ/mol). As such, extensive-reversible trapping most likely occurs at (Fe,Cr,Mo)₂C precipitates in AerMet[®]100. These trap sites may be surrounded by an atmosphere of dissolved H such that the outermost H atoms are trapped with lower E_B .

In a closed system with fixed $C_{H,tot}$, homogeneously distributed and strong- E_B trap states impede the flux of mobile H to the FPZ and improve resistance to IHE. Irreversible and strong-reversible H trapping is substantial in AerMet[®]100, as evidenced by the larger $C_{H,tot}$ compared to $C_{H,diff}$ for a given η_{chg} (Fig. 4 and Ref. 63). While this strongly trapped H could be involved in the H effect on MVC, it is relatively immobile and does not shield the FPZ from deleterious H repartitioning during subcritical IHE. If the attraction to the stressed FPZ is stronger than the binding to one or more reversible trap states, then such traps are "drained" of H. If the transport kinetics of this H are rapid, if the diffusion distance is short, or if the time under stress is long, then equilibrium-H partitioning can be assumed. Extensive reversible trapping characterized by the E_B of 12 kJ/mol, plus lattice-dissolved H, provide an important reservoir of mobile H, quantified by

the large levels of $C_{H,diff}$ in AerMet[®]100 compared to older UHSS such as AISI 4130.

Hydrogen-martensite interface binding energies between 25 and 80 kJ/ mol were reported, with higher E_B associated with higher misorientation boundaries [24]. Since the martensite lath boundaries in AerMet[®]100 are often highly misoriented [7], trapping likely occurs with the higher binding energies in this range and these sites are not an important source of mobile H for IHE. Since these interfaces were not embrittled at the higher dK/dt (Figs. 8 and 9), H trapping at this feature during precharging is not sufficient for H damage. However, repartition of H to martensite interfaces in the FPZ, during loading at lower dK/dt , could augment this in-place H to promote interfacial cracking and subcritical TG IHE.

H Repartition: High crack tip stresses and extensive reversible H trapping in AerMet[®]100 support the scenario illustrated in Fig. 14. The E_B of 12 kJ/mol for H trapped at finely distributed alloy carbides in AerMet[®]100 is within the range of the $V_H\sigma_H$ values typical of the crack tip stress field, 9 to 30 kJ/ mol. Hydrogen drains from traps with these E_B , diffuses during stressing to the dilated lattice in the FPZ, and there associates with available trap sites in concentrations dictated by the various E_B . The M_2C precipitates provide the unique reservoir of mobile H to govern IHE of AerMet[®]100.

The total amount of H that segregates to FPZ sites such as martensite lath interfaces depends on the interaction of trapping and stress. Assuming that σ_H elevates C_0 to $C_{H\sigma}$ according to Eq. 4, and that this C_0 is in local equilibrium with the amount of H trapped at a given site, then hydrostatic stress further enhances trapped H according to [24,116,117]:

$$C_{H\sigma,T} = C_0 \exp\left(\frac{E_B + V_H\sigma_H}{RT}\right) \quad (5)$$

For a martensite lath boundary, E_B is 25-80 kJ/mol, and $V_H\sigma_H$ is 9-30 kJ/mol atom for an UHSS. Using a low-bound total energy of 40 kJ/mol in Eq. 5, the total H concentration possibly trapped at a martensite lath interface ($C_{H\sigma,T}$) is $6 \times 10^6 C_0$. The lattice solubility of H in AerMet[®]100 is unknown, but C_0 is 3×10^{-4} wppm for pure iron exposed to 100 kPa H_2 at 298K [58]. This environment produces a hydrogen fugacity equivalent to electrochemical charging at $\eta_{chg} = 0.0$ V [118], and hence equals the lattice solubility for Fe precharged in $Ca(OH)_2$ at zero overpotential. Lattice H solubility may be higher in AerMet[®]100 due to the Ni and Co in solid solution [110,115].

Using this lower estimate of C_o , $C_{H\sigma,T}$ is on the order of 1600 wppm (9 atom pct) at 23°C and for charging at zero overpotential.⁷ Therefore, high hydrostatic tensile stress coupled with reversible trapping are capable of concentrating a large amount of H at crack tip fracture sites such as martensite lath interfaces in AerMet®100. This $C_{H\sigma,T}$ is further increased if the martensite interface is damaged mechanically during stressing to raise E_B . The data in Fig. 4 show that charging at $\eta_{chg} = 0.0$ V ($C_{H,diff} = 0.8$ wppm) resulted in a K_{TH} that was reduced dramatically to 20% of K_{JIC} . This level of severe IHE, produced by a mild H charging condition, is consistent with the predicted substantial enrichment of H in the FPZ of AerMet®100. As η_{chg} is made more negative, H is more highly enriched at martensite lath interfaces due to increased C_o . The data in Fig. 4 show that such enrichment only mildly reduces K_{TH} , suggesting that martensite interface damage is saturated due to the large accumulation of H for 0 overpotential; more H from more negative η_{chg} is unnecessary.

Modeling K_{TH} vs. $C_{H,diff}$ for IHE of AerMet®100: IHE was modeled micromechanically to predict K_{TH} that decreases with increasing H concentration in the FPZ [42]. A recent model, from analysis of dislocation-crack tip interactions that relate the crack tip Griffith toughness to the measured-global K_{IC} , predicts K_{TH} for H-decohesion based TG cleavage fracture [119].

$$K_{TH} = \frac{1}{\beta'_{IHE}} \exp \left[\frac{(k_{IG} - \alpha C_{H\sigma,T})^2}{\alpha'' \sigma_{YS}} \right] \quad (6)$$

In this formulation, the Griffith threshold stress intensity for hydrogen embrittlement, k_{IH} , equals $(k_{IG} - \alpha C_{H\sigma,T})$ where α is a coefficient in units of $\text{MPa}\sqrt{\text{m}}/\text{atom fraction H}$ and $C_{H\sigma,T}$ is the concentration of H localized at the embrittlement site from Eq. 5. The k_{IG} is the critical Griffith stress intensity factor for cleavage fracture without H ($G_C \sim \gamma_s \sim k_{IG}^2/E$), E is elastic modulus, and γ_s is the energy required to produce unit crack surface. The β' and α'' are constants determined by computer simulation of the dislocation structure about the crack tip.

This model explains the measured $C_{H,diff}$ dependence of K_{TH} for AerMet®100 shown in Fig. 4a. In Fig. 15 these K_{TH} are plotted vs. the $C_{H\sigma,T}$ dependent reduction in k_{IG} from Eq. 6. This local

⁷ Equations 4 and 5 result from simplification of a complex thermodynamic expression, assuming that the effect of dissolved H on the material elastic constants is negligible [91], and that there is no negative deviation from the logarithmic proportionality between $C_{H\sigma}$ and σ_H [21]. These assumptions are likely invalid at high H concentrations and stresses. The effect of H on the elastic constants of steel has not been studied extensively and such effects are neglected when calculating H enrichment [24,58,92,108].

FPZ hydrogen concentration is calculated using the calibration value of $C_{H,diff}$ (Eq. 2) for each K_{TH} in Fig. 4a and stress enhanced through Eq. 4 with $\sigma_H = 9$ GPa. This is the mobile H content available for diffusion to the FPZ. The parameters reported for Fe-Si ($k_{IG} = 0.85$ MPa \sqrt{m} and $\alpha = 0.5$ MPa \sqrt{m} /atom fraction H [119]) were used to calculate the concentration term in Eq. 6. The K_{TH} values less than 30 MPa \sqrt{m} represent H charged specimens that failed by brittle TG cracking and are well described with the regression line; the slope yields $\alpha'' = 3 \times 10^{-4}$ MPa $\cdot m$ and $\beta'_{IHE} = 0.13$ (MPa \sqrt{m}) $^{-1}$. Gerberich reported good fits between modeled and experimental measurements of K_{TH} vs. H_2 pressure and temperature for HEE of UHSS using $\alpha'' = 2 \times 10^{-4}$ MPa $\cdot m$ and $\beta'_{IHE} = 0.2$ (MPa \sqrt{m}) $^{-1}$ [119]. The K_{TH} above 30 MPa \sqrt{m} in Fig. 15 correlate with a mixed mode of brittle-TG and MVC cracking, and are not analyzed by Eq. 6. The good fit between the model predictions and measurements of K_{TH} vs. $C_{H_0,T}$ in Fig. 15 support the argument that IHE at low K_{TH} is due to the large amount of H that localizes in the highly stressed and trap laden FPZ.

H Accumulation Kinetics

While H repartitioning to the stressed FPZ in UHSS is favored thermodynamically, IHE is affected by the kinetics of H diffusion during loading and crack growth. Brittle TG cracking at high dK/dt , the magnitude of subcritical crack growth rates, and the low D_H measured for AerMet[®]100 [63] indicate that H repartitioning occurs over a very short distance.

Time Dependent K_{TH} and H Repartitioning: Severe transgranular IHE persists in AerMet[®]100 at low K_{TH} to loading rates as high as 0.3-0.6 MPa $\sqrt{m/s}$, as established in Fig. 8 for a constant $C_{H,diff}$ within the lower plateau of Fig. 4a. When stressed at $dK/dt = 0.6$ MPa $\sqrt{m/s}$, brittle TG crack growth initiated in 50 s. The distance, x , over which substantial H movement occurs in time, t , is approximated by $x = \sqrt{D_H t}$. D_H in AerMet[®]100 with $C_{H,diff} = 3.9$ wppm is $1-2 \times 10^{-8}$ cm $^2/s$ at 23°C [63]. For this D_H and $t = 50$ s, $x = 7-10$ μm , suggesting that H repartitioning occurs over a distance contained within a single prior- γ grain.

The dK/dt at which fracture transitions from brittle TG to MVC (Fig. 8) should depend on the diffusible H concentration in AerMet[®]100. As $C_{H,diff}$ increases, less H repartitioning may be necessary to induce brittle cracking because more H is present at fracture sites after charging and D_H increases with increasing $C_{H,diff}$ [63]. Consequently, the critical dK/dt in Fig. 8 should increase with increasing $C_{H,diff}$. Considering the H concentration dependence of K_{TH} at fixed dK/dt (Fig. 4a), the MVC at low $C_{H,diff}$ may be due to insufficient time for repartition of H to the fracture

process zone. Slower dK/dt may exacerbate TG IHE at $C_{H,diff} < 1-2$ wppm.

Crack Growth Rate and H Repartitioning: Analysis of the H-enhanced subcritical crack growth rate data for H-precharged AerMet[®]100 supports the scenario in Fig. 14 and a short H repartition distance. The experimental results in Fig. 11 show a Stage II, K-independent plateau velocity of 1.6×10^{-5} mm/s for AerMet[®]100 containing a high $C_{H,diff}$. This growth rate was obtained for rising-CMOD loading at dK/dt 2×10^{-4} MPa \sqrt{m}/s . The governing repartition distance is best defined based on the da/dt for brittle TG IHE at the fastest possible value of dK/dt . From Fig. 8, fully transgranular IHE is sustained at a low K_{TH} for dK/dt up to 0.3-0.6 MPa \sqrt{m}/s . The H-enhanced crack growth rate should increase, proportionate to a function of dK/dt , but this behavior has not been quantified for UHSS. Experiments with H-precharged low strength Cr-Mo steel showed that K_{TH} depends on dK/dt , analogous to the behavior of AerMet[®]100 (Fig. 8) and that da/dt was directly proportional to dK/dt [120]. Accordingly, a Stage II da/dt of 0.02 mm/s is expected for IHE in AerMet[®]100 at a dK/dt of 0.3 MPa \sqrt{m}/s . This very high crack growth rate, 20 $\mu m/s$ or 2 austenite grain diameters per second, is consistent with a short repartition distance.

Stage II crack growth rate is likely rate limited by the diffusion of H to crack tip damage sites for both IHE and HEE. Diffusion modeling predicts [36]:

$$\frac{da}{dt_{II}} = \frac{D_H}{\chi_{CRIT}} \left[\xi \left(\frac{C_o}{C_{CRIT}}, D_H, \chi_{CRIT}, \sigma_{YS}, t \right) \right] \quad (7)$$

where χ_{CRIT} is the repartition distance for IHE. The function, ξ , varies from 0.4 to 4 depending on the initial-H boundary condition (C_o), D_H , χ_{CRIT} , σ_{YS} , time (t), and the importance of concentration and stress gradients that drive H migration. For IHE of AerMet[®]100, D_H is $1-2 \times 10^{-8}$ cm²/s at 23°C. From Eq. 7 with an upper-bound ξ of 4, the upper bound χ_{CRIT} is 0.2-0.4 μm for the fastest da/dt_{II} . This range of distances is smaller than the values of 7-10 μm inferred from the dK/dt dependence of K_{TH} . It is not possible to better determine the critical H-transport distance because each diffusion analysis involves substantial assumptions [36]; however, the modeling based on da/dt (Eq. 7) is more rigorous suggesting that a ~ 1 μm repartition distance is reasonable.

Source of Damaging Diffusible H in AerMet[®]100

The high crack tip stress associated with IHE in AerMet[®]100 implies that H damage sites

are located within 1 μm of the tip for the scenario in Fig. 14. The time dependencies of IHE imply that the trap sites for H damage are fed by H diffusing within a 0.4 to 10 μm zone surrounding this FPZ. Analysis of H segregation at trap sites vs. the crack tip stress field indicates that modest binding energy traps, particularly coherent M_2C , release H to the FPZ lattice dilated by high-hydrostatic tension. This H is retrapped at crack tip sites with significant H-binding energies, particularly misoriented martensite lath interfaces, that provide a connected-brittle transgranular crack path through the AerMet[®]100 microstructure. The nm-scale size and close spacing of $(\text{Fe,Cr,Mo})_2\text{C}$ in AerMet[®]100 [7,8] guarantee a large number of trap sources for H within a prior austenite grain. The fine-martensitic microstructure, with 0.1-0.3 μm wide laths within $\sim 10 \mu\text{m}$ prior austenite grains, provides ample high energy traps to accept the embrittling H that enables damage within the FPZ. This fine microstructure in AerMet[®]100 is consistent with a 0.4-10 μm H-repartition distance.

The cause of the time dependent TG IHE susceptibility of AerMet[®]100 is the high concentration of $C_{\text{H,diff}}$ provided by reversible trapping at strengthening precipitates and other sites in the martensite, high crack tip stresses, and a connected path for TG cracking. Avenues to improve the IHE resistance of UHSS by controlling these elements have not been investigated. For example, E_{B} increases with increasing disorder at a precipitate-matrix interface [58,93,96,109], and less diffusible H would be attracted from this reservoir to the crack tip stress field at fixed $V_{\text{H}}\sigma_{\text{H}}$. Overaging to affect this change in AerMet[®]100 will result in some strength loss and more precipitated austenite at martensite lath interfaces. The role of this austenite in IHE is uncertain. Alternately, carbides retained after solution treatment of AerMet[®]100 appear to be strong H traps [63]. The volume fraction of such carbides can be increased by changes in solution treatment temperature or steel composition [8]. The $C_{\text{H,diff}}$ would be reduced by strong and homogeneously distributed trap states, and time-dependent TG IHE resistance improved. However, these carbides likely degrade K_{IC} by promoted void sheeting and trapped H exacerbates this microvoid damage. Time dependent IHE resistance may be improved if martensite interfaces could be altered to lower the H-binding energy to reduce the H that is strongly trapped and available for embrittlement.

CONCLUSIONS

1. Near-peak aged AerMet[®]100 is susceptible to severe internal hydrogen embrittlement, as evidenced by a threshold stress intensity for subcritical IHE, K_{TH} , as low as 10% of the plane strain fracture toughness ($K_{\text{JIC}} = 132\text{-}143 \text{ MPa}\sqrt{\text{m}}$). Decreasing K_{TH} due to

predissolved H is accompanied by a fracture mode change from microvoid damage to transgranular cracking apparently along martensite interfaces and cleavage planes.

2. The IHE susceptibility of AerMet[®]100 increases as the diffusible and total H concentrations increase. K_{TH} decreases sharply from K_{JIC} to 30 MPa \sqrt{m} , and the amount of brittle transgranular fracture increases to near 100%, as $C_{H,diff}$ increases from 0 to 1-2 wppm. Further increases in $C_{H,diff}$ to 8 wppm degrade IHE resistance modestly; K_{TH} decreases from 30 to 12 MPa \sqrt{m} . A micromechanical model reasonably predicts this concentration dependence.
3. IHE in AerMet[®]100 is time dependent, as evidenced by K-independent crack growth rates of 0.02 $\mu m/s$ and higher, and increasing K_{TH} with increasing dK/dt only above 0.3 MPa $\sqrt{m/s}$. The time dependence of IHE is consistent with repartitioning of H from reversible-trap sites to the stressed crack tip. The repartition distance from micromechanical modeling is 0.4-10 μm , with $\sim 1 \mu m$ the likely value, consistent with the fine-scale microstructure of AerMet[®]100.
4. The root causes of the susceptibility of AerMet[®]100 to TG IHE are: (a) very high crack tip stresses over a small volume that contains a large area of H-sensitive martensite interfaces, and (b) a reservoir of H that is trapped reversibly at a uniformly distributed high density of (Fe,Cr,Mo)₂C strengthening precipitates. These features enable H repartition to misoriented martensite lath interfaces and cleavage planes about the crack tip, with each prone to decohesion along a connected path.
5. The ductile-fracture toughness of AerMet[®]100 is reduced 2-fold by predissolved H at high loading rates, correlating with reduced size and spacing of microvoids. Immobile H, trapped strongly at secondary void-initiation sites such as TiC, appears to degrade stable-void growth that is responsible for the outstanding toughness of AerMet[®]100.

ACKNOWLEDGEMENTS

This research was supported by the Office of Naval Research (Grant N00014-91-J-4164), with Dr. A. John Sedriks as Scientific Monitor. Dr. Daoming Li and Mr. Hakan Dogan provided experimental assistance. These contributions are gratefully acknowledged.

REFERENCES

1. P.M. Novotny, in Gilbert R. Speich Symposium-Fundamentals of Aging and Tempering in Bainitic and Martensitic Steel Products, Iron and Steel Society, Warrendale, PA, p. 215-236, 1992.
2. "Alloy Datasheet-AerMet®100 Alloy", *Advanced Materials & Processes*, Vol. 154, p. 53-54, 1998.
3. P.M. Novotny and T.J. McCaffrey, "An Advanced Alloy for Landing Gear and Aircraft Structural Applications - AerMet®100", Paper No. 922040, in Aerotech '92, SAE, Inc., Warrendale, PA, 1992.
4. R.M. Hemphill, in Metallic Materials for Lightweight Applications, 40th Sagamore Army Materials Research Conference, M.G.H. Wells, E.B. Kula and J.H. Beatty, editors, US Army Laboratory Command, Watertown, MA, p. 377-388, 1993.
5. M.G.H. Wells, *Key Engineering Materials*, Vol. 77-78, p. 71-80, 1993.
6. W.M. Garrison Jr., *J. Metals*, May, p. 20-24 1990.
7. R. Ayer and P.M. Machmeier, *Metall. Trans. A*, Vol. 24A, p. 1943-1955, 1993.
8. C.J. Kuehmann, *Thermal Processing Optimization of Nickel-Cobalt Ultrahigh-Strength Steels*, Ph.D. Dissertation, Northwestern University, Evanston, IL, 1994.
9. R. Ayer and P.M. Machmeier, *Metall. Trans. A*, Vol. 27A, p. 2510-2517, 1996.
10. P.M. Machmeier, T. Matuszewski, R. Jones and R. Ayer, *J. Materials Engineering and Performance*, Vol. 6, p. 279-288, 1997.
11. Y. Oh, P.M. Machmeier, T. Matuszewski and R. Ayer, *J. Materials Engineering and Performance*, Vol. 6, p. 289-298, 1997.
12. C.H. Yoo, H.M. Lee, J.W. Chan and J.W. Morris Jr., *Metall. Trans. A*, Vol. 27A, p. 3466-3472, 1993.
13. D.A. Berman, *Materials Performance*, Vol. 24, p. 36-41, 1985.
14. J.B. Boodey and V.S. Agarwala, "Hydrogen in Metals: Cadmium Plated Steels", Paper No. 224, Corrosion 87, NACE, Houston, TX, 1987.
15. T. Zhong-Zhuo, H. Chi-Mei, L. Rong-Bong, F. Yi-Feng and C. Xiang-Rong, in Current Solutions to Hydrogen Problems in Steels, C.G. Interrante and G.M. Pressouyre, editors, ASM International, Materials Park, OH, p. 98-103, 1982.
16. E.A. Steigerwald, F.W. Schaller and A.R. Troiano, *Trans. TMS-AIME*, Vol. 218, p. 832-841, 1960.
17. H.H. Johnson, J.G. Morlet and A.R. Troiano, *Trans. TMS-AIME*, Vol. 216, p. 528-536, 1958.
18. C.F. Barth and E.A. Steigerwald, *Met. Trans.*, Vol. 1, p. 3451-3455, 1970.
19. D.P. Dautovich and S. Floreen, *Met. Trans.*, Vol. 4, p. 2627-2630, 1973.
20. D.P. Dautovich and S. Floreen, in Stress Corrosion Cracking and Hydrogen Embrittlement of Iron Alloys, R.W. Staehle, et al., editors, p. 798-815, NACE, Houston, TX, 1977.

21. R.A. Oriani and P.H. Josephic, *Acta Metall.*, Vol. 22, p. 1065-1074, 1974.
22. R.A. Oriani, *Corrosion*, Vol. 43, p. 390-397, 1987.
23. W.W. Gerberich, T. Livne and X. Chen, in Modeling Environmental Effects on Crack Growth Processes, R.H. Jones and W.W. Gerberich, editors, The Minerals, Metals & Materials Society, Warrendale, PA, p. 243-257, 1986.
24. W.W. Gerberich, T. Livne, X.-F. Chen and M. Kaczorowski, *Metall. Trans. A*, Vol. 19A, p. 1319-1334, 1988.
25. P. McIntyre, in Hydrogen Degradation of Ferrous Alloys, R.A. Oriani, J.P. Hirth, and M. Smialowski, editors, Noyes Publications, Park Ridge, NJ, p. 763-798, 1985.
26. Y. Yamaguchi, H. Nonaka and K. Yamakawa, *Corrosion*, Vol. 53, p. 147-155, 1997.
27. K. Yamakawa, S. Yonezawa and S. Yoshizawa, in International Congress on Metallic Corrosion, National Research Council, Toronto, Canada, p. 254-261, 1984.
28. C.J. McMahon, Jr., *Engr. Frac. Mech.*, Vol. 68, p. 773-788, 2001.
29. N. Bandyopadhyay, J. Kameda and C.J. McMahon, Jr., *Metall. Trans. A*, Vol. 14A, p. 881-888, 1983.
30. S.K. Banerji, H.C. Feng and C.J. McMahon, Jr., *Metall. Trans. A*, Vol. 9A, p. 237-247, 1978.
31. K. Yoshino and C.J. McMahon, Jr., *Metall. Trans. A*, Vol. 5A, p. 363-370, 1974.
32. K.N. Akhurst and T.J. Baker, *Metall. Trans. A*, Vol. 12A, p. 1059-1070, 1981.
33. R.P. Gangloff and R.P. Wei, in Fractography in Failure Analysis, ASTM STP 645, B.M. Strauss and W.H. Cullen Jr., editors, ASTM, West Conshohocken, PA, p. 87-106, 1978.
34. R.P. Gangloff, in Corrosion Prevention and Control, M. Levy and S. Isserow, editors, U.S. Army Materials Technology Laboratory, Watertown, MA, p. 64-111, 1986.
35. R.P. Gangloff and R.P. Wei, *Metall. Trans. A*, Vol. 8A, p. 1043-1053, 1977.
36. R.P. Gangloff, "Diffusion Control of Hydrogen Environment Embrittlement in High Strength Alloys", in Hydrogen Effects in Materials, N.R. Moody and A.W. Thompson, editors, The Minerals, Metals & Materials Society, Warrendale, PA, in press, 2002.
37. M. Gao, M. Lu and R.P. Wei, *Metallurgical Transactions A*, Vol. 15A, p. 735-746, 1984.
38. R.P. Wei and M. Gao, in Hydrogen Degradation of Ferrous Alloys, R.A. Oriani, J.P. Hirth, and M. Smialowski, editors, Noyes Publications, Park Ridge, NJ, p. 579-607, 1985.
39. G.E. Kerns, M.T. Wang and R.W. Staehle, in Stress Corrosion Cracking and Hydrogen Embrittlement of Iron Alloys, R.W. Staehle, et al., editors, NACE, Houston, TX, p. 700-735, 1977.
40. G.B. Olson, *Advanced Materials and Processes*, July, p. 72-79, 1997.
41. G.B. Olson, in Innovations in Ultrahigh Strength Steel Technology, 34th Sagamore Army Materials Research Conference, G.B. Olson, M. Azrin, and E.S. Wright, editors, US Army Laboratory Command, Watertown, MA, p. 549-593, 1987.

42. R.P. Gangloff, *Materials Science and Engineering*, Vol. A103, p. 157-166, 1988.
43. E.U. Lee, H. Sanders and B. Sarkar, "Stress Corrosion Cracking of High Strength Steels", CD file S08p2a.pdf, in Proceedings of the Tri-Service Conference on Corrosion, J.V. Kelley and B. Placzankis, editors, Army Research Laboratory, Aberdeen, MD, 2000.
44. G.N. Vigilante, J.H. Underwood and D. Crayton, in Fatigue and Fracture Mechanics: Proceedings of the 30th National Symposium, ASTM STP 1360, ASTM International, West Conshohocken, PA, p. 377-387, 2000.
45. J. Kozol and C.E. Neu, "Stress Corrosion Susceptibility of Ultra-High Strength Steels for Naval Aircraft Applications", Report No. NAWCADWAR-92018-60, Naval Air Warfare Center, Warminster, PA, 1992.
46. A. Oehlert and A. Atrens, *Matls. Forum*, Vol. 17, p. 415-429, 1993.
47. A. Oehlert and A. Atrens, *J. Matls. Sci.*, Vol. 33, p. 775-781, 1998.
48. P. Buckley, B. Placzankis, J. Beatty and R. Brown, "Characterization of the Hydrogen Embrittlement Behavior of High Strength Steels for Army Applications", *Corrosion/94*, Paper No. 547, NACE, Houston, TX, 1994.
49. E.U. Lee, *Metall. Trans. A*, Vol. 26A, p. 1313-1316, 1995.
50. D.S. McDarmaid, *Br. Corros. J.*, Vol. 15, p. 172-174, 1980.
51. P.F. Buckley, R. Brown, G.H. Graves, E.U. Lee, C.E. Neu and J. Kozol, in Metallic Materials for Lightweight Applications, 40th Sagamore Army Materials Research Conference, M.G.H. Wells, E.B. Kula and J.H. Beatty, editors, US Army Laboratory Command, Watertown, MA, p. 377-388, 1993.
52. J. Kameda and C.J. McMahon, Jr., *Metall. Trans. A*, Vol. 14A, p. 903-911, 1983.
53. Y. Takeda and C.J. McMahon, Jr., *Metall. Trans. A*, Vol. 12A, p. 1255-1266, 1981.
54. J.F. Knott, in Hydrogen Effects in Materials, A.W. Thompson and N.R. Moody, editors, The Minerals, Metals, & Materials Society, Warrendale, PA, p. 287-408, 1996.
55. X. Chen and W.W. Gerberich, *Metall. Trans. A*, Vol. 22A, p. 59-70, 1991.
56. M. Gao and R.P. Wei, *Acta Metall.*, Vol. 32, p. 2115-2124, 1984.
57. M. Gao and R.P. Wei, *Metall. Trans. A*, Vol. 16A, p. 2039-2050, 1985.
58. J.P. Hirth, *Metallurgical Transactions A*, Vol. 11A, p. 861-90, 1980.
59. A.W. Thompson and I.M. Bernstein, in Hydrogen Effects in Metals, I.M. Bernstein and A.W. Thompson, editors, The Minerals, Metals & Materials Society, Warrendale, PA, p. 291-308, 1981.
60. R.J. Asaro and D. Kwon, *Acta Metall.*, Vol. 38, p. 1595-1606, 1990.
61. O. Onyewuenyi and J.P. Hirth, *Metall. Trans. A*, Vol. 14A, p. 259-269, 1983.
62. T.D. Lee, T. Goldenberg and J.P. Hirth, *Metall. Trans. A*, Vol. 10A, p. 439-449, 1979.

63. R.L.S. Thomas, D. Li, R.P. Gangloff and J.R. Scully, *Metall. Mater. Trans. A*, Vol. 33A, p. 1991-2004, 2002.
64. G.M. Pressouyre and I.M. Bernstein, *Acta Metall.*, Vol. 27, p. 89-100, 1979.
65. M.J. Morgan and C.J. McMahon, Jr., in Hydrogen Degradation of Ferrous Alloys, R.A. Oriani, J.P. Hirth, and M. Smialowski, editors, Noyes Publications, Park Ridge, NJ, p. 608-40, 1985.
66. M.F. Stevens and I.M. Bernstein, *Metall. Trans. A*, Vol. 16A, p. 1879-1886, 1985.
67. L. Coudreuse and P. Bocquet, in Hydrogen Transport and Cracking in Metals, A. Turnbull, editor, University Press, Cambridge, UK, p. 227-252, 1995.
68. J.R. Scully, M.J. Cieslak and J.A. Van Den Avyle, *Scripta Metall. et Matl.*, Vol. 31, p. 125-130, 1994.
69. J.R. Scully, J.A. Van Den Avyle, M.J. Cieslak, A.D. Romig and C.R. Hills, *Metall. Trans. A*, Vol. 22A, p. 2429-2443, 1991.
70. *Alloy Data-AerMet® 100 Alloy*, Carpenter Technology Corporation Carpenter Steel Division: Reading, PA, 1992.
71. J.S. Montgomery and G.B. Olsen, in Gilbert R. Speich Symposium-Fundamentals of Aging and Tempering in Bainitic and Martensitic Steel Products, Iron and Steel Society, Warrendale, PA, p. 177-214, 1992.
72. *E 1820-99 Standard Test Method for Measurement of Fracture Toughness*, in 1999 Annual Book of ASTM Standards Vol. 3.01, ASTM International, West Conshohocken, PA, p. 972-1005, 1999.
73. M.J. Haynes and R.P. Gangloff, *Journal of Testing and Evaluation*, Vol. 25, p. 82-98, 1997.
74. R.P. Gangloff, "Fracture Mechanics Characterization of Hydrogen Embrittlement in Cr-Mo Steel", in Present Situation on Steels for Hydrogen Pressure Vessels, Creusot-Loire Industrie, Le Creusot, France, 1998.
75. J.K. Donald and J. Ruschau, in Fatigue Crack Measurement Techniques and Applications, K.J. Marsh, R.O. Ritchie, and R.A. Smith, editors, EMAS, West Midlands, U.K., p. 11-37, 1991.
76. M.J. Haynes and R.P. Gangloff, *Metall. Trans. A*, Vol. 29A, p. 1599-1613, 1998.
77. K. George and R.P. Gangloff, Unpublished Research, University of Virginia, Charlottesville, VA, 2000.
78. J.P. Hirth, in Hydrogen Effects in Materials, A.W. Thompson and N.R. Moody, editors, The Minerals, Metals & Materials Society, Warrendale, PA, p. 507-522, 1996.
79. G.P. Tiwari, A. Bose, J.K. Chakravartty, S.L. Wadekar, M.K. Totlani, R.N. Arya and R.K. Fotedar, *Mater. Sci. Engr. A*, Vol. A286, p. 269-281, 2000.
80. T.L. Anderson, Fracture Mechanics Fundamentals and Applications, CRC Press, Boca Raton, FL, p. 180-198, 1991.
81. A.H.M. Krom, R.W.J. Koers and A. Bakker, *J. Mech. Phys. Solids*, Vol. 47, p. 971-992, 1999.

82. A. Taha and P. Sofronis, *Engr. Frac. Mech.*, Vol. 68, p. 803-837, 2001.
83. A. Turnbull, D.H. Ferriss and H. Anzai, *Matls. Sci. Engr.*, Vol. A206, p. 1-13, 1996.
84. R.O. Ritchie, M.H. Castro Cedeno, V.F. Zackay and E.R. Parker, *Metall. Trans. A*, Vol. 9A, p. 35-40, 1978.
85. J.F. Watton, G.B. Olson and M. Cohen, in Innovations in Ultrahigh Strength Steel Technology, 34th Sagamore Army Materials Research Conference, G.B. Olson, M. Azrin, and E.S. Wright, editors, US Army Laboratory Command, Watertown, MA, p. 549-593, 1987.
86. W. Beck, J.O.M. Bockris, M.A. Genshaw and P.K. Subramanyan, *Metall. Trans.*, Vol. 2, p. 883-888, 1972.
87. G. Krauss, Steels: Heat Treatment and Processing Principles, ASM International, Materials Park, OH, p. 57-77, 1990.
88. G. Mayer, *Metall. Mater. Technol.*, Vol. 9, p. 255-261, 1977.
89. K. Yamakawa, H. Tsubakino and S. Yoshizawa, in Critical Issues in Reducing the Corrosion of Steels, H. Keidheiser Jr. and S. Haruyama, editors, NACE, Houston, TX, p. 348-358, 1986.
90. D.G. Enos, A.J. Williams Jr. and J.R. Scully, *Corrosion*, Vol. 53, p. 891-908, 1997.
91. H.P. van Leeuwen, in Review on Coatings and Corrosion, The Technion, Haifa, Israel, p. 5-93, 1979.
92. W.W. Gerberich, in Hydrogen in Metals, I.M. Bernstein and A.W. Thompson, editors, The Minerals, Metals & Materials Society, Warrendale, PA, p. 115-147, 1974.
93. I.M. Bernstein and G.M. Pressouyre, in Hydrogen Degradation of Ferrous Alloys, R.A. Oriani, J.P. Hirth, and M. Smialowski, editors, Noyes Publications, Park Ridge, New Jersey, p. 641-711, 1985.
94. R.A. Oriani, *Acta Metallurgica*, Vol. 18, p. 147-157, 1970.
95. P. Kedzierzawski, in Hydrogen Degradation of Ferrous Alloys, R.A. Oriani, J.P. Hirth, and M. Smialowski, editors, Noyes Publications, Park Ridge, New Jersey, p. 271-320, 1985.
96. G.M. Pressouyre and I.M. Bernstein, *Metall. Trans. A*, Vol. 9A, p. 1571-1580, 1978.
97. C. Paes de Oliveira, M. Aucouturier and L. Lacombe, *Corrosion*, Vol. 36, p. 53-59, 1980.
98. J.R. Rice, *Corrosion*, Vol. 32, p. 22-25, 1976.
99. J.R. Rice and G.R. Rosengren, *J. Mech. Phys. Solids*, Vol. 16, p. 1-12, 1968.
100. J.R. Rice and M.A. Johnson, in Inelastic Behavior of Solids, M.F. Kannin, W.G. Adler, A.R. Rosenfield, and R.I. Jaffee, editors, McGraw Hill, NY, NY, p. 641-671, 1970.
101. X. Chen, T. Foeche, M. Lii, Y. Katz and W.W. Gerberich, *Engr. Frac. Mech.*, Vol. 35, p. 997-1017, 1990.
102. H. Huang and W.W. Gerberich, *Acta Metall.*, Vol. 42, p. 639-647, 1994.

103. W. Zielinski, M.J. Lii, P.G. Marsh, H. Huang and W.W. Gerberich, *Acta Metall.*, Vol. 40, p. 2883-2894, 1992.
104. J.W. Hutchinson, *Intl. J. Solids and Struct.*, Vol. 37, p. 225-238, 2000.
105. Y. Wei and J.W. Hutchinson, "Models of Interface Separation Accompanied by Plastic Dissipation", Harvard University Report No. Mech 341, Cambridge, MA, 1998.
106. H. Jiang, Y. Huang, Z. Zhuang and K.C. Hwang, *J. Mech. Phys. Solids*, Vol. 49, p. 979-993, 2001.
107. Y. Wei and J.W. Hutchinson, *J. Mech. Phys. Solids*, Vol. 45, p. 1253-1273, 1997.
108. R.A. Oriani, *Hydrogen in Metals*, in Fundamental Aspects of Stress Corrosion Cracking, NACE, Houston, TX, p. 32-50, 1969.
109. G.M. Pressouyre, in Current Solutions to Hydrogen Problems in Steels, C.G. Interrante and G.M. Pressouyre, editors, ASM International, Materials Park, OH, p. 18-34, 1982.
110. D. Li, J.R. Scully and R.P. Gangloff, *Hydrogen Diffusion and Trapping Behavior in Ultrahigh-Strength AerMet®100 Steel*, University of Virginia Report, Charlottesville, VA, in press, 2002.
111. S. Hinotani, Y. Ohmori and F. Terasaki, *Matls. Sci. and Engr.*, Vol. 76, p. 57-69, 1985.
112. F. Gehrman, H.J. Grabke and E. Riecke, in Hydrogen Transport and Cracking in Metals, A. Turnbull, editor, The University Press, London, England, p. 216-26, 1995.
113. R. Gibala and A.J. Kumnick, in Hydrogen Embrittlement and Stress Corrosion Cracking, R. Gibala and R.F. Hehemann, editors, ASM International, Materials Park, OH, p. 61-77, 1984.
114. A.J. Kumnick and H.H. Johnson, *Acta Metall.*, Vol. 28, p. 33-39, 1980.
115. H. Hagi, *J. Japan Inst. Metals*, Vol. 55, p. 1283-1290, 1991.
116. D.M. Symons, *Engr. Frac. Mech.*, Vol. 68, p. 751-771, 2001.
117. P. Sofronis, J. Lufrano and D. Symons, *Engr. Fract. Mech.*, Vol. 59, p. 827-845, 1998.
118. P.K. Subramanyan, in Comprehensive Treatise of Electrochemistry Volume 4: Electrochemical Materials Science, J.O.M. Bockris, *et al.*, editors, Plenum Press, NY, NY, p. 411-462, 1981.
119. W.W. Gerberich, P.G. Marsh and J.W. Hoehn, in Hydrogen Effects in Metals, A.W. Thompson and N.R. Moody, editors, The Minerals, Metals & Materials Society, Warrendale, PA, p. 539-551, 1996.
120. R.P. Gangloff, Unpublished research, University of Virginia, Charlottesville, VA, 2001.

FIGURE CAPTIONS

Figure 1. Calibration relationship between applied-cathodic overpotential and the resulting diffusible H content at 23°C produced in AerMet®100 steel exposed in saturated-aqueous $\text{Ca}(\text{OH})_2$ solution at pH 12.1 and either 23°C (•) or 60°C (o).

Figure 2. Load and dcPD vs. δ data for an AerMet®100 CT specimen with $C_{\text{H,diff}} = 2.1$ wppm. The analysis method used to determine K_{TH} for the onset of crack growth is illustrated by the dcPD data in (b) and is consistent with the first nonlinear compliance (P- δ) data, as indicated by the vertical arrow.

Figure 3. Stress intensity, K , versus crack extension, Δa , for AerMet®100 with $C_{\text{H,diff}} = 0$ and 7.6 wppm. Predissolved H causes a substantial decrease in K_{TH} and eliminates resistance to stable crack growth. The break in the data for the H-free specimen resulted from a burst of crack growth.

Figure 4. Threshold stress intensity for internal hydrogen embrittlement, K_{TH} , at constant dK/dt of 2.2×10^{-4} MPa $\sqrt{\text{m/s}}$ and varying: (a) diffusible H concentration, and (b) total H concentration. A significant decrease in K_{TH} was observed for all H concentrations dissolved in near peak aged AerMet®100.

Figure 5. Scanning electron images of the fracture surfaces of AerMet®100 specimens with diffusible H concentrations of: (a) 0 wppm, showing cracking by MVC at K_{IC} of 132-142 MPa $\sqrt{\text{m}}$, and (b) 7.6 wppm, showing transgranular IHE at K_{TH} of 13 MPa $\sqrt{\text{m}}$, with some IG cracking (arrow). The corresponding fracture mechanics data are presented in Fig. 3, crack growth was from top to bottom, and the marker bars represent 10 μm .

Figure 6. Scanning electron fractographs of crack surfaces in near peak aged AerMet®100, precharged with $C_{\text{H,diff}}$ of: (a) ~0.5 wppm H, showing a mixture of predominantly MVC and brittle TG features (arrows) for $K_{\text{TH}} = 73\text{-}76$ MPa $\sqrt{\text{m}}$, (b) 0.8 wppm H, showing an increased amount of brittle-transgranular features (arrows) and nil MVC for $K_{\text{TH}} = 27$ MPa $\sqrt{\text{m}}$, (c) 2.1 wppm H, showing a TG crack path with regions of possible martensite lath interface cracking (arrows) for $K_{\text{TH}} = 24$ MPa $\sqrt{\text{m}}$, and (d) 5.9 wppm H, showing a fully-brittle TG fracture surface for $K_{\text{TH}} = 18$ MPa $\sqrt{\text{m}}$. The applied loading rate was $dK/dt = 2.2 \times 10^{-4}$ MPa $\sqrt{\text{m/s}}$, crack growth was from top to bottom in each image, and the marker in each fractograph represents 10 μm .

Figure 7. High magnification SEM fractographs showing brittle TG features that are typical IHE of AerMet®100, including: (a) possible martensite lath interface cracking (arrows) in a specimen with $C_{\text{H,diff}} = 3.9$ wppm and $K_{\text{TH}} = 18$ MPa $\sqrt{\text{m}}$, and (b) and (c) cleavage-like TG fracture (arrows) in a specimen with $C_{\text{H,diff}} = 7.6$ wppm and $K_{\text{TH}} = 13$ MPa $\sqrt{\text{m}}$. The applied loading rate was $dK/dt = 2.2 \times 10^{-4}$ MPa $\sqrt{\text{m/s}}$ and crack growth was from top to bottom.

Figure 8. Threshold stress intensity, K_{TH} , vs. applied-initial dK/dt for AerMet®100 precharged to $C_{\text{H,diff}} = 3.9$ wppm. At dK/dt less than 0.3 MPa $\sqrt{\text{m/s}}$, brittle-TG fracture occurs at $K_{\text{TH}} < 20$ MPa $\sqrt{\text{m}}$. At dK/dt greater than 0.7 MPa $\sqrt{\text{m/s}}$, fracture occurs by MVC at $K_{\text{TH}} < 60$ MPa $\sqrt{\text{m}}$. The H-free plane strain elastic-plastic fracture toughness of AerMet®100 is 132-143 MPa $\sqrt{\text{m}}$.

Figure 9. SEM images of the fracture surfaces of AerMet®100 with: (a) $C_{H,diff} = 0$ wppm stressed at $dK/dt = 0.2 \text{ MPa}\sqrt{\text{m/s}}$, and (b) $C_{H,diff} = 3.9$ wppm stressed at $2.7 \text{ MPa}\sqrt{\text{m/s}}$. MVC occurred on a finer scale in (b), consistent with the significantly lower initiation toughness ($K_{TH} = 48.3 \text{ MPa}\sqrt{\text{m}}$) compared to $K_{JIC} = 132\text{-}142 \text{ MPa}\sqrt{\text{m}}$ for the low-H case represented in (a). Crack growth was from top to bottom in both images.

Figure 10. Stress intensity, K , versus crack extension, Δa , for AerMet®100 with nonuniform $C_{H,diff}$ across the specimen thickness and subjected to rising δ at an initial-constant dK/dt of $2.2 \times 10^{-4} \text{ MPa}\sqrt{\text{m/s}}$. Crack growth is brittle-TG at $K_{TH} = 24 \text{ MPa}\sqrt{\text{m}}$ and in regions adjacent to the fatigue crack tip and specimen edges where $C_{H,diff} > 90\%$ of 2.1 wppm. $C_{H,diff}$ is lower in the center region, resulting in MVC fracture and increasing resistance to crack propagation.

Figure 11. Crack growth rate, da/dt , vs. applied K for AerMet®100 precharged with a high level of H ($C_{H,diff} = 7.6$ wppm) and subjected to rising- δ loading at a constant-initial dK/dt of $2.2 \times 10^{-4} \text{ MPa}\sqrt{\text{m/s}}$. Data were limited to H cracking within $1500 \mu\text{m}$ of the fatigue precrack tip where the precharged H distribution was uniform.

Figure 12. The effect of post-H charging heating at 190°C for 24 h in reversing severe transgranular IHE in H precharged ($C_{H,diff} = 4.0$ wppm) AerMet®100.

Figure 13. (a) The diffusible-hydrogen concentration dependencies of K_{TH} for IHE of AerMet®100 (\square from Fig. 4a), the combined IHE/HEE of 4340-type steels (dotted trend line and correlation equation from Yamakawa et al. [27]), and IHE of 4335 steel (\circ [27]). (b) The total-hydrogen concentration dependencies of K_{TH} for IHE of AerMet®100 (\square from Fig. 4b), and IHE of 18Ni (270) and (290) Maraging steels (\circ from Ref. [19]).

Figure 14. The hypothesized scenario for IHE of ultra-high strength steel such as AerMet®100, containing H trapped at a variety of microstructural sites and subjected to high crack tip stresses. The upper-bound location of the maximum hydrostatic tension, predicted by continuum mechanics, is between 1 and 4 times the blunted crack tip opening displacement, or $1\text{-}4 \mu\text{m}$ for AerMet®100 at a K level of $30 \text{ MPa}\sqrt{\text{m}}$. The volume fraction of M_2C carbides is higher than the few that are indicated and martensite laths are enlarged for clarity.

Figure 15. The measured and model-predicted effects of hydrostatic-stress enhanced H concentration, $C_{H\sigma,T}$ on the threshold for IHE of AerMet®100. The x-axis parameter used $C_{H\sigma,T}$ calculated from the measured $C_{H,diff}$ stress enhanced through Eq. 4 with $\sigma_H = 9 \text{ GPa}$, $\alpha = 0.5 \text{ MPa}\sqrt{\text{m/atom}}$ fraction, and $k_{IG} = 0.85 \text{ MPa}\sqrt{\text{m}}$ [119]. All measured K_{TH} values less than $30 \text{ MPa}\sqrt{\text{m}}$ relate to brittle-transgranular IHE and the associated regression line is $\log K_{TH} = 0.90 + 0.80 (k_{IG} - \alpha C_H)^2$ with $r^2 = 0.85$. Cracking at higher K_{TH} involved some MVC.

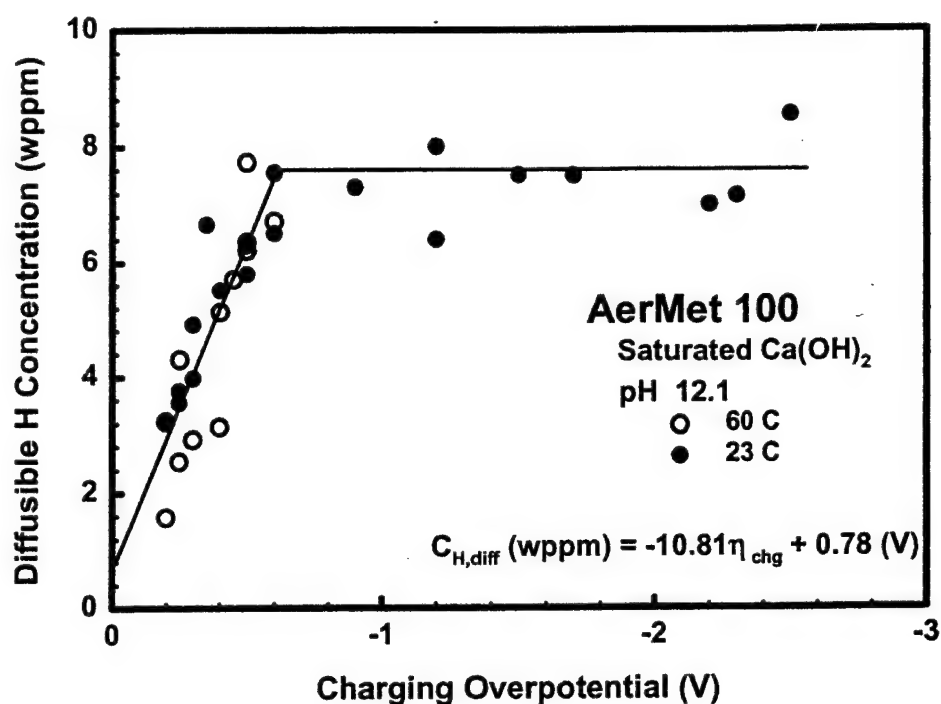


Figure 1. Calibration relationship between applied-cathodic overpotential and the resulting diffusible H content at 23°C produced in AerMet[®]100 steel exposed in saturated-aqueous $\text{Ca}(\text{OH})_2$ solution at pH 12.1 and either 23°C (●) or 60°C (○).

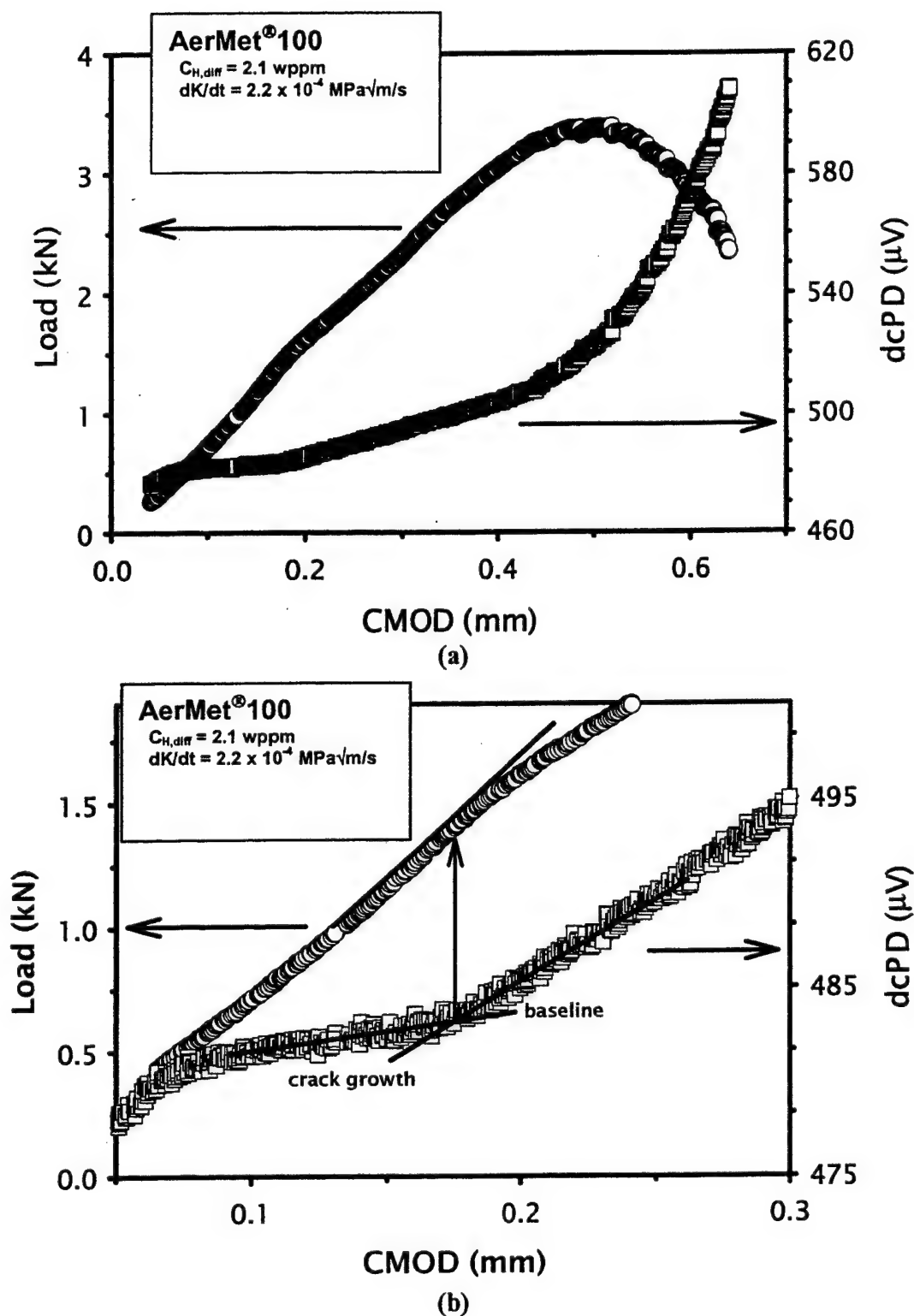


Figure 2. Load and dcPD vs. δ data for an AerMet®100 CT specimen with $C_{H,diff} = 2.1$ wppm. The analysis method used to determine K_{TH} for the onset of crack growth is illustrated by the dcPD data in (b) and is consistent with the first nonlinear compliance (P- δ) data, as indicated by the vertical arrow.

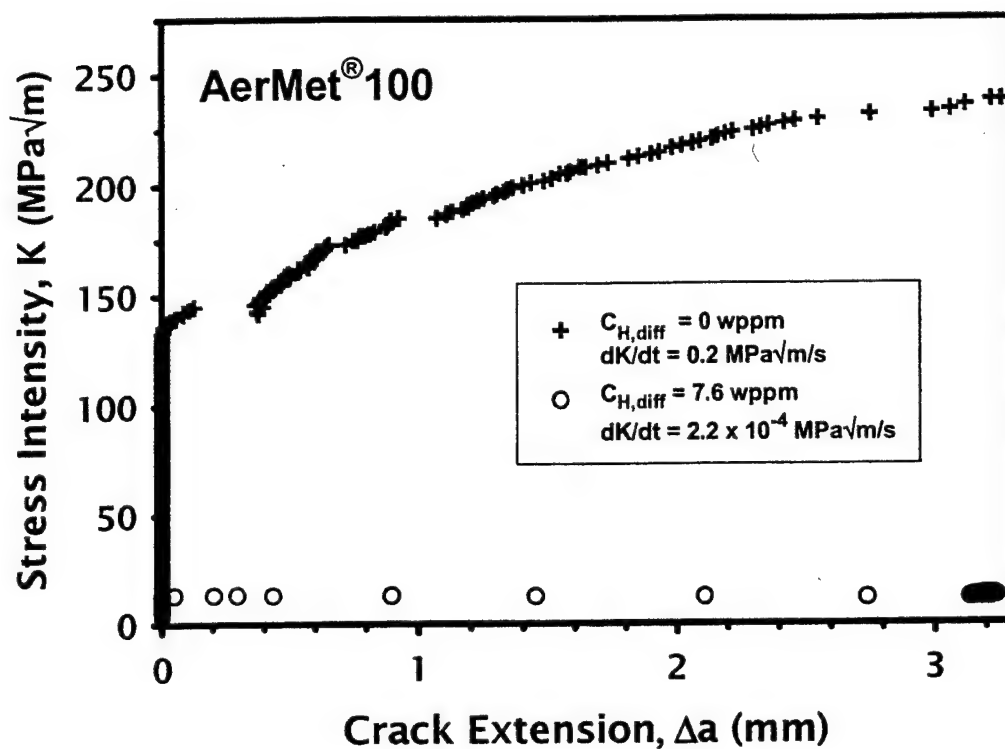
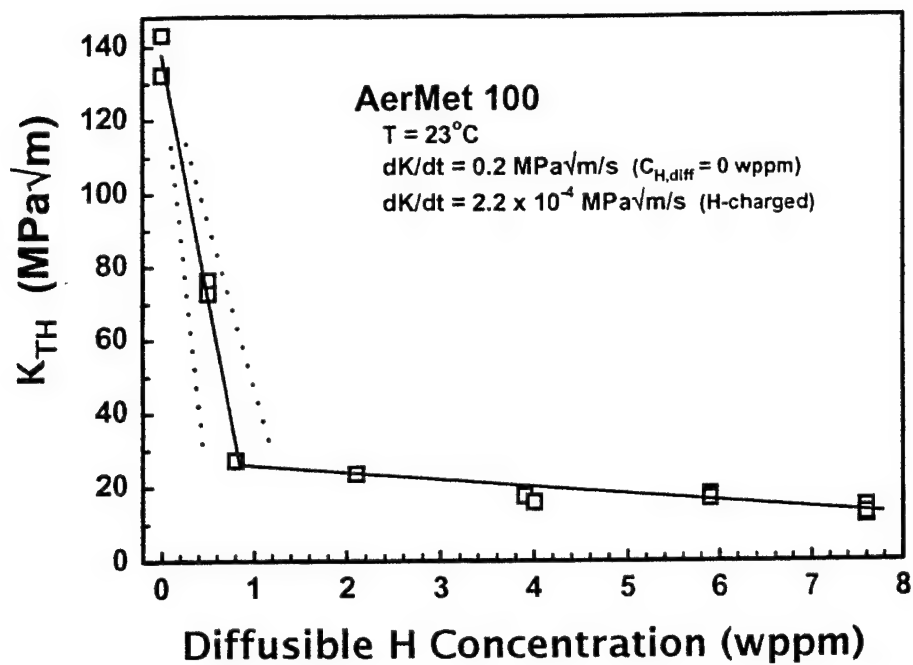
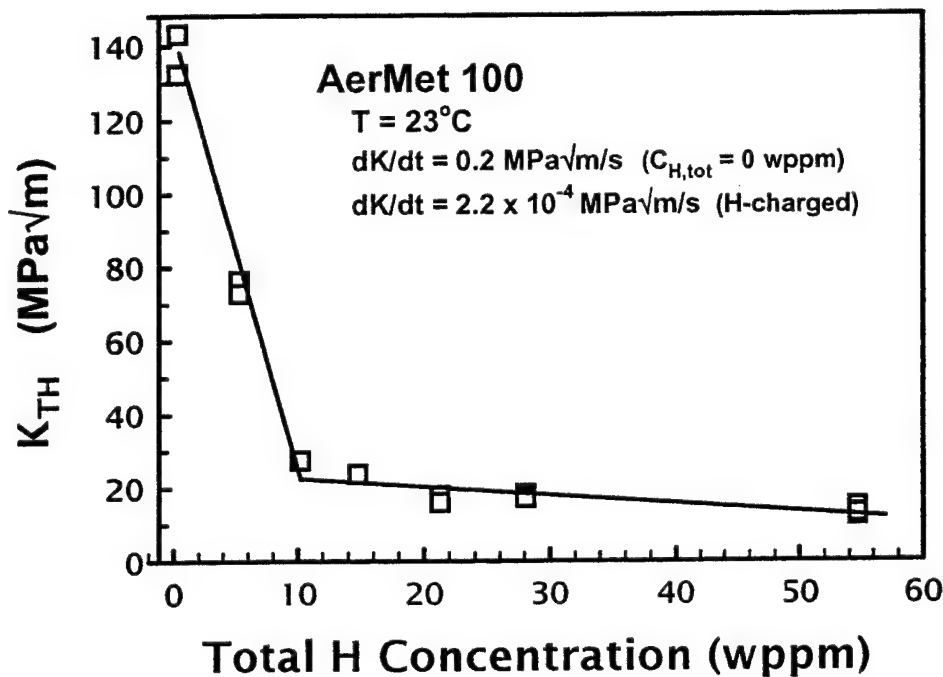


Figure 3. Stress intensity, K , versus crack extension, Δa , for AerMet®100 with $C_{H,diff} = 0$ and 7.6 wppm. Predissolved H causes a substantial decrease in K_{TH} and eliminates resistance to stable crack growth. The break in the data for the H-free specimen resulted from a burst of crack growth.



(a)



(b)

Figure 4. Threshold stress intensity for internal hydrogen embrittlement, K_{TH} , at constant dK/dt of $2.2 \times 10^{-4} \text{ MPa}\sqrt{\text{m/s}}$ and varying: (a) diffusible H concentration, and (b) total H concentration. A significant decrease in K_{TH} was observed for all H concentrations dissolved in near peak aged AerMet[®]100.

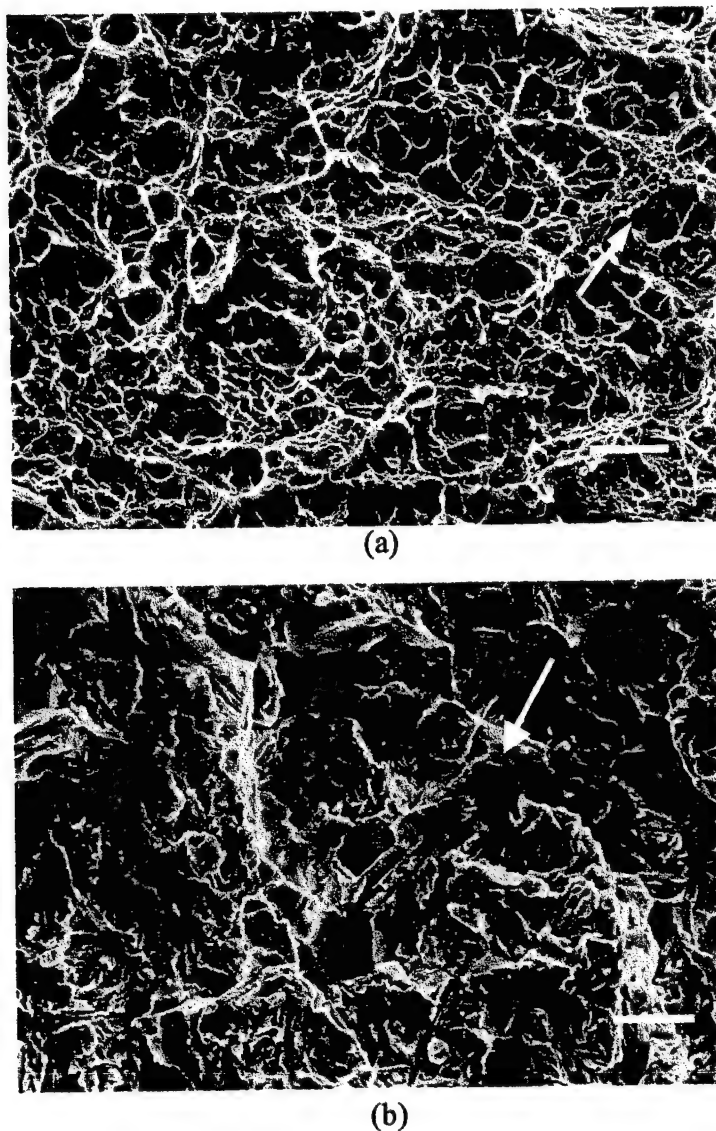


Figure 5. Scanning electron images of the fracture surfaces of AerMet®100 specimens with diffusible H concentrations of: (a) 0 wppm, showing cracking by MVC at K_{JIC} of 132-142 MPa \sqrt{m} , and (b) 7.6 wppm, showing transgranular IHE at K_{TH} of 13 MPa \sqrt{m} , with some IG cracking (arrow). The corresponding fracture mechanics data are presented in Fig. 3, crack growth was from top to bottom, and the marker bars represent 10 μm .

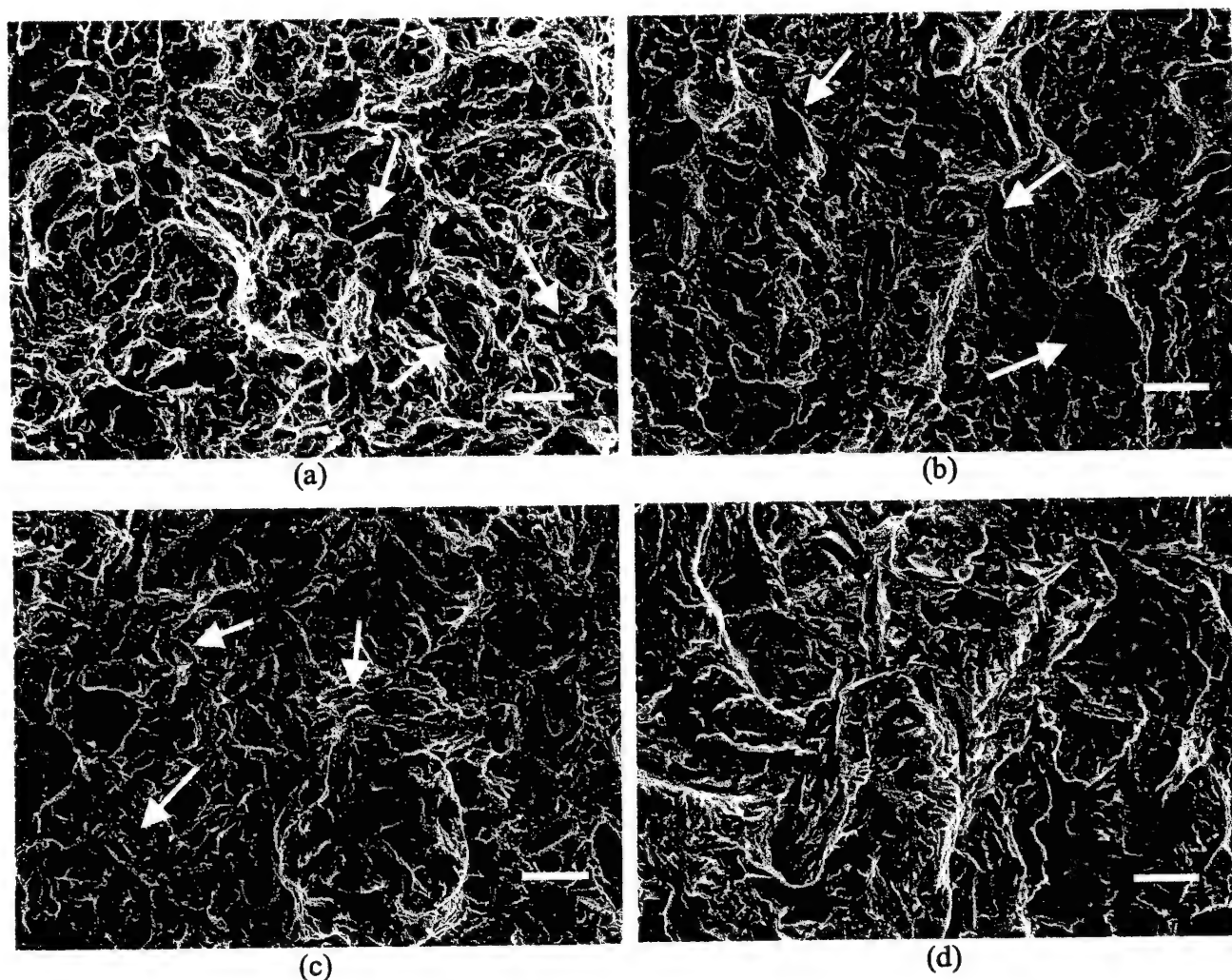


Figure 6. Scanning electron fractographs of crack surfaces in near peak aged AerMet[®]100, precharged with $C_{H,diff}$ of: (a) ~ 0.5 wppm H, showing a mixture of predominantly MVC and brittle TG features (arrows) for $K_{TH} = 73-76$ MPa \sqrt{m} , (b) 0.8 wppm H, showing an increased amount of brittle-transgranular features (arrows) and nil MVC for $K_{TH} = 27$ MPa \sqrt{m} , (c) 2.1 wppm H, showing a TG crack path with regions of possible martensite lath interface cracking (arrows) for $K_{TH} = 24$ MPa \sqrt{m} , and (d) 5.9 wppm H, showing a fully-brittle TG fracture surface for $K_{TH} = 18$ MPa \sqrt{m} . The applied loading rate was $dK/dt = 2.2 \times 10^{-4}$ MPa $\sqrt{m/s}$, crack growth was from top to bottom in each image, and the marker in each fractograph represents 10 μm .

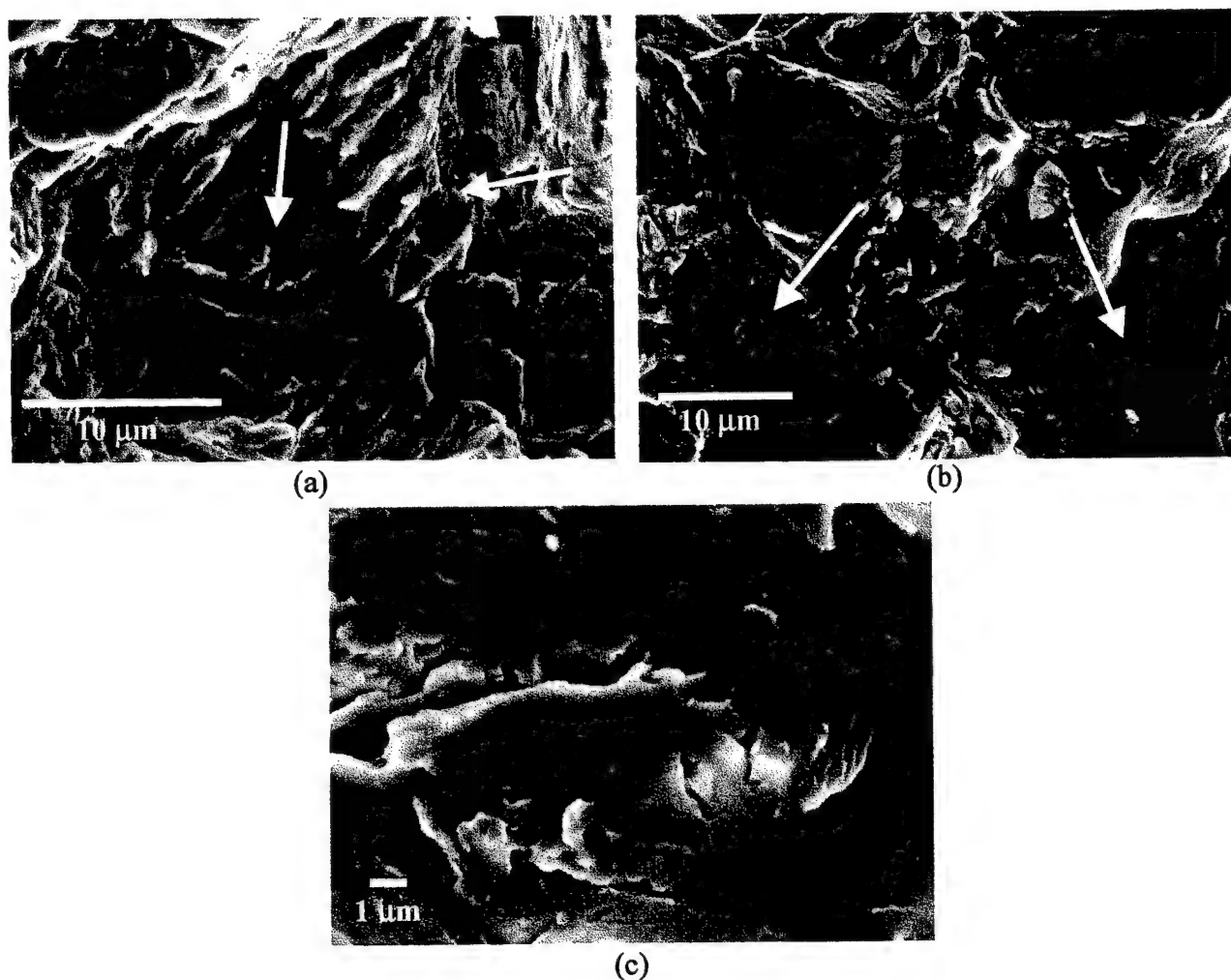


Figure 7. High magnification SEM fractographs showing brittle TG features that are typical IHE of AerMet®100, including: (a) possible martensite lath interface cracking (arrows) in a specimen with $C_{H,diff} = 3.9$ wppm and $K_{TH} = 18$ MPa√m, and (b) and (c) cleavage-like TG fracture (arrows) in a specimen with $C_{H,diff} = 7.6$ wppm and $K_{TH} = 13$ MPa√m. The applied loading rate was $dK/dt = 2.2 \times 10^{-4}$ MPa√m/s and crack growth was from top to bottom.

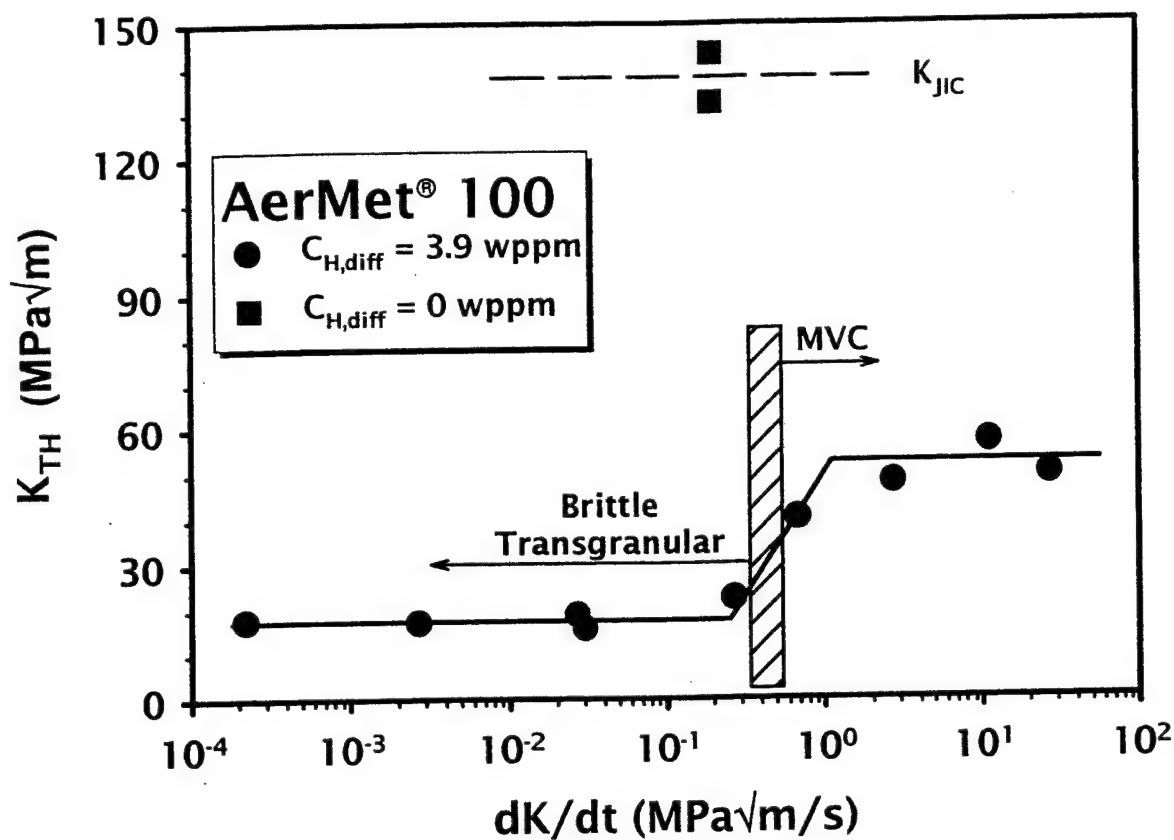


Figure 8. Threshold stress intensity, K_{TH} , vs. applied-initial dK/dt for AerMet®100 precharged to $C_{H,diff} = 3.9$ wppm. At dK/dt less than 0.3 MPa√ms, brittle-TG fracture occurs at $K_{TH} < 20$ MPa√m. At dK/dt greater than 0.7 MPa√m/s, fracture occurs by MVC at $K_{TH} < 60$ MPa√m. The H-free plane strain elastic-plastic fracture toughness of AerMet®100 is 132-143 MPa√m.

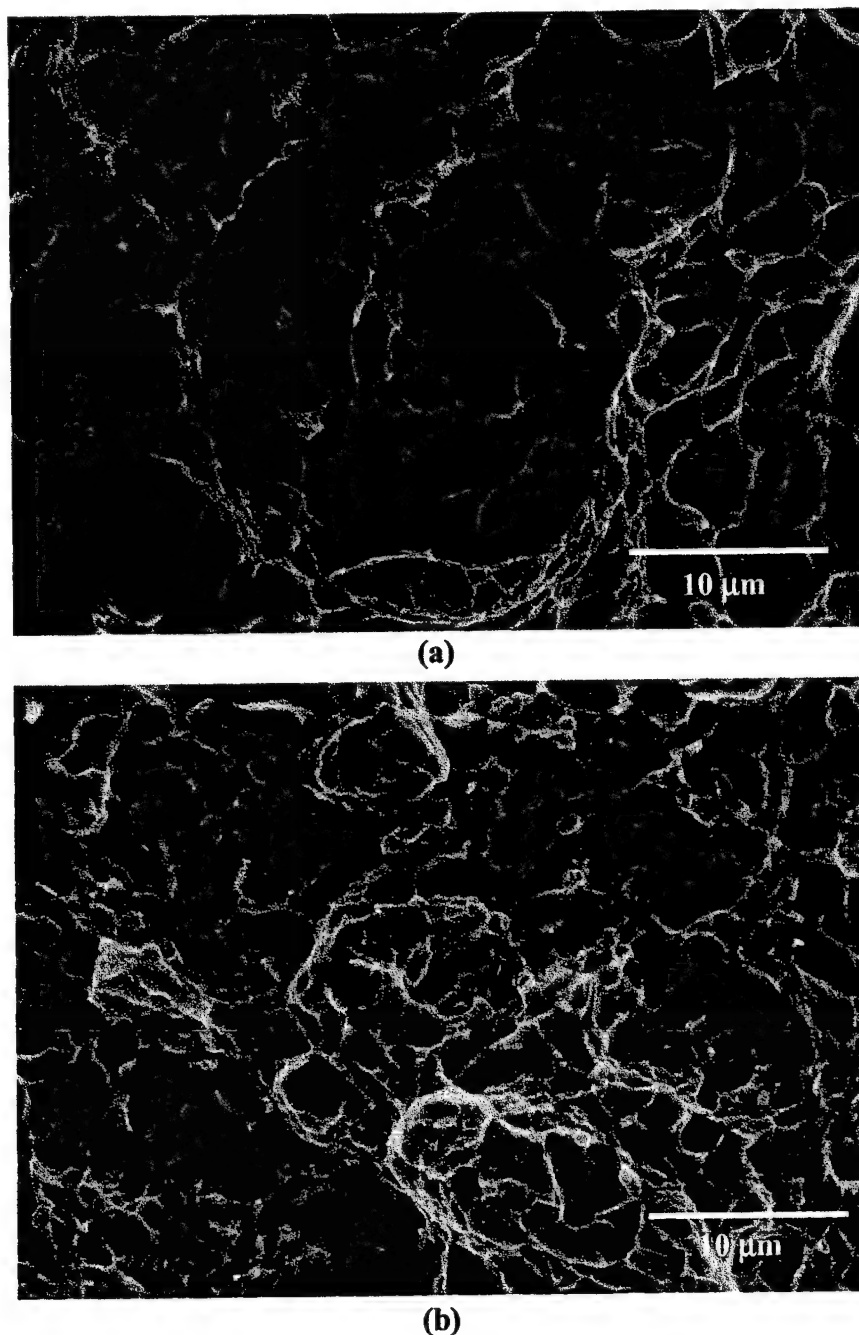


Figure 9. SEM images of the fracture surfaces of AerMet®100 with: (a) $C_{H,diff} = 0$ wppm stressed at $dK/dt = 0.2 \text{ MPa}\sqrt{\text{m/s}}$, and (b) $C_{H,diff} = 3.9$ wppm stressed at $2.7 \text{ MPa}\sqrt{\text{m/s}}$. MVC occurred on a finer scale in (b), consistent with the significantly lower initiation toughness ($K_{TH} = 48.3 \text{ MPa}\sqrt{\text{m}}$) compared to $K_{JIC} = 132\text{--}142 \text{ MPa}\sqrt{\text{m}}$ for the low-H case represented in (a). Crack growth was from top to bottom in both images.

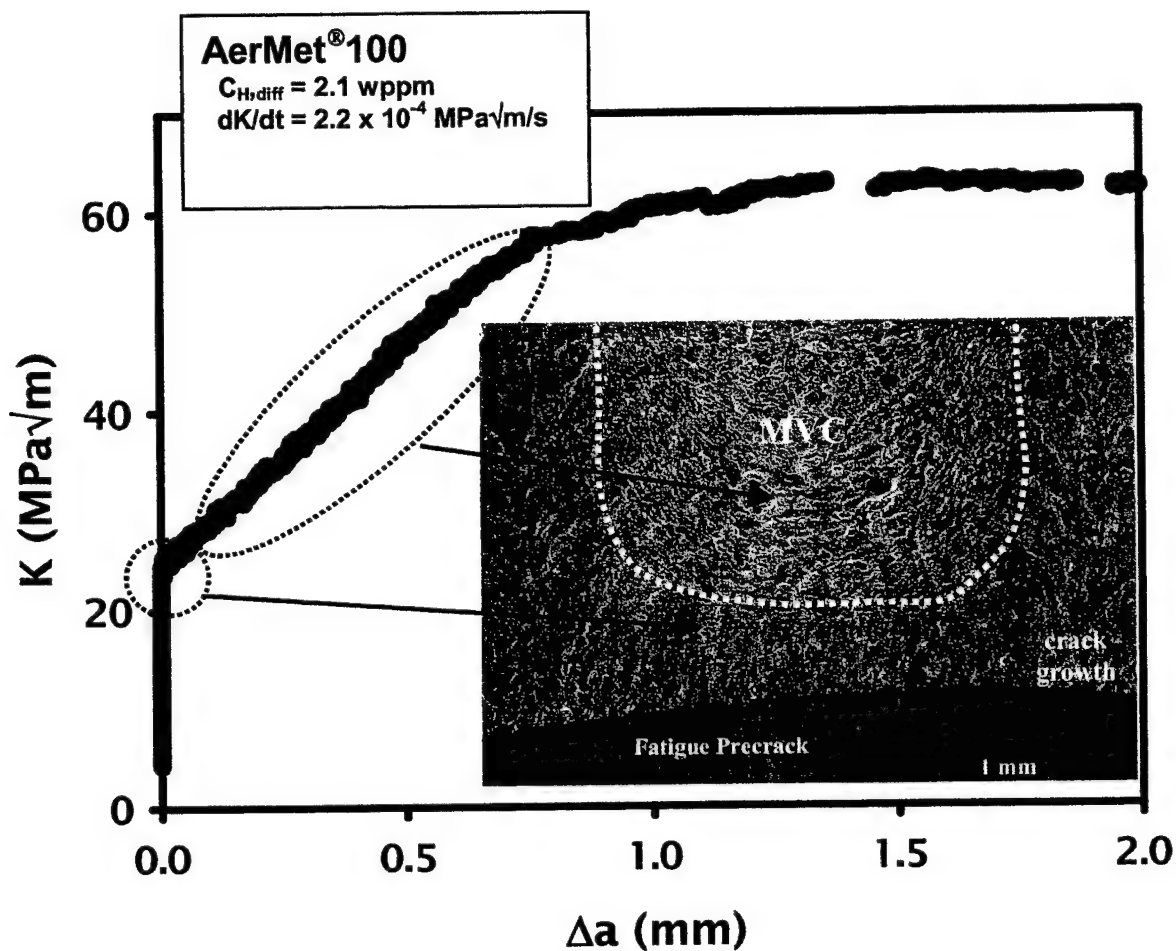


Figure 10. Stress intensity, K , versus crack extension, Δa , for AerMet®100 with nonuniform $C_{H,diff}$ across the specimen thickness and subjected to rising δ at an initial-constant dK/dt of 2.2×10^{-4} MPa√m/s. Crack growth is brittle-TG at $K_{TH} = 24$ MPa√m and in regions adjacent to the fatigue crack tip and specimen edges where $C_{H,diff} > 90\%$ of 2.1 wppm. $C_{H,diff}$ is lower in the center region, resulting in MVC fracture and increasing resistance to crack propagation.

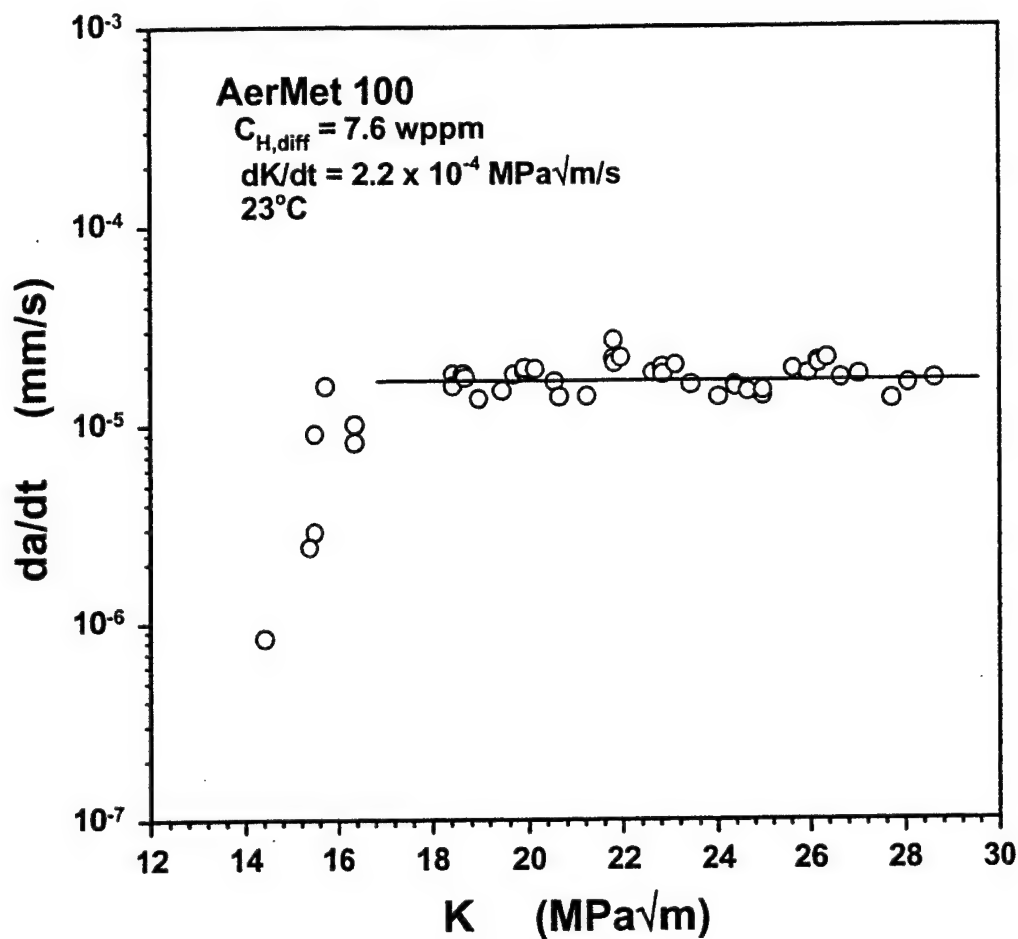


Figure 11. Crack growth rate, da/dt , vs. applied K for AerMet[®]100 precharged with a high level of H ($C_{H,diff} = 7.6 \text{ wppm}$) and subjected to rising- δ loading at a constant-initial dK/dt of $2.2 \times 10^{-4} \text{ MPa}\sqrt{\text{m/s}}$. Data were limited to H cracking within $1500 \mu\text{m}$ of the fatigue precrack tip where the precharged H distribution was uniform.

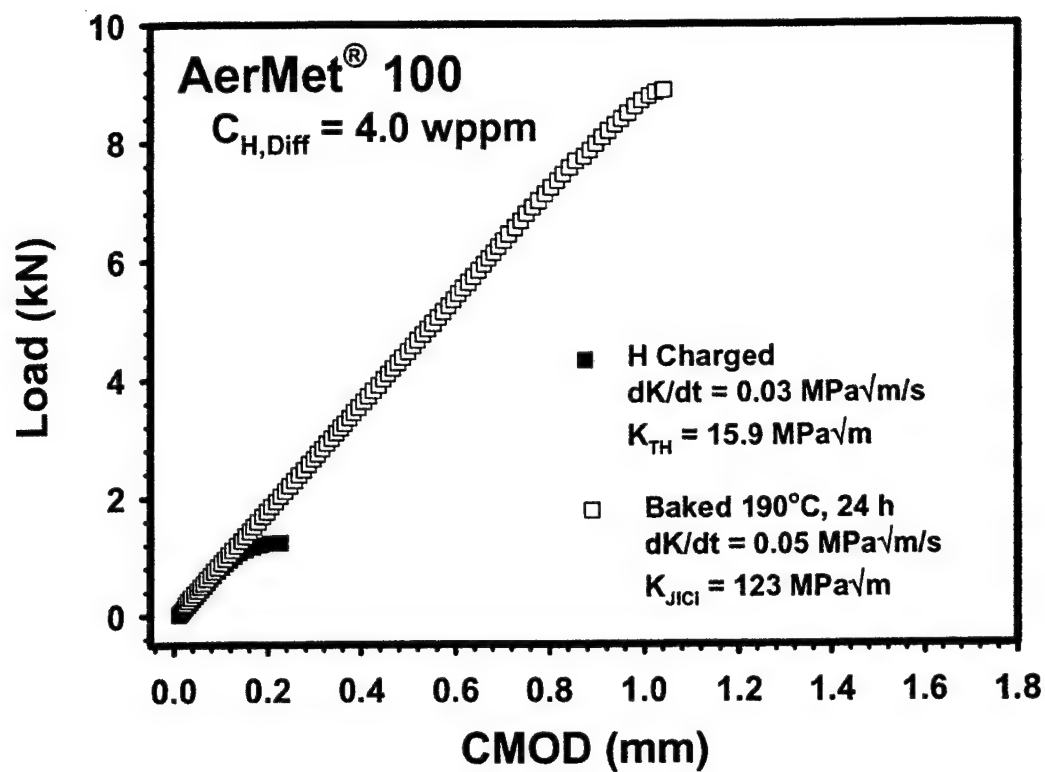
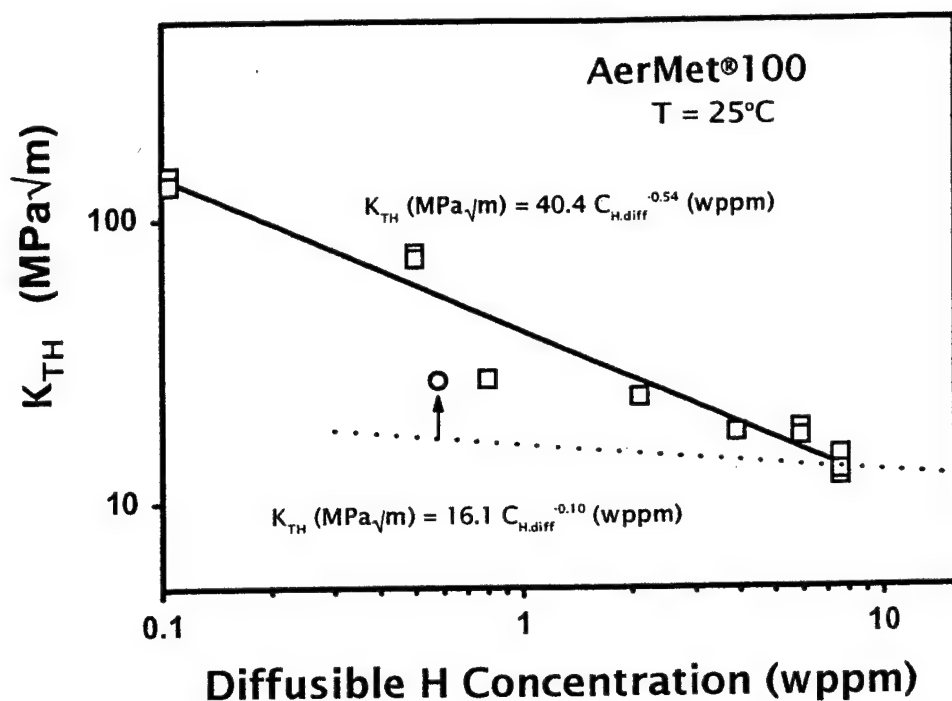
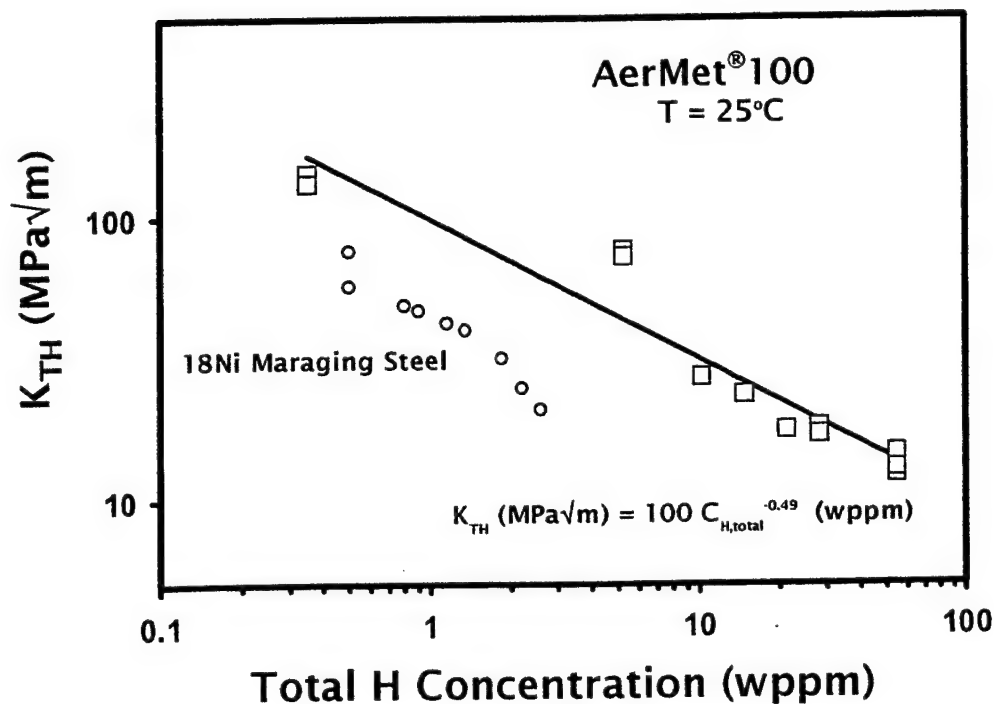


Figure 12. The effect of post-H charging heating at 190°C for 24 h in reversing severe transgranular IHE in H precharged ($C_{H,diff} = 4.0$ wppm) AerMet®100.



(a)



(b)

Figure 13. (a) The diffusible-hydrogen concentration dependencies of K_{TH} for IHE of AerMet®100 (□ from Fig. 4a), the combined IHE/HEE of 4340-type steels (dotted trend line and correlation equation from Yamakawa et al. [27]), and IHE of 4335 steel (○ [27]). (b) The total-hydrogen concentration dependencies of K_{TH} for IHE of AerMet®100 (□ from Fig. 4b), and IHE of 18Ni (270) and (290) Maraging steels (○ from Ref. [19]).

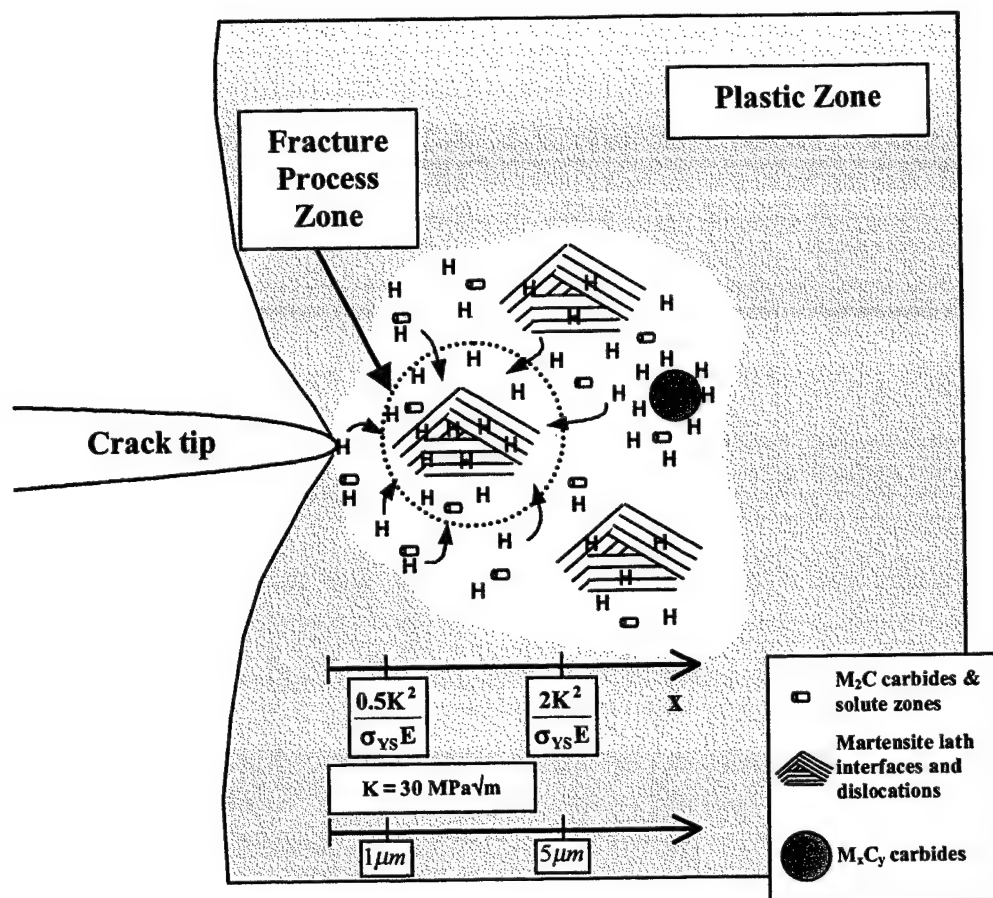


Figure 14. The hypothesized scenario for IHE of ultra-high strength steel such as AerMet[®]100, containing H trapped at a variety of microstructural sites and subjected to high crack tip stresses. The upper-bound location of the maximum hydrostatic tension, predicted by continuum mechanics, is between 1 and 4 times the blunted crack tip opening displacement, or 1–4 μm for AerMet[®]100 at a K level of 30 $\text{MPa}\sqrt{\text{m}}$. The volume fraction of M_2C carbides is higher than the few that are indicated and martensite laths are enlarged for clarity.

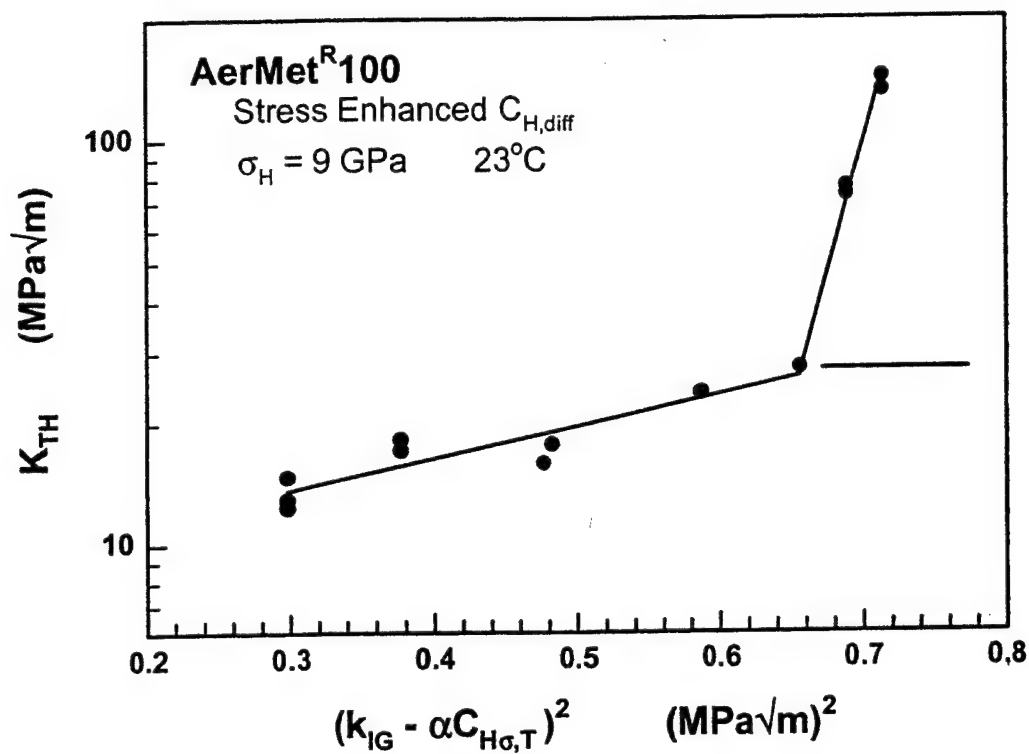


Figure 15. The measured and model-predicted effects of hydrostatic-stress enhanced H concentration, $C_{H\sigma,T}$ on the threshold for IHE of AerMet[®]100. The x-axis parameter used $C_{H\sigma,T}$ calculated from the measured $C_{H,diff}$ stress enhanced through Eq. 4 with $\sigma_H = 9 \text{ GPa}$, $\alpha = 0.5 \text{ MPa}\sqrt{\text{m}}/\text{atom fraction}$, and $k_{IG} = 0.85 \text{ MPa}\sqrt{\text{m}}$ [119]. All measured K_{TH} values less than $30 \text{ MPa}\sqrt{\text{m}}$ relate to brittle-transgranular IHE and the associated regression line is $\log K_{TH} = 0.90 + 0.80 (k_{IG} - \alpha C_{H\sigma,T})^2$ with $r^2 = 0.85$. Cracking at higher K_{TH} involved some MVC.

**HYDROGEN DIFFUSION AND TRAPPING BEHAVIOR IN
ULTRAHIGH-STRENGTH AERMET[®] 100 STEEL**

D. Li, R.P. Gangloff and J.R. Scully

Department of Materials Science and Engineering
University of Virginia
Charlottesville, VA 22904-4745
USA

Hydrogen Diffusion and Trapping Behavior in Ultrahigh-Strength AerMet® 100 Steel

Daoming Li, Richard P. Gangloff, John R. Scully

Center for Electrochemical Science and Engineering
University of Virginia, Charlottesville, VA 22904-4745, USA

ABSTRACT

H diffusion and trapping behavior in ultra-high strength AerMet® 100 is characterized after various electrochemical charging and baking conditions using thermal desorption spectroscopy (TDS). Due to heavy trapping, the apparent H diffusivity D_{app} ($< 3 \times 10^{-8} \text{ cm}^2/\text{s}$ at 23°C) is over 10-fold less than values typical of tempered martensitic steels such as AISI 4130. The temperature dependence of D_{app} ranging from 23°C to 200°C results in activation energy for diffusion (E_m^{app}) of 17.7 kJ/mol and 18.0 kJ/mol, for specimens charged at overpotentials of -1.17V and -0.62V , respectively. D_{app} decreases with decreasing diffusible H concentration from less severe charging or increased baking, indicating a H-concentration dependent diffusion behavior. The ramp TDS experiments identifies at least three major desorption peaks in association with three distinct trap states. Analysis of H binding energies suggests that both reversible and irreversible H-traps are responsible for the slow H diffusivity and high H uptake observed. M_2C precipitates are identified to be the main source of reversible H trap sites (with binding energies, E_b , of $11.4\text{--}11.6 \pm 0.2 \text{ kJ/mol}$), together with the portion of Cr and Mo atoms that are not consumed in carbides. This low-energy reversible H trap sites may also include dislocations. Irreversible trap sites (with E_b of $61.3\text{--}62.2 \pm 0.3 \text{ kJ/mol}$) may include various interfaces including martensitic and autenitic boundaries and grain boundaries, mixed dislocation cores. Undissolved metal carbides and highly disorientated grain boundaries may irreversibly trap H with the highest binding energy level (with E_b of $89.1\text{--}89.9 \pm 0.3 \text{ kJ/mol}$). Baking at room temperature and $190\text{--}200^\circ\text{C}$ removes, to varying degrees, diffusible and reversibly-trapped H ($E_b = 11.4\text{--}11.6 \pm 0.2 \text{ kJ/mol}$). For a plate specimen of about 0.5 mm thick charged to $\sim 30 \text{ wppm H}$, baking at 190°C for about 2 h essentially removes diffusible and reversibly-trapped H from bare AerMet® 100. However, considerable amount of H is still trapped in irreversible trap sites ($E_b \geq 61.3\text{--}62.2 \pm 0.3 \text{ kJ/mol}$), even after baking at 190°C for 200 h. The trapping-affected slow H diffusivity, high H uptake and residual trapped H are important issues to consider regarding the internal hydrogen embrittlement after Cd-plating and subsequent baking.

INTRODUCTION

Despite the weight restrictions limiting the use of steels in aircraft applications, ultrahigh-strength steels (UHSS) are indispensable in certain application areas requiring high strength and fracture toughness, such as landing gear and elements of the catapult. High strength, low-alloy quenched and tempered martensitic alloys, initially AISI 4340 and then 300M, were put in use for such applications [1]. Later, a more highly alloyed secondary hardening steel AF1410 [2] was developed to improve the plane strain fracture toughness (K_{IC}) to greater than two-fold that of AISI 4340 or 300M, but at a significant strength penalty. In 1990, Carpenter Technology Corporation developed a new secondary hardening UHSS, AerMet[®] 100, which can be heat-treated to provide K_{IC} in excess of 100 MPa \sqrt{m} , while maintaining strength at the level of 300M [3]. The high K_{IC} in AerMet[®] 100 is achieved by controlling impurities to a very low level of S + P and inclusion contents, like in AF1410, and by heat-treating to yield a highly stable γ phase along martensite lath interfaces. Its high strength is attributed to a fine, homogeneous distribution of nanoscale coherent M_2C alloy carbides in a highly dislocated Fe-Ni lath martensitic matrix [4]. Due to the good combination of strength and toughness, AerMet[®] 100 is currently the specified material in producing landing gear of two carrier-based aircraft, the F/A-18 and F-22 [5, 6].

In the process of electroplating Cd-coatings to improve aqueous corrosion resistance in carrier-based aircraft applications, H is co-deposited in the Cd and steel substrate [7-9]. To remove the dissolved H for preventing hydrogen embrittlement, a post-plating process is necessary which typically involves baking/heating the Cd-plated component to 190°C for 5 - 24 h [7]. On one hand, since H solubility in Cd is higher than that in Fe, the electroplated Cd-layer serves as a H source during the initial stages of baking, and hence, the H concentration in the steel substrate can increase during the first several hours of baking [7-9]. On the other hand, due to a much slower H diffusivity

in Cd than that in steel, the Cd-layer also acts as a diffusion barrier during baking and considerable amount of diffusible H may remain in the steel, even after heating times of 100 hours [7]. Consequently, for modern UHSS steels like AerMet[®] 100, it may be necessary to either increase temperature or prolong time to remove the dissolved H from the steel substrate. With this uncertainty in the baking process post electroplating, internal hydrogen embrittlement (IHE) may become a major concern in Cd-plated UHSS components [7-9].

As the susceptibility of steels to IHE generally increases with strength [10, 11], UHSS are more susceptible to IHE than common high strength steels. The severity of IHE likely depends strongly on the concentration of dissolved H, since the fracture strength of susceptible sites may degrade with increasing segregated H concentration [11-13]. IHE can occur as H diffuses to regions of tensile-stress concentration, such as a crack tip, thus decreasing the local fracture strength of microstructural features involved [10]. Like other UHSS, the heat-treated AerMet[®] 100 contains many microstructural features that are potential H-trapping sites, such as dislocations, carbides, martensite lath interfaces, solutes, and prior- γ grain boundaries. Because increasing density and/or strength of traps in a steel generally decreases apparent diffusivity and increases apparent solubility of H, relative to values for pure iron [14-19], H trapping significantly affects the resistance of a steel to H-induced fracture [10, 20-22]. Weak or reversible trap sites provide a reservoir of highly mobile H, which may diffuse to areas of lower H chemical potential, such as the dilated region under triaxial tensile stress ahead of a crack tip, and exacerbate IHE [23], as exemplified by the degradation of the resistance to H-cracking in AISI 4135 steel with increasing the concentration of predissolved-diffusible H [13, 24]. In contrast, a homogeneous distribution of irreversible or strong-reversible traps can prevent H from segregating to lower-interaction energy sites, e.g. martensite lath or prior austenite boundaries, thus alleviating susceptibility to IHE [25-27].

In view of the above, it is of key importance to investigate the hydrogen diffusion and trapping behavior in AerMet[®] 100 alloy, in order to provide fundamental insight into the underlying IHE mechanisms and to guide the relevant design of material processing (e.g. baking procedures). The present research work is aimed at characterizing the binding energies associated with the dominant trapping states and the effects of thermal baking time and temperatures on residual trapped hydrogen in uncoated steel. A subsequent paper will consider residual trapped hydrogen in Cd-plated steel. Experimental investigations aimed at determining H diffusivity and desorption characteristics are accompanied by model calculations of activation energies responsible for the diffusion and trapping processes. Attempts are also made to correlate the observed trapping-governed behavior with specific microstructural features of AerMet[®] 100.

EXPERIMENTAL PROCEDURES

Material, Processing and Microstructure

A modern UHSS, AerMet[®] 100, was selected for the present research. The original material was received as an annealed bar with dimensions of 15.2 cm in diameter and 30.5 cm in length. Its chemical composition is shown in Table I. Upon cutting, specimens were vacuum heat-treated following these procedures: solution treated at 885°C for 1 h, air cooled to room temperature in 2 h, chilled at -73°C for 1 h, and tempered at 482°C for 5 h. This heat-treatment is designed to achieve an optimal strength and toughness [28]. Table II shows the mechanical properties as a result of the treatment. The microstructure corresponding to the heat-treating conditions was detailed elsewhere [4,29,30] and is briefly introduced here. Tempering at 482°C produces an extremely fine microstructure [4,29,30] having the following features: (1) less than 0.1 μm diameter incoherent carbides (i.e. $(\text{MoCr})_7\text{C}_3$, $(\text{FeCr})_x\text{C}_y$, TiC , $(\text{TiCrMo})\text{C}$) that provide grain refinement, (2) martensite

laths (or plates) on the order of $0.15\text{ }\mu\text{m}$ thick, both twinned and un-twinned, with interfaces that are qualitatively high-angle, and arrayed in packets, (3) prior austenite grain boundaries, (4) dislocations in martensite and not recovered at this tempering temperature, (5) finely distributed, partly coherent and partly incoherent M_2C (where $\text{M} = 75\text{ atom pct Cr, } 13\text{ Fe and } 12\text{ Mo}$) in martensite, averaging 2 nm diameter \times 8 nm length, (6) solute clusters preceding M_2C precipitation, (7) precipitated austenite, and (8) Ni, Cr and Mo dissolved in martensite and austenite. The amount of retained austenite is negligible due to refrigeration [4]. Precipitated austenite is present exclusively as a thin layer ($\sim 3\text{ nm}$) at martensite lath interfaces based on electron microscopy, but the volume fraction from X-ray diffraction measurements is uncertain, ranging from an average volume pct of 0.8 [4] to 4 [29] for the $482\text{ }^\circ\text{C}$ temper. For comparison, samples were also made in the as-quenched state, i.e. without the $482^\circ\text{C} \times 5\text{ h}$ tempering treatment.

Table I. Chemical Compositions (wt%) of AerMet[®] 100

Fe	Co	Ni	Cr	Mo	C	Ti	P	S	H (wppm)
Bal.	13.43	11.08	3.00	1.18	0.23	0.009	0.003	0.0008	0.35

Table II. Mechanical Properties of AerMet[®] 100

Hardness (Rockwell C)	σ_{YS} MPa (ksi)	σ_{UTS} MPa (ksi)	RA (%)	K_{IC} MPa $\sqrt{\text{m}}$ (ksi $\sqrt{\text{in}}$)
54	1765 (256)	1985 (288)	61	139 [LR] (120) 127 [CR] (116)

Electrochemical H-Charging

The specimen of AerMet[®] 100 used for H-charging was a bare thin plate type having nominal dimensions of $12.7 \times 6.4 \times 0.5$ (mm). Prior to charging, each specimen was ground to a 600-grit finish and degreased ultrasonically. H-charging was performed at constant electrochemical potential under potentiostatic control. The charging solution was saturated $\text{Ca}(\text{OH})_2$ in pre-electrolyzed, 18.2 M Ω deionized water, having a pH value of ~ 12.1 . During charging, the temperature of this charging solution was maintained at $60^\circ\text{C} \pm 2^\circ\text{C}$. The total time interval for charging was 3 days (~ 72 h). This period was about 30% longer than that determined using a solution to Fick's Second Law for one-dimensional diffusion in a plane-sheet and a conservative estimate of H diffusivity of $3 \times 10^{-8} \text{ cm}^2/\text{s}$ at 60°C [31]. This prolonged time was used to ensure producing a uniform H concentration profile throughout specimen thickness [32]. The reversible H oxidation/reduction potential, $E_{\text{R}_{\text{H}^+/\text{H}}}$, in this solution was -1.33 V (vs $\text{Hg}/\text{Hg}_2\text{SO}_4$). For the present study, two different electrochemical potentials (E_{applied}) were applied, -1.95V and -2.5V , giving corresponding H-overpotentials ($\eta_{\text{chg}} = E_{\text{applied}} - E_{\text{R}_{\text{H}^+/\text{H}}}$) of -0.62V and -1.17V , respectively. The as-charged specimens were stored in liquid nitrogen for testing as needed.

Thermal Desorption Measurements

The principal method used for characterizing H diffusion and trapping was thermal desorption spectroscopy (TDS). The system was composed of a pre-pumping system (Tribodyn oil-free vacuum pump) for preparing vacuum condition needed for specimen exchange in the upper chamber, a continuous pumping system for providing normal testing vacuum condition ($\sim 1\mu\text{Pa}$ and lower) in the lower chamber, and a gas analyzing system for collecting data of gaseous composition.

In addition, an electrical furnace was mounted around the lower (at high vacuum for testing) chamber to provide isothermal and ramp heating conditions as needed. The TDS method was utilized to detect H by monitoring the change in H_2 partial pressure (P_{H_2}) versus time (t) in the lower chamber with the quadrupole gas analyzer, which was controlled by a computer program named Motf™ * for data acquisition. The normalized P_{H_2} - t data were transformed by computer programming to data set of H-concentration (C_H) and its rate of variation (dC_H/dt) versus time or temperature. The latter were further used to calculate parameters of H diffusion and trapping/detrapping, as detailed in the next section. An isothermal TDS testing mode was used for measuring H diffusivity parameters, where a constant temperature (in the range of 60 – 200°C) was established prior to the specimen loading into the lower chamber. A temperature programmed desorption mode was used for characterizing H desorption/detrapping behavior by observing the variation of desorption maxima with heating rate. Locating the temperature for the desorption maxima, T_m , was facilitated by a software named PeakFit™ ** in dealing with ambiguous or hidden peaks. Also, a peak was recognized only if it was reproducible in multiple-sample tests. In this temperature programmed TDS, the specimen was heated from room temperature to 550°C at a constant ramp rate in the range of 1 - 10°C/min upon loading into the lower chamber. The background P_{H_2} in the vacuum chamber was approximately 0.02 ~ 0.04 μ Pa, depending on temperature, as determined by performing TDS experiments on uncharged specimens. This information was used to establish background P_{H_2} for later subtraction from the apparent pressure data. In either isothermal or temperature programmed TDS modes, to restore the vacuum in the chamber upon specimen installation, specimens were first held at room temperature for ~ 30

* Motf™ is a software made by Ametek, Paoli, PA 19301.

** PeakFit is a product of AISN Software Inc., Mapleton, OR 97453.

minutes in the upper chamber, then dropped into the lower chamber (preheated in the case of isothermal TDS) for immediate testing by starting-up the gas analyzer. This hold time is small compared to the 72 h charging time, taking account of the low diffusivity at room temperature.

Diffusible and Total H Capacity Measurements

For selected H-charging and/or baking conditions, the barnacle electrode method [33] was used to measure the diffusible H concentration, $C_{H,diff}$. H-charging procedures were the same as stated earlier. Deaerated-saturated $\text{Ca}(\text{OH})_2$ was used as the extraction solution for H oxidation. An extraction potential of -1.00 V (vs $\text{Hg}/\text{Hg}_2\text{SO}_4$) was maintained potentiostatically. Temperature was constant at 23°C during extraction. More detailed information was included elsewhere [34].

For selected cases, the total H concentration ($C_{H,tot}$) was determined using a modification of the LECO/ASTM E1447 melt-extraction method [35]. The same H-charging procedures were used as described earlier. Immediately following charging, the specimens were submersed in liquid nitrogen. Rather than melting, the specimen was heated to a temperature slightly below the fusion temperature to extract the H into an inert-carrier gas. This method produced less scatter in H concentration data than the LECO-fusion method [35].

THEORETICAL BASES FOR DATA DEDUCTION

Determination of Diffusivity

From the H partial pressure (after background P_{H_2} subtraction) – time ($P_{H_2} - t$) data obtained in isothermal TDS tests, the area under the $P_{H_2} - t$ curve ($\int P_{H_2} dt$), is calculated using the trapezoidal

integration method. The time needed to generate one-half of this amount of area, $t_{1/2}$, is determined, as demonstrated in Fig. 1. Then the H diffusivity, D , is calculated using [36]:

$$D = \frac{0.0492B^2}{t_{1/2}} \quad \text{Eq. 1}$$

where B is specimen thickness. For using Eq. 1 it is assumed that a hydrogen diffusion coefficient is independent of the H concentration profile during testing and is valid for flat-plate specimens.

For lattice H diffusion, such as in the case for a pure iron, D is denoted as D_L to represent the diffusivity in a microstructural environment without trap sites. By distinction, D for the effective or apparent H diffusivity is denoted as D_{app} which takes account of trapping and detrapping effects.

Temperature Dependence of Diffusivity and Activation Energy

In general terms, temperature dependence of H diffusivity $D(T)$ is described by [37]:

$$D(T) = D_0 \exp\left(-\frac{E_m}{RT}\right) \quad \text{Eq. 2}$$

where D_0 is the pre-exponential diffusion coefficient, E_m is the activation energy for lattice migration of H, R is the gas constant (8.31 J/mol-K), and T is the absolute temperature. Likewise, for the apparent H diffusivity, D_{app} , the corresponding activation energy is denoted as E_m^{app} to represent the trapping-affected migration energy. In either case, the activation energy, E_m or E_m^{app} , can be determined via the slope of a $\ln D(T)$ versus $1/T$ plot by linear regression.

Diffusion-Limited H Desorption

If the process of H desorption is surface-reaction limited, H diffusivities determined from TDS data (and hence Eq. 1) do not accurately represent D in the bulk specimen. Consequently, diffusion-controlled desorption must be ensured during TDS experiments in order to justify the validity of the diffusivity data. One of analytical expressions that describes thermal desorption from a homogeneously charged specimen is [38]:

$$\frac{dX_d}{dt} = v_x (1-X_d)^n \exp\left(\frac{-E_d}{RT}\right) \quad \text{Eq. 3}$$

where v_x is a constant, X_d is the fraction of integrated quantity of H desorbed and E_d is the activation energy for desorption. E_d may be estimated as the sum of E_m and E_b (the binding energy for H trapping) for a H egress process that dominated by rate-limiting detrapping and lattice migration followed by non-rate-limiting surface desorption. If $n = 1$ then dX_d/dt versus $(1-X_d)$ is linear and the desorption process is a first order process controlled by detrapping and diffusion of H atoms. If $n = 2$ then dX_d/dt versus $(1-X_d)^2$ is linear and the H egress is surface reaction-limited, a 2nd order process governed by recombinative H desorption of di-hydrogenation or H_2 .

Activation Energy for H Desorption

In Eq. 3, the apparent activation energy for H desorption, E_d , can be calculated using ramp TDS data obtained at different heating rates (dT/dt). It is observed that the temperature for the peak of the desorption rate, T_m , shifts with variation in dT/dt , as demonstrated in TDS [39] as well as differential thermal analysis [40]. Then E_d depends on T_m and dT/dt according to [40]:

$$\frac{d \left[\ln \left(\frac{dT/dt}{T_m^2} \right) \right]}{d \left[\frac{1}{T_m} \right]} = -\frac{E_d}{R} \quad \text{Eq. 4}$$

Thus, using TDS data of T_m at various dT/dt , E_d can be calculated through the slope of the $\ln[(dT/dt)/T_m^2]$ versus $1/T_m$ plot by linear regression. This type of analysis can be applied to each trap peak observed during temperature programmed desorption.

Trapping-Affected H Transport

For reversible traps, it is assumed that dynamic equilibrium exists between the reversibly trapped H population and H in interstitial lattice sites [18]. Then H diffusion is slowed because of this interaction between diffusing H and low binding energy reversible traps. In contrast to this effect, strong irreversible traps are generally not in equilibrium with the lattice H and do not further interact with lattice H upon saturating. With this assumption, Oriani [18] proposed an equation describing the apparent or trapping-affected H diffusivity (D_{app}) in terms of the density of trap sites and trap binding energies. Assuming a low-reversible trap site coverage and low lattice solubility of H, D_{app} is related to the number of reversible trap sites of each type per unit volume, N_r , with binding energy, E_b , according to [18]:

$$D_{app} = \frac{D_L}{1 + \frac{N_r}{N_L} \exp \left(\frac{E_b}{RT} \right) (1 - \Theta_T)^2} \quad \text{Eq. 5}$$

where N_L is the number of ordinary interstitial sites available for H in the pure lattice, and Θ_T is fractional trap-site coverage.

As the trap site coverage is generally far less than unity ($\Theta_T \ll 1$), Eq. 5 can be simplified with satisfactory precision as:

$$D_{app} = \frac{D_L}{1 + \frac{N_r}{N_L} \exp\left(\frac{E_b}{RT}\right)} \quad \text{Eq.6}$$

or

$$\ln\left(\frac{D_L}{D_{app}} - 1\right) = \ln\left(\frac{N_r}{N_L}\right) + \frac{E_b}{RT} \quad \text{Eq.6a}$$

Thus, by conducting TDS analysis to obtain D_{app} at various temperatures (T), a single overall binding energy E_b and a single trap fraction N_r/N_L can be determined from the slope and intercept, respectively, of the $\ln[(D_L/D_{app})-1]$ versus $1/T$ curve, by linear regression. This analysis requires estimation of D_L which is discussed further below.

Modeling H Desorption Rate

Assuming that H desorption is dominated by diffusion and detrapping processes, Ono and Meshii [41] proposed a solution for the net desorption of H from a bulk specimen in the presence of a single trap state with N_r sites and a binding energy of E_b . According to their model, the desorption (or evolution) rate, expressed in the variation of H concentration in normal interstitial sites (C_L) over a incremental time, $\partial C_L/\partial t$, can be described using

$$\frac{\partial C_L}{\partial t} = C_H \left(\frac{\pi}{2d}\right)^2 D_0 \exp\left(\frac{-E_m}{RT}\right) \left[1 + \gamma \frac{N_r}{N_L} \exp\left(\frac{E_b}{RT}\right)\right]^{-1} \quad \text{Eq.7}$$

where C_H is the total H concentration, $2d$ is the thickness of a semi-infinite plate specimen, and

$$\gamma = \frac{Z_i v_i \exp\left(\frac{S_i}{k}\right)}{Z_d v_d \exp\left(\frac{S_d}{k}\right)} \quad \text{Eq.8}$$

in which k is Boltzmann's constant, Z_d and Z_i are the coordination numbers for H in interstitial and trap sites, v_d and v_i are the vibrational frequencies, and S_d and S_i are the entropies of detrapping and trapping, respectively [41]. Eq. 7 has been used to simulate the H desorption rate – time spectrum, and its validity is examined in the present work.

RESULTS

Temperature and Overpotential Dependence of Apparent H Diffusivity

From the isothermal TDS tests conducted at various temperatures ranging from 60°C to 200°C, data sets of H partial pressure versus time ($P_{H_2} - t$) were collected and the apparent H diffusivity, D_{app} , calculated according to Eq. 1 using the trapezoidal integration method introduced earlier. These data sets were also transformed to desorption rate (expressed as dC_H/dt where C_H denotes the instantaneous H concentration) versus time, a representative example is given in Fig. 2. Fig. 2 shows that, within the time interval set for the TDS detection, the saturation of H desorption is observed. The fraction of H desorbed, X_d , has also been calculated and is plotted against time together with the $dC_H/dt - t$ curve in Fig. 2. To check the diffusivity data validity, as described in the preceding section, H desorption rate is expressed alternatively as the rate of X_d , dX_d/dt , against X_d and $(1 - X_d)$, as shown in Fig. 3. As required by Eq.3, a satisfactory linearity of the $dX_d/dt - X_d$ (or $1 - X_d$) relationship confirms that the H egress during the TDS test is a first order process. Thus it describes a process of volume diffusion-limited desorption, and hence, the corresponding diffusivity data calculated based on these TDS data describe the transport of H in the steel.

In Fig. 4a, the apparent H diffusivity, D_{app} , is plotted against reciprocal absolute temperature, $1/T$, for two groups of specimens that were H charged at 60°C and at overpotentials, η_{chg} , of -1.17V and -0.62V, with diffusible H concentration of about 8 and 7.5 wppm, respectively. Using Eq. 2, a linear regression analysis of the data in Fig. 4a results in the apparent activation energies for H diffusion, E_m^{app} , of 17.7 kJ/mol (0.18 eV/atom) and 18.0 kJ/mol (0.19 eV/atom) for $\eta_{chg} = -1.17V$ and -0.62V, respectively. The standard error of E_m^{app} is 0.18 - 0.2 kJ/mol (0.002 eV/atom) for the regression. The pre-exponential constants in Eq. 3, D_0 , are $3.71 \times 10^{-5} \text{ cm}^2/\text{s}$ and $1.59 \times 10^{-5} \text{ cm}^2/\text{s}$, respectively. The standard error of D_0 is $1.5 - 3.6 \times 10^{-7} \text{ cm}^2/\text{s}$. Then, the temperature dependence of D_{app} for AerMet® 100 charged at 60°C in relation to the two overpotentials can be described using:

$$D_{app} [\text{cm}^2 / \text{s}] = \begin{cases} 3.71 \times 10^{-5} \exp \left\{ \frac{-17.7 [\text{kJ} / \text{mol}]}{RT} \right\} & (\eta_{chg} = -1.17V) \\ 1.59 \times 10^{-5} \exp \left\{ \frac{-18.0 [\text{kJ} / \text{mol}]}{RT} \right\} & (\eta_{chg} = -0.62V) \end{cases} \quad \text{Eq.9}$$

Values of D_{app} at 23°C was predicted by the regressed curve in Fig. 4a, to be $2.83 \times 10^{-8} \text{ cm}^2/\text{s}$ and $1.05 \times 10^{-8} \text{ cm}^2/\text{s}$ for $\eta_{chg} = -1.17V$ and -0.62V, respectively.* Since diffusivity curves in Fig. 4a are basically parallel and the calculated values of E_m^{app} are roughly equal (with 1.6% difference, or equal to the standard error) for the two charging overpotentials (or H concentrations), the gross H capacity does not seem to affect the activation energy for the trapping-affected diffusion process. Instead, the influence on the apparent H diffusivity is reflected by increasing D_0 with increasing H concentration through enhanced charging.

As a comparison, Fig. 4b shows D_{app} versus $1/T$ curves over temperatures of 70 – 120°C for the as-quenched AerMet® 100 specimens, together with the tempered specimens H-charged at the

same η_{chg} of -0.62V. E_m^{app} has been calculated to be 18.2 kJ/mol (0.19 eV/atom) using the same linear regression method, with a standard error of 0.2 kJ/mol (0.002 eV/atom). D_0 for the as-quenched specimens is $3.97 \times 10^{-5} \text{ cm}^2/\text{s}$, with a standard error of $3.8 \times 10^{-7} \text{ cm}^2/\text{s}$. Similar to the results in Fig. 4a, the difference in D_{app} between the tempered and the as-quenched martensitic alloys is not seen by a change in the activation energy for migration, since the difference in their E_m^{app} values is still within the standard error. Instead, D_0 contributes dominantly to the different apparent diffusivities in the two different microstructures.

Effects of Baking on Apparent H Diffusivity

The effect of baking procedure on D_{app} determined over temperatures of 60 – 200°C was investigated for specimens H-charged at 60°C for one fixed overpotential value, i.e. $\eta_{\text{chg}} = -0.62\text{V}$ for 3 days. Isothermal TDS was performed to determine D_{app} for specimens under two post-charging conditions, i.e. (1) 3 days exposure at 23°C (or 23°C baking), and (2) baking at 200°C for 2.3 h (2.3 h = 2 data acquisition intervals in the testing program for TDS), in addition to the as-charged condition described in the preceding subsection. Fig. 5 shows a comparison of net H_2 pressure versus time at typical desorption temperatures. Different y-axis scales are used to display the shapes of curves under baked and as-charged conditions. In fact, for baked conditions, especially at 200°C, the H partial pressure level is about 3 decades lower as compared with that of as-charged condition, suggesting substantial H egress during the elevated temperature baking. From the TDS data including those shown in Fig. 5, the apparent H diffusivity, D_{app} , was calculated using Eq.1 for the two baked conditions as well as the as-charged condition. In Fig. 6, D_{app} is plotted against the reciprocal of absolute temperature, $1/T$, comparing the effect of baking on the apparent

* TDS was not suitable for H diffusivity measurements at temperatures as low as room temperature.

diffusivity. The apparent activation energy for diffusion, E_m^{app} , was determined by linear regression (Eq.2) for the three test conditions. Values of E_m^{app} thus obtained are 18.0 kJ/mol (0.19 eV/atom), 18.2 kJ/mol (0.19 eV/atom) and 18.9 kJ/mol (0.20 eV/atom) for specimens tested under as-charged, 23°C baked and 200°C baked conditions, respectively. The standard error of E_m^{app} is 0.2 kJ/mol (0.002 eV/atom) for the regression. The parameters D_0 in Eq.3 are 1.59×10^{-5} cm²/s, 1.23×10^{-5} cm²/s and 1.13×10^{-5} cm²/s in the corresponding order. The standard error of D_0 is $1.1 - 1.5 \times 10^{-7}$ cm²/s. As such, the temperature dependence of D_{app} for the as-charged and baked conditions can be described by:

$$D_{app} [cm^2 / s] = \begin{cases} 1.59 \times 10^{-5} \exp \left\{ \frac{-18.0 [kJ / mol]}{RT} \right\} & (\text{as - charged}) \\ 1.23 \times 10^{-5} \exp \left\{ \frac{-18.2 [kJ / mol]}{RT} \right\} & (23^\circ \text{C baked for 72h}) \\ 1.13 \times 10^{-5} \exp \left\{ \frac{-18.9 [kJ / mol]}{RT} \right\} & (200^\circ \text{C baked for 2.3h}) \end{cases} \quad \text{Eq.10}$$

Also, values of D_{app} at 23°C were determined by linear regression (Fig. 6) to be 1.05×10^{-8} cm²/s, 7.11×10^{-9} cm²/s and 4.90×10^{-9} cm²/s for as-charged, after 23°C baked and 200°C baked conditions, respectively.

As expected, H diffusivity depends on the amount of H remaining after outgassing exposure following electrochemical charging. As shown in Fig. 6, baking at room temperature leads to a general drop in the diffusivity at all temperatures as compared with the as-charged specimen group. Elevating the baking temperature to 200°C further decreases D_{app} at all test temperatures. This H concentration dependent diffusion behavior will be discussed later. In contrast to the obvious change in D_{app} , the apparent activation energy is basically insensitive to the baking treatments, since the value of E_m^{app} is still within the range of standard error (0.2 kJ/mol) after 23°C baking and only

about 4% increase in E_m^{app} after 200°C baking, compared with the as-charged condition. The influence of baking on apparent diffusivity is mainly attributed to the variation of D_0 .

Effect of Baking on Total and Diffusible H Capacity

To investigate the baking effect on the H capacity, the total and diffusible H concentrations were measured for the as-charged (at $\eta_{\text{chg}} = -0.62\text{V}$ only) and the room temperature and 200°C baked specimens (detailed in the preceding section). Data for the total H concentration ($C_{\text{H,tot}}$) determined from LECO and diffusible H concentration ($C_{\text{H,diff}}$) are listed in Table III for these three conditions. After 23°C baking for 72h, $C_{\text{H,tot}}$ decreased about 1/3 from that contained in the as-charged specimen, and further decreased about another 1/3 of the as-charged level by baking at 200°C for 2.3h. Regarding the diffusible H concentrations, in the as-charged condition, $C_{\text{H,diff}}$ is about 1/4 that of $C_{\text{H,tot}}$. Upon the 23°C baking, $C_{\text{H,diff}}$ decreases to less than 1 wppm (0.34 wppm), close to the total H concentration in the as-received AerMet® 100 (0.35 wppm in Table I – likely irreversibly trapped). While substantial total H remains after the 200°C baking, the diffusible H concentration, $C_{\text{H,diff}}$, is too low to be detectable by the Barnacle cell method performed at room temperature. However, as seen from tiny desorption peaks in Fig. 5, there is still a finite amount of diffusible or weakly trapped H remaining after the 200°C baking. Processing of the corresponding TDS data suggests a residual amount of $\sim 10^{-2}$ wppm H desorbed in the isothermal TDS test (190°C) for a specimen previously baked at 200°C.

Table III. Total H and Diffusible H in AerMet® 100 Affected by Baking

Condition prior to TDS	$C_{H,tot}$ (wppm) (60°C)	$C_{H,diff}$ (wppm) (23°C)
As-charged ($\eta_{chg} = -0.62V$)	27.4	7.5
Charged + baked at 23°C for 72 h	20.2	0.34
Charged + baked at 200°C for 2.3 h	9.67	undetectable

Baking Temperature Effect on H Desorption from Bare AerMet® 100

Instead of an isothermal TDS test mode, the H trapping/detrapping behavior is more readily studied by detecting how H detraps from each specific type of site as desorption temperature increases, i.e. by conducting a ramp TDS test in which the sample is heated to a proper maximum temperature at a fixed heating rate. For investigating the effect of baking temperature on H trapping/detrapping in AerMet® 100, TDS tests were performed at a ramp rate of 5°C/min for specimens charged at $\eta_{chg} = -0.62V$ and then baked for 3 days (72 h) at room temperature (23°C) and 2 h at various temperatures from 100 °C to 500 °C. Fig. 7 shows H desorption rate (expressed as variation of H concentration with time, dC_H/dt) versus temperature curves obtained by TDS for specimens baked at 23°C and various elevated temperatures, in comparison with the as-charged specimen. Each peak on a H desorption rate curve reveals a maxima of H egress rate as a result of H release from a specific type of trap site when the thermal energy of the steel exceeds the apparent H desorption energy. Three distinct trap states are identified in Fig. 7, denoted peak 1, peak 2 and peak 3 in the order of temperature at which each peak is centered. As discussed later, peak 1 contributes to the majority of the amount of H desorbed (>90%). The magnitude of the desorption rate over a range of desorption temperatures is decreased after baking at room temperature, especially in the

temperature range covered under peak 1, i.e. about 20% decrease in the amount of desorbed H compared with the as-charged specimen. Baking at 100°C further decreases the general H desorption rate in the whole temperature range, particularly under peak 1 where the amount of desorbed H decreases ~ 75%. Up to this baking temperature, the effect of baking on H detrapping can be classified as a quantitative change, since all the three trap states are retained, with decreased height of each peak. In contrast, baking at 200°C essentially removes H associated with peak 1 from the alloy and thus leads to the disappearance of the first peak on the desorption curve in Fig. 7. As estimated from the dC_H/dt versus time curves obtained from TDS, the amount of H associated with peak 1 in Fig. 7 decreases by nearly 100% for the 200°C baked specimen, compared to the as-charged case. However, the peak height change is marginal for peak 2 and peak 3 under this 200°C baked conditions. As indicated by Fig. 7, baking at 300°C removes H associated with both peak 1 and peak 2 and substantially decreases the height of peak 3. Further increasing baking temperature to 350°C, 400°C and 450°C gradually decreases the magnitude of peak 3. Finally, baking at 500°C totally removes H associated with peak 3. It is noted that, starting from the baking temperature of 400°C, peak 3 shifts to a higher temperature as baking temperature increases. This is probably attributed to the microstructural change during the 2 h baking when the baking temperature is close to or higher than the tempering temperature (482°C) used for the present alloy. It seems that a further tempered martensite structure and coarsened precipitates may increase the binding energy associated with relevant deep H-traps and the number of trap sites.

Baking Time Effect on H Desorption from Bare AerMet® 100

In order to have a fundamental assessment of baking effect on residual trapped H, time dependence of the H desorption behavior is studied systematically for a baking temperature that is

adopted in industry, i.e. 190°C [42]. As before, specimens for this investigation were first charged at 60°C for 3 days at an overpotential of -0.62V. Except for the specimens that were tested under as-charged conditions, other specimens were then baked at 190°C for varied time intervals from 0.5h to 200h. TDS tests were conducted at a ramp heating rate of 5°C/min. The desorption rate versus temperature curves are given in Fig. 8 corresponding to these test conditions to compare the effect of baking time on residual trapped H.

As shown in Fig. 8, when baking time is shorter than 2h, the amount of H egress increases significantly with increasing baking time, as indicated by an obvious decrease in the height and area associated with the desorption rate curves, especially that of the first peak on each curve. At a critical value of baking time, around 2h for the present study, the first peak on the desorption rate curve disappears as a result of substantial H egress. As baking time further increases, no significant change is evidenced regarding the location, height and area of the desorption rate peaks, even for the specimen baked for as long as 200h. In fact, 2h is quite enough for H egress to reach a state of saturation at 190°C, as evidenced by the fraction of H desorption (X_d) versus time curve in Fig. 2.

For each peak in Fig. 8, the H concentration has been calculated by integrating the dC_H/dt versus time curve for the range of time corresponding to the peak coverage. Fig. 9 shows the variation of H concentration for baked specimens ($C_{H,baked}$) relative to that of the as-charged specimen ($C_{H,as-charged}$), expressed by the ratio $C_{H,baked}/C_{H,as-charged}$ for each peak. For peak 1, there is a dramatic change in the relative H concentration in the initial 2 h of baking. As indicated by Fig. 9, $C_{H,baked}/C_{H,as-charged}$ dropped to ~ 2% after baking for 0.5 h and to ~ 0.1% after baking for 2 h. For baking time longer than 2 h, there is no sizeable change in $C_{H,baked}/C_{H,as-charged}$ for peak 1. The relative H concentration change for peak 2 is less evident. After baking for half a hour, the amount of H desorbed for peak 2 is ~ 80% of the as-charged one, and dropped to ~ 30% of the as-charged one when baking time increases to 2 h. Baking for longer than 2 h does not make any appreciable

further change in $C_{H,baked}/C_{H,as-charged}$ for peak 2. The relative H concentration change with baking time for peak 3 is the least of the three. For baking time of less than 5 h, $C_{H,baked}/C_{H,as-charged}$ is around 30% and is around 20% for baking time of 5 h and longer. As such, data in Fig. 9 confirms, in a quantitative manner, that the initial 2 h baking is of key importance in removing diffusible and weakly trapped hydrogen from the H-charged alloy.

Apparent (Total) Activation Energy for H Desorption

To associate a H trap state with a responsible microstructural feature, it is of key importance to determine the binding energy (E_b) with which H is trapped into the type of traps, since an individual microstructural feature binds H with a specific amount of energy. Using Eq.6 to determine E_b requires temperature dependent data sets for both D_{app} and D_L , the latter in turn requires the value of the migration energy for lattice diffusion (E_m). Unlike pure iron, the values of D_L and E_m are unknown for the multi-component alloy system of AerMet[®] 100. For a system in which surface reaction is insignificant, the thermal desorption is principally controlled by diffusion and detrapping processes. Accordingly, the apparent or total desorption energy, E_d , can be approximated to equal the sum of E_m and E_b . Therefore, E_d will provide a solid basis to estimate E_b once E_m is known, or to estimate the range of E_b if the range of E_m can be predicted. To provide data necessary for analysis through Eq.4, ramp TDS tests were conducted at various heating rates (dT/dt) from 1 to 10 °C/min for specimens charged at 60°C and two overpotentials of -0.62V and -1.17V (with different total H capacities).

Fig. 10 shows representative H desorption curves obtained from the ramp TDS tests. For the temperature range from room temperature to 500°C, three persistent desorption peaks can be identified and are marked peak 1, peak 2 and peak 3 in the order of increasing T_m . Fig. 10 shows

that the position of T_m shifts as dT/dt varies, as expected from similar studies [39,40]. The ramp TDS data were processed to generate $\ln[(dT/dt)/T_m^2]$ plotted against the reciprocal absolute temperature, $1/T_m$, as shown in Fig. 11, for the H detrapping associated with the first desorption rate peak (peak 1). According to Eq.4, E_d can be calculated from the slope of the $\ln[(dT/dt)/T_m^2]$ versus $1/T_m$ curve. Using a linear regression analysis, E_d for H detrapping associated with peak 1 was determined for $\eta_{\text{chg}} = -0.62\text{V}$ and -1.17V , respectively. Data plots similar to Fig. 11 were also made for peak 2 and peak 3 as shown in Fig. 12 and Fig. 13, respectively. Linear regression was used to calculate the values of E_d , according to Eq.4, for peak 2 and peak 3, for specimens charged at the above two overpotentials. E_d values, along with their standard error in the regression, are listed in Table IV for all these conditions.

Table IV. Calculated Values of E_d [kJ/mol (eV/atom)] using Eq. 4

Trap State	Peak 1	Peak 2	Peak 3
$\eta_{\text{chg}}=-0.62\text{V}$	21.6 ± 0.2 (0.224 ± 0.002)	72.2 ± 0.3 (0.748 ± 0.003)	99.1 ± 0.3 (1.027 ± 0.003)
$\eta_{\text{chg}}=-1.17\text{V}$	21.4 ± 0.2 (0.222 ± 0.002)	71.3 ± 0.3 (0.739 ± 0.003)	99.9 ± 0.3 (1.035 ± 0.003)

The calculated results in Table IV suggest that, for each trap state, values of E_d are basically independent of the H-charging overpotential level or $C_{\text{H,diff}}$ as well as $C_{\text{H,tot}}$ levels, since the difference in E_d is within the standard error for peak 1, about 1% for peak 2 and less than 1% for peak 3. Rather, E_d is intrinsically linked to specific types of trap sites or types of relevant

microstructural features represented by each peak in Fig. 10, regardless of the two trap coverage obtained.

Determination of Binding Energies for H Trapping

1. Analytical Work to Determine Lattice Diffusivity D_L (E_m , D_0)

The establishment of E_d values, as accomplished above, provides an estimation of the scope of E_b , the binding energy for H trapping, assuming that $E_d \approx E_m + E_b$. The challenge is to separate E_b from E_m associated with interstitial transport in a perfect lattice. The theoretical basis for doing this is expressed by Eq. 6, with $D_L = D_0 \exp(E_m/RT)$ according to Eq. 2. The value of D_L (and hence E_m) is unavailable in the literature for AerMet[®] 100. Consequently, instead of using Eq. 6 to determine E_b directly, an analytical procedure assuming the applicability of Eq. 6 is used to approach a logically plausible value (or range of values) of E_m according to information currently available for several alloys and pure iron. *

The calculated results provide a range of values (D_0 , E_m) that meet the above requirements, with selected results for discrete parameters shown in Fig. 14 and Fig. 15. Each plot in Fig. 14 or 15 provides a means of understanding how each qualified value plotted is determined, that is: (1) for each selected E_m , qualified values of D_0 are determined by equating ($E_b + E_m$) to E_d ; (2) with these

* This procedure is subject to the following guidelines: (a) selected E_m should be smaller than trap-affected E_m^{app} for heat-treated AerMet[®] 100 (17 – 18 kJ/mol) but larger than the reported E_m for pure iron (7 – 10 kJ/mol) [43], (b) D_0 should be so selected that the resultant lattice diffusivity at room temperature ($D_{L,RT}$) is significantly larger than $D_{app,RT}$ for heat-treated AerMet[®] 100 ($\sim 10^{-8}$ cm²/s), (c) calculated E_b should meet the requirement: $E_m + E_b = E_d$, and (d) calculated N_t/N_L should be significantly less than 1. Qualified values of E_m for perfect lattice should meet all of these 4 guidelines as the minimum requirement, though other criteria may be incorporated. The calculation was performed by a recursive program to output only the valid range of parameters that meet the above guidelines. The key points are as follows. For each selected combination of E_m and D_0 , and each temperature T at which there was experimental value of D_{app} , D_L is determined per Eq. 2. Using values of D_{app} and D_L at various temperatures, linear regression is conducted to generate E_b according to Eq. 6a. If $E_b = E_d - E_m$ considering the experimentally determined range of E_d (Table IV), $D_L = f(D_0, E_m)$ is chosen as a valid candidate, otherwise the selection is rejected. In either case the calculation is re-initiated with a newly selected combination of E_m and D_0 , until all the values in the logically plausible range (per the above guidelines) are tried.

qualified D_0 , $D_{L,RT}$ and N_i/N_L are determined (see dashed lines). It is found from examples in Figs. 14-15 that, with perfect lattice E_m approaching the upper bound (i.e. E_m^{app} of 17 – 18 kJ/mol for the heat-treated AerMet[®] 100), either $D_{L,RT}$ approaches $D_{app,RT}$ for heat-treated AerMet[®] 100 ($\sim 10^{-8}$ cm²/s), or the valid E_d range found by experiment cannot be accessed. On the other hand, selecting the lower bound of perfect lattice E_m value tends to result in both a higher value of $D_{L,RT}$ and a lower value of N_i/N_L . This selectable range of E_m is summarized in Fig. 16. In brief, the analysis conducted justifies selecting E_m value(s) that approach the value(s) reported for pure iron [43].

Summarizing the extensive diffusion data on iron obtained by various investigators [43], it is found that the most concentrated data points are located on a narrow band that suggests an E_m value of ~ 10 kJ/mole for α -Fe. In view of statistical credibility, this E_m value should be used in the present approach to determine binding energies. According to the above analytical results, using lower bound values of E_m , i.e. that of pure iron, tends to generate values for the lattice diffusivity of the alloy that fit the expected effects of alloying elements in α -Fe on D_L , than using the upper bound values of E_m . The effects of alloying elements may be divided into roughly two parts, one to affect the apparent diffusion by acting as H trap sites with an appropriate binding energy [44], the other to affect the lattice diffusion as a result of lattice structure change by replacing a fraction of the Fe sites by the alloy elements present in substitutional solid solution. D_L is altered by changing either E_m or D_0 or both. In connection with this, the alloying effect on the lattice diffusion is reflected in the decreased D_0 compared with that of pure iron, as a result of taking $E_m = 10$ kJ/mol to perform the above analytical procedures (Figs. 14-15). Table V shows a comparison between lattice diffusion parameters in AerMet[®] 100 (Figs 14-15) and in pure iron by assuming the same E_m value in both.

Table V. Lattice Diffusion Properties Assuming Fixed $E_m = 10\text{kJ/mol}$

		AerMet [®] 100		Pure iron [43]
		$\eta_{\text{chg}} = -0.62\text{V}$	$\eta_{\text{chg}} = -1.17\text{V}$	
D_0	(cm^2/s)	5.6×10^{-6}	6.4×10^{-6}	7.5×10^{-4}
$D_L(25^\circ\text{C})$	(cm^2/s)	9.8×10^{-8}	1.1×10^{-7}	1.2×10^{-5}

As shown in Table V, when E_m is fixed at 10 kJ/mol, D_0 for lattice diffusivity is found to be $5.6 \times 10^{-6} \text{ cm}^2/\text{s}$, compared to D_0 of $7.5 \times 10^{-4} \text{ cm}^2/\text{s}$ for pure iron [42]. This result is consistent with literature data detailed as follows. Hagi [45] conducted a systematic investigation on the alloying effects on the diffusivity of $\alpha\text{-Fe}$, in which a series of elements including Co, Cr, Mo and Ni were individually added with varying amount into iron and used heat-treatment to ensure single phase $\alpha\text{-Fe}$ absent of other trap states. The values of the assumed perfect lattice D_L exhibited a consistent decrease in D_0 with increasing amount of alloying element (at.%M – where M denotes the alloying element in question), showing $\log D_L - T^{-1}$ curves for varying at.%M being basically parallel to that for pure iron [45]. In the present study, Hagi's data [45] were used to model the dependence of D_0 on at.%M for alloying with Co, Cr, Mo and Ni in AerMet[®] 100 individually. Then the total effect on D_0 for the alloy was generated by adding linearly the effect of each element. While it was hard to consider fully the complicated interaction between these elements, the calculation was simplified by considering only the role of relative atom radius. Calculated results with this assumption are plotted in Fig. 17, showing an equivalent alloying element effect on D_0 . When extrapolated to at.% ≈ 27.4 , corresponding to the total at.% of (Co+Cr+Mo+Ni) in AerMet[®] 100, $D_0 \approx 5 \times 10^{-6}$, which is very close to those listed in Table V. Therefore, the present analysis using the parameters in Table V is justified by the expected results based on solute additions to $\alpha\text{-Fe}$.

II. Determination of E_b from Experimental D_{app} and Analytical D_L by Eq. 6

Fig. 18 shows the determination of the global binding energy from $D_{app}(T)$ according to Eq. 6, where the values of $D_{app}(T)$ were taken from the experimental values for AerMet[®] 100 (Fig. 4a) and those of D_L were calculated by Eq. 2 using values of E_m and D_0 established in Table V. It is indicated in Fig. 18 that, although experimentally determined D_{app} values at various temperatures obviously differ for the two different H charging overpotentials (η_{chg}), or two different total H concentrations (C_H), which makes the two corresponding curves in Fig. 18 distinctly separate, the resultant values of global E_b are substantially equal (11.6 vs 11.4 kJ/mol, which are within the standard error of 0.2kJ/mol). Thus, like the independence of E_d on C_H in temperature-programmed TDS experiments, E_b is also shown to be independent of C_H when Eq. 6 is used. This confirms that the activation energy for H trapping is essentially determined by the specific trap site or type of trap sites associated with corresponding microstructural features.

E_m value for interstitial transport can now be used invariantly for determining E_b from E_d data for other trap sites of the same alloy. Assuming that E_m is constant, the values of E_b for other trap sites identified by peak 2 and peak 3 were calculated by subtracting E_m from E_d (since $E_d \approx E_m + E_b$). Table VI lists all E_b values determined for H trapped in these trap sites in specimens charged to two different C_H levels obtained from Table IV. The insensitivity of E_b to η_{chg} (or C_H) further confirms that the binding energy for H trapping depends primarily on the specific trap site or types of trap sites in connection with corresponding microstructural features. The association of trap peaks 1-3 with microstructural features in heat-treated AerMet[®] 100 is discussed later.

Table VI. Calculated Values of E_b , kJ/mol (eV/atom)

Trap State	Peak 1	Peak 2	Peak 3
$\eta_{\text{chg}} = -0.62\text{V}$	11.6 ± 0.2 (0.120 ± 0.002)	62.2 ± 0.3 (0.644 ± 0.003)	89.1 ± 0.3 (0.924 ± 0.003)
$\eta_{\text{chg}} = -1.17\text{V}$	11.4 ± 0.2 (0.118 ± 0.002)	61.3 ± 0.3 (0.635 ± 0.003)	89.9 ± 0.3 (0.932 ± 0.003)

H Trapping/Detrapping in As-quenched AerMet[®] 100

To clarify the potential contribution of precipitates, typically M_2C , in trapping H, especially with a low energy trapping state as depicted by peak 1, temperature-programmed TDS tests were also performed at various heating rates (dT/dt) for specimens with the as-quenched microstructure. Fig. 19 shows the results of H desorption rate versus temperature curve for the as-quenched martensitic AerMet[®] 100 charged at $\eta_{\text{chg}} = -0.62\text{V}$ (60°C) and TDS tested at $dT/dt = 5^\circ\text{C}/\text{min.}$, in comparison with the tempered alloy under the same charging and TDS conditions. TDS tests under other dT/dt conditions show a similar trend. It is interesting to note that the magnitude of peak 1 for the as-quenched alloy substantially decreases as compared with the tempered one. As estimated by calculating the area under the dC_H/dt versus time curve, the amount of H desorbed in the temperature range of peak 1 decreases to $\sim 2\%$ of that for the tempered alloy, under different dT/dt conditions. Although the as-quenched martensitic microstructure may still complex, it is certain that it does not contain M_2C precipitates as the tempered alloy does. Therefore, the results in Fig. 19 suggest that M_2C plays a dominant role in trapping H with an energy state associated with peak 1, which is to be discussed further. The magnitude of peak 2 or peak 3 for the as-quenched alloy is also less than that for the tempered alloy, but the extent of change is much less evident than the change with peak 1.

It was found that there is a minor change in the desorption maxima temperature T_m for peak 1 of the as-quenched alloy, as exemplified in Fig. 19, while the corresponding changes of T_m for peak 2 and peak 3 are negligible. Then, data of T_m obtained at various ramp rates (dT/dt) were processed to generate $\ln[(dT/dt)/T_m^2]$ versus $1/T_m$ for linear regression to calculate E_d according to Eq. 4. The value of E_d thus obtained for the as-quenched alloy is 18.9 kJ/mol for peak 1. Following the same analytical procedure as in the preceding section, E_b is estimated to be 8.9 kJ/mol as the binding energy for H-trapping associated with the evolution of peak 1 occurring in the as-quenched alloy.

H Thermal Desorption Modeling

As stated earlier, when H thermal desorption is governed primarily by two processes, diffusion and detrapping, Eq. 7 can be used to describe the rate of H desorption versus time or temperature, i.e. the evolution of a desorption peak. In the present analysis, Eq. 7 was used as the sole theoretical base to calculate the instantaneous rate in the variation of lattice H concentration (C_L). The analytical simulation was performed for the case of H desorption at a constant thermal ramp rate (dT/dt) for a specimen in the as-charged state. Since the total H concentration, C_H , changes during desorption, a recursive procedure is required to update C_H using the instantaneous values of $\Delta C_L/\Delta t$ and Δt in order to continue the simulation. For this purpose, a computer program coded with the programming language C++ was used to simulate the H desorption process. Its output file provides the data series of time, temperature and $\Delta C_L/\Delta t$. As the present ramp TDS results show a multiple trapping behavior (with multiple desorption peaks as in Figs. 7-8,10), the simulation was conducted individually for each trap state.

Values of all parameters in Eq. 7 are known except that of γ . Without prior knowledge of the physical characteristics of a trap site, it is hard to estimate γ by Eq. 8. In the present modeling work, key parameters regarding diffusion and detrapping, D_0 , E_m , E_b , and N_t/N_L , were assigned values exactly the same as those generated by the trapping analysis in the preceding section (Tables V-VI and Fig. 18). Various values of γ in the valid range suggested by Ono and Meshii [40] were tried and γ was chosen according to the best confidence level for the desorption curve fitting.

Typical modeling results for the evolution of peak 1 is shown in Fig. 20, in comparison with the corresponding experimental curves resulted from TDS ramp tests. The value of γ chosen for modeling peak 1 is 1.1. The results in Fig. 20, which represent the case of H-charged at $\eta_{\text{chg}} = -0.62\text{V}$, indicate that the model desorption curve predicts correctly the temperature for the H egress maxima, T_m , with variation in dT/dt , although there is an obvious difference in the shapes of curves between the experimental results and the model. Similar results have been obtained for the cases of the other two trapping states (peak 2 and peak 3) and for specimens charged at $\eta_{\text{chg}} = -1.17\text{V}$, i.e. the corresponding modeling procedures predicted the positions of T_m correctly, while it was still unable to predict the desorption peak shape. As for the change in the total H concentration by changing η_{chg} from -1.17V to -0.62V , there is no sensible effect on the outcome of modeling as long as the values of E_b are selected according to Table IV. Also, the same value of γ can be used for each peak in both η_{chg} conditions. The inability of the model in giving the right desorption spectrum (the shape) may result from more complicated factors including the over-simplified assumptions associated with Eq. 7, and will be further discussed in a latter section.

DISCUSSION

Concentration-Dependent Diffusion

A previous investigation on the trap-affected H diffusion in AerMet[®] 100 established the dependence of the apparent diffusivity, D_{app} , on both diffusible and total H concentrations, $C_{H,diff}$ and $C_{H,tot}$ [46]. Specifically, logarithmic values of D_{app} increase linearly with increasing $C_{H,diff}$ or $C_{H,tot}$. These trends of concentration-dependent H diffusivity have also been found by other investigators studying H diffusion in iron and steel [19, 47]. In the present research, D_{app} increases with the total H capacity as a result of increased charging overpotential (Fig. 4a). A similar trend of D_{app} is also found in the baking effect, i.e. D_{app} decreases with increasing the degree of baking post H charge (Fig. 6), since this corresponds to a decrease in both $C_{H,diff}$ and $C_{H,tot}$ (Table III). Therefore, the influences of either the charging overpotential or the baking procedure on D_{app} confirm the concentration dependence of D_{app} in AerMet[®] 100.

The extensively observed D_{app} dependence on H concentration most probably results from the change in trap occupancy by H. Either increased η_{chg} or reduced baking increases the perfect lattice-H concentration (C_L), and leads to an increase in the coverage of trap sites in equilibrium with lattice sites. This tends to decrease the interaction between lattice-dissolved H and the more highly occupied trap sites and hence, an increase in apparent H diffusivity. For instance, with an estimated $2.1 \pm 0.5 \times 10^{18}$ reversible trap sites per cm^3 in AISI 4340, D_{app} increases by more than an order of magnitude when C_L increases from 10^{-3} to 0.1 wppm [47]. By comparison, with an estimated $4.9 \pm 0.6 \times 10^{18}$ reversible trap sites per cm^3 in the 3.5% Ni-Cr-Mo-V steel, D_{app} increases much more for the same increase in lattice-H concentration [47]. For AerMet[®] 100 studied presently, the H trap occupancy change is evidenced clearly in Fig. 7 where baking at room temperature and 200°C decreases, to varying degrees, the trap occupancy indicated by the height

and existence of desorption peak(s). Then, this change in trap occupancy may account for the consistent decrease in D_{app} shown in Fig. 6.

The H concentration dependent D_{app} can also be predicted from Eq. 5 through the effect of H trap occupancy. In Eq. 5, the trapping properties, E_b and N_t/N_L , are primarily determined by the corresponding microstructural features that generate the relevant trap sites. E_b was not seen to be affected by H concentration, as indicated in Table IV. Then, an increase in the fractional trap site occupancy, Θ_T , due to either enhanced charging or reduced baking, will lead to an increase in D_{app} , according to Eq. 5. Of course, D_{app} never approaches D_L since Θ_T never approaches 1 in Eq. 5 for a high density of low strength reversible traps.

Apparent Diffusion Parameters

Equation 2 indicates that temperature dependence of diffusion is controlled by E_m and D_0 , and experimental results for D_{app} of H in 482°C tempered AerMet® 100 are summarized by Eq. 9. As indicated, when charging overpotential η_{chg} changes from -1.17V to -0.62V, values of E_m^{app} are statistically equal (within the standard error), whereas D_0 shows a more significant decrease of 57% (3.71×10^{-5} to 1.59×10^{-5} cm²/s). Similarly, for the results of the baking effect on H diffusion, Eq. 10, values of E_m^{app} are statistically equal for 23°C and 200°C baked specimens as well as the as-charged specimens (18.2 and 18.9 versus 18.0 kJ/mol), whereas D_0 decreases about 23% and 29% (1.23×10^{-5} cm²/s and 1.13×10^{-5} versus 1.59×10^{-5} cm²/s) for the two baking conditions, respectively. The effect of H concentration on D_{app} is mainly attributed to variation in D_0 rather than E_m^{app} , as evidenced by parallel $\log(D_{app}) - 1/T$ curves in Fig. 4a and Fig. 6 under different H capacity conditions. As for the microstructural effect, difference in E_m^{app} between the tempered and as-quenched alloys is also well within the standard error, while D_0 for the as-quenched alloy is about

2.5 times that for the tempered alloy, as demonstrated by parallel $\log(D_{\text{app}}) - 1/T$ curves in Fig. 4b. This D_0 -dominated diffusion behavior is also demonstrated by the alloying effect on diffusivity observed by Hagi [45] where $\log(D) - 1/T$ curves for different amounts of alloying element addition are basically parallel, revealing similar E_m but distinct D_0 values.

A well-known theoretical expression of D_0 is provided by Wert and Zener [48] as:

$$D_0 = n\alpha va^2 \exp\left(\frac{\Delta S_m}{R}\right) \quad \text{Eq. 11}$$

where n is the number of nearest neighbor jump sites, α is a coefficient depending on the location of the interstitial positions (e.g. $\alpha=1/24$ for b.c.c. and $1/12$ for f.c.c.), a is the lattice parameter, v is the vibration frequency of a solute atom in an interstitial site, and ΔS_m is the change in molar entropy of migration. For apparent H diffusion in AerMet[®] 100 under different conditions of microstructure (tempered and as-quenched, Fig. 4b) and H-concentration (via charging and/or baking, Fig. 4a, Fig. 6), values of a , n , α and v are basically the same. Hence, the change of D_0 in response to the variation in microstructure and H concentration is attributed to the different ΔS_m values associated with each case. Currently, limited knowledge of ΔS_m as well as its experimental determination makes it difficult to analyze the this driving force parameter in evaluating D_0 .

The apparent diffusivity has also been studied for an older UHSS, i.e. AISI 4130 [46]. An identical analysis in [46] generated a value of $E_m^{\text{app}} = 8.7$ kJ/mol (0.09 eV/atom) for AISI 4130 under similar H charging conditions. As an increase in the activation energy for D_{app} is most likely a result of increased strength and density of reversible traps [15], the approximately two-fold increase in E_m^{app} for AerMet[®] 100, as compared with that for AISI 4130, suggests that reversible H trapping is more extensive in AerMet[®] 100, and is consistent with the diffusible H concentration and H diffusivity data for each steel [46]. However, these E_m^{app} values for AerMet[®] 100 and AISI

4130 determined from TDS data are generally lower than those determined from electrochemical permeation measurements for other quenched and tempered steels. Typical apparent activation energies are 30 - 40 kJ/mol (0.31-0.41 eV/atom) by H permeation measurements for quenched and tempered UHSS [49-52]. In the quenched and tempered conditions, E_m^{app} for apparent H diffusion is 37 kJ/mol (0.38 eV/atom) in Fe-Mo-C [49], 30.7 kJ/mol (0.32 eV/atom) in PH 13-8 Mo stainless steel [50], and ~32 kJ/mol (~ 0.33 eV/atom) in AISI 4130 steel (yield strengths not specified) [51, 52]. As such, E_m^{app} values determined from TDS experiments for either AerMet[®] 100 (Fig. 4a) and AISI 4130 [46] are lower than these reported values. Despite differences in E_m^{app} from TDS versus permeation data, room temperature D_{app} values extrapolated from TDS data are consistent with the corresponding D_{app} values determined using the permeation method for both AISI 4130 [13] and AerMet[®] 100 [31]. In view of these contrasting facts, while differences exist between the TDS and permeation methods for determining diffusivity [53, 54], it is not reasonable to fully attribute the difference in the E_m^{app} values to the method used, since there may be distinct difference in microstructural characteristics among these UHSSs.

Reversible versus Irreversible H-Traps

Whether H detraps from a specific trap site depends on thermal activation conditions, among which temperature is a key factor, as reflected in Eqs. 5-7 by the term RT . In view of this, an absolute criterion is hard to set to differentiate between reversible and irreversible H traps. According to the present results of baking temperature effect (Fig. 7), the three types of traps can be removed one after another as baking temperature increases up to 500°C, provided that enough holding time is given at each temperature. Considering this temperature dependence, it might be more appropriate to state the temperature at which a specific H trap is referred to as reversible or

irreversible when discussing this reversibility issue. Currently this temperature is, by default, room temperature for most research results reported in literature. Since microstructural features are so various for different alloys studied, it seems difficult to reach a unified criterion in terms of E_b values. For instance, traps with binding energies greater than 77 kJ/mol (0.8 eV/atom) were found to irreversibly trap H at room temperature in some steels [20], while in Fe-M-C (where M = V, Nb, Ti) alloys, binding energy greater than 55 kJ/mol (0.57 eV/atom) were found high enough to irreversibly trap H [55]. With these facts in mind, it might not be meaningful to differentiate reversible versus irreversible traps exclusively on the basis of E_b values. On the other hand, there may be some practical criteria to specify for a definite alloy plus its application. To prevent IHE, a baking treatment is frequently used and the baking temperature is generally so selected that it is high enough to remove substantially diffusible H but still low enough to preserve the microstructure/mechanical properties. Thus, baking temperature can be used as a critical condition to judge the status of traps for a specific alloy. In the present study, peak 1 is essentially removed after baking at 190°C for 2 h, whereas peak 2 and peak 3 are persistent even after baking at 190°C for hundreds of hours. Then it is suggested that trap states identified by peak 2 and peak 3 are of irreversible trap types, while peak 1 represents a reversible trap state.

Potential H-Trap Sites in AerMet® 100

Through the ramp mode TDS experiments, at least three distinct trap states have been identified in the present investigation, as exemplified in Fig. 10. In Table VII, a comparison is made between the values of E_b obtained in the present study and those reported in the literature. The validity of these data is not fully ensured because: (a) they are from different models as their analytical bases, (b) experimental data sources are different, and (c) sometimes only one E_b value

was reported for an alloy having other potential trap site(s) than the targeted one. Nevertheless, the present discussion will be made considering both approximation to E_b values and the known microstructural features in AerMet® 100.

Table VII. Comparing E_b Values in This Work with References

Trap site	E_b (kJ/mol)	E_b (kJ/mol)	Trap site description
This work	This work	References	References
Peak 1	11.4 – 11.6	7.7, 9.7	Substitutional alloying with Ni, Cr in Fe [44]
	± 0.2	8.4, 9.2, 10.85, 13.4	Ferrite-cementite interface [55, 56, 57, 58]
Peak 2	61.3 – 62.2 ± 0.3	~ 52	Austenite-ferrite interface [59]
		~ 58	Mixed dislocations cores [60]
		~ 59	Grain boundaries [25, 61, 62]
		~ 68	Cr carbides in Fe-Cr steel [62]
Peak 3	89.1 – 89.9 ± 0.3	67.5 – 96.5	Various incoherent particles in Fe [46]
		~ 95	TiC in Fe-Ti-C alloy [21]
		up to 97	Incoherent carbides [21, 25, 62-64]

Peak 1 The trap state marked by peak 1 represents a reversible H-trap with an E_b level of 11.4 – 11.6 kJ/mol. A comparison of H desorption curves (Fig. 19) shows that the amount of H desorption associated with peak 1 for as-quenched alloys lacking substantial carbide precipitates is just about 2% that for the tempered alloy. This confirms distinctly that the M_2C precipitates in the tempered martensitic AerMet® 100 are the most responsible trapping sites to contribute the formation of peak 1, even without the knowledge of E_b for the trap. Furthermore, the following

analysis on atomic availability about the M_2C precipitates in the tempered AerMet[®] 100 also tends to support this argument.

Table VIII lists data on the total available atomic H and its distribution in the three peaks as a result of desorption. In calculating data in Table VIII, the total H concentration in wppm [46] were converted to the number of H atoms per unit volume. Then, from the ramp TDS test results (similar to Fig. 10 but presented as dC_H/dt versus time), the area under each desorption peak can be calculated to give the distribution of H egressed during the evolution of each peak. The calculated results show that the ratio of H among the three types of trap sites is 95-98%, 1-2%, and 1-3%, corresponding to peak 1, peak 2 and peak 3, respectively. It is especially noted that this ratio of distribution is constant for specimens H-charged at two different overpotentials (-1.17V and -0.62V) and TDS tested at different thermal heating rates from 1 to 10 °C/min.

Table VIII. Availability and distribution of H in AerMet[®] 100 (atoms/cm³)

Total 100 %	Peak 1 95-98 %	Peak 2 1-2 %	Peak 3 1-3 %
1.52×10^{20}	$1.44-1.49 \times 10^{20}$	$1.52-3.03 \times 10^{18}$	$1.52-4.55 \times 10^{18}$

Note: H concentration data for $\eta_{chg} = -0.62V$

On the other hand, according to the geometry and volume percentage of M_2C [65, 66], the amount of H needed for single layer full coverage on M_2C cylindrical surfaces is estimated to be $\sim 1.5 \times 10^{20}$ atoms/cm³ (See Appendix A). This value agrees well with the atomic amount of H desorbed in evolving peak 1, $1.44-1.49 \times 10^{20}$ atoms/cm³ (Table VIII). This further justifies the M_2C precipitates as the dominant H-trap sites revealed by desorption peak 1.

The existence of tiny peak 1 for the as-quenched alloy (Fig. 19) suggests that some solute atoms are potential source of H-traps. Bernstein and Pressouyre [44] have reported the binding energy of H to Ni atoms in Fe to be 7.7 kJ/mol (0.08 eV/atom). And, H-binding energy of 9.7 kJ/mol (0.10 eV/atom) have been determined by the same authors [44] for Cr substitutional atoms in Fe. In the present study, E_b is determined to be 8.9 kJ/mol for H-traps associated with peak 1 in the as-quenched alloy (Fig. 19), very close to the values reported for Ni or Cr in Fe [44]. Major alloying elements in AerMet® 100 are Co, Ni, Cr and Mo. Cr and/or Mo are probably more suitable as H-traps than Co and Ni, since (refer to the periodic table of elements) Co and Ni are in the same group (VIII) as Fe while Cr and Mo are in another group (VIB). Table IX shows the atomic availability of these elements per unit volume in the alloyed Fe lattice, where the calculation is based on the weight percentage of each element (Table I), the composition of M_2C (i.e. $(0.75Cr+0.13Fe+0.12Mo)_2C$) [4], and percentage of M_2C [65,66]. It is indicated that the M_2C precipitation consumes just a small portion of total Cr and Mo atoms. The majority of them, which cannot be consumed by other minor carbides [4], are massively available as lattice elements.

Table IX. Availability and distribution of major elements (atoms/cm³) in AerMet® 100

Element	Total	In M_2C	In sites other than M_2C
Co	1.1×10^{22}	--	--
Ni	9.2×10^{21}	--	--
Cr	2.8×10^{21}	5.6×10^{19}	2.7×10^{21}
Mo	6.1×10^{20}	9.0×10^{18}	6.0×10^{20}

The cementite-ferrite interface was reported to trap H with E_b values of 8.4 – 13.4 kJ/mol in a series of steels [55-58], which are very close to the E_b value determined for peak 1 in the present work (Table VII). This is not the case for the present study since cementite is not present in 482°C tempered AerMet® 100 [4]. On the other hand, the dislocation density in AerMet® 100 is large due

to the unrecovered martensitic microstructure that is promoted by Co [67]. Common dislocation structure was reported to trap H with a moderate level of E_b of 20-30 kJ/mol [61], which is somewhat higher than that determined for peak 1. It is unknown whether the actual E_b for dislocations (or part of them) in AerMet[®] 100 tempered at 482°C is close to this reported value or lower. If it is as low as the E_b determined for peak 1, then at least part of dislocations should act as reversible H trap sites.

Peak 2 The H-traps associated with peak 2 are irreversible traps with E_b values of 61.3 – 62.2 kJ/mol. There are quite a few potential trap sites with reported E_b values close to the presently determined range for peak 2. Several studies [25, 61, 62] resulted in a consistent value of E_b for trapping at grain boundaries of ~ 59 kJ/mol, very close to the 61.3 – 62.2 kJ/mol for peak 2. For the fine microstructure of AerMet[®] 100, there is a substantial area covered by various forms of interfaces and grain boundaries [4]. Therefore, there is no doubt that these boundaries can serve as irreversible H trap sites. Specifically, the ferrite-austenite interface has been documented as H trap site with an E_b value of ~ 52kJ/mol [59], slightly lower than the one set for peak 2. It is reasonably assumed that martensite-austenite interface can trap H with a similar binding energy level. As relevant data is unavailable, it is not clear whether the martensite-martensite boundaries can act as similar traps with an E_b value of the level for peak 2.

Dislocation cores have been identified to trap H in steels with E_b value as high as ~ 58kJ/mol [60], which is also quite close to the present E_b set for peak 2 (Table VII). This may be the case for AerMet[®] 100 in which the density of dislocations is very high and a large portion may be configured as mixed dislocation cores. Thus, mixed dislocation cores are possibly another source that traps H irreversibly and contribute to peak 2. Still another type of trap sites may be associated with peak 2. Chromium carbides in an Fe-9Cr alloy have been detected to trap H with a binding

energy of about 68kJ/mol [62], larger than but still close to the 61.3 – 62.2 kJ/mol set for peak 2. In addition, the lower bound of E_b for H trapping with incoherent particles is about 67.5kJ/mol [44]. Hence, it is probable that at least part of the incoherent particles in AerMet[®] 100, like (MoCr)₇C₃, (FeCr)_xC_y, TiC, (TiCrMo)C, etc. [30], are potential H-traps with the E_b values approaching the range determined for peak 2.

Peak 3 The trap sites associated with peak 3 are surely representative of an irreversible trap state, with E_b values as high as 89.1 – 89.9kJ/mol. Solutionizing AerMet[®] 100 at 885°C dissolves almost all of the metal carbides such as (MoCr)₇C₃, (FeCr)_xC_y, TiC, (TiCrMo)C, etc. [30]. However, a certain fraction of these carbides remain in the alloy for grain refinement. A binding energy of 95 kJ/mol (0.98 eV/atom) has been reported for TiC in Fe-Ti-C [21]. Similar binding energies of 67.5 – 96.5 kJ/mol (0.7 - 1 eV/atom) were determined for various incoherent particles in Fe [44]. In addition, incoherent carbides have been identified to trap H with very high binding energies of up to 97 kJ/mol (1 eV/atom) [21, 25, 62-64]. Some interfaces can also trap H at this high level of E_b [21]. These reported E_b values can be viewed as at the same level as the presently determined values for peak 3. Therefore, possible trap sites responsible for peak 3 may include undissolved metal carbides, and some highly-disorientated grain boundaries or interfaces in AerMet[®] 100.

H-Trap Site Availability The parameter N_t/N_L in Oriani's analysis on trap-affected diffusion in Eqs. 5-6 [18] can be compared to experimental results for AerMet[®] 100. Conventional treatment has been that N_L is the total interstitial sites in the alloy. For *bcc* Fe and its alloys, $N_L = 2.6 \times 10^{23}$ sites per cm³ (octahedral sites) is usually adopted. In the present analytical work, the values of N_t/N_L are determined (using Eq. 6) to be 0.037 – 0.056 for the reversible trap sites identified by peak 1 (see Fig. 18). Then, using $N_L = 2.6 \times 10^{23}$ sites/cm³ would result in $N_t =$

$9.6 \times 10^{21} - 1.5 \times 10^{22}$ sites/cm³. This value roughly agrees with the available alloying elements in lattice (Table IX) as well as the atom coverage on interfaces of M₂C ($\sim 1.5 \times 10^{20}$ atoms/cm³). This is a high number of trap sites which agrees with the high density of sites along the fine M₂C interfaces. As discussed above, H-traps associated with peak 1 may also include dislocations, whose density is yet to be quantified.

Modeling Desorption

It is interesting to note that Eq. 4, which depicts the shift of T_m with dT/dt , and Eq. 6, the analysis of which provides key input values for modeling (D_0 , E_m , E_b , and N_T/N_L), are derived from different theoretical backgrounds than that of Eq. 7 used for modeling. Then the capability of Eq. 7 in predicting T_m should be an indication that major analytical models used to characterize the diffusion and detrapping behavior (Eqs. 4-7) are theoretically consistent among each other. This capability may be also considered a justification for the major diffusion and trapping parameters (D_0 , E_m , E_b , and N_T/N_L) determined in the previous section, since they have been inputs to the modeling.

As exemplified in Fig. 20, the H desorption model (Eq. 7) correctly predicts the temperature for desorption rate maxima, but the exact trace/shape of desorption rate versus time (or temperature) curve is poorly described. This shortcoming is expected considering the assumptions and uncertainties in some parameters. First, this model assumes diffusion and detrapping as the rate-limiting processes. Second, each trap state is considered separately, ignoring H retrapping by a trap site after it has been detrapped from a site of different binding energy. This is an important factor to consider when studying an alloy such as AerMet[®] 100 that contains multiple trap sites of similar binding energies [67]. Lastly, a theoretically justified value of γ , one of important input parameters,

is not known. Without prior knowledge of the physical construction of a specific trap site, it is difficult to estimate γ according to Eq.8. However, since the modeling through Eq. 7 requires prior knowledge of all the key parameters for diffusion and trapping (D_0 , E_m , E_b , N_T/N_L , etc.), such theoretical work may not be essentially important, as compared to approaches using all feasible experimental and analytical methods to determine these key parameters. With all these parameters (D_0 , E_m , E_b , N_T/N_L , etc.), the diffusion and/or trapping behavior should be basically made certain.

Engineering Implications

The present and previous [46] studies show that apparent H diffusivity is slower and H capacity is higher in AerMet[®] 100 than older generation UHSS, such as quenched and tempered AISI 4130 steel. Even after irreversible traps are filled, the apparent H diffusivity in AerMet[®] 100 is an order of magnitude slower than in other UHSSs with a similar strength and dislocation substructure [13, 69]. The high H concentrations produced in AerMet[®] 100 result from a high capacity for H trapping and are produced even by charging at modest hydrogen overpotentials, η_{chg} [46]. The present investigation further indicates that most H atoms in AerMet[®] 100 are either diffusible or trapped at low binding energy reversible trap sites, because N_T/N_L is very large. A relatively slow diffusivity tends to decelerate the kinetics of embrittlement since H transport to critical sites in the plastic zone ahead of crack tip is deemed a necessity for failure by IHE [70]. On the other hand, plentiful diffusible or weakly/reversibly trapped H presents a large reservoir of H available for transporting to crack tip region and hence influences the mechanism of IHE. Consequently, depending on the local details of H-microstructure interaction, the severity of IHE for AerMet[®] 100 may or may not be lessened relative to other UHSSs.

In estimating the depth to which H penetrates during Cd-electroplating for corrosion resistant components, the relatively slow H diffusivity in AerMet[®] 100 should be taken into consideration. This slow H diffusion, along with the substantial H uptake in AerMet[®] 100, should be considered in defining thermal treatments (e.g. baking) to remove H dissolved during such processes [7, 8]. The temperature for baking should not be too high so as to compromise the optimum mechanical properties achieved by tempering. The present experiments used 190°C as conventionally adopted in relevant industries [42]. In view of the fact that most H in AerMet[®] 100 is either diffusive or trapped in reversible trap sites (marked by peak 1) as indicated in Table VIII, and considering the baking kinetics shown in Fig. 8, baking at 190°C for 2 h should be sufficient to remove the majority of diffusive and reversibly trapped H, for AerMet[®] 100 charged to maintain a total H level of about 30 wppm. However, this baking time dependence as shown in Fig. 8 is for a single plate of alloy only, without considering the Cd-plating layer. As H diffusion in Cd is slower and H dissolves substantially in Cd, specific baking kinetics for Cd-plated AerMet[®] 100 must be investigated. The H-concentration dependence of the apparent D_{app} in AerMet[®] 100 must be considered in modeling H diffusion and egress during baking. A decrease in H content during baking leads to lower D_{app} , hence longer time may be required to reduce $C_{H,diff}$ compared to that predicted using a concentration-independent value of H diffusivity. Due to the susceptibility of AerMet[®] 100 to IHE [34], this issue is of key importance.

CONCLUSIONS

1. The trap-affected apparent H diffusion in AerMet[®] 100, at temperatures between 20 and 200°C, is described by:

$$D_{app}[cm^2/s] = \begin{cases} 3.71 \times 10^{-5} \exp\left\{\frac{-17.7[kJ/mol]}{RT}\right\} & (\eta_{chg} = -1.17V) \\ 1.59 \times 10^{-5} \exp\left\{\frac{-18.0[kJ/mol]}{RT}\right\} & (\eta_{chg} = -0.62V) \end{cases}$$

The apparent diffusivity is $1.05 \sim 2.83 \times 10^{-8} \text{ cm}^2/\text{s}$ at room temperature, which is substantially lower than conventional UHSS such as AISI 4130.

2. The apparent H diffusivity in AerMet[®] 100 is lowered by baking after H-charging at $\eta_{chg} = -0.62V$, with the temperature dependence expressed by:

$$D_{app}[cm^2/s] = \begin{cases} 1.59 \times 10^{-5} \exp\left\{\frac{-18.0[kJ/mol]}{RT}\right\} & (\text{as - charged}) \\ 1.23 \times 10^{-5} \exp\left\{\frac{-18.2[kJ/mol]}{RT}\right\} & (23^\circ \text{C baked for 72h}) \\ 1.13 \times 10^{-5} \exp\left\{\frac{-18.9[kJ/mol]}{RT}\right\} & (200^\circ \text{C baked for 2.3h}) \end{cases}$$

3. Apparent H diffusivity in AerMet[®] 100 decreases with decreasing diffusible and total H concentrations, produced either by reduced H-charging overpotential or baking.
4. Binding energy analysis suggests that extensive H trap sites are associated with the fine-scale microstructure of AerMet[®] 100, which is responsible for low apparent H diffusivity and high H uptake. Three distinct trap states are identified by ramp TDS tests, with H binding energies analyzed to be 11.4-11.6kJ/mol, 61.3-62.2kJ/mol and 89.1-89.9kJ/mol, respectively. The first trap state is associated with reversible trap sites while the higher energy sites are associated with irreversible traps.
5. The M_2C precipitates are identified to the dominant reversible H-trap sites that is involved in the majority of H desorption. Solute elements, especially Cr and Mo in lattice, and dislocations

may also take part in the low-energy reversible H trapping. Various interfaces including martensitic and austenitic boundaries and grain boundaries, mixed dislocation cores and incoherent part of M_2C precipitates may serve as irreversible H trap sites. Undissolved metal carbides and highly disorientated grain boundaries may irreversibly trap H with the highest binding energy level determined for this alloy.

6. Room temperature baking decreases the level of diffusible H. Baking at 190 ~ 200°C for 2 h essentially removes all diffusible and reversibly trapped H in AerMet® 100. Baking at this temperature for longer time (up to 200h) makes no significant change to this condition, and a considerable amount of H remains in two or more higher energy trap states.

Acknowledgement

Financial Support from the Office of Naval Research (Grant Number N00014-98-1-0740) under the direction of contract monitor Dr. A. John Sedriks is gratefully acknowledged. We acknowledge contributions of electrochemical instrumentation by Perkin Elmer Corporation and Scribner Associates, Inc., and Barnacle experimental results by Mr. Hakan Dogan.

REFERENCE

1. M.G.H. Wells, *Key Engineering Materials*, Vol. 77-78, p. 71-80, 1993.
2. R. Ayer, in *Microstructures and Mechanical Properties of Aging Materials*, P.K. Liaw, *et al.*, editors, The Minerals, Metals, and Materials Society, Warrendale, PA, p. 251-62, 1993.
3. Hemphill, R.M. and D.E. Wert, U.S. Patent Number 5,087,415, Carpenter Technology Corporation, Reading, PA, February 11, 1992.

4. R. Ayer and P.M. Machmeier, *Metallurgical Transactions A*, 1993, Vol. 24A, p. 1943-55.
5. P.M. Novonty and M. Maguire, *Foundary Management and Technology*, Vol. December, p. 33-6, 1993.
6. E.U. Lee and J. Waldman, *Naval Engineers Journal*, Vol. 106, p. 77-83, 1994.
7. J.B. Boodey and V.S. Agarwala, in *Corrosion 87*, NACE, Houston, TX, 1987.
8. D.A. Berman, *Materials Performance*, Vol. 24, p. 36-41, 1985.
9. T. Zhong-Zhuo, H. Chi-Mei, L. Rong-Bong, F. Yi-Feng, and C. Xiang-Rong, in *Current Solutions to Hydrogen Problems in Steels*, C.G. Interrante and G.M. Pressouyre, editors, ASM International, Materials Park, OH, p. 98-103, 1982.
10. W.W. Gerberich, T. Livne, X.-F. Chen, and M. Kaczorowski, *Metallurgical Transactions A*, Vol. 19A, p. 1319-34, 1988.
11. P. McIntyre, in *Hydrogen Degradation of Ferrous Alloys*, R.A. Oriani, J.P. Hirth, and M. Smialowski, editors, Noyes Publications, Park Ridge, NJ, p. 763-98, 1985.
12. Y. Yamaguchi, H. Nonaka and K. Yamakawa, *Corrosion*, Vol. 53, p. 147-55, 1997.
13. K. Yamakawa, S. Yonezawa and S. Yoshizawa, in *International Congress on Metallic Corrosion*, National Research Council, Toronto, Canada, p. 254-61, 1984.
14. C.D. Kim and A.W. Loginow: *Corrosion*, 1968, Vol. 24, pp. 313-18.
15. H.H. Johnson and R.W. Lin: in *Hydrogen Effects in Metals*, I.M. Bernstein and A.W. Thompson, editors, The Minerals, Metals, and Materials Society, Warrendale, PA, 1980, pp. 3-25.
16. G.M. Evans and E.C. Rollason: *Journal of the Iron and Steel Institute*, 1969, Vol. 207, pp. 1591-98.

17. M. Wang and P.G. Shewmon: in *Hydrogen Embrittlement: Prevention and Control*, ASTM STP 962, L. Raymond, editor, ASTM, Philadelphia, PA, 1988, pp. 117-24.
18. R.A. Oriani: *Acta Metallurgica*, 1970, Vol. 18, pp. 147-57.
19. L.S. Darken and R.P. Smith: *Corrosion*, 1949, Vol. 5, pp. 1-16.
20. G.M. Pressouyre and F.M. Faure: in *Hydrogen Embrittlement: Prevention and Control*, ASTM STP 962, L. Raymond, editor, ASTM, Philadelphia, PA, 1988, pp. 353-71.
21. G.M. Pressouyre and I.M. Bernstein: *Metallurgical Transactions A*, 1978, Vol. 9A, pp. 1571-80.
22. G.M. Pressouyre: in *Hydrogen Effects in Metals*, I.M. Bernstein and A.W. Thompson, editors, The Minerals, Metals, and Materials Society, Warrendale, PA, 1981, pp. 27-36.
23. R.A. Oriani: in *Fundamental Aspects of Stress Corrosion Cracking*, NACE, Houston, TX, 1969, pp. 32-50.
24. R.P. Gangloff: in *Corrosion Prevention and Control*, M. Levy and S. Isserow, editors, U.S. Army Materials Technology Laboratory, Watertown, MA, 1986, pp. 64-111.
25. G.M. Pressouyre and I.M. Bernstein: *Acta Metallurgica*, 1979, Vol. 27, pp. 89-100.
26. M.F. Stevens and I.M. Bernstein: *Metallurgical Transactions A*, 1985, Vol. 16A, pp. 1879-86.
27. M.J. Morgan and C.J. McMahon Jr.: in *Hydrogen Degradation of Ferrous Alloys*, R.A. Oriani, J.P. Hirth, and M. Smialowski, editors, Noyes Publications, Park Ridge, NJ, 1985, pp. 608-40.
28. *Alloy Data-AerMet[®] 100 Alloy*, Carpenter Technology Corporation Carpenter Steel Division: Reading, PA, 1992.
29. C.H. Yoo, H.M. Lee, J.W. Chan and J.W. Morris, *Metallurgical and Materials Transactions - A*, 1996, Vol. 27A, pp. 3466-3472.

30. C.J. Kuehmann: *Thermal Processing Optimization of Nickel-Cobalt Ultrahigh-Strength Steels*, Ph.D. Dissertation, Northwestern University, Evanston, IL, 1994.
31. B.P. Pound: *Acta Metallurgica*, 1998, Vol. 46, pp. 5733-43.
32. J. Crank: *The Mathematics of Diffusion*, Oxford University Press, Inc., New York, NY, 1975, p. 414.
33. J.J. DeLuccia and D.A. Berman: in *Electrochemical Corrosion Testing (ASTM STP 727)*, F. Mansfeld and U. Bertocci, editors, ASTM, Philadelphia, PA, 1981, pp. 256-73.
34. R.L.S. Thomas: *Internal Hydrogen Embrittlement of a Trap-Rich Ultra-High Strength Steel AerMet® 100 (M. Sc. Dissertation)*, 2000, University of Virginia, Charlottesville, VA.
35. *1999 Annual Book of ASTM Standards Vol. 3.06*, ASTM, Philadelphia, PA, 1999, pp. 398-400.
36. F. Iacoviello, J. Galland and M. Habashi: *Corrosion Science*, 1998, Vol. 40, pp. 1281-93.
37. P. Shewmon: *Diffusion in Solids*, The Minerals, Metals, & Materials Society, Warrendale, PA, 1989, pp. 9-51.
38. D.P. Woodruff and T.A. Delchar: *Modern Techniques of Surface Science*, Cambridge University Press, Cambridge, UK, 1986, p. 284.
39. J.Y. Lee, J.L. Lee and W.Y. Choo, *Current Solutions to Hydrogen Problems in Steels*, ASM, Metals Park, OH, 1982, pp.423-27.
40. H.E. Kissinger, *Analytical Chemistry*, 1957, vol.29, pp. 1702-06.
41. K.Ono and M.Meshii, *Acta Metallurgica*, 1992, vol. 40, pp.1357-64.
42. R.J.H. Wanhill and P. de Rijk, *Metal Finishing*, January 1975, pp. 32-37.

43. J.Völkl and G.Alefeld, in: *Hydrogen in Metals I – Basic Properties*, G.Alefeld and J.Völkl, editors, Springer-Verlag, New York, 1978, pp.326-29.
44. I.M. Bernstein and G.M. Pressouyre, in: *Hydrogen Degradation of Ferrous Alloys*, R.A. Oriani, J.P. Hirth, and M. Smialowski, editors, Noyes Publications, Park Ridge, NJ, 1985, pp. 641-711.
45. H.Hagi, *Journal of the Japan Institute of Metals*, 1991, vol.55, No. 12, pp.1283-90.
46. R.L.S. Thomas, D. Li, R.P. Gangloff and J.R. Scully, *Metallurgical and Materials Transactions - A*, 2002, vol.33A, pp. 1991-2003.
47. A.J. Griffiths and A. Turnbull: *Corrosion Science*, 1995, Vol. 37, pp. 1879-81.
48. C. Wert and C. Zener: *Physical Review*, 1949, Vol. 76(8), pp. 1169-75.
49. S. Hinotani, Y. Ohmori and F. Terasaki: *Materials Science and Engineering*, 1985, Vol. 76, pp. 57-69.
50. J.R. Scully, J.A. Van Den Avyle, M.J. Cieslak, J. Romig and C.R. Hills: *Metallurgical Transactions A*, 1991, Vol. 22A, pp. 2429-43.
51. W.J. Kass: in *Effect of Hydrogen on Behavior of Materials*, A.W. Thompson and I.M. Bernstein, editors, The Minerals, Metals, and Materials Society, Warrendale, PA, 1976, pp. 327-36.
52. H.G. Nelson and J.E. Stein: *Report No. NASA TN D-7265*, National Aeronautics and Space Administration, Washington, D.C., 1973.
53. M.A.V. Devanthan and Z. Stachurski: *Proceedings of the Royal Society of London*, 1962, Vol. 270A, pp. 90-102.
54. R.S. Lillard, D.G. Enos and J.R. Scully: *Corrosion*, 2000, Vol. 56, pp. 1119-32.
55. G.W. Hong and J.Y. Lee, *Scripta Metallurgica*, 1983, vol. 17, pp. 823-26.

56. G.W. Hong and J.Y. Lee, *Metallurgical Transactions*, 1983, vol. 14A, pp. 156-62.
57. G.W. Hong and J.Y. Lee, *Journal of Materials Science*, 1983, vol. 18, pp. 271-77.
58. B.D. Craig, *Acta Metallurgica*, 1979, vol. 25, pp.1027-35.
59. A.Turnbull and R.B. Hutchings, *Materials Science and Engineering*, 1994, A177, pp.161-71.
60. R. Gibala and A.J. Kumnick: in *Hydrogen Embrittlement and Stress Corrosion Cracking*, R. Gibala and R.F. Hehemann, editors, American Society for Materials International, Materials Park, OH, 1984, pp. 61-77.
61. E. Serra, A. Perujo and G. Benamatti, *Journal of Nuclear Materials*, 1997, vol. 245, pp.108-15.
62. C. Paes de Oliveira, M. Aucouturier and L. Lacombe: *Corrosion*, 1980, Vol. 36, pp. 53-9.
63. J.P. Hirth: *Metallurgical Transactions A*, 1980, Vol. 11A, pp. 861-90.
64. G.M. Pressouyre: in *Current Solutions to Hydrogen Problems in Steels*, C.G. Interrante and G.M. Pressouyre, editors, American Society for Materials International, Materials Park, OH, 1982, pp. 18-34.
65. R. Ayer and P.M. Machmeier, *Metallurgical Transactions*, 1996, 27A, pp.2510-21.
66. J.S. Montgomery and G.B. Oslon, in: *Gilbert R. Speich Symposium on the Fundamentals of Aging and Tempering in Bainitic and Martensitic Steel Products* (Proc. 34th MSWP Conf.), ISS-AIME, Warrendale, PA pp. 177-214, 1992.
67. G.R. Speich, D.S. Dabkowski and L.F. Porter: *Metallurgical Transactions*, 1973, Vol. 4, pp. 303-15.
68. A.Turnbull, R.B. Hutchings and D.H. Ferriss, *Materials Science and Engineering*, 1997, vol. A238, pp.317-28.

69. W. Beck, J.O.M. Bockris, M.A. Genshaw and P.K. Subramanyan: *Metallurgical Transactions*, 1971, Vol. 2, pp. 883-8.
70. R.P. Wei and M. Gao, in: *Hydrogen Degradation of Ferrous Alloys*, R.A. Oriani, J.P. Hirth, and M. Smialowski, editors, Noyes Publications, Park Ridge, NJ, 1985, pp. 579-607.

Appendix A

Estimation of H Coverage on M_2C /Alloy Interfaces

M_2C is needle-shaped, 2 nm in diameter and 8 nm long, upon aging at 482°C for 5h [65]. This gives the cylindrical surface area of an M_2C "needle" to be:

$$A_0 = \pi \times 2 \times 8 \text{ (nm)}^2 = 5.027 \times 10^{-17} \text{ m}^2 \quad \text{A-1}$$

As the number density of M_2C precipitates in peak-hardened temper is $1.5 \times 10^{23}/\text{m}^3$ [66], then the total area of cylindrical surfaces of M_2C (m^2) per one m^3 of alloy is:

$$S_v = A_0 \times 1.5 \times 10^{23} \text{ (m}^2/\text{m}^3) = 7539816 \text{ (m}^2/\text{m}^3) \quad \text{A-2}$$

For simplicity, it is assumed that H is mostly trapped on the cylindrical surface of M_2C /alloy interface (neglecting the H coverage on base surface), then the maximum coverage ratio of carbide (cylindrical) surfaces by H atoms can be estimated as (see Fig. A1 and recall the radius of H atom being 0.12 nm):

$$R_\phi = (3 \times \pi \times 0.12^2 \div 6) \div (2 \times 0.12 \times \sqrt{3} \times 0.12 \div 2) = 0.9069 \quad \text{A-3}$$

Thus, the number of trapped H atoms per unit volume of the alloy is:

$$N_H = R_\phi \times S_v \div (\pi \times 0.12^2 \times 10^{-18}) \text{ (atoms/m}^3) = 1.51 \times 10^{20} \text{ (atoms/cm}^3) \quad \text{A-4}$$

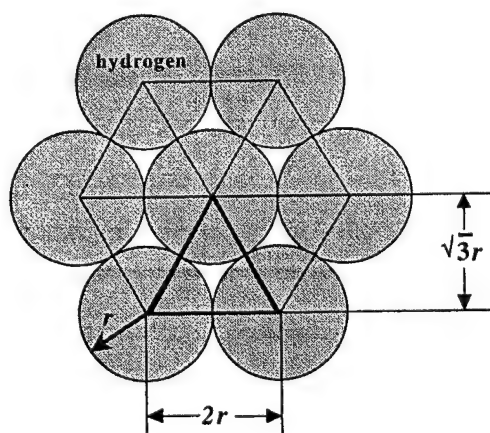


Fig. A1. A rigid contact model for H atoms

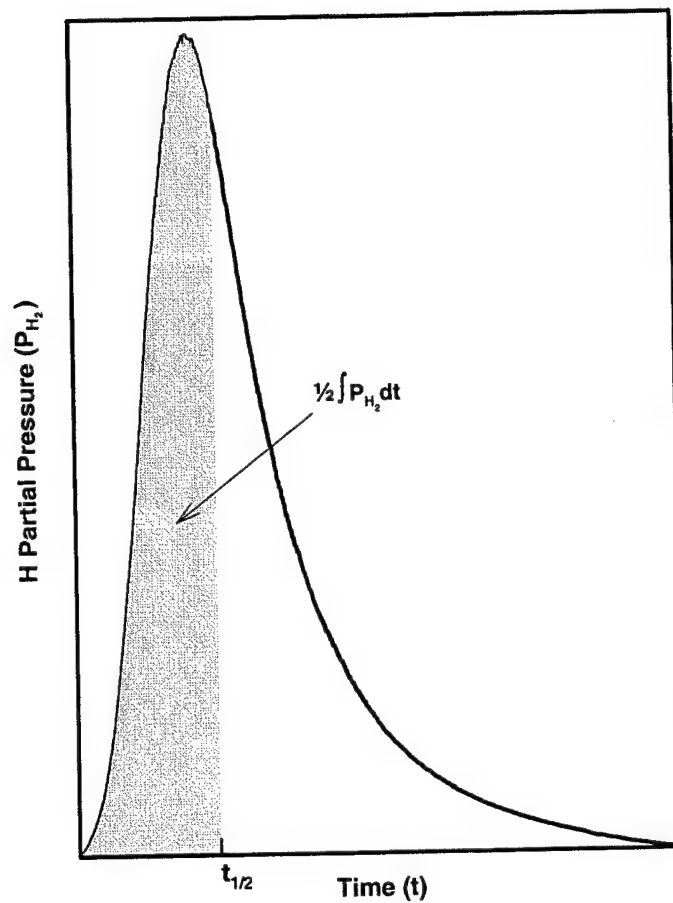


Fig. 1. Schematic diagram of H₂ partial pressure versus time, as evidenced in a TDS test, showing the determination of $t_{1/2}$ used in Eq.1.

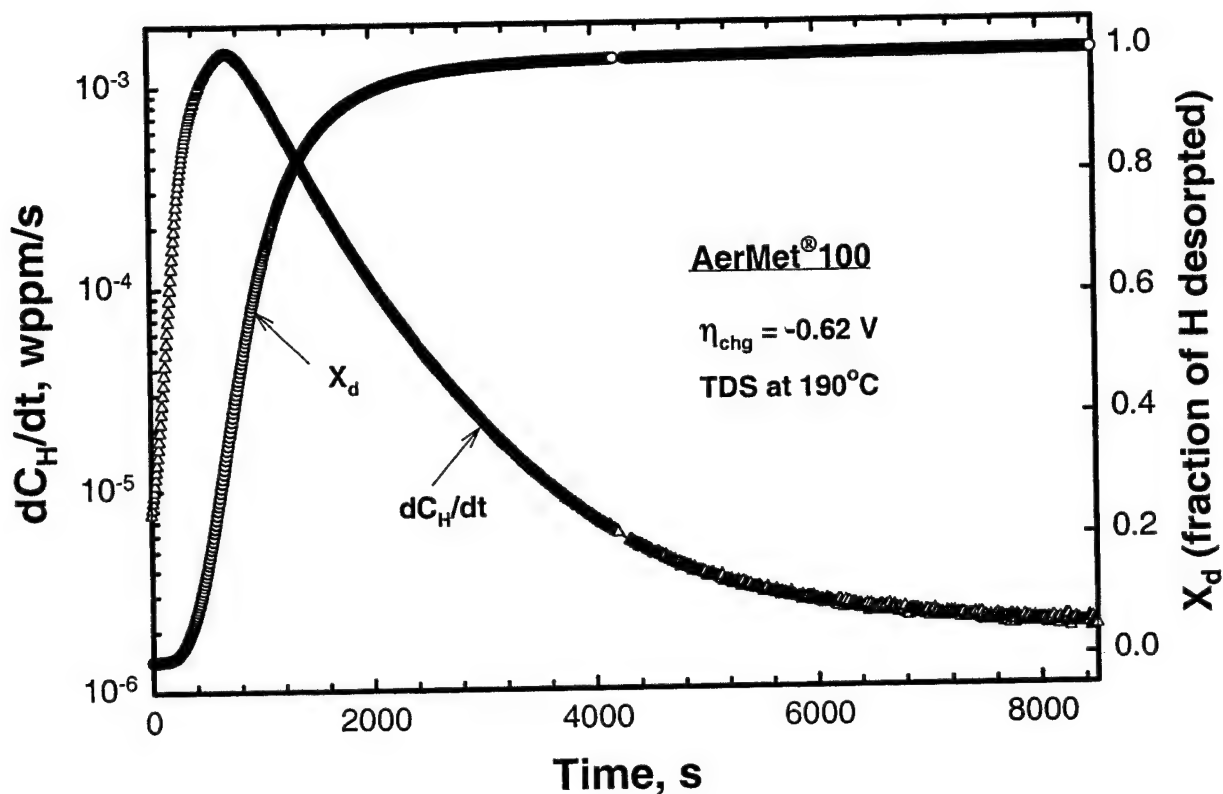


Fig. 2. Desorption rate, dC_H/dt , and the fraction of H egressed, X_d , versus desorption time during thermal desorption of H at 190°C from the specimen charged at $\eta_{chg} = -0.62$ V.

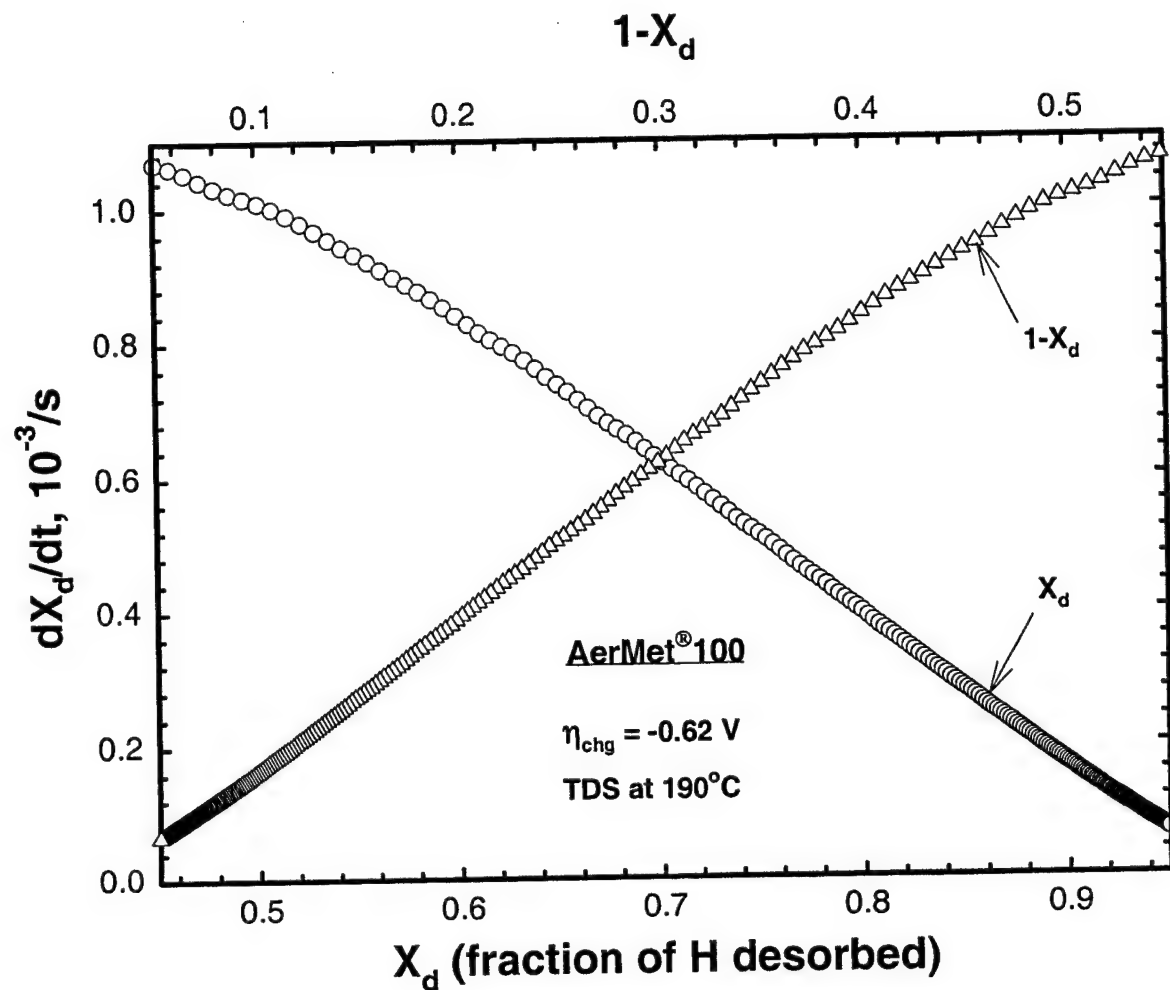


Fig. 3. The rate of H egress expressed as the derivative of X_d (the fraction of H desorbed), dX_d/dt , versus X_d and $(1-X_d)$ during thermal desorption of H at 190°C from the specimen charged at $\eta_{chg} = -0.62 \text{ V}$. An approximately linear relationship is obtained.

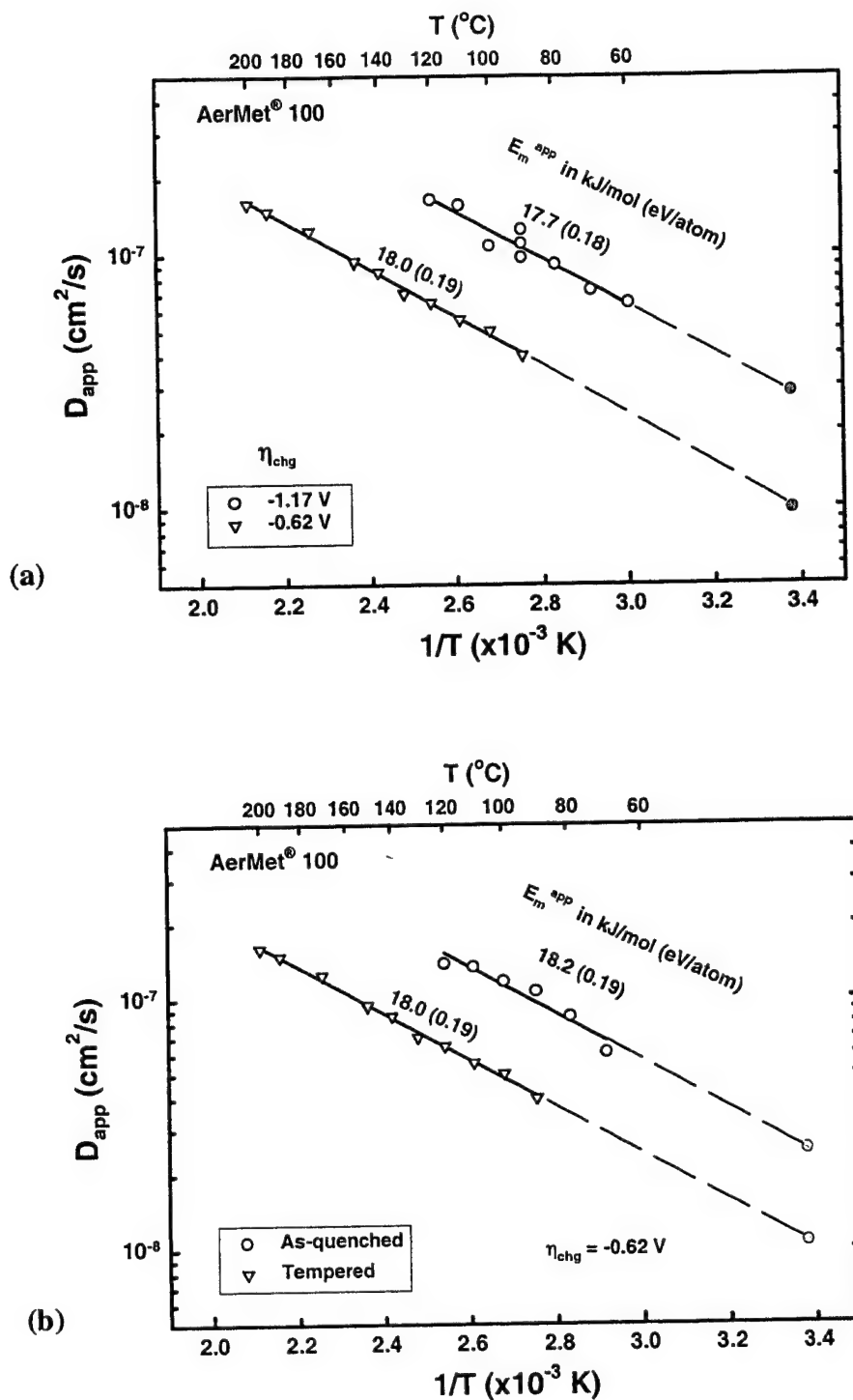


Fig. 4. Apparent hydrogen diffusivity, D_{app} , versus $1/T$ (a) for tempered AerMet[®] 100 specimens charged at H overpotentials, η_{chg} , of -1.17V and -0.62V and (b) for comparing with as-quenched AerMet[®] 100 specimens at $\eta_{chg} = -0.62$ V. All specimens were H charged at 60°C. Filled data points were D_{app} extrapolated for room temperature (23°C).

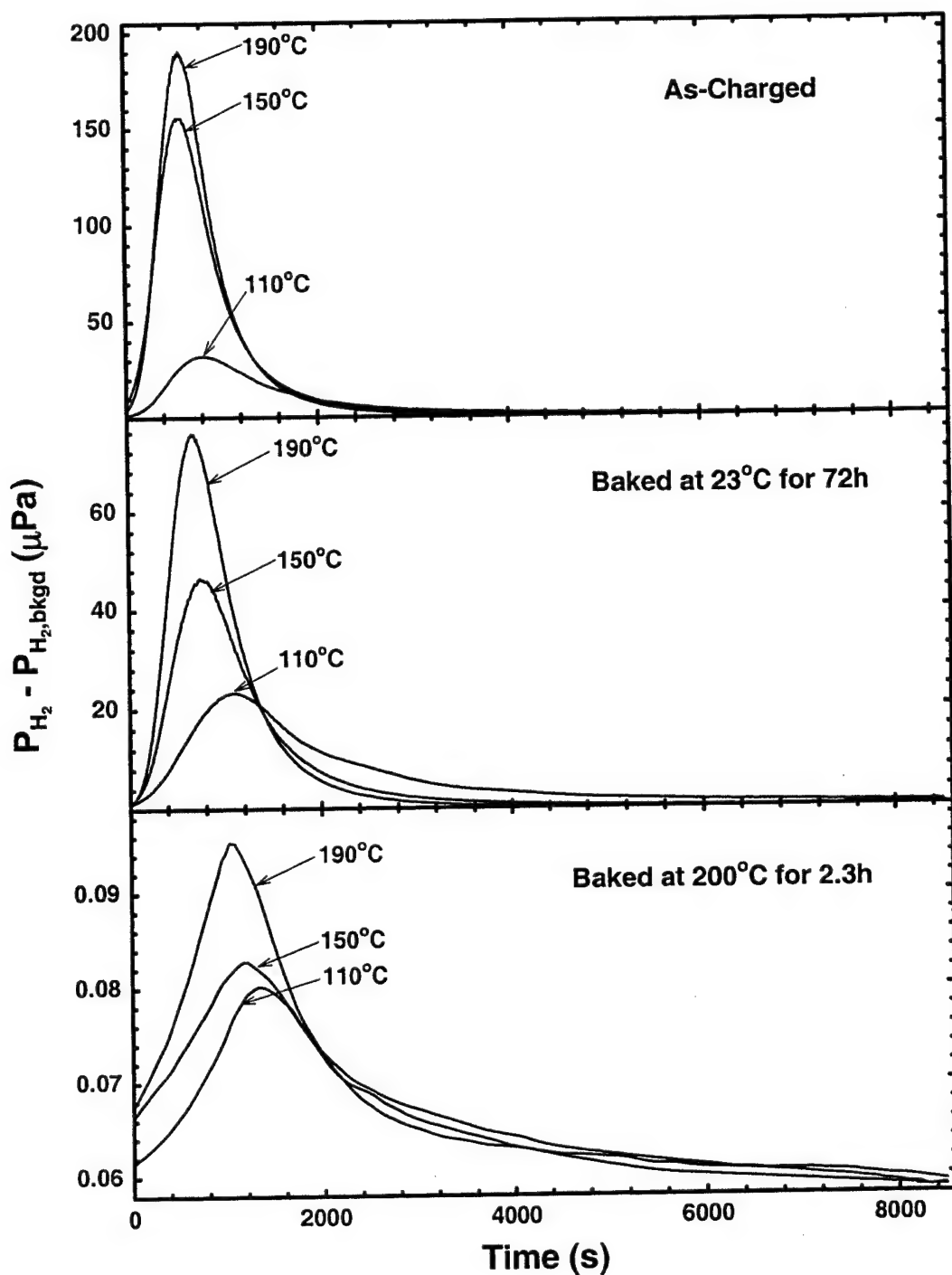


Fig. 5. Net H₂ pressure versus time at typical desorption temperatures for AerMet® 100 specimens charged at $\eta_{chg} = -0.62$ V and 60°C (background H₂ pressure, $P_{H_2,bkgd} \approx 0.04 \mu Pa$). Conditions prior to the desorption are labeled on each plot.

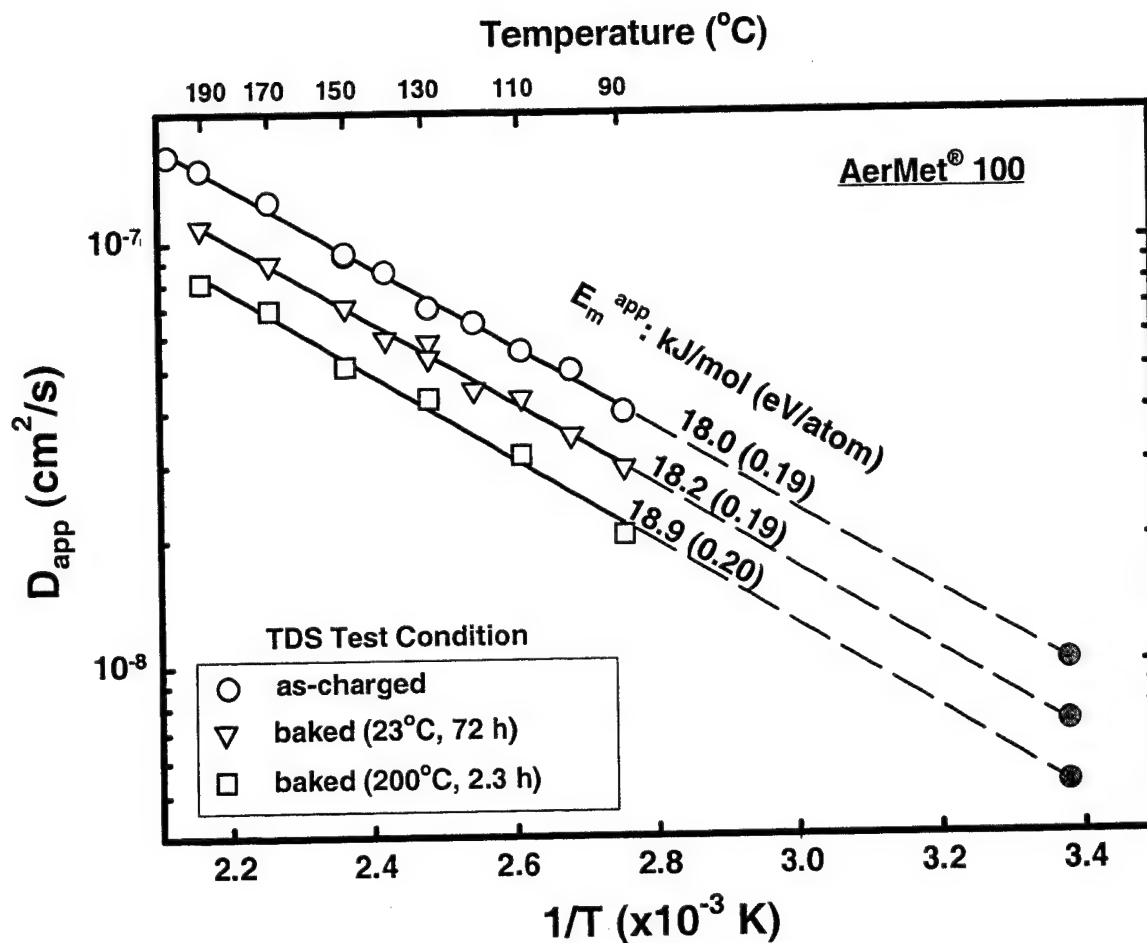


Fig. 6. Apparent hydrogen diffusivity, D_{app} , versus reciprocal absolute temperature, $1/T$, for specimens of AerMet® 100 charged at a H overpotential of -0.62 V and 60°C. Tests were performed in the as-charged condition and after two different baking conditions as indicated.

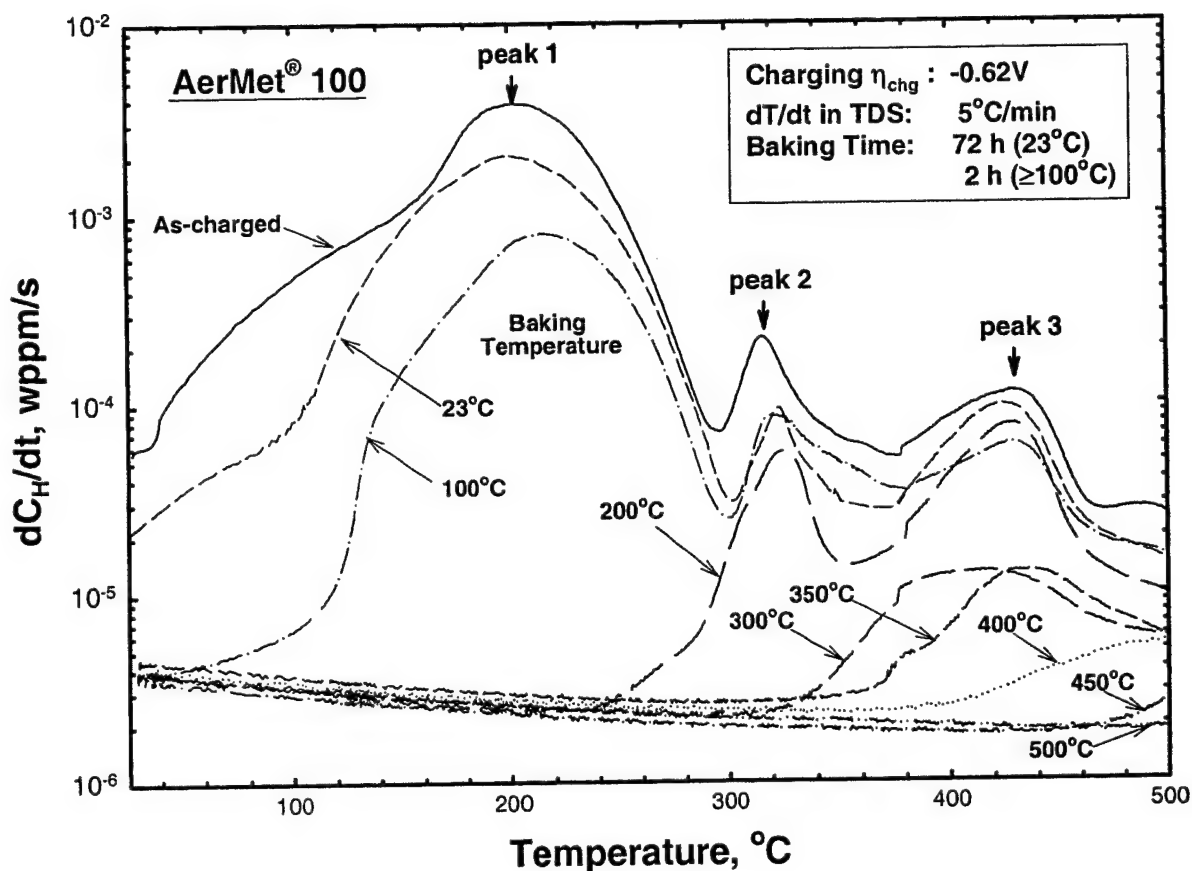


Fig. 7. H desorption rate (dC_H/dt) versus temperature curves obtained by TDS tests at a heating rate $dT/dt = 5^\circ\text{C}/\text{min}$ for specimens baked at various temperatures after charged at $\eta_{\text{chg}} = -0.62$ V and 60°C , in comparison with the as-charged state. Baking time is 72 h for 23°C baking and 2 h for elevated temperature baking. Three peaks are observed, as indicated by the arrows.

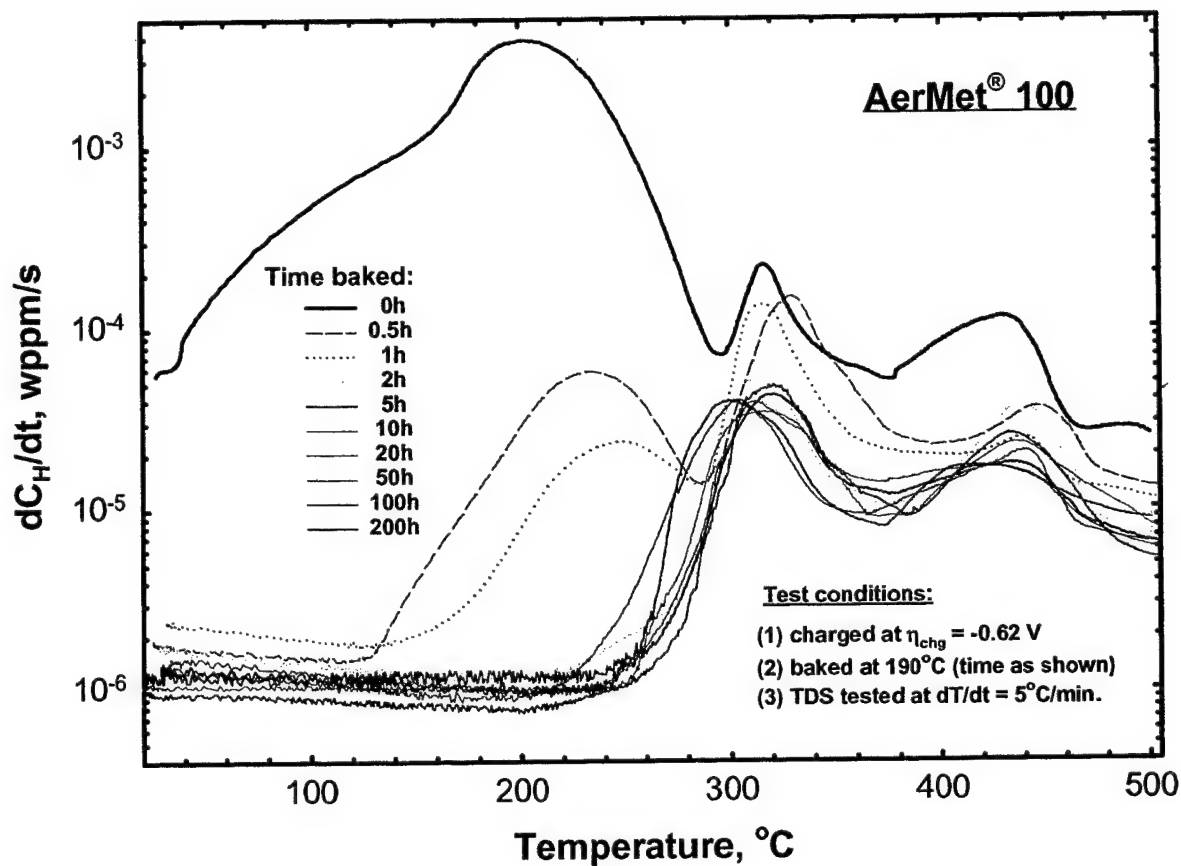


Fig. 8. H desorption rate (dC_H/dt) versus temperature relationship obtained by TDS tests at a ramp rate of 5°C/min for H-charged (at 60°C and $\eta_{\text{chg}} = -0.62\text{V}$) specimens under as-charged and 190°C -baked conditions, showing the baking time effect on H egress from AerMet® 100.

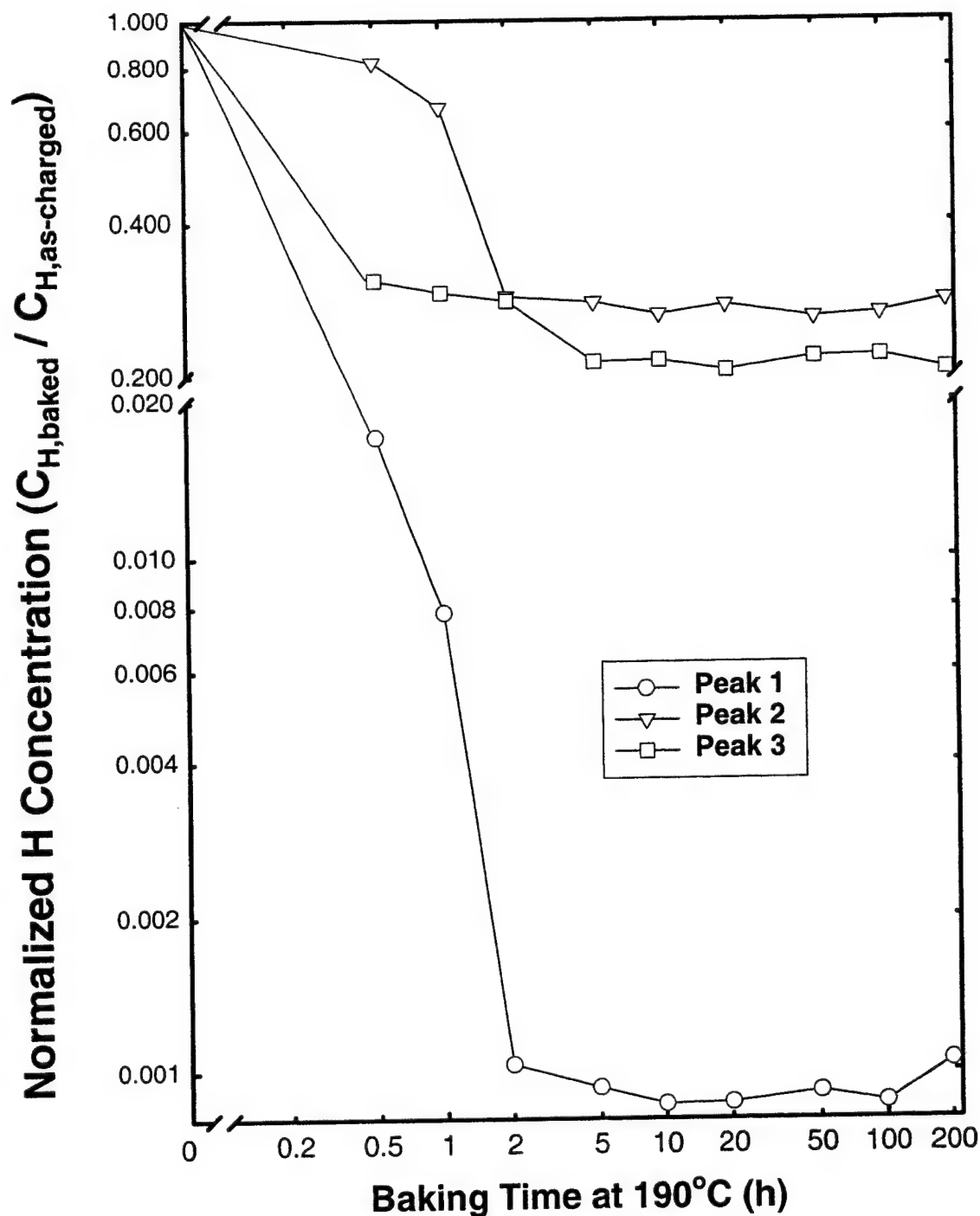


Fig. 9. Baking time dependence of normalized H concentration expressed as the ratio of H concentration egressed during the evolution of each peak in Fig. 9 for the baked specimen, $C_{H,baked}$, to that for the as-charged specimen, $C_{H,as-charged}$. Baking temperature was 190°C. C_H was calculated by integrating area under each individual peak in Fig. 9 distinguished by a peak-fitting software.

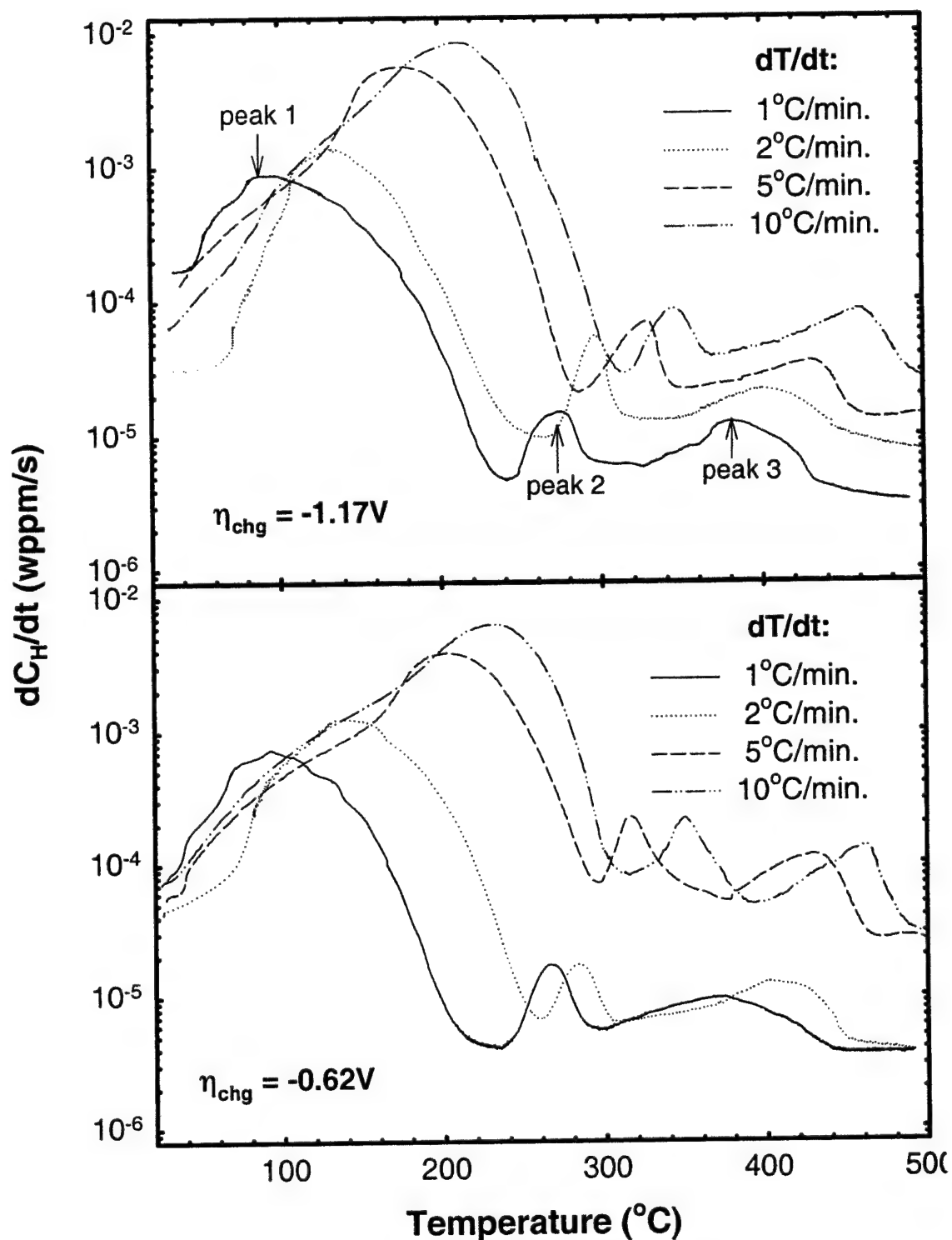


Fig. 10. H desorption rate (dC_H/dt) as a function of temperature obtained from TDS experiments at various ramp rates ($dT/dt = 1 - 10^{\circ}\text{C/min}$) for specimens charged at 60°C and at two overpotentials ($\eta_{\text{chg}} = -0.62\text{V}$ and -1.17V), showing shift of the temperature for desorption rate peak (T_m) with variation in dT/dt .

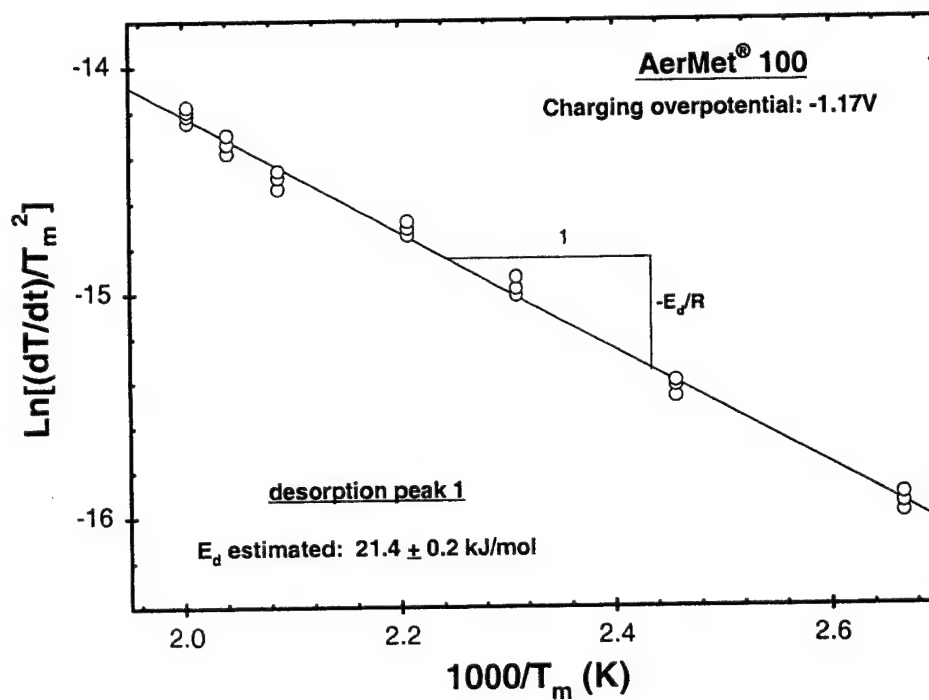
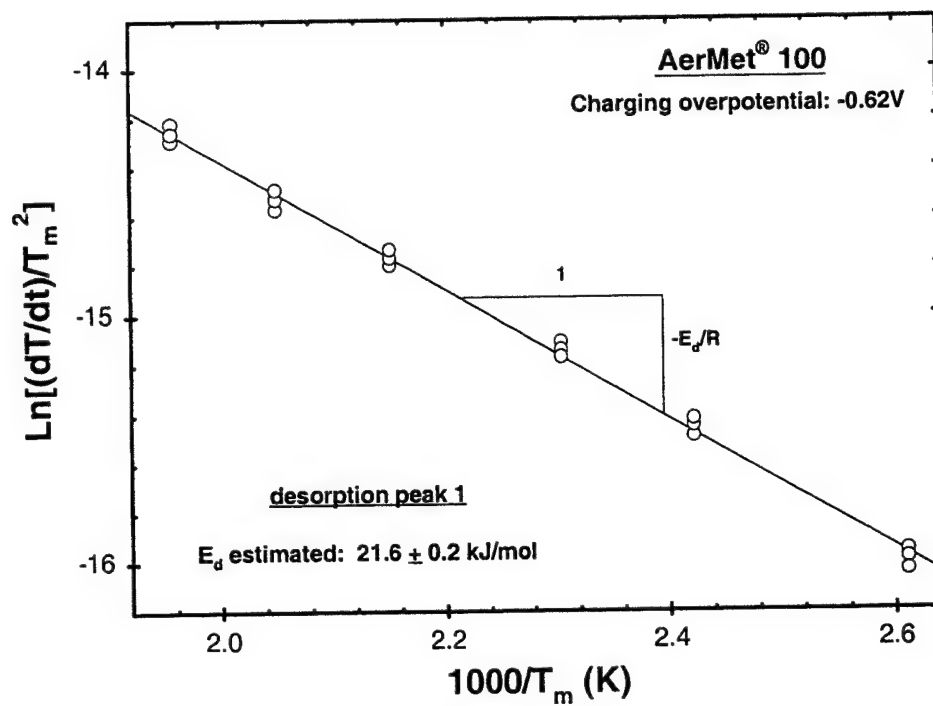


Fig. 11. Plots of ramp TDS data showing the determination of the total activation energy for H desorption, E_d , associated with the first peak (peak 1) on the H desorption curves in Fig. 10, according to Eq.4.

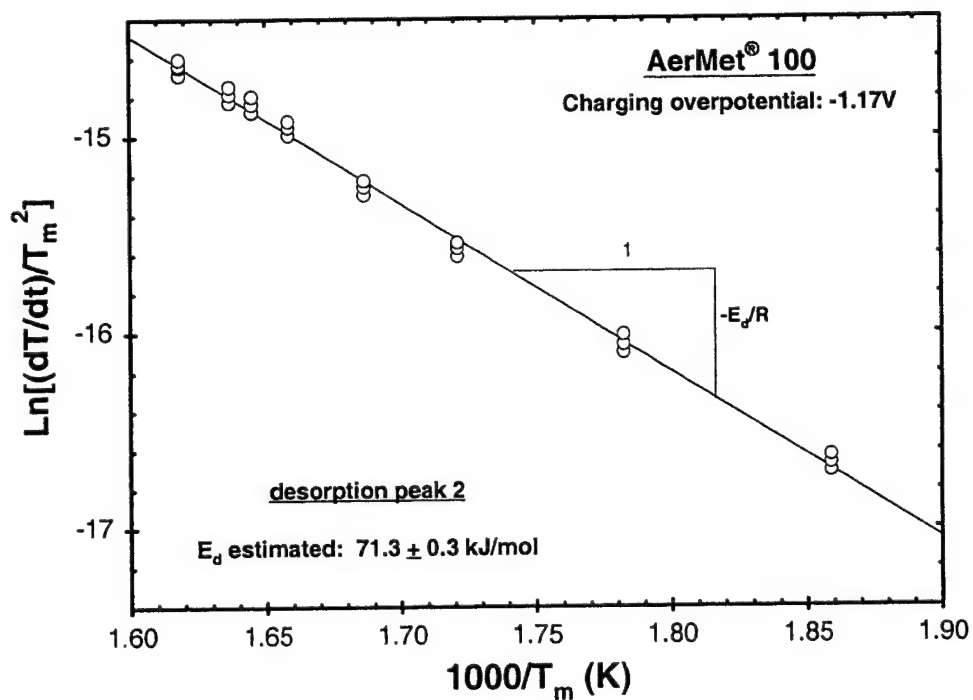
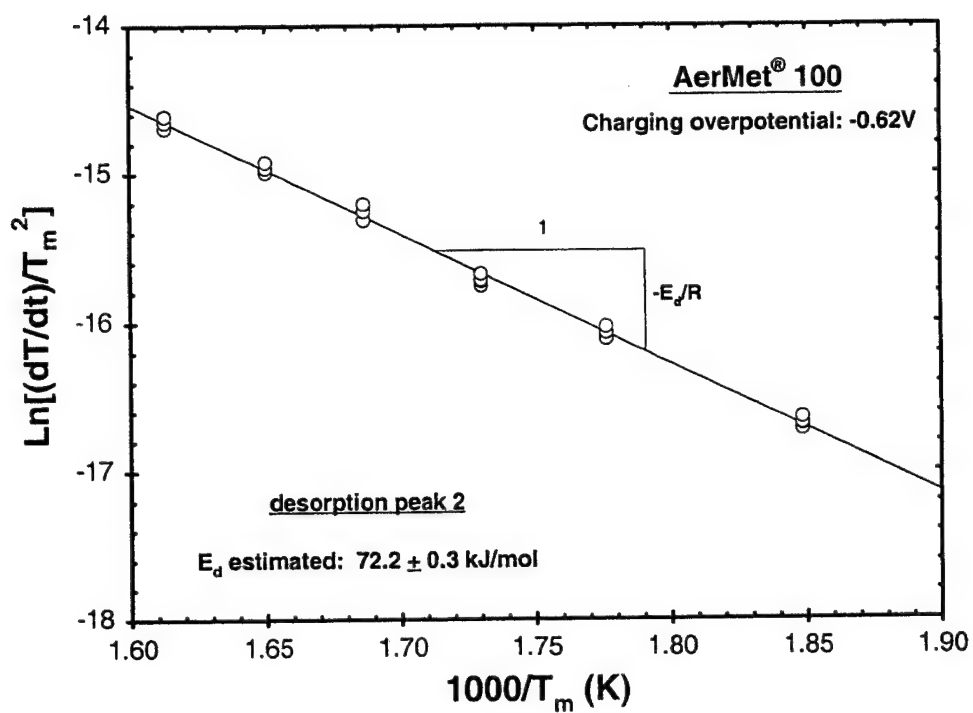


Fig. 12. Plots of ramp TDS data showing the determination of the total activation energy for H desorption, E_d , associated with the second peak (peak 2) on the H desorption curves in Fig. 10, according to Eq.4.

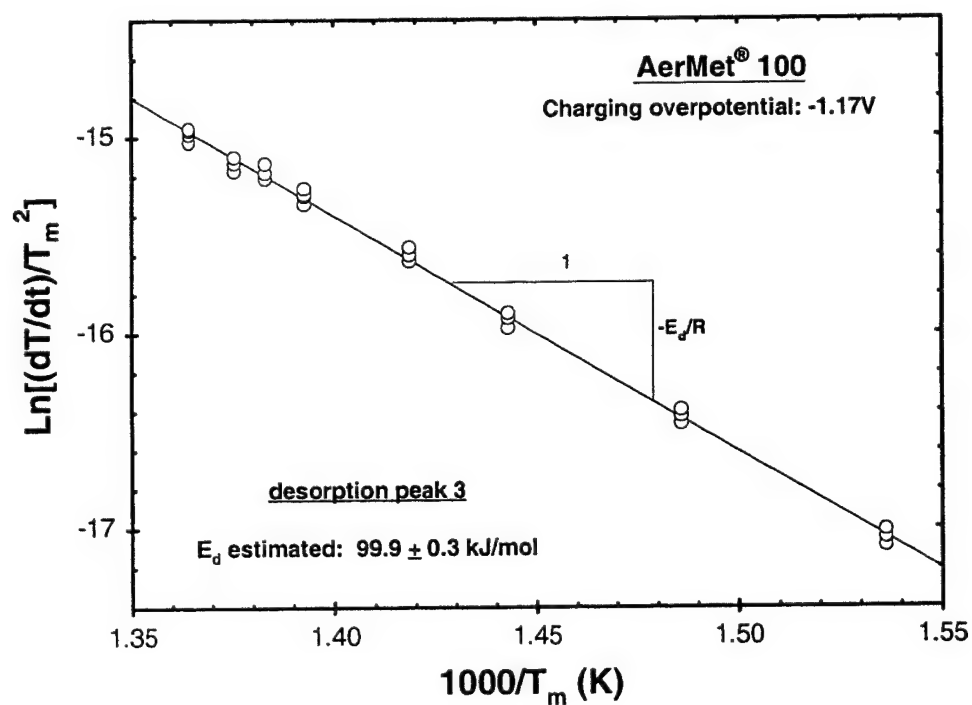
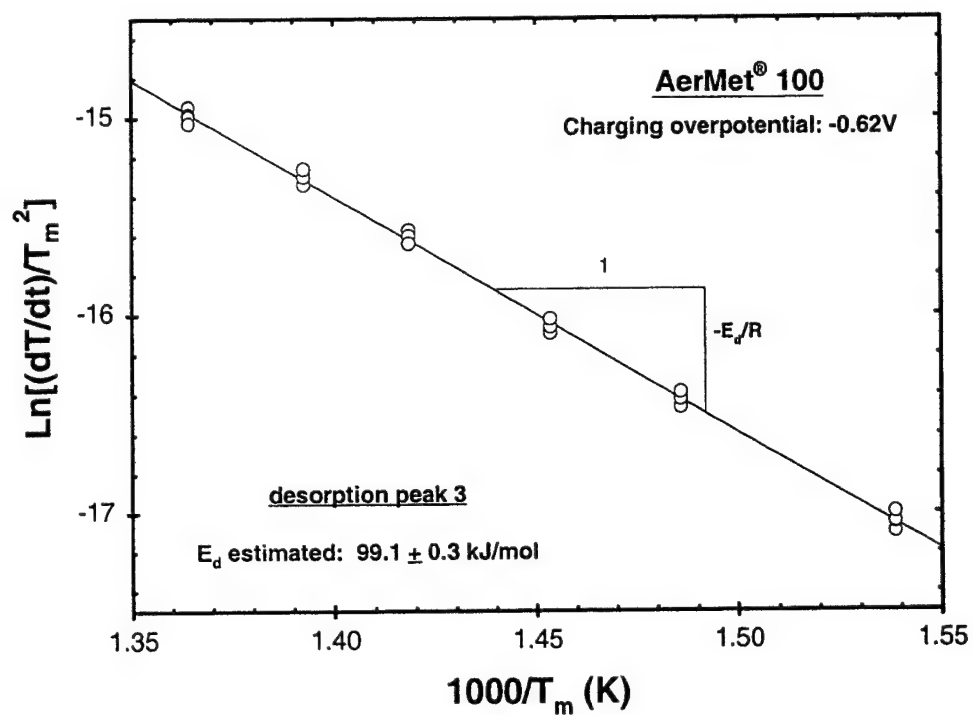


Fig. 13. Plots of ramp TDS data showing the determination of the total activation energy for H desorption, E_d , associated with the third peak (peak 3) on the H desorption curves in Fig. 10, according to Eq.4.

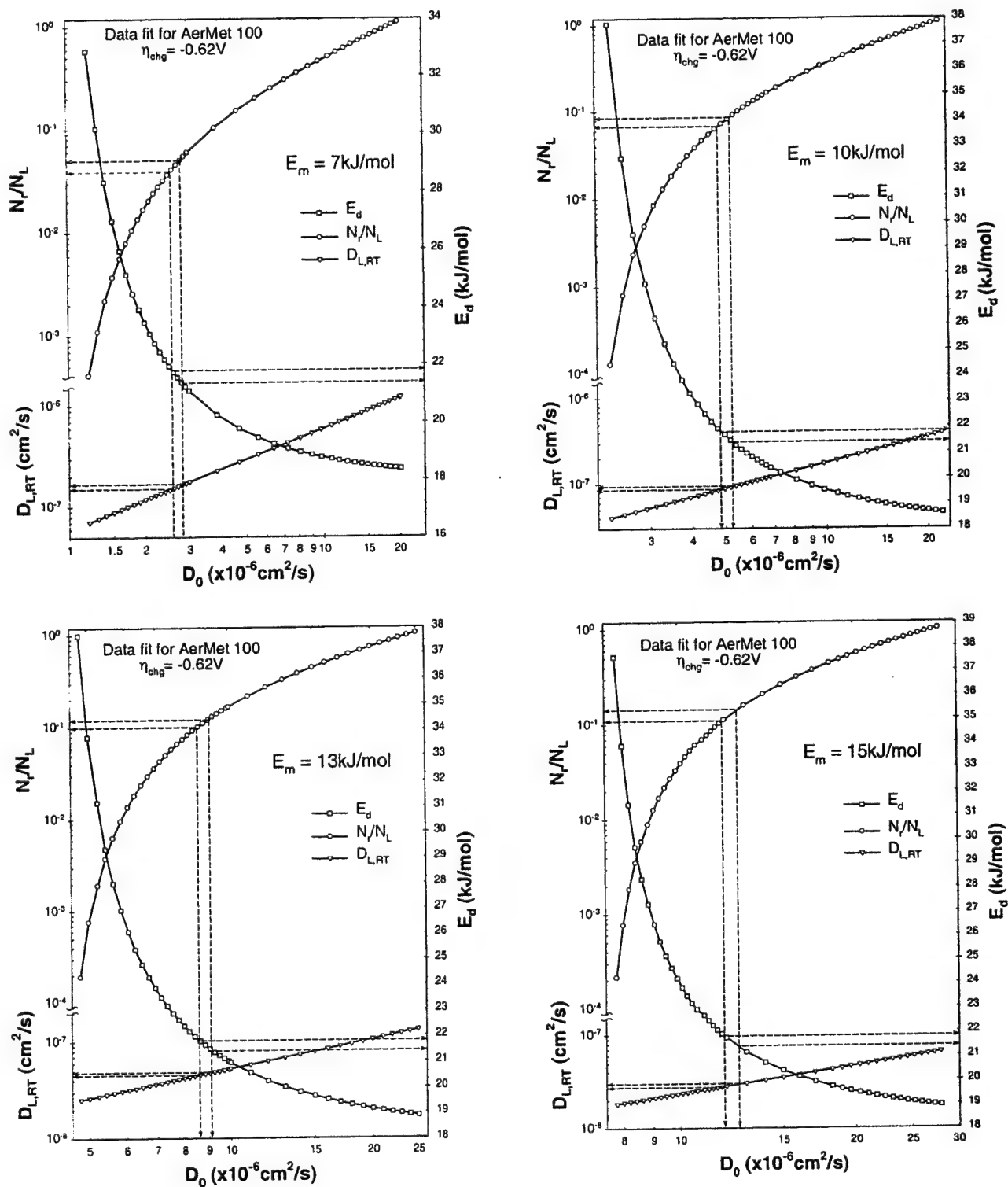


Fig. 14. Selected analytical results for optimizing desorption energy (E_d), trap fraction (N_t/N_L) and lattice diffusivity at room temperature ($D_{L,RT}$) by varying the pre-exponential constant D_0 and the migration energy E_m (data of D_{app} from AerMet[®] 100 charged with $\eta_{\text{chg}} = -0.62\text{V}$)

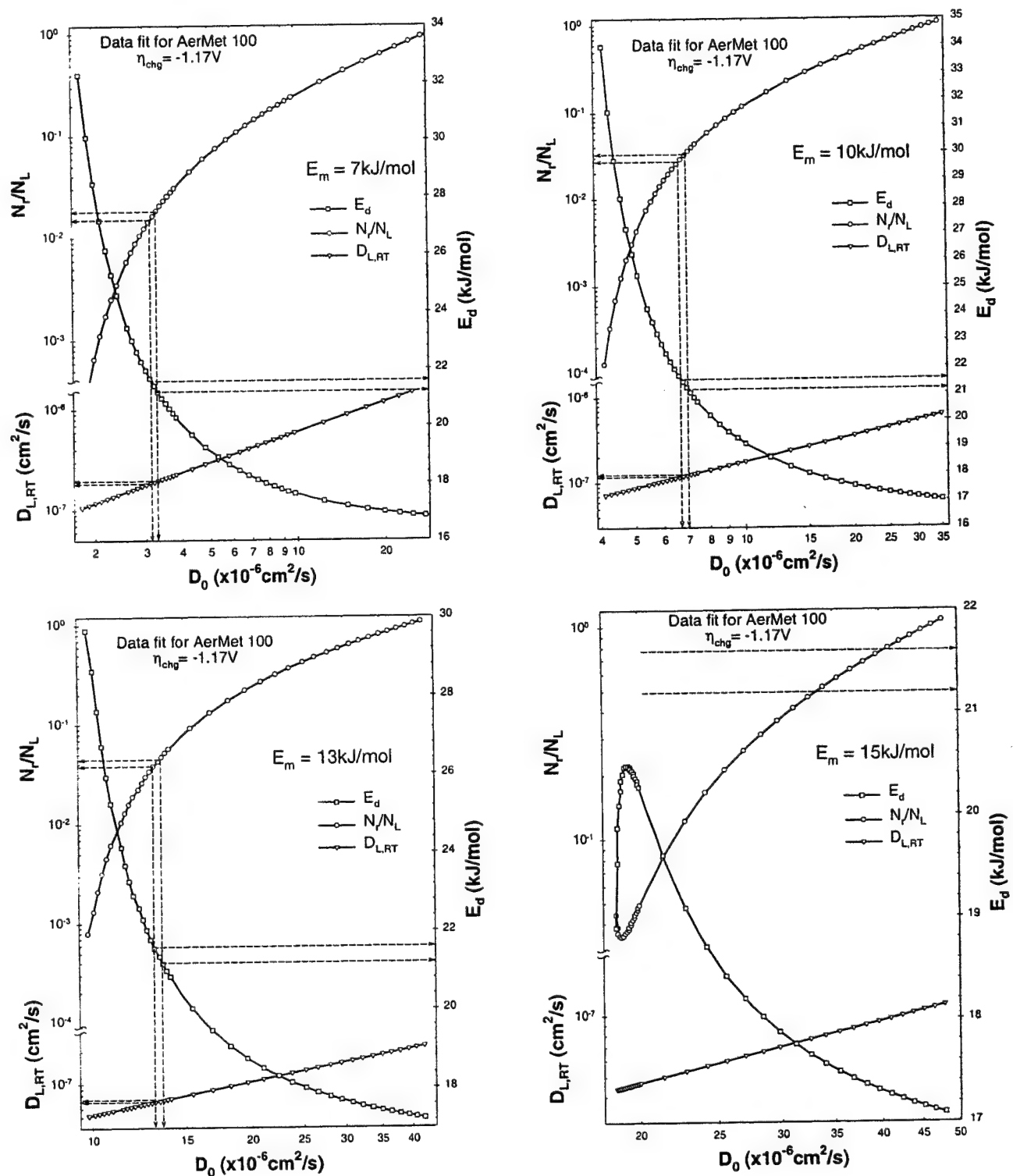


Fig. 15. Selected analytical results for optimizing desorption energy (E_d), trap fraction (N_t/N_L) and lattice diffusivity at room temperature ($D_{L,RT}$) by varying the pre-exponential constant D_0 and the migration energy E_m (data of D_{app} from AerMet[®] 100 charged with $\eta_{\text{chg}} = -1.17\text{V}$)

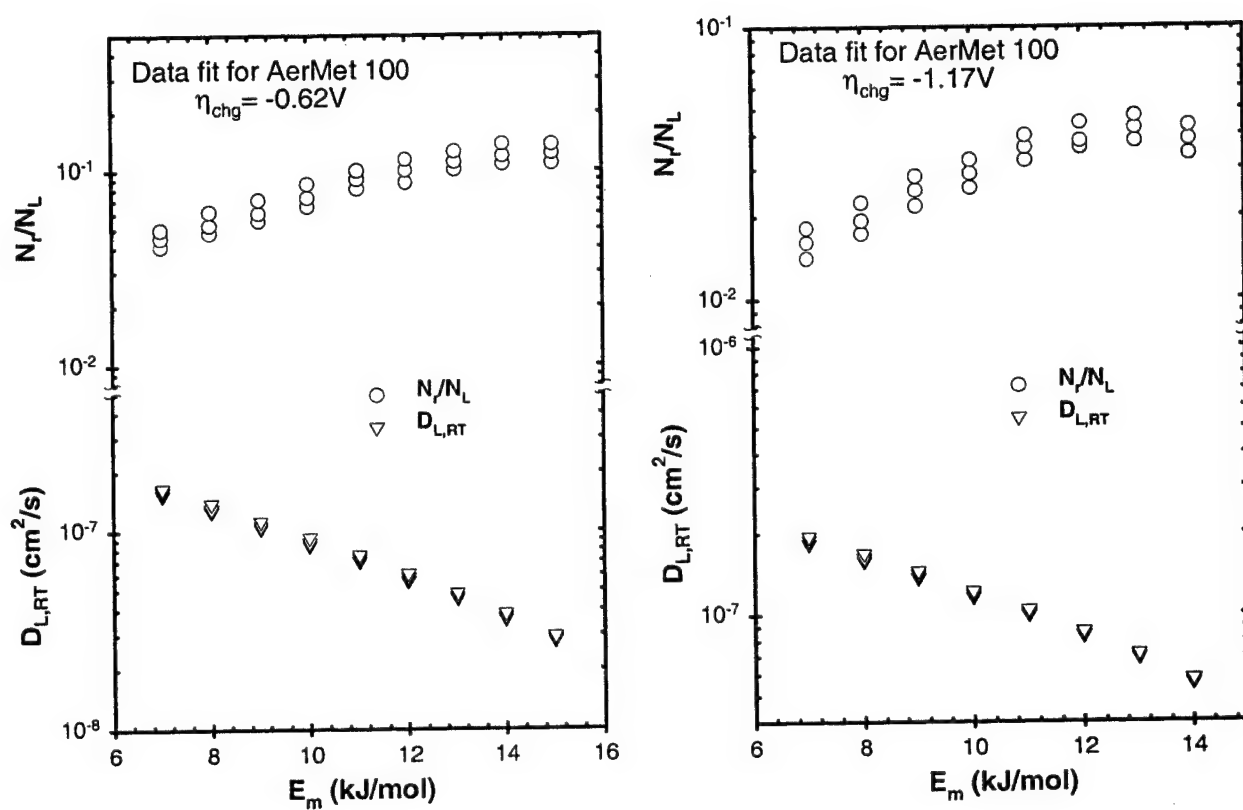


Fig. 16. Analytical results showing variation of $D_{L,RT}$ and N_r/N_L with selected E_m as summarized from Figs. 14-15.

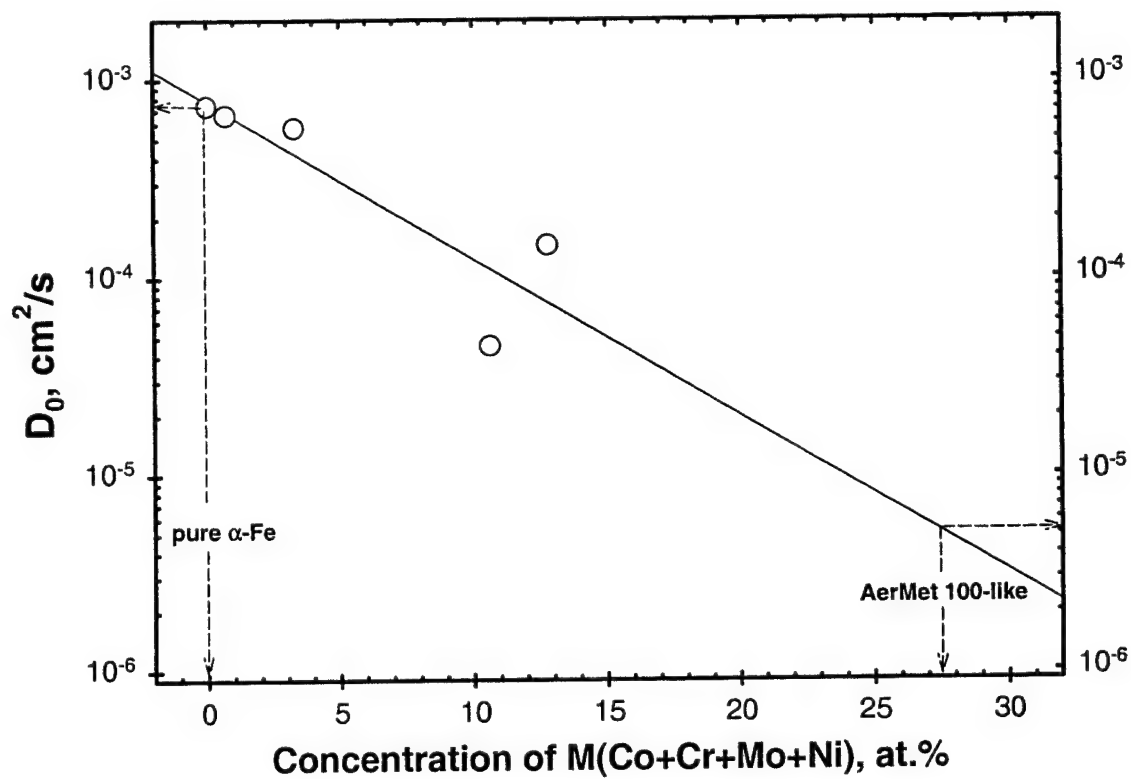


Fig. 17. Effect of the addition of an equivalent element (Co, Cr, Mo or Ni) on the pre-exponential coefficient, D_0 , in Eq. 2. Data for individual alloying element effect come from [45].

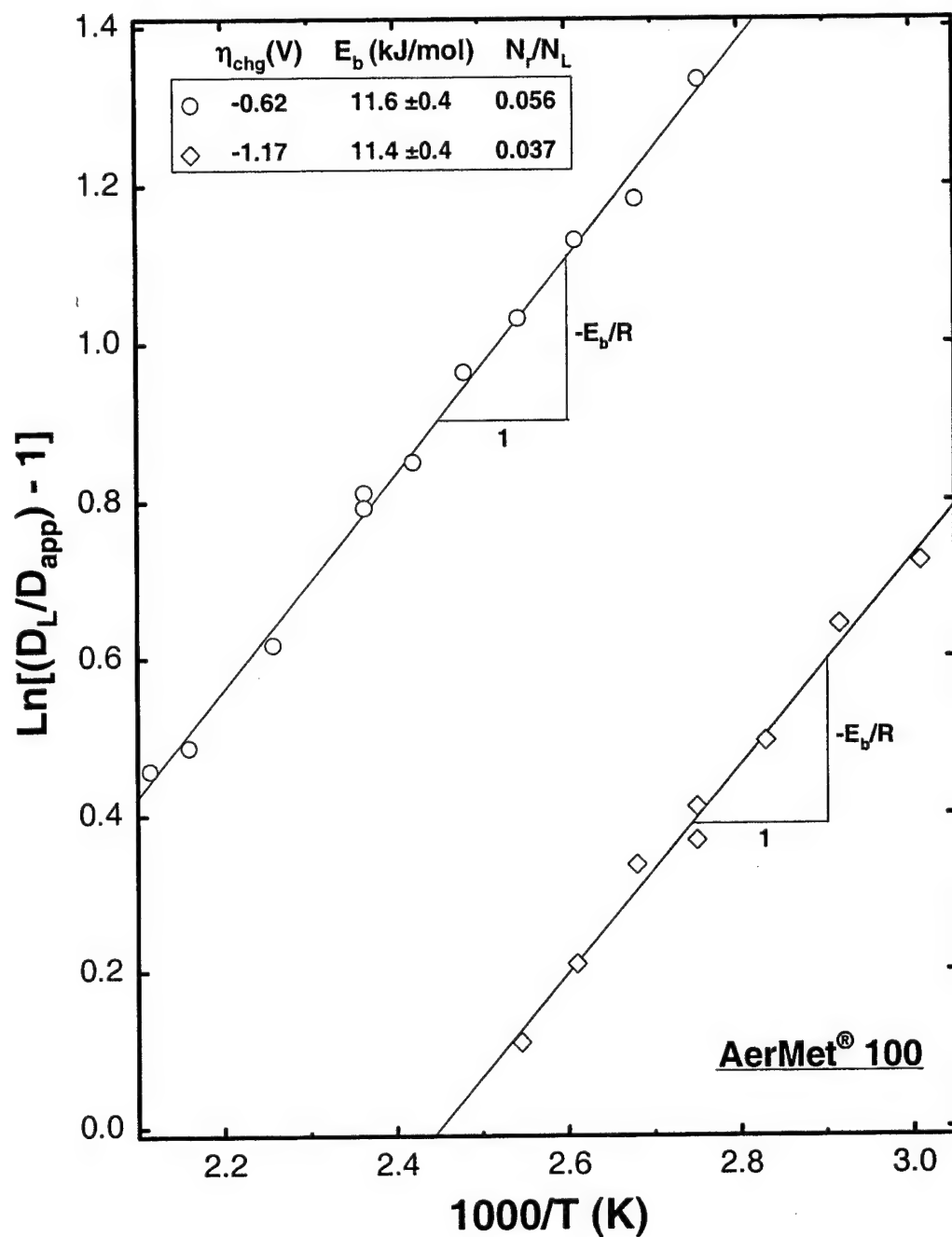


Fig. 18. Data plot demonstrating the determination of the H binding energy with traps associated with the first desorption peak (peak 1). D_{app} is from TDS test data on diffusivity as shown in Fig. 4a, and D_L is calculated according to Eq.2 using E_m and D_0 listed in Table V.

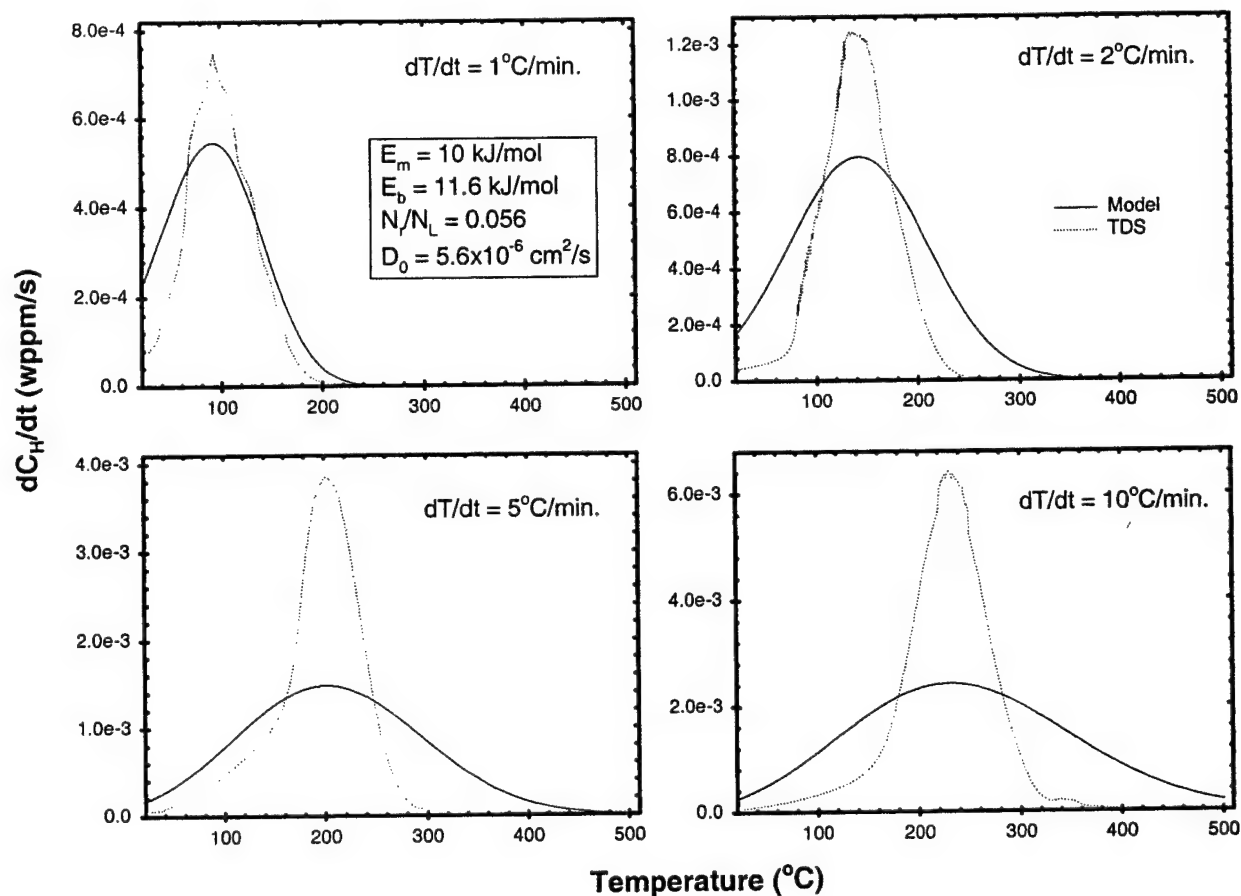


Fig. 20. A comparison of the H thermal desorption rate versus temperature curves obtained by TDS ramp experiments and by a programmed (C^{++}) modeling using Eq. 7, for specimens charged at $\eta_{\text{chg}} = -0.62\text{V}$ and TDS tested at varying heating rates ($dT/dt = 1 - 10\text{ }^\circ\text{C/min.}$)

**USE OF CREVICE SCALING LAWS TO INVESTIGATE LOCAL
HYDROGEN UPTAKE IN RESCALED MODEL PITS**

M.A. Switzer, R.P. Gangloff and J.R. Scully

Department of Materials Science and Engineering
University of Virginia
Charlottesville, VA 22904-4745
USA

USE OF CREVICE SCALING LAWS TO INVESTIGATE LOCAL HYDROGEN UPTAKE IN RESCALED MODEL PITS

Michael A. Switzer, Richard P. Gangloff, John R. Scully

Center for Electrochemical Science and Engineering
Department of Materials Science and Engineering
University of Virginia
Charlottesville, VA 22904-4745

ABSTRACT

The objective of this study was to identify the extent to which occluded pit/crevice geometry and electrochemical conditions affect local hydrogen production and uptake in PH 13-8 Mo stainless steel exposed to aqueous environments. Crevice corrosion scaling laws of the type x^2/gap , where x is the crevice depth and "gap" is the crevice width, were successfully exploited to rescale the sizes of model pits from micrometer to millimeter-scale dimensions. Such rescaling enabled successful hydrogen measurements on global and local length scales as a function of rescaled pit depth. Severe local hydrogen uptake was observed in pits under electrochemical conditions where planar electrodes were in a passive state. Moreover, nuclear reaction analysis revealed that concurrent metal dissolution and hydrogen uptake lead to severe local hydrogen absorption within tenths of micrometers of the simulated pit surface. Possible explanations are discussed.

INTRODUCTION

Pits and other occluded sites serve several roles that promote stress corrosion (SCC) and hydrogen environment-assisted cracking (HEAC) of engineering alloys in aqueous environments. Pits can act as stress concentrators that facilitate crack initiation, expose susceptible grain boundaries and interfaces not available on machined surfaces, and provide a local environment for accelerated corrosion as well as hydrogen production and entry. The latter occurs as a consequence of hydrolytic acidification of dissolved metal cations and ohmic potential drop such that the pit bottom potential is below the reversible hydrogen potential. The environment within pits can be dramatically different from that of the bulk electrolyte. Hydrolysis of metal cations can drastically lower the pit pH so that it is much more acidic than the bulk solution.¹ This by itself may lead to activation of the pit walls and surfaces away from the most active dissolution site in a pit by chemical dissolution of any pre-existing oxide film that can serve as a hydrogen permeation barrier. Also, ohmic potential drop through the pit due to the solution resistance of the pit electrolyte and restricted pit geometry may cause an active-passive metal to activate by reductive dissolution below the Flade potential, even though the

external surface of the metal is held at a potential where it is passive. Moreover, the local potential may drop below $E_{\text{rev}}^{\text{H}/\text{H}^+}$ enabling generation of hydrogen that can readily diffuse into the metal. Metal dissolution along the pit walls can inject vacancies into the metal, change its near-surface metallurgical condition and possibly trigger dynamic trap state creation when vacancies function as hydrogen traps that lower the chemical potential of hydrogen injected into the metal from a crack tip. The amount of hydrogen generation within the pit coupled with slow hydrogen diffusivity within the metal results in large local hydrogen concentration gradients at such pits or crevices sites, despite large chemical and mechanical driving forces for hydrogen diffusion into the metal. These factors can may lead to an underestimation of hydrogen surface concentration in some hydrogen uptake experiments.

Quantifying hydrogen uptake and local hydrogen concentrations in pits, crevices and cracks has been difficult due to the size scale of the regions of interest. Brown described a method for determining the solution chemistry within a stress corrosion crack by freezing the crack and the solution present in the crack tip. The samples were then broken to expose the crack tip solution, and indicator papers were used to identify the solution pH and the presence of metal ions.² While these procedures determine the presence of certain ions within the crack tip solution, few method for measuring H uptake have been employed.

Experiments utilizing the thermal emission (e.g., LECO) methods for determining total hydrogen concentrations require a large sample mass. Such techniques yield globally averaged concentrations since measurements obtained in the presence of severe hydrogen concentration gradients represent the average of high near surface hydrogen concentrations as well as regions of more dilute concentration. Hydrogen permeation measurements using a charging solution that mimics the composition of acid pits in order to estimate hydrogen uptake in pits and cracks have a number of shortcomings. Uncertainty exists over the exact surface state of the metal within the pits that may be difficult to duplicate. Different surface states may affect hydrogen absorption. Metal dissolution may significantly alter the surface state of the pit wall compared to polished surfaces and thickness changes during permeation confound accurate measurements. The exact crack tip solution composition and ohmic potential drop within pits or cracks can be uncertain due to the difficulty in analyzing the micro-liters of solution present in real occluded sites and the large size of experimental potential probes. The solutions used in permeation experiments, therefore, are approximations of the pit solution chemistry. Micron-scale potential changes and chemical gradients in real pits, crevices, and cracks are difficult to quantify and reproduce because most commercial microelectrodes are too large to employ in real pits. Finally, the exact hydrogen production mechanism within the pit may be unknown making it difficult to duplicate in H uptake experiments utilizing permeation methods. Consequently, it is difficult to accurately represent hydrogen uptake in pits using planar electrodes that mimic crack tips. It is possible that uncontrollable local factors conspire to produce high local hydrogen concentrations

Precipitation aged hardened martensitic stainless steels (e.g., Fe-Cr-Ni-Mo alloy) that release hydrolysable chromium as well as Fe cations during dissolution are ideal

candidates for high local hydrogen uptake at pits that is not seen in global measurements of hydrogen. Hydrogen production is thermodynamically assured during acid pitting when the remainder of surfaces remain passive in near-neutral chloride solutions. These alloys have known susceptibility to internal hydrogen embrittlement and hydrogen-environment embrittlement sensitive to crack tip hydrogen concentration.³ They are also susceptible to pitting by the acid-pit stabilization mechanism.⁴ Moreover, such alloys have slow effective diffusion rates that restrict rapid transport of high levels of diffusible hydrogen away from hot spots such as pits where local hydrogen uptake may be severe.¹² The K_{th} vs yield strength data for PH 13-8 Mo suggest an extreme sensitivity to electrochemical conditions that enable such local hydrogen uptake.⁵ For instance, K_{TH} differs significantly for open-circuit potential (OCP) exposure in 3.5% NaCl⁶ versus 20% NaCl, which likely establishes a different OCP and resulting different local crack tip chemistry and level of hydrogen uptake. Cathodic polarization results in bulk hydrogen charging with a clear evidence of hydrogen embrittlement. At issue is the critical need to develop a better understanding of the conditions under which pits and recesses might promote locally high hydrogen concentrations when hydrogen production and uptake is not expected on passive surfaces exposed to the bulk electrolyte. One way to accomplish this would be to exploit pit scaling law⁷s to enlarge pits enough to make local hydrogen measurements in rescaled pits that are equivalent to those expected in realistic micrometer scale versions.

OBJECTIVE

The objective of this research project was to characterize locally hydrogen concentrations over small length scales in model pits utilizing appropriate geometric crevice scaling laws to design and manufacture model pits of millimeter dimensions that are analogous to actual pits of micron dimensions. These pits were then used to examine hydrogen uptake at various locations within the pits under selected electrochemical conditions. Quantification of the absorbed hydrogen was facilitated by the use of thermal desorption spectroscopy (TDS) and nuclear reaction analysis because of their ability to analyze small-scale samples and provide depth resolution over small length scales, respectively. This paper seeks to demonstrate the concept of rescaling for the purposes of local hydrogen measurement.

APPROACH

Materials

The focus for investigation of local hydrogen uptake was a precipitation hardened stainless steel. These steels are susceptible to acid pitting resulting in sufficient ohmic voltage drop and local acidification to promote hydrogen production and uptake in pits. Under such pitting conditions, adjacent surfaces remain passive and at electrochemical potentials above reversible hydrogen. PH 13-8 Mo stainless steel (H1050 condition, σ_{YS} = 1241 MPa, K_{IC} = 96-165 MPa m) with the alloy composition indicated in Table 1 was selected for investigation. Both planar electrodes and model localized corrosion sites were studied under conditions mimicking those encountered during acid pitting.

Table 1. Composition of PH 13-8 Mo

	<u>Cr</u>	<u>Ni</u>	<u>Mo</u>	<u>Al</u>	<u>Mn</u>	<u>C</u>	<u>Si</u>	<u>P</u>	<u>S</u>	<u>N</u>	<u>Fe</u>
Wt. %	12.5	8.14	2.12	1.1	0.09	0.03	0.04	0.006	0.0004	0.005	75.97
At. %	13.3	7.66	1.22	2.3	0.09	0.14	0.08	0.011	0.001	0.020	75.24

Rescaling methods to enable spatially resolved hydrogen analysis in pits

In this study, two approaches were used to overcome many of the experimental difficulties inherent to the problem of local crack tip or pit hydrogen analysis. First, local corrosion scaling laws were implemented to duplicate occluded site conditions representative of a small pit or crevice in larger sized "rescaled" model pits more assessable to hydrogen measurements but that could reproduce equivalent mass transport, ohmic potential, and electrochemical properties over larger scaled dimensions. The precise scaling laws that apply to PH 13-8 Mo were developed using the CREVICERv2 computer program available in the Center for Electrochemical Science and Engineering at the University of Virginia.⁸ Various crevice geometries were modeled using actual experimental electrochemical parameters obtained from PH 13-8 Mo such as critical current density, passivation potential, and solution conductivity. These were used to determine the interfacial potential inside both small and large pits as a function of the pit depth dimension (x) for various pit mouth dimensions. The pit mouth is similar to a crevice gap (G) and in this study represents the dimensions of the square pit. In these studies the model pit possessed a square crevice opening and depth to produce a pit cavity shaped as a right angle prism. Relationships between two critical depths (the depth for depassivation and activation of the stainless steel in reducing acid solutions, $x_{crit1} = x_P$, as well as the depth for the local potential to drop below reversible hydrogen, $x_{crit2} = x_{HER}$) and pit gap were developed. Potential versus depth data obtained from CREVICESv2 computer simulations in selected pit sizes produced relationships between x_{crit}^2 vs. gap for the selected martensitic stainless steel in a simulated acidic pit solution. The complexity of this task was reduced by conducting experiments and performing modeling in concentrated reducing acidic solutions containing metal salts. These solutions were selected to minimize pit chemistry changes as a function of pit depth with the intent of minimizing changes in electrochemical parameters such as anodic and cathodic half-cell currents with time. This enabled use of the same electrochemical kinetic parameters and solution conductivity at all positions, x , within the simulated pit. After constructing plots of local potential versus depth, x , for various potentials and dimensions G , x_{crit1} and x_{crit2} were plotted versus G . The nearly linear x^2/G relationships obtained from modeling served as scaling laws that guided development of rescaled pits for experimental study. x_{crit}^2 vs. gap relations were used to select larger dimension pits capable of allowing spatially resolved hydrogen measurements. These pits were electrochemically equivalent to small-scale versions over larger length scales with one exception. Hydrogen bubbled formation was not incorporated in modeling but likely occurs in real as well as actual rescaled pits. Bubbles restrict ionic transport in crevices and pits and are expected to induce greater IR drop. However, recesses subjected to

hydrogen evolution were previously found to follow the x^2/G relationship when equivalence of Tafel kinetics was considered.⁹

A variety of hydrogen probes with enhanced combinations of lateral and depth resolution, as well as great sensitivity to hydrogen concentration, were utilized to quantify absorbed hydrogen concentrations in model-occluded sites. Methods utilized included thermal desorption spectroscopy (TDS) and nuclear reaction analysis (NRA). The TDS system utilizes a quadrupole mass spectrometer to measure the change in H_2 partial pressure via monitoring of selected mass/charge ratios in a high vacuum chamber containing a hydrogen charged sample that is the source of the outgassing.¹⁰ The UVA system is sensitive enough to enable hydrogen analysis from specimens with mass of only a fraction of a gram and corresponding small volume of material. The amount of hydrogen egressed from the samples is dependent on the programmed temperature of the furnace surrounding the analysis chamber since the total hydrogen released at a given temperature includes both diffusible and trapped hydrogen.¹¹ Hydrogen trapping sites within PH 13-8 Mo include grain and lath boundaries, dislocations and strengthening precipitates. Each trapping site has an associated binding energy.¹² Exactly the same temperature program was used during TDS experiments to analyze each sample since varying test temperatures would affect the amount of hydrogen liberated from various trapping states. A programmed ramp rate of $3^\circ\text{C}/\text{min}$ from room temperature to a maximum temperature of 330°C was confirmed to release hydrogen from lattice and major trap states. The integrated amount of hydrogen released was used to quantify the global diffusible and trap-affected hydrogen concentrations in specimens removed from LN_2 storage after potentiostatic polarization. This was conducted after subtraction of the background hydrogen detected without a hydrogen charged specimen. Nuclear reaction analysis was performed on hydrogen charged planar electrodes of PH 13-8 Mo at the ion beam facility at the University of Albany of New York. Hydrogen was detected using $^1\text{H}(^{15}\text{N}, \gamma\alpha)^{12}\text{C}$ nuclear reaction (6.385 ± 0.005 MeV resonant energy) using a beam of high-energy $^{15}\text{N}^+$ ions to bombard a sample over a lateral area of square millimeters. The gamma ray output results from the nuclear reaction of the N^{15} ions with atomic hydrogen and is proportional to the hydrogen concentration over a finite depth range. Depth profiling is achieved by varying the kinetic energy of the ionized nitrogen beam above the threshold resonant energy. In this way the beam of N^{15} ions penetrated the material, energy loss occurred, and the resonant energy was obtained at a given sample depth. Thus the gamma ray output was proportional to hydrogen concentration at that depth. In this way, energy loss was exploited to sample hydrogen concentration over precise ranges of depth perpendicular to planar electrode surfaces. Advantages of this technique include a depth resolution as good as nanometer. This resolution is due to the four order of magnitude difference in cross-section and hence gamma-ray yield at the resonance energy compared to off-resonance energies.¹³

Environments for simultaneous electrochemical corrosion and hydrogen charging

Studies without model localized corrosion sites were conducted on planar electrodes exposed to room temperature deaerated solutions of 0.1 M HCl (simulating an acidic solution associated with occluded sites) and 5 M H_2SO_4 solution ($\text{pH} = -0.57$) plus

dissolved iron, chromium, and nickel ions (simulating a acid pit environment in a stainless steel after metal dissolution). PH 13-8 Mo exhibits an active-passive transition in both environments such that the active open circuit potential resides below the reversible hydrogen potential. This was confirmed by IR-corrected E-Log(i) curves measured on planar electrodes in the two N₂ deaerated solutions. Likewise, cathodic E-Log(i) data was recorded and analyzed over a range of pH levels to provide reaction kinetics for the hydrogen evolution reaction (HER) as a function of pH and cathodic hydrogen overpotential. Hydrogen uptake was subsequently studied at selected potentials.

Planar Electrode Experiments to Elucidate Hydrogen Uptake under IR-free Conditions

The thermal desorption spectroscopy system was first used to determine the effective room temperature hydrogen diffusivity in order to effectively charge planar electrode samples to achieve uniform hydrogen concentrations. Steady state C_H values were then characterized at various potentials along the polarization curves for PH 13-8 Mo exposed to 0.1M HCl and 5M H₂SO₄ with dissolved metal ions. Hydrogen uptake was investigated under conditions where bulk hydrogen charging occurs at cathodic potentials, under local pitting conditions, as well as under conditions promoting pit depassivation and surface activation simultaneous with hydrogen production. TDS and NRA were performed on exposed materials that were charged for time periods enabling homogeneous global hydrogen distributions. Two separate cleaning procedures were used (methanol rinse and nitric acid cleaning) and specimens were immediately stored in LN₂. TDS analysis of the hydrogen charged samples was used to produce relationships between absorbed hydrogen concentration and charging potential. These global hydrogen concentrations provided data on the effective hydrogen solubility (lattice and trapped hydrogen concentration) versus hydrogen fugacity. Hydrogen concentrations in the stainless steel alloy were measured in conjunction with global electrochemical parameters, and global hydrogen production rates (proportional to hydrogen gas evolution). H₂ gas volume was determined using a specially designed electrochemical cell utilizing an inverted burette/funnel arrangement to collect hydrogen gas as it evolved and bubbled from the surface of the alloy (Figure 1). Hydrogen absorption efficiency was determined according to Equation 1:

$$\xi_{abs} = \frac{Q_{H,abs}}{Q_{H,tot}} \times 100 \quad [\text{Eq. 1}]$$

where ξ_{abs} is the total hydrogen absorption efficiency expressed as a percent, $Q_{H,abs}$ is the charge associated with monatomic hydrogen that absorbs into the bulk lattice and trap sites (Coulombs), and $Q_{H,tot}$ is the charge due to the reduction of protons on the surface of the metal during the time taken to saturate planar electrodes assuming volume controlled hydrogen uptake. $Q_{H,abs}$ was calculated from the hydrogen concentration measured in the TDS system. $Q_{H,tot}$ was determined by three different methods: 1) calculation from Tafel kinetics; 2) Total charge measured by integration of the HER current recorded by the potentiostat under net cathodic conditions; 3) hydrogen gas

evolved on the surface of the metal and collected by the inverted burette of the charging cell show in Figure 1. Local surface hydrogen concentrations with nm depth resolution were measured using NRA on cleaned and uncleaned specimens. The depth profile from cleaned but unexposed specimens was then subtracted from results on exposed specimens to minimize the influence of surface hydrogen associated with oxide or films and or cleaning.

Model Rescaled Pits

Experiments in model occluded sites simulating pits involved cylindrically shaped samples of PH 13-8 Mo with concentric cylindrical holes of various diameters drilled into the center of the samples. Pit scaling laws were used to produce rescaled pits. Specimens were potentiostatically charged under conditions where the pit mouth resided in the passive region and hydrogen uptake was possible given sufficient IR drop at a certain pit depth. Specimens were held under these conditions until uniformly charged from interior surfaces (in the radial direction) according to the hydrogen diffusivities determined from bulk charging. Micro-reference electrode (World Precision Instruments Driref-450 Micro-ref. Electrode) measurements recorded local pit potential as a function of pit depth using a micrometer resolution positioning system (see Figure 2) during potentiostatic holds. Thus, the depth at which the local potential dropped below E_P and $E_{rev(H/H^+)}$ could be determined by comparison to $E\text{-log}(i)$ data and from knowledge of the reversible hydrogen potential. Absorbed hydrogen concentration versus rescaled pit depth profiles were constructed by two methods. First, the cylindrical pits were stored in LN_2 , then cold sectioned at various depths from the exposed pit mouth, stored in LN_2 again, and the TDS system was used to measure global hydrogen concentration at various pit depths. Secondly, the previously established relationships between C_H versus true electrochemical charging potential obtained from planar electrodes were used. Knowledge of local potentials within pits obtained from micro-reference electrodes was compared to planar electrode data at precise potentials to predict the absorbed hydrogen concentration at each local potential measured. Local anodic and cathodic half-cell reaction rates were also determined using this data.

RESULTS

Electrochemistry associated with passive-to-active transitions and HER

$E\text{-Log}(i)$ data for PH 13-8 Mo exposed to various concentrations of sulfuric acid containing dissolved metal ions can be seen in Figure 3. PH 13-8 Mo exhibits an active-passive transition in each of these solutions. As seen, a passive region is seen above $-0.5 V_{Hg/Hg_2SO_4}$. The alloy exposed to 5 M sulfuric acid plus dissolved metal ions shows a large critical current density of approximately $3 \times 10^{-3} A/cm^2$. This curve contains a cathodic loop in the anodic region that was reproducibly obtained in scans. This solution was chosen to examine hydrogen uptake in the model pits. The reversible hydrogen potential for this solution is $-0.59 V_{Hg/Hg_2SO_4}$. It is possible that a rescaled pit held in the passive range will under a passive to active transition and the OCP of the active material

will be below $-0.75 \text{ V}_{\text{Hg/Hg}_2\text{SO}_4}$. Thus, the primary local cathodic reaction in deep pits that undergo active to passive transitions is the HER.

Concerning the HER, IR correction of the cathodic E-Log(i) data was used to generate an expression for cathodic current density as a function of hydrogen overpotential and pH. The following expression was obtained:

$$i_{\text{H}_2} = (1.31 \times 10^{-4})[\text{H}^+]^{0.525} \exp^{(-14.45\eta_c)} \quad [\text{Eq. 2}]$$

where i_{H_2} is the cathodic current density (A/cm^2), $[\text{H}^+]$ is the hydronium ion concentration (mole/L), and η_c is the hydrogen overpotential (V). This expression is consistent with a Tafel slope of approximately 160 mV/decade. For a given solution pH, Equation 2 can be used to predict the cathodic current density for various hydrogen overpotentials, a representation of which can be seen in Figure 4.

Similarly, E-Log(i) data for various hydrochloric acid concentrations shows active-passive transitions and clear indications of pitting potentials for 0.1, 0.001, and 0.0001 M HCl (Figure 5). More concentrated HCl solutions exhibit pitting potentials near the OCP. All HCl solutions tested exhibited deaerated OCPs more negative than reversible hydrogen. The alloy exposed to 0.1 M HCl solution shows the largest critical current density at $2 \times 10^{-5} \text{ A}/\text{cm}^2$. This alloy exhibits a several hundred mV passive range above reversible hydrogen where minimal hydrogen production and uptake would be expected. This solution was chosen for focus of remaining experiments. The reversible hydrogen potential for this alloy/solution combination is $-0.30 \text{ V}_{\text{SCE}}$ while the OCP is nearly $-0.4 \text{ V}_{\text{SCE}}$. The cathodic E-Log(i) data were IR corrected and an expression for cathodic current density as a function of pH and overpotential was developed:

$$i_{\text{H}_2} = (5.45 \times 10^{-5})[\text{H}^+]^{0.185} \exp^{(-12.74\eta_c)} \quad [\text{Eq. 3}]$$

where i_{H_2} is the cathodic current density (A/cm^2), $[\text{H}^+]$ is the hydronium ion concentration (mole/L), and η_c is the hydrogen overpotential (V). This expression is consistent with an HER Tafel slope of 181 mV/decade. This expression, again, enables determination of hydrogen evolution half-cell reaction rates over the potential range where the applied current density is net anodic. A plot of this equation for varying pH and cathodic overpotential can be seen in Figure 6.

Hydrogen Uptake on Planar Electrodes as a Function of IR-Corrected Potential

Large planar samples of PH 13-8 Mo charged in 5 M sulfuric acid plus dissolved ions in the charging cell shown in Figure 1 were analyzed using the TDS system to determine the global concentration of hydrogen, C_{H} , adsorbed after charging to achieve a homogeneous global hydrogen distribution. The error in the TDS results and represented in the figure by error bars was determined by analyzing multiple samples charged in the same bulk solution under the same electrochemical conditions Figure 7 shows the results of these experiments. C_{H} is greatest at potentials cathodic to the reversible hydrogen

potential as expected. Absorbed hydrogen concentration increase with hydrogen overpotential; uptake at a charging potential of $-1.10 V_{\text{Hg/Hg}_2\text{SO}_4}$ is 40 times greater than uncharged levels (uncharged levels were a fraction of a wpppm). Generally the absorbed hydrogen concentration decreased as the hold potential became more noble. It is interesting to note that hydrogen absorption is observed above the reversible hydrogen potential. Figure 7 also illustrates that considerable hydrogen uptake would occur in pits assuming that ohmic voltage drop places the pit wall near OCP1 at some depth far enough within a deep pit even if the pit mouth were polarized to a more positive potential.

The total hydrogen absorption efficiencies at various charging potentials in 5 M sulfuric acid plus dissolved ions is shown in Figure 8. The figure legend reports the technique by which efficiencies were calculated using the various HER charge density determination methods. Generally the three methods used to determine charging efficiency were consistent, though the efficiencies determined from hydrogen gas collection tended to be higher than the other two methods. The trend in the data shows an increase in absorption efficiency with more positive charging potentials, i.e., at lower hydrogen overpotentials. The highest efficiency from all three methods (for the specimen charged at $-0.65 V_{\text{Hg/Hg}_2\text{SO}_4}$) is only 0.1% for this system, and occurs below the reversible hydrogen potential where anodic dissolution occurs simultaneous with hydrogen production and uptake. The lowest efficiencies were measured for samples charged at the highest hydrogen overpotentials with the least efficient measuring $1 \times 10^{-5}\%$. Hence, C_H increases with hydrogen overpotential but not as significantly as the integrated hydrogen production rate increases as a function of hydrogen overpotential. In other words, the HER far exceeds hydrogen absorption reaction rate at increasing cathodic potentials.

Results of nuclear reaction analysis of planar electrodes charged at open circuit and $-1.2 V_{\text{Hg/Hg}_2\text{SO}_4}$ (cathodically polarized) for 10 hours in 5 M sulfuric acid plus dissolved metal ions can be seen in Figure 9. In this charging period, hydrogen penetrates to a depth of at least $270 \mu\text{m}$ assuming a $D_{\text{eff}}^{\text{H}} = 1.9 \times 10^{-8} \text{ cm}^2/\text{s}$. H/total atom ratio was calculated from γ -ray yield as a function of specimen depth. For both samples, the hydrogen concentration measured by nuclear reaction analysis for an uncharged specimen was subtracted from the data presented in Figure 8 so that only hydrogen due to charging at the two potentials is represented. The results after cathodic polarization show a negligible H concentration profile as expected because the global hydrogen concentration obtained from TDS for $-1.2 V_{\text{Hg/Hg}_2\text{SO}_4}$ polarization is far below the detection limit of NRA (ca. $<10^{-3}$ H/total atoms).¹⁴ However, Figure 9 illustrates a near surface H/total atom ratio of >0.04 that remains above 0.01 until a depth of approximately $0.25 \mu\text{m}$ for samples charged at open circuit as compared to samples charged for the same time period at $-1.2 V_{\text{Hg/Hg}_2\text{SO}_4}$. Recall that the sample charged at open circuit exhibited much more extensive metal dissolution compared to the cathodically polarized sample. Both samples show a higher hydrogen concentration at lower analysis depths that could be associated with surface hydrogen contamination, as often seen in NRA. However, the hydrogen concentration for the sample charged at $-1.2 V_{\text{Hg/Hg}_2\text{SO}_4}$ decreased close to zero between 0.02 - $0.05 \mu\text{m}$ of depth within the sample suggestive of surface hydrogen, possibly in the form of an hydroxide layer. In contrast, the hydrogen concentration for the sample

charged at OCP remained significantly higher through 0.30 μm of depth. This is inconsistent with surface contamination.

Hydrogen concentration as a function of charging potential for the PH 13-8 Mo exposed to 0.1 M HCl is shown in Figure 10. These data show a similar trend to that of the 5 M sulfuric acid plus dissolved metal salts data. Specifically, hydrogen uptake on an IR free planar electrode is minimal near and above the reversible hydrogen potential in the passive region. Uptake occurs under cathodic polarization and anodic polarization above pitting thresholds when acid pits are formed. Hydrogen uptake under cathodic polarization in 0.1 M HCl is significantly greater than seen in 5 M H_2SO_4 with metal salts. The fact that absorbed hydrogen concentration also is elevated for samples charged above the pitting potential ($E_{\text{pit}} = 0.05 \text{ V}_{\text{SCE}}$) confirms hydrogen production and entry in acid pits. A sample charged 150 mV above the pitting potential exhibited a normalized hydrogen concentration slightly higher than that of a sample charged 150 mV below the reversible hydrogen potential.¹

Below the reversible hydrogen potential, hydrogen absorption efficiency calculations (Figure 11) show a decrease in absorption efficiency as hydrogen overpotential increased or as metal dissolution decreased, as was seen in the data for sulfuric acid plus dissolved metal ions. Again this is due to the fact that the HER rate increases markedly with cathodic potential compared with the increase in effective hydrogen solubility with cathodic potential. However, much higher efficiencies can be seen for the samples that were charged above the pitting potential where the efficiency reaches 0.45% for the sample charged at 0.20 V_{SCE} . This is 4.5 times greater than the highest absorption efficiency exhibited by samples charged in sulfuric acid with dissolved metal ions. High efficiency seems to be promoted by simultaneous hydrogen production and metal dissolution.

Pit Scaling Relations and Hydrogen Uptake in Rescaled Model Pits

An example of local potential profiles calculated using the crevice modeling program (CREVICERv2) is shown in Figure 12. The electrochemical parameters used in the model were specified to approximate the actual parameters from the E-Log(i) data for PH 13-8 Mo exposed to 5 M sulfuric acid plus dissolved ions. For an applied potential of $-0.475 \text{ V}_{\text{Hg}/\text{Hg}_2\text{SO}_4}$ in the passive region (Figure 3), the potential profiles were determined for various gaps and depths, x . Additionally experiments were conducted at different applied potentials (not shown). It can be seen in Figure 12 that the local potential is equivalent to the applied potential at the crevice mouth. However, ohmic potential drop forces a decrease such that the local potential decreases towards the open circuit potential. This decrease occurs over shorter depths as the pit mouth dimension (gap) decreases. The local potential drops below the reversible hydrogen potential at one depth ($x_{\text{crit1}} = x_{\text{HER}}$) and the stainless steel reaches a passivation potential at a further depth ($x_{\text{crit2}} = x_{\text{p}}$). Thus beyond a critical depth, the passive stainless steel undergoes an active-

¹ Anodically polarized samples which pitted experienced local hydrogen uptake which was normalized in a conventional manner to the entire specimen mass. Normalization by a small area surrounding each pit was not attempted but clearly would result in a 10-100 fold increase in the local hydrogen concentration.

passive transition and hydrogen production is thermodynamically favorable. However, pit mouths less than several hundred micrometers are too small for hydrogen measurements. From these results, relationships for two critical distances from the mouth of the crevice were developed. The second critical distance, $x_{\text{crit}2}(E_{\text{pass}})$, was designated as the distance from the mouth of the crevice at which the local crevice potential drops to E_{pass} . The first critical distance, is the distance from the crevice mouth at which the pit potential equals the reversible hydrogen potential, $x_{\text{crit}1} = x_{\text{HER}}$. The relationship between these two depth parameters and gap size for PH 13-8 Mo in 5 M H_2SO_4 plus metal salts are shown in Figure 13. The square of each critical distance is, indeed, a approximately linear function of the gap size. A plot of the two defined critical distances versus Gap size (not shown) does not share this linear relationship, confirming that the square of the critical distance versus gap size is the correct operating geometrical scaling relationship for both the case of hydrogen evolution and passive-to-active transitions in this system. This linearity is critical to translating actual pits of micron scale to manufactured pits of millimeter scale.¹⁵

Using these relationships, model pits of millimeter scale (e.g., 1500 μm inside diameter (gap) and 40 mm length) were produced using PH 13-8 Mo. These samples were cylindrical with holes drilled through the center (not completely through the length of the sample) to approximate cylindrical pits. It can be seen from the modeling results of Figure 12 that these rescaled model pits would be expected to possess distinctly different hydrogen uptake over lengths of millimeters instead of micrometers typical of actual pits. These samples were held in 5 M sulfuric acid plus dissolved metal ion and 0.1 M hydrochloric acid solutions under potentiostatic control. Local potential was measured versus depth. Using separate specimens, potentials were held at potentials ranging from -0.4 to -0.60 $\text{V}_{\text{Hg}/\text{Hg}_2\text{SO}_4}$. IR drop was insufficient at high passive potentials such as -0.40 $\text{V}_{\text{Hg}/\text{Hg}_2\text{SO}_4}$ to produce significant changes in local potential inside one-dimensional pits. The reason for this was that pits walls exhibited low anodic current densities that were insufficient towards producing enough ohmic voltage drop to activate the stainless steel. However, when the applied potential was decreased to -0.60 $\text{V}_{\text{Hg}/\text{Hg}_2\text{SO}_4}$ significant potential drop was seen such that the bottom of the pit approached the limiting or open circuit potential near -0.76 V (Figure 3). Rescaled pit specimens were removed, stored in LN_2 and sectioned radially for hydrogen analysis versus depth x , an example of which can be seen in Figure 14 and Figure 15. Figure 14 shows the potential profile experimentally measured using the micro-reference electrode for a sample held in 5 M sulfuric acid plus dissolved metal ions at -0.60 $\text{V}_{\text{Hg}/\text{Hg}_2\text{SO}_4}$ (applied potential) with dimensions of 1500 μm inside diameter and 40 mm length. The pit exhibits a 150 mV potential drop from crevice mouth to crevice tip. Most of the potential drop occurs in the first 10 mm of depth, which is consistent with the modeling results (Figure 12). True i_{an} and i_{ca} were obtained from electrochemical kinetics on planar electrodes (e.g., Eq. 1)). The potential levels off as the open circuit potential is achieved within the pit. Both true i_{an} and i_{ca} increase with depth, x , as expected since HER is promoted by potential drop and the material undergoes a passive-active transition. An indication of the true anodic current density within the pit can be seen by examining the increase in inside diameter of the pit due to corrosion with increasing depth. This increase in pit diameter is indicative of increased anodic dissolution with pit depth after the passive-to-active transition. The

decrease in diameter to the original value at the pit bottom is consistent with a decrease in anodic current density near the OCP associated with the pit bottom.

True cathodic current density also is shown to increase with decreasing local potential within the model pit as is expected (Figure 15), and reaches a constant value as the potential gradient levels near the limiting potential which is the OCP of the pit. This increase in cathodic current density manifests itself in an increase in absorbed hydrogen concentration with increase in depth through the crevice as measured by TDS analysis of the sectioned crevice (Figures 14-15). The local hydrogen concentration within pits increases even when uptake is minimal on passive electrodes outside pits. Independent corroboration is obtained by adding data on C_H predicted from the planar electrode studies at each interfacial potential (Figure 14). The predicted values from the bulk electrode studies are consistent with the values measured by the TDS system. The local hydrogen concentrations within the model pit increase from approximately 4 times an uncharged specimen near the pit mouth to almost 7 times an uncharged specimen greater than 10 mm within the pit where potential is lowest and cathodic current density is at its highest value. Therefore, a planar electrode held just in the passive region at -0.6 V would be expected produce and concentrate hydrogen in pits where $x > x_{HER}$.

DISCUSSION

Global and local hydrogen uptake in passive stainless steel exposed to reducing acids

The results of the electrochemical testing on planar electrodes in various reducing acid solutions show PH 13-8 Mo exhibits an active-passive transition (sulfuric acid) and pitting threshold potentials (HCl solutions). Moreover, this material exhibits a deaerated open circuit potential that is below the reversible hydrogen potential (Figures 3 and 5). Given these electrochemical properties, there are a variety of ways that pit, crevice or crack that experiences IR drop, acidification and/or even O_2 depletion could lead to hydrogen uptake under conditions where boldly exposed planar PH 13-8Mo surfaces would be expected to remain passive and above the reversible hydrogen potential. For instance, O_2 depletion could shift the OCP from a hypothetical aerated OCP in the passive regions shown in Figures 3 and 5 to the deaerated OCP indicated in these figures. Also, hydrogen uptake was observed in 5 M sulfuric acid + dissolved metal salts at the deaerated OCP (Figure 7) as well as when a rescaled pit was held in at -0.6 V the passive region. This occurred presumably because the passive-active transition generated relatively large ($i_{crit} \sim 10^{-2}$ A/cm²) anodic current densities and possibly evolved hydrogen gas that constricted electrolyte path. The result was enough IR drop to drive the local potential within a pit or crevice below the reversible hydrogen potential at $x > x_{HER}$ even though the applied potential was above the passive-active transition. Moreover, pitting of planar electrodes induced hydrogen production and absorption as shown in Figure 10. All of these conditions promote local activation of passive surfaces concurrent with hydrogen generation and absorption on PH 13-8 Mo. Thus they point to a way other than the traditional route involving severe cathodic polarization to produce hydrogen environment embrittlement in PH 13-8 Mo. It has been demonstrated in this paper that such phenomena could occur in such occluded sites in PH 13-8 Mo under conditions where a

planar electrode might be passive and experience limited hydrogen uptake at noble electrode potentials. This explains the finding that PH 13-8 Mo can be susceptible to hydrogen embrittlement at OCP. Hydrogen production has been also observed in model pits in iron,¹⁶ carbon steel¹⁶ and a duplex stainless steel¹⁷ polarized to noble potentials in the passive region when $x > x_{\text{HER}}$. Hydrogen uptake has also been reported in the literature during permeation experiments on anodically polarized planar electrodes under pitting conditions,¹⁸ as well as during intergranular corrosion.¹⁹ At issue, is accurate quantification of local hydrogen concentrations in such corrosion sites. This requires the use of rescaled pits.

Global hydrogen absorption efficiency is highest for potential ranges over which hydrogen production is coupled with anodic dissolution, as shown in Figure 8. This relationship is further exhibited by bulk samples above the pitting potential in 0.1 M hydrochloric acid where hydrogen absorption efficiency is greater than for those samples potentiostatically held at passive potentials. This is a curious finding that could be a straightforward coincidence of the fact that hydrogen production rates increased faster with hydrogen overpotential than did effective hydrogen solubility. However, given the NRA results of Figure 9 showing a high hydrogen concentration at the surface of a dissolving specimen, a much more profound implication may exist. This is discussed below. Few prior experiments have reported such a result, possibly because techniques with high spatial resolution have only recently become available.

Examination of Local Hydrogen Uptake in Rescaled Pits

The results of the computer modeling experiments show that a relationship can be developed for crevice geometry such that the IR drop mechanism (independent of chemistry change) can be sufficient to produce local crevice potentials that would allow for local activation of the metal surface within the crevice concurrent with hydrogen production and uptake. The relationship $x^2/G = \text{constant}$ was found to hold for both the passive-active potential and a reversible hydrogen potential. Such scaling relationships are not a surprise and have been seen before,^{7,8} the difference being that the exact values of the constant specific to PH 13-8 Mo are reported here. An interesting contribution of the present work is the fact that different regimes have been identified for crevices or pits in PH 13-8 Mo. There is a combination of depth and gap where the stainless steel would be passive and remain above reversible hydrogen, a region where hydrogen production could occur but not a passive-active transition of the material, and a deep pit depth ($x_{\text{crit}2}$) beyond which both activation and hydrogen production both occur. The $x^2/G = \text{constant}$ relationship was a reasonably approximation which described both the activation phenomena (similar to the IR* model of Pickering)^{7,9,16,17} and the equivalent conditions for onset of hydrogen evolution. In this study both $x_{\text{crit}1}$ and $x_{\text{crit}2}$ have been specified, although in theory such relations should hold over a range of potentials. Obviously, there is no reason why a variety of systems could not exhibit this generic behavior albeit with different details. The system requirements would be a passive-to-active transition in a solution analogous to the pit chemistry, an open circuit potential or limiting potential in the active deaerated state that is below the reversible hydrogen potential, and $x > x_{\text{HER}}$ at appropriate G. There are obviously many candidate materials for such behavior such as

precipitation age hardened stainless steels in neutral and acidified chloride solutions. The former solutions would require acidification at local sites. These materials would have the potential for local hydrogen uptake at occluded sites when the external boldly exposed planar surfaces were passive.

These relationships can provide guidance for construction of model pits of a large enough scale to measure local potentials and absorbed hydrogen concentrations that would be analogous to an actual crevice of micron scale that prohibit interrogation by commercially available probes and instruments. As suggested by the bulk electrode experiments given sufficient IR drop, the model pit results in Figures 14 and 15 show hydrogen uptake can occur under conditions where the rescaled pit mouth is held in the passive range (e.g., that such IR drops can occur) when $x > x_{crit}$. The local millimeter scale C_H value increases to 7 times the value in an uncharged specimen exposed to humid air and could not be precisely predicted from global results on planar specimens containing crevices. These experiments also show an increased local absorbed hydrogen concentration at depths within the crevice where anodic and cathodic current densities are greatest; that is they show increased metal dissolution and hydrogen reduction, respectively. This is either a coincidence or supports the hypothesis that hydrogen production concurrent with anodic dissolution results in increased absorption efficiency. Thermal desorption spectroscopy and Nuclear Reaction Analysis have proven to be effective methods for analyzing absorbed local hydrogen concentrations under such conditions.^{20,21}

Local hydrogen uptake in surfaces undergoing simultaneous dissolution and hydrogen production

The NRA results of Figure 9 indicate a high hydrogen concentration at the surface of the specimen exposed at open circuit. This concentration profile extended to a depth of almost 0.35 μm (350 nm). This depth exceeds likely oxide film²² and selectively dissolved metallic film thicknesses² but does not extend to the full depth to which diffusible hydrogen might penetrate (i.e., ~300 μm) during the 10 h charging period. It is likely that diffusible hydrogen penetrates to a 0.35 μm depth but that such a global concentration of hydrogen is below the detection limit of the NRA method. Also, TDS measurements at OCP conducted on mm thick specimens would have difficulty detecting such high local hydrogen concentrations owing to the fact that specimen thicknesses used in planar electrode tests exceed the thin layer detected by NRA by many orders of magnitude. Thus NRA results detect high near surface hydrogen concentrations within tens of microns of the charging surface that is not consistent with Fickian transport of diffusible hydrogen. In summary, two possibilities exist: that high detected levels of local near-surface hydrogen reside in both lattice and trapped sites or that high levels of detected near-surface hydrogen are present in some other state (i.e., such as OH^- present

² One explanation is that the high hydrogen concentration detected by NRA is really hydrogen associated with OH^- instead of hydrogen at lattice or trap sites. In order for this to be possible the oxide film on the corroded surface and /or the dealloyed layer would have to reach 0.35 μm which appears unlikely given that typical oxide and dealloyed layer thicknesses (below the parting limit) are often restricted to less than 100 nm (0.1 μm).

in oxide films or dealloyed layers) that is mistaken for hydrogen within the bulk metal. The latter is not supported by layer thickness estimates in the literature associated with selective dissolution below the parting limit²³ but this assertion awaits further confirmation by Auger depth profiling. High hydrogen concentrations within the bulk metallic phase would be hard to attribute to lattice solubility alone since the electrochemical fugacity within active pits, albeit high, does not necessarily support such equilibrium concentrations assuming that the perfect solubility of hydrogen in PH 13-8 Mo is similar to that in iron²⁴ and the normal density of trap sites in such steels.¹² This is especially true at OCP where the hydrogen overpotential is hundreds of mV or less.

One alternative explanation is that hydrogen-vacancy or divacancy trap-like complexes formed at corroding surfaces account for a very high near-surface hydrogen concentration that would not be seen at equilibrium or normal quenched in vacancy concentrations. That is, that vacancy injection via corrosion concurrent with hydrogen production may produce abnormally high hydrogen concentrations restricted to limited surface regions. Few prior experiments have reported direct evidence of such a result, possibly because techniques with high spatial resolution have only recently become available and applied to H uptake in electrochemical charging at occluded sites.²⁵ However, high room temperature hydrogen concentrations recently have been observed in electrochemically charged Al^{26,27} and at Al crack tips.^{20,21} Little prior evidence of this phenomena has been reported in bcc stainless steel.

CONCLUSIONS

Exposure of a martensitic stainless steel to reducing acids and acidified chloride solution confirms that hydrogen uptake may occur under extreme cathodic polarization but also locally when pitting occurs at $x > x_{\text{HER}}$, and on planar electrodes at the deaerated open circuit potential that might be experienced by pits, cracks and crevices. Moreover, such occluded sites polarized to passive potentials but that experience sufficient IR drop could drop to potentials below reversible hydrogen. These local conditions for hydrogen uptake exist in technologically significant situations such as those involving reducing acid-chloride environments.

Pit scaling relationships can be used to rescale pits to sizes that enable spatially resolved quantification of local hydrogen concentrations in a martensitic stainless steel. Rescaling can be used to demonstrate and quantify hydrogen concentration as a function of position. The x^2/G type relationship was found to apply for passive-to-active potentials and the reversible hydrogen potential.

Local hydrogen uptake was demonstrated and quantified at $x > x_{\text{HER}}$ in a rescaled pit under conditions where the pit mouth remained in the passive region when the passive potential was just above the Flade potential. However, it is clear that more positive passive potentials would have not resulted in hydrogen uptake.

High hydrogen concentrations are observed on surfaces that undergo active dissolution and hydrogen production. The depths of this enhanced concentration profile exceeds

typical dealloyed and/or corrosion product layer thicknesses. Vacancy-hydrogen complexes provide one explanation for this observation.

ACKNOWLEDGMENTS

This work was funded by the Office of Naval Research under Grant No. N00014-98-1-0740 with Dr. A.J. Sedriks as contract monitor. Mr. Jason Lee provided significant help with the CREVICERv2 software. The CESE also is grateful to acknowledge the continued support of Princeton Applied Research and Scribner Associates, Inc.

REFERENCES

- ¹ C.F. Baes, Jr., R.E. Mesmer, The Hydrolysis of Metal Cations, Robert Krieger Publishing Co., Malabar FL, (1986).
- ² B.F. Brown, "Solution Chemistry Within Cracks in Steels," Stress Corrosion Cracking and Hydrogen Embrittlement of Iron Base Alloys, Eds., J. Hockmann and R. W. Staehle, NACE, Houston, TX, pp. 747-750, (1973).
- ³ C.T. Fujii, In Stress Corrosion Cracking - New Approaches, ASTM STP 610, ASTM, Philadelphia, PA, pp. 213-225, (1976).
- ⁴ W.R. Cieslak, R.E. Semarge, F.S. Bovard, "The Initiation of Pitting Corrosion in Martensitic Stainless Steels," Microbeam Analysis, editors: A.D. Romig, W.F. Chambers, pp. 303-306, (1986).
- ⁵ L.M. Young, M.R. Eggleston, H.D. Solomon, L.R. Kaisand, Materials Science and Engineering Journal, A203, p. 377, (1995).
- ⁶ P.S. Tyler, M. Levy, L. Raymond, Corrosion, 47, p. 82, (1991).
- ⁷ H.W. Pickering, "Status of the IR Mechanism for Describing Crevice Corrosion," NACE 2001 Topical Research Symposium, CORROSION 2001, eds. G.S. Frankel, J.R. Scully, NACE, Houston, TX, (2001).
- ⁸ R.G. Kelly, "Critical Factors and Challenges in Crevice Corrosion," NACE 2001 Topical Research Symposium, CORROSION 2001, eds. G.S. Frankel, J.R. Scully, NACE, Houston, TX, (2001).
- ⁹ B.G. Ateya, H.W. Pickering, J. Electrochem. Soc., 122, p. 1025, (1975).
- ¹⁰ S.W. Smith, Ph.D. Dissertation, The University of Virginia, (1995).
- ¹¹ S.W. Smith, J.R. Scully, "The Identification of Hydrogen Trapping States in an Al-Li-Cu-Zr Alloy Using Thermal Desorption Spectroscopy," Metallurgical and Materials Transactions A, 31A, pp. 179-193, (2000).
- ¹² J.R. Scully, J.A. Van Den Avyle, M.J. Cieslak, A.D. Romig, Jr., C.R. Hills: "The Influence of Palladium on the Hydrogen-Assisted Cracking Resistance of PH 13-8 Mo Stainless Steel", Metallurgical and Materials Transactions A, 22A, pp. 2429-2444, (1991).
- ¹³ H. Bakhru, U. of Albany, Department of Physics and School of Nanosciences and Nano Engineering, Albany, NY.

-
- ¹⁴ L.C. Feldman, J.W. Mayer, *Fundamentals of Surface and Thin Film Analysis*, North Holland, NY, p. 283, (1986).
- ¹⁵ H.W. Pickering, "Status of IR Mechanism for Describing Crevice Corrosion," NACE 2001 Topical Research Symposium, CORROSION 2001, eds. G.S. Frankel, J.R. Scully, NACE, Houston, TX, (2001).
- ¹⁶ K. Cho, M.I. Abdulsalam, H.W. Pickering, *J. Electrochem. Soc.*, 145, p. 1862, (1998).
- ¹⁷ J.N. Al-Khamis, H.W. Pickering, *J. Electrochem. Soc.*, 148, pp. B314, (2001).
- ¹⁸ R.J. Gest, A.R. Troiano, *Corrosion*, 30, p. 274-279, (1974).
- ¹⁹ A. Sehgal, B.G. Ateya, H.W. Pickering, *Acta Mater.* 45, p. 3389 (1997).
- ²⁰ G.A. Young, Jr., J.R. Scully, "The Effects of Test Temperature, Temper and Alloyed Copper on Hydrogen Controlled Crack Growth of an Al-Zn-Mg-(Cu) Alloy," *Metallurgical and Materials Transactions A*, 33A, pp. 1167-1181, (2002).
- ²¹ L.M. Young, G.A. Young, Jr., J.R. Scully, R.P. Gangloff, "The Effects of Electrode Potential and Temper on Environment Assisted Cracking in AA 7050," In *Light Weight Alloys for Aerospace Applications IV*, edited by E.W. Lee, W.E. Frazier, N.J. Kim. K. Jata, TMS, pp. 3-20, (1997).
- ²² C.R. Clayton, I. Olefjord, *Passivity of Austenitic Stainless Steels*, in *Corrosion Mechanisms in Theory and Practice*, ed. By P. Marcus, J. Oudar, pp. 175-199, (1995)
- ²³ B.G. Ateya, G.Geh, A.H. Carim, H.W. Pickering, *J. Electrochem. Soc.*, 149, pp. B27-33, (2002).
- ²⁴ N. Lewis, S.A. Attanasio, D.S. Morton, G.A. Young, in "Chemistry and Electrochemistry of Corrosion and Stress Corrosion Cracking," Ed. R.H. Jones, TMS, pp. 421-445, (2001).
- ²⁵ G.A. Young, Jr., J.R. Scully, "The Effects of Test Temperature, Temper and Alloyed Copper on Hydrogen Controlled Crack Growth of an Al-Zn-Mg-(Cu) Alloy," *H-CDI Conference Proceedings*, Ed. N. Moody, A.W. Thompson, TMS, (2002).
- ²⁶ C.E. Buckley, H.K. Birnbaum, *J. of Alloys and Compounds*, 330-332, pp. 649-653 (2002).
- ²⁷ C.E. Buckley, H.K. Birnbaum, J.S. Lin, S. Spooner, D. Bellmann, P. Staron, T.J. Udovic, E. Hollar, *J. of Applied Crystallography*, 34, pp. 119-129, (2001).

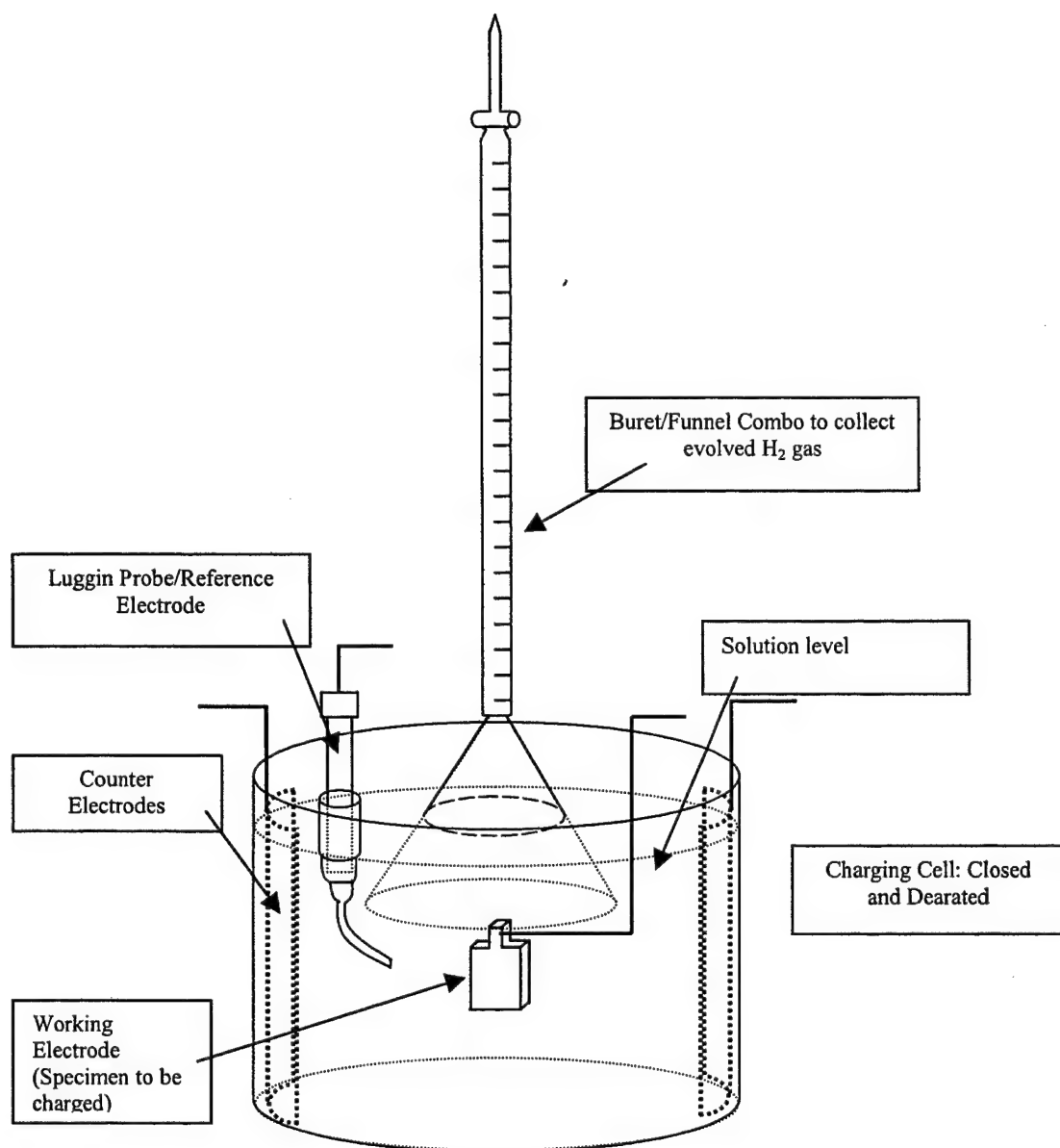


Figure 1. Charging cell equipped with buret/funnel combination to collect total hydrogen gas evolved from the HER reaction during potentiostatic polarization experiments involving planar electrodes with minimal IR drop.

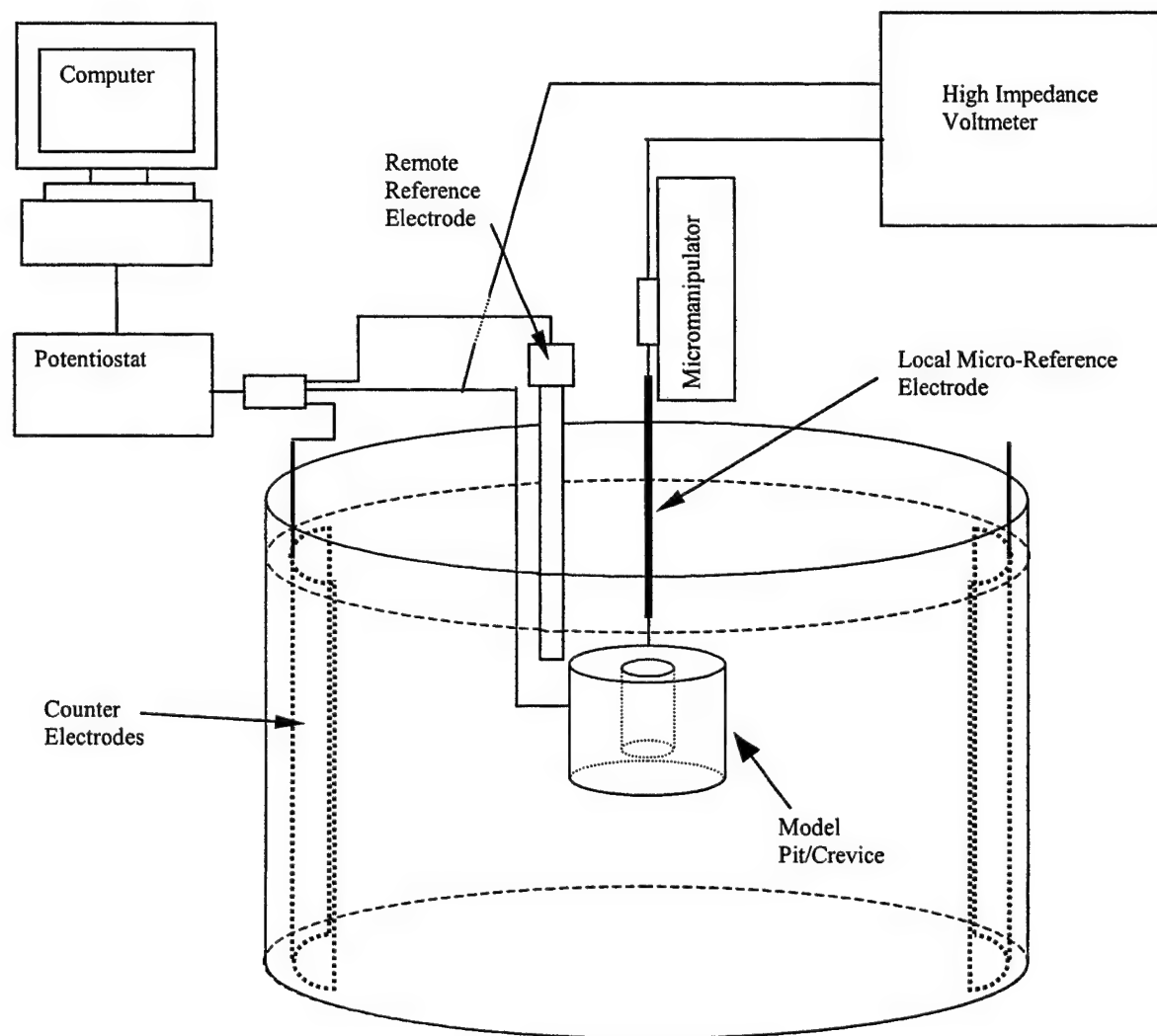


Figure 2. Test cell for measuring local potentials in model rescaled pit electrodes consisting of a cylindrical cavity. The local potential can be monitored in the cavity using a micro-reference electrode. The external reference electrode is used to control the applied potential.

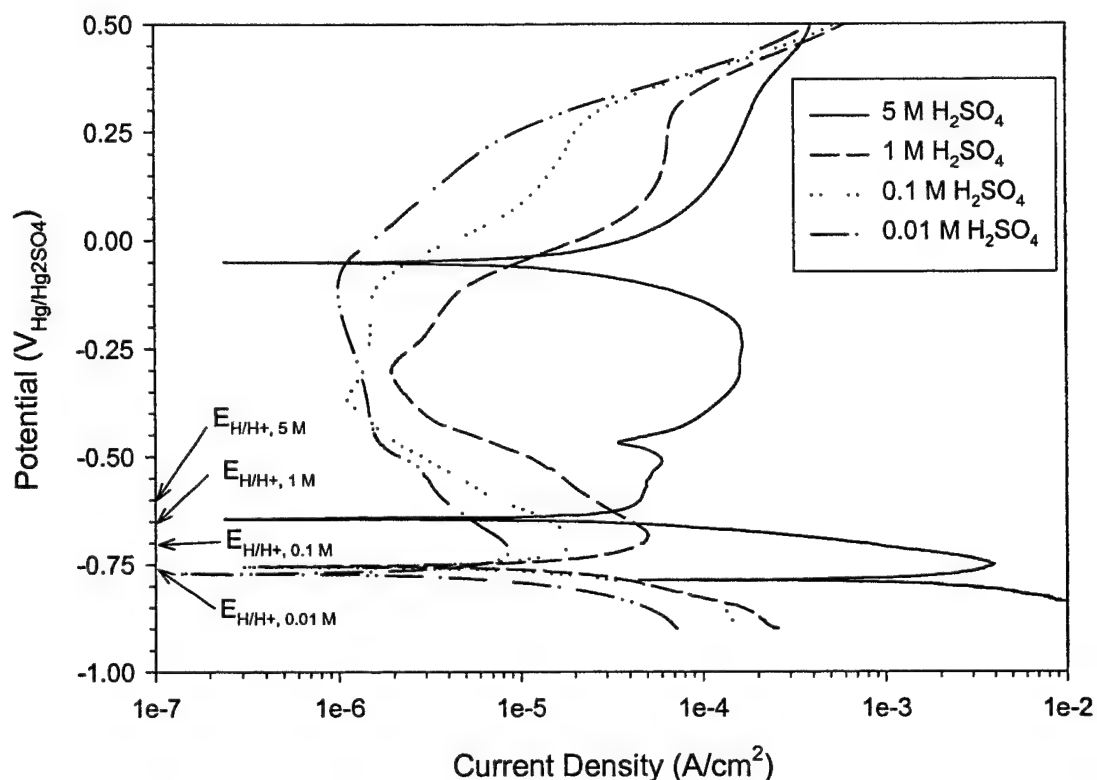


Figure 3. Anodic E-Log(i) data for planar PH 13-8 Mo alloy exposed to various deaerated sulfuric acid plus 0.1 M Fe^{+2} , 0.018 M Cr^{+3} and 0.01 M Ni^{+2} solutions at 25 °C. The sulfuric acid concentration was varied as indicated in the key. Measurements taken versus a $\text{Hg}/\text{Hg}_2\text{SO}_4/\text{K}_2\text{SO}_4$ reference electrode.

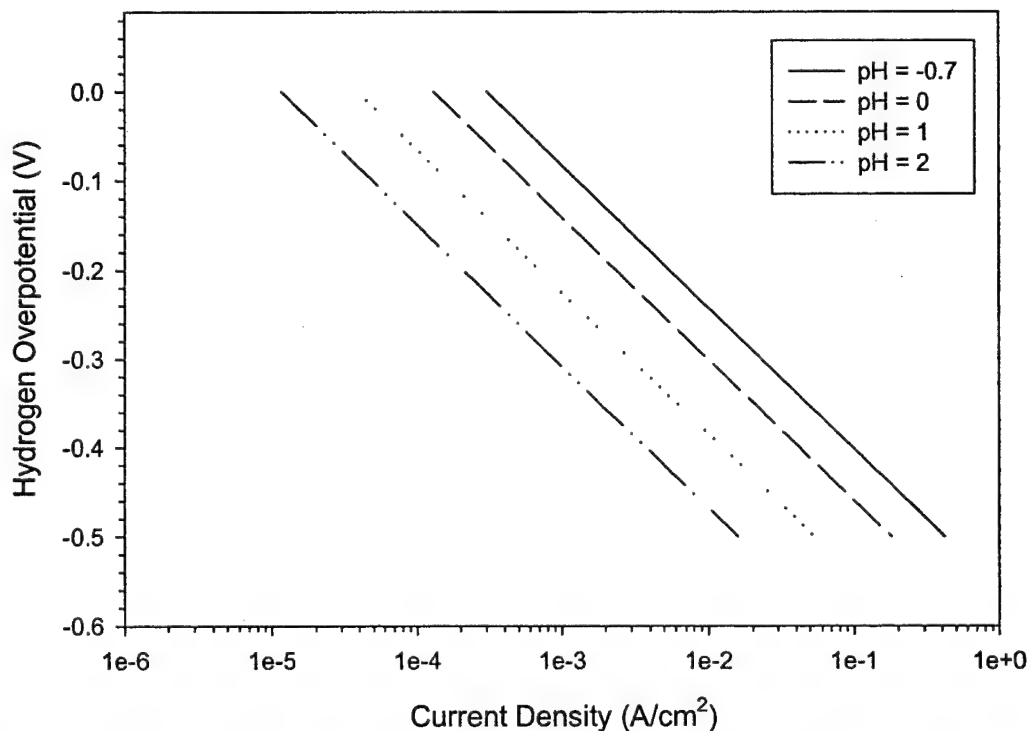


Figure 4. Cathodic hydrogen overpotential versus true cathodic current density for planar PH 13-8 Mo alloy exposed to deaerated sulfuric acids of various concentrations plus 0.1 M Fe^{+2} , 0.018 M Cr^{+3} and 0.01 M Ni^{+2} solutions at 25 °C.

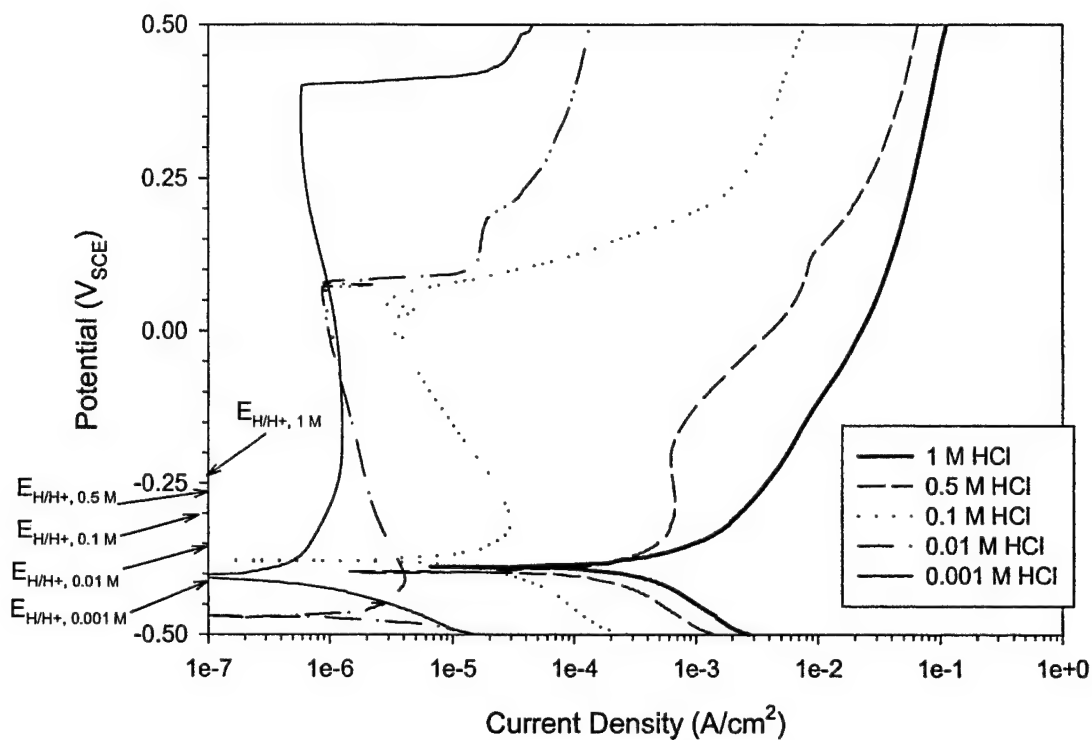


Figure 5. Anodic E-Log(i) data for PH 13-8 Mo alloy in planar electrode configuration exposed to various deaerated hydrochloric acid solutions at 25°C. Measurements taken versus a saturated calomel reference electrode.

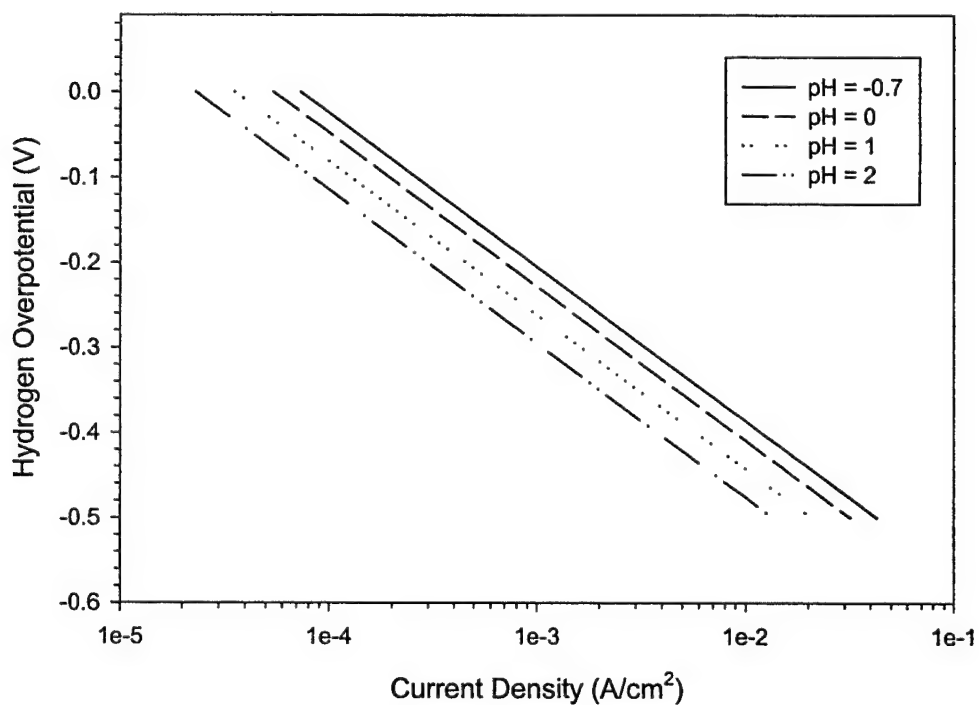


Figure 6. Cathodic hydrogen overpotential versus true cathodic current density for PH 13-8 Mo alloy in planar electrode configuration exposed to deaerated hydrochloric acid solutions of various concentrations at 25 °C.

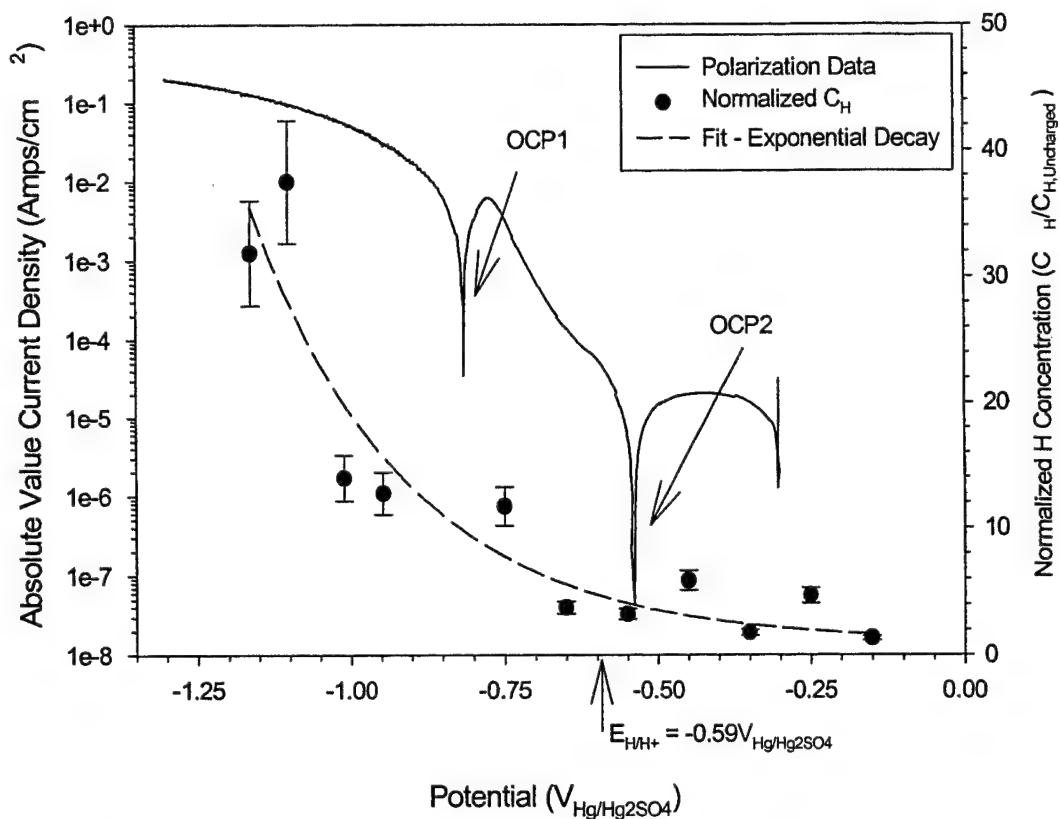


Figure 7. Relationship between C_H versus E_{true} for PH 13-8 Mo planar electrodes in deaerated 5 M H_2SO_4 plus dissolved metal salts at 25°C (IR corrected).

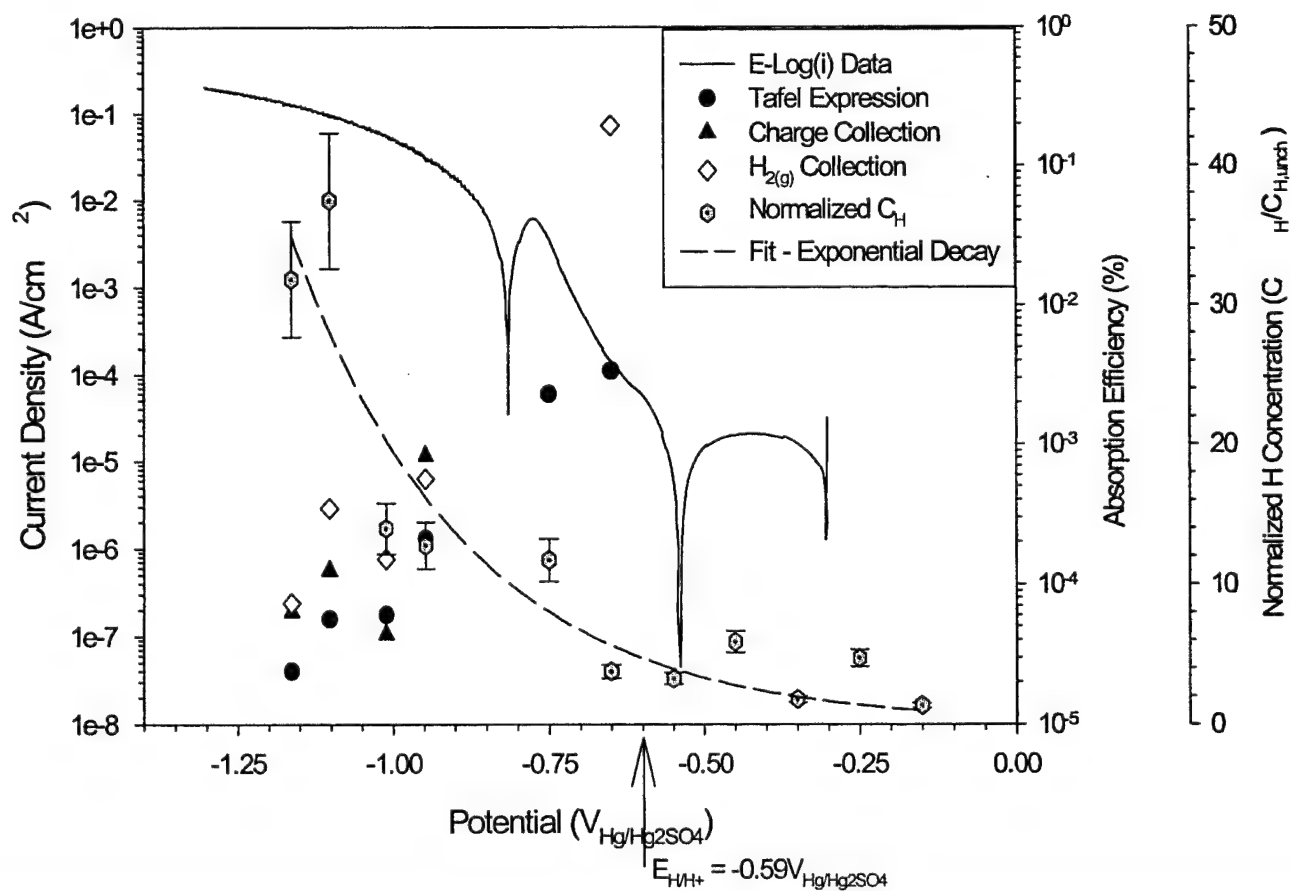


Figure 8. Hydrogen absorption efficiency vs. potential for different charge collection methods on planar electrodes of PH 13-8 Mo charged in deaerated 5 M H_2SO_4 plus dissolved metal ions at 25 °C.

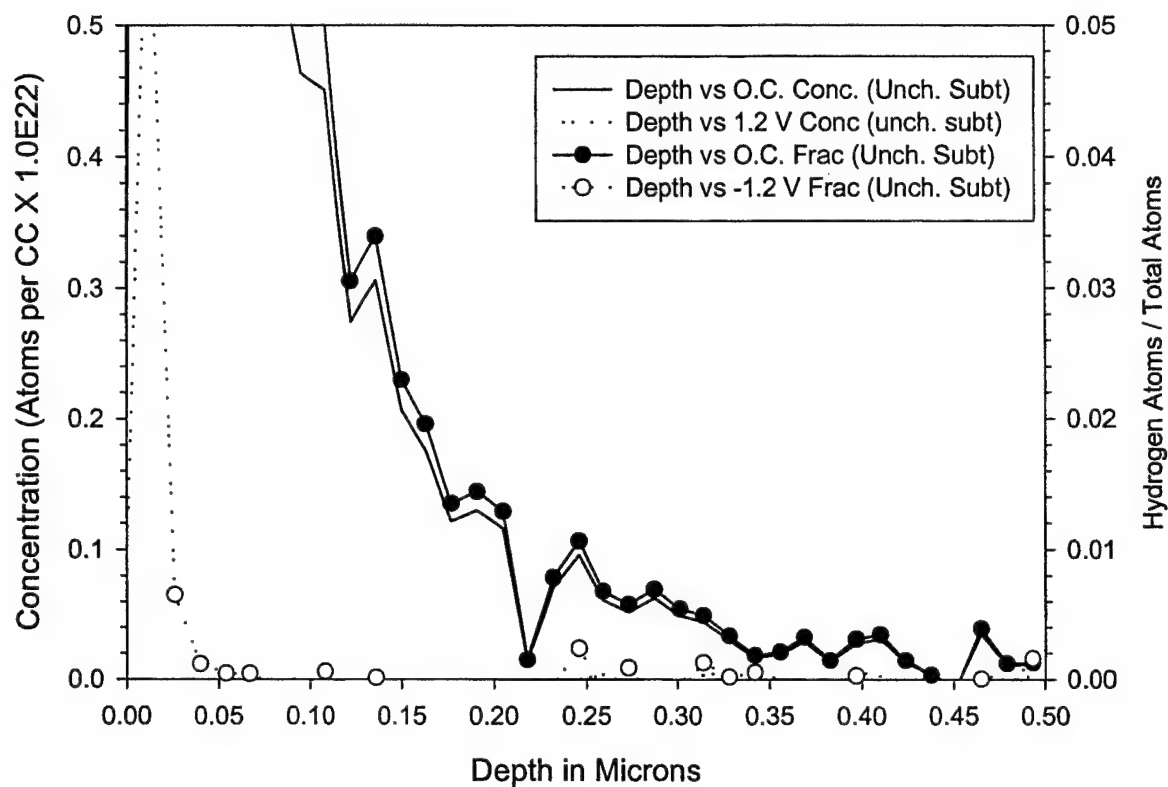


Figure 9. NRA results for flat PH 13-8 Mo electrodes charged at OCP and $-1.2 V_{\text{Hg/Hg}_2\text{SO}_4}$ for 1 hour. Samples were charged in deaerated 5 M H_2SO_4 plus dissolved metal salts at 25 °C and cleaned with methanol prior to NRA analysis. The background hydrogen profile obtained from uncharged specimens was subtracted from the data shown.

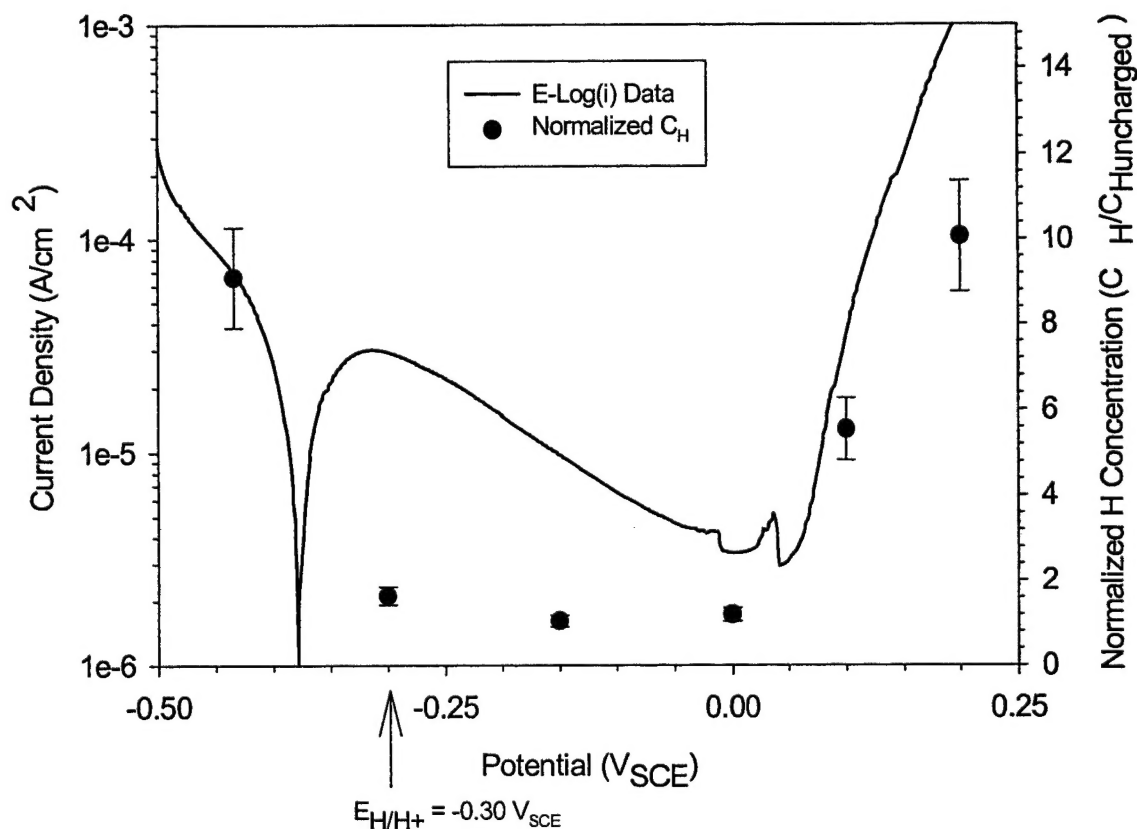
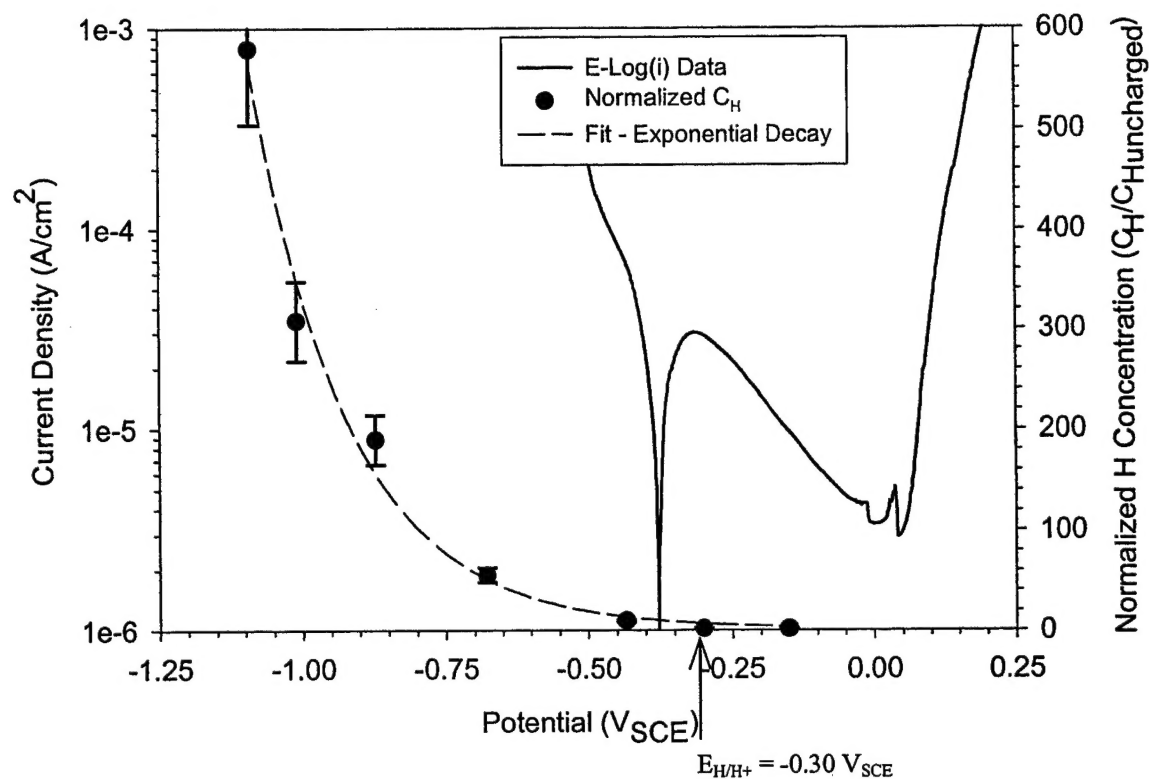


Figure 10. Relationship between C_H versus E_{true} from planar PH 13-8 Mo electrodes in deaerated 0.1 M HCl at 25°C (IR corrected). Top Figure illustrates exponential fit to data from near reversible hydrogen toward negative applied potentials (data at anodic potentials is omitted). Bottom plot illustrates enlarged view of hydrogen absorption near open circuit and after anodic polarization.

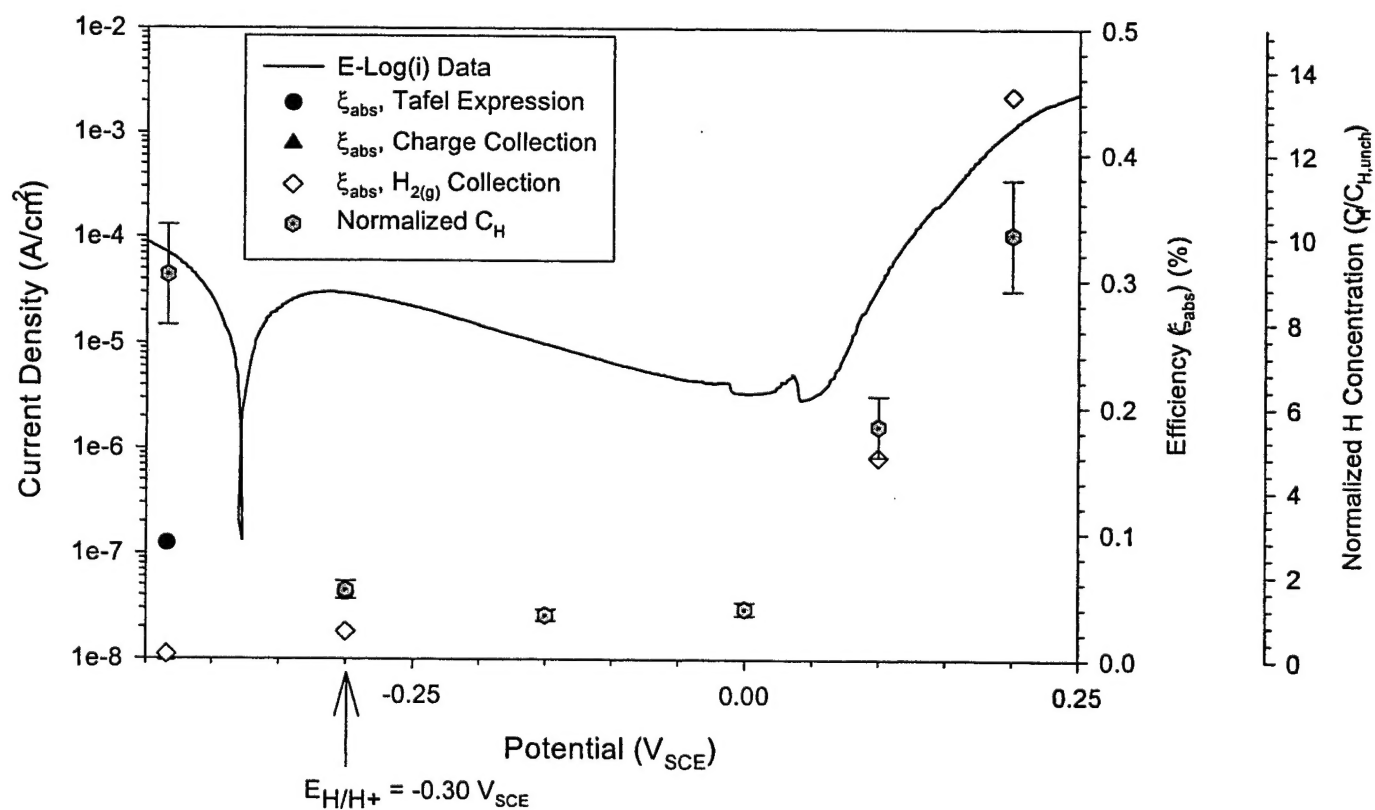
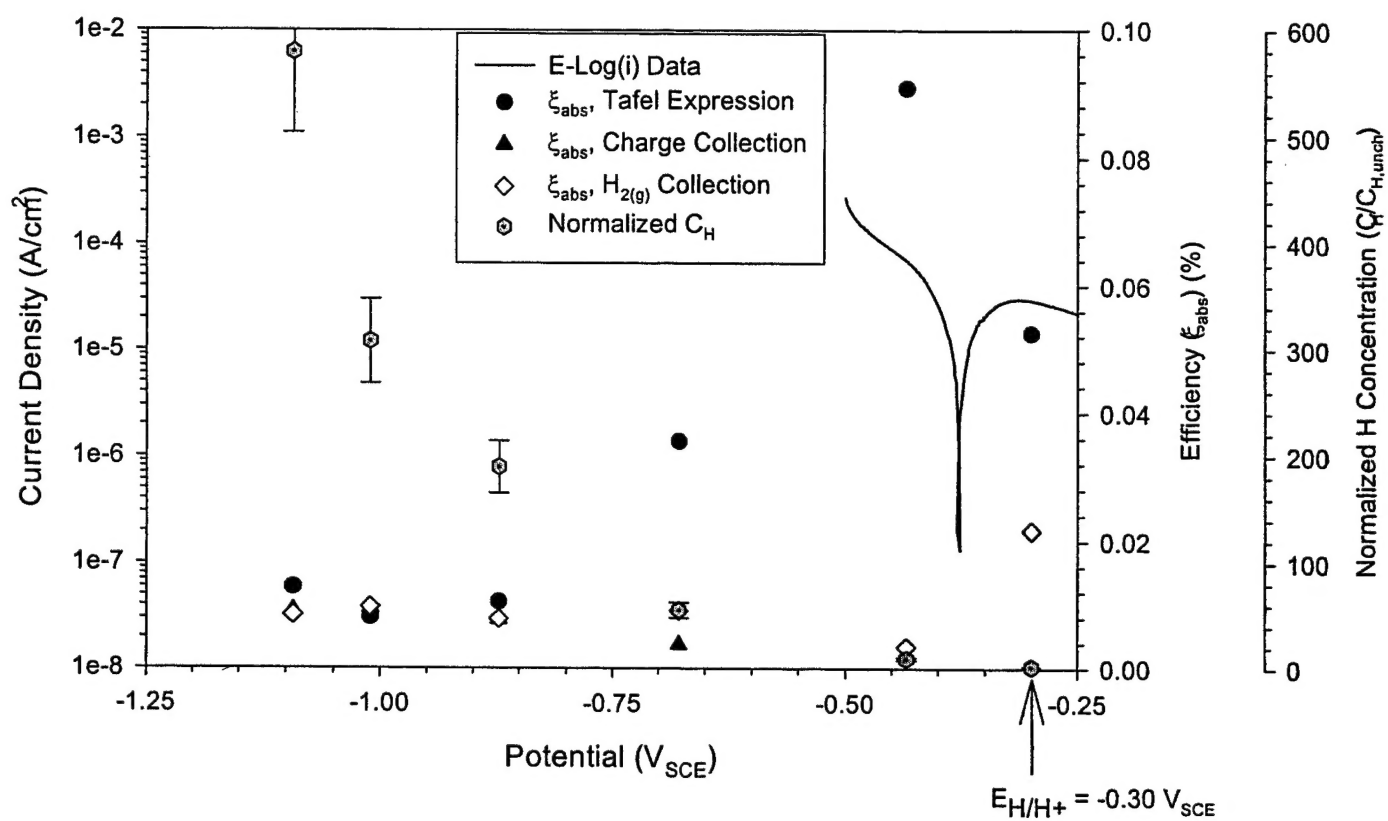


Figure 11: Hydrogen absorption efficiency data obtained from different HER charge collection methods on bulk electrodes of PH 13-8 Mo charged in deaerated 0.1 M HCl at 25 °C.

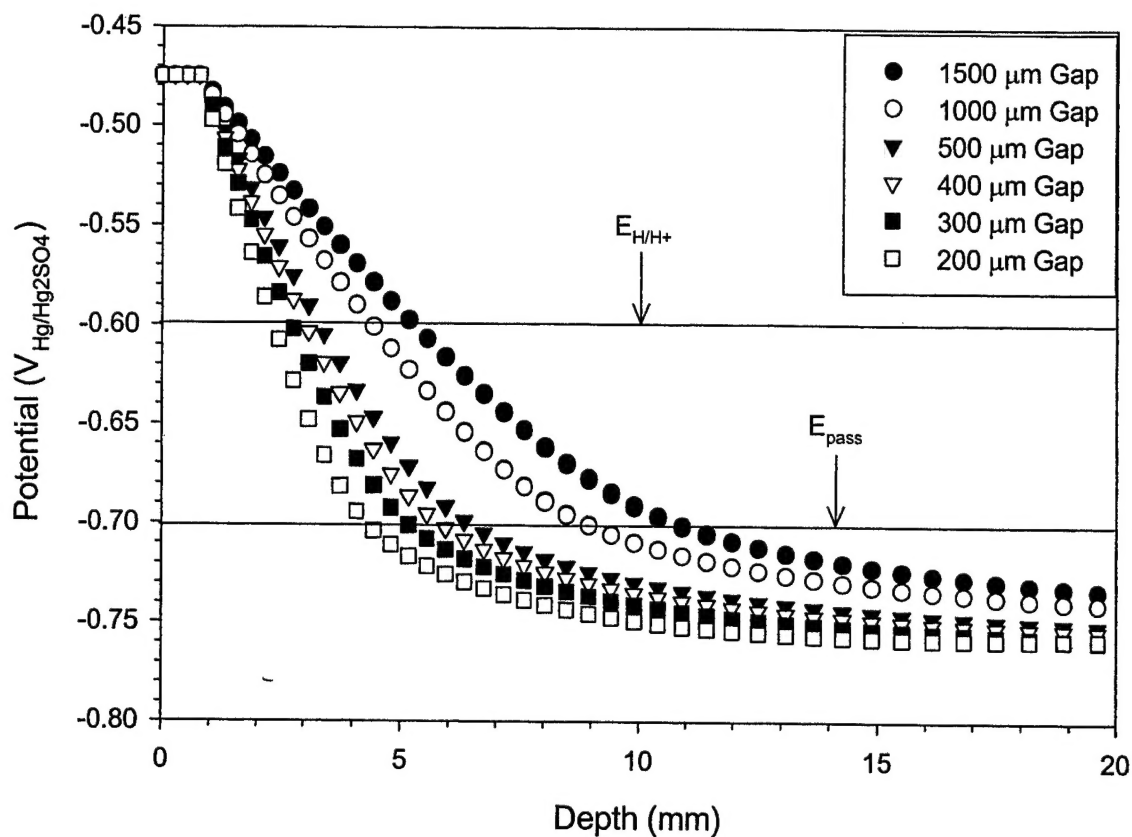


Figure 12. Theoretical potential versus depth data using the 0.1 M sulfuric acid plus dissolved metal ions E-Log(i) curve shape modified with the 5 M sulfuric acid plus metal ions parameters. Assumed externally applied potential was $E_{app} = -0.475 V_{Hg/Hg_2SO_4}$.

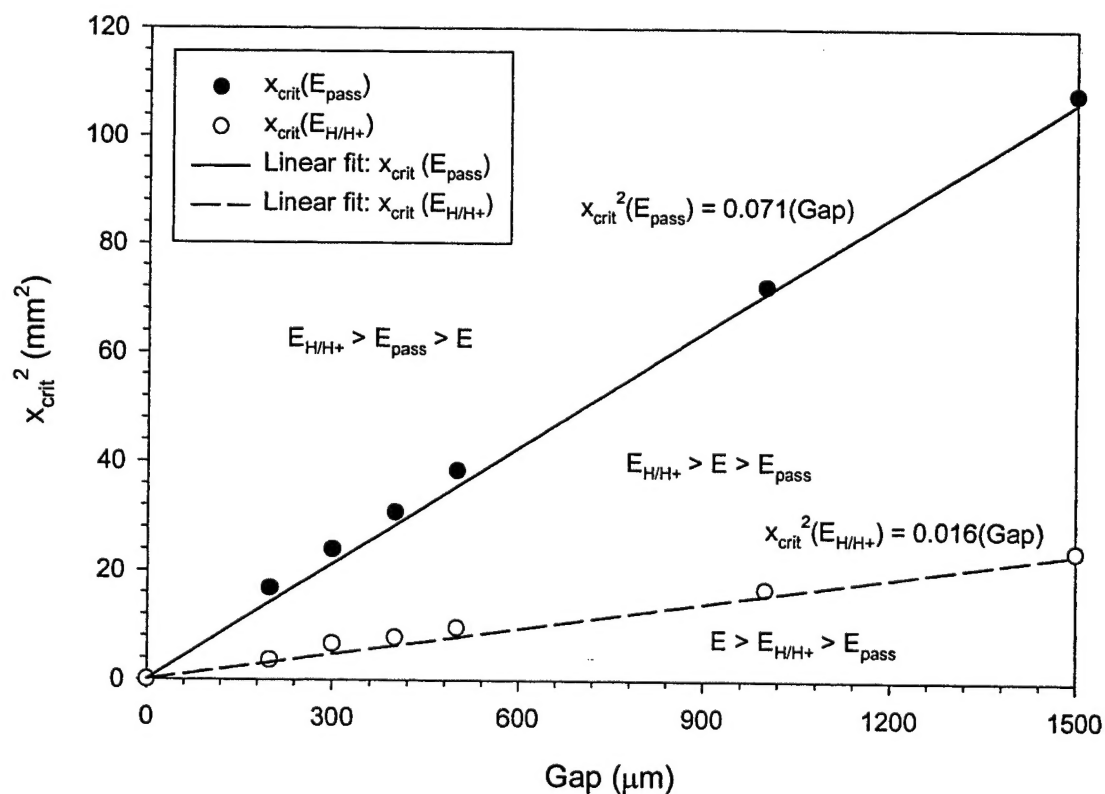


Figure 13. x_{crit}^2 versus gap data as modeled by the CREVICERv2 program. Two x_{crit} parameters are plotted for conditions: $i_{crit} = 10^{-2} A/cm^2$, $E_{H/H+} = -0.59 V_{Hg/Hg_2SO_4}$, $E_{pass} = -0.70 V_{Hg/Hg_2SO_4}$, $E_{app} = -0.475 V_{Hg/Hg_2SO_4}$

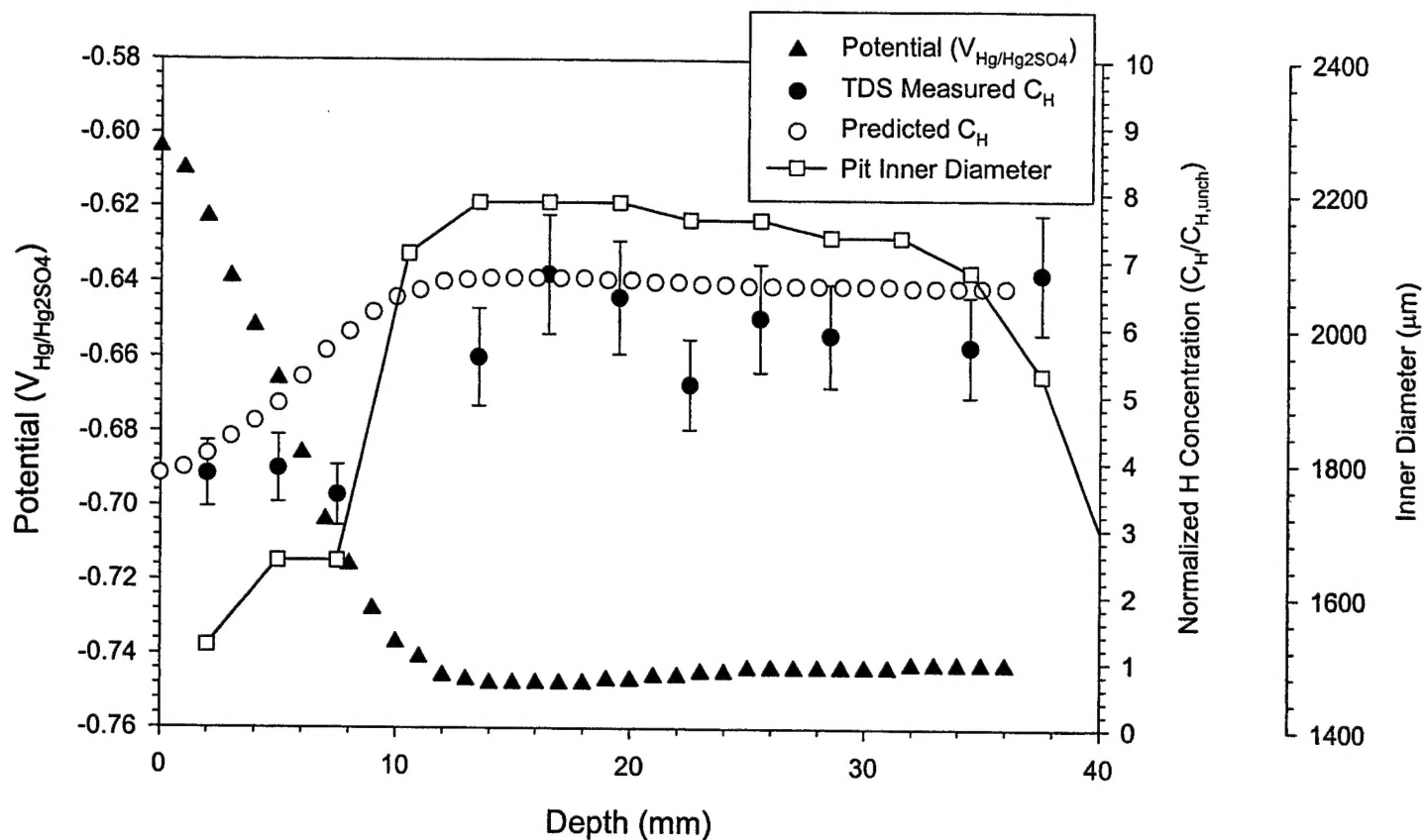


Figure 14. Potential, predicted C_{H} , measured C_{H} and pit diameter from scaled experimental pit for a 1500 μm gap by 40 mm depth cylinder exposed to 5 M sulfuric acid plus dissolved metal ions. $E_{\text{app}} = -0.60 V_{\text{Hg/Hg}_2\text{SO}_4}$.

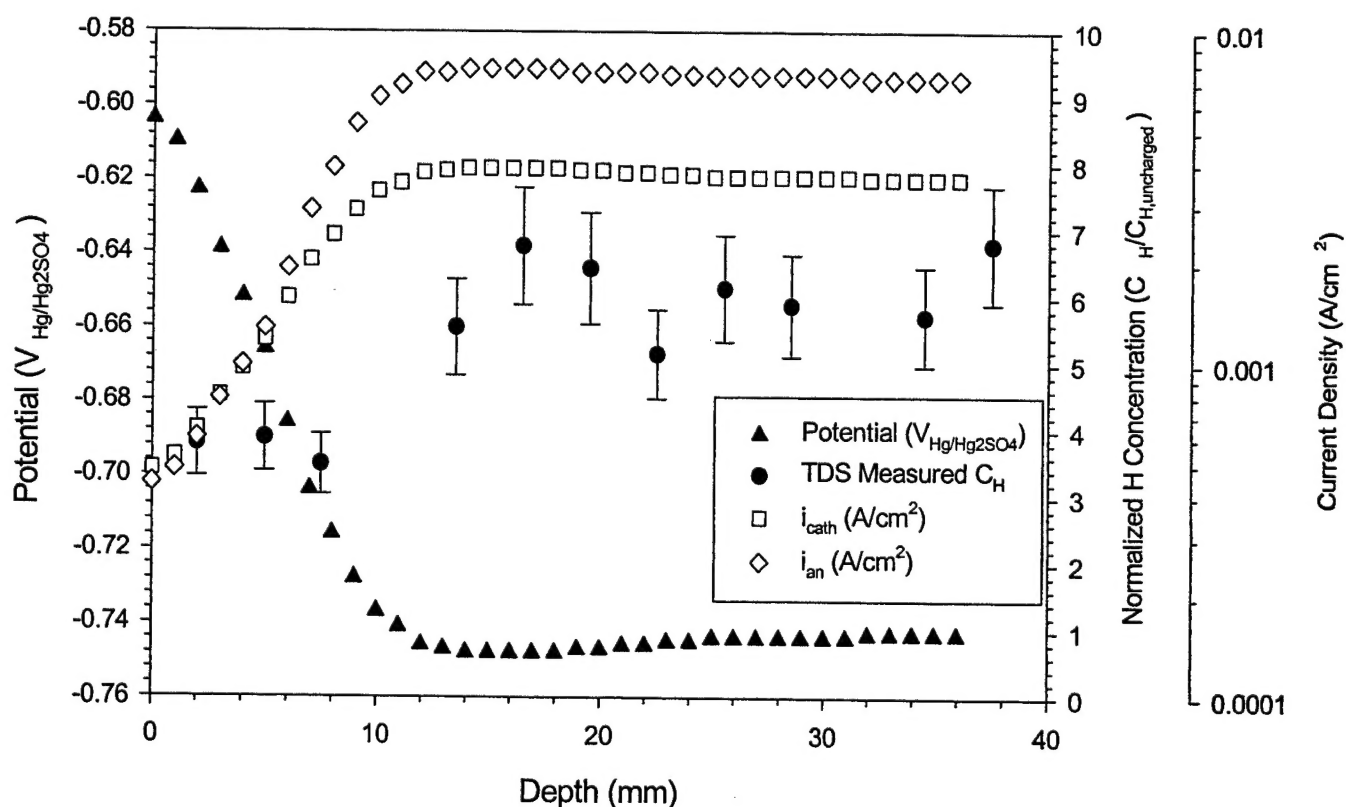


Figure 15. Potential, anodic and cathodic half cell current densities, and measured C_{H} results from scaled experimental pit for a 1500 μm gap by 40 mm depth cylinder exposed to 5 M sulfuric acid plus dissolved metal ions. $E_{\text{app}} = -0.60 V_{\text{Hg/Hg}_2\text{SO}_4}$.